

---

<sup>b</sup>  
**UNIVERSITÄT  
BERN**

# **A new Time-Of-Flight Mass Spectrometer (TOF-MS) for noble gas analysis**

Inauguraldissertation  
der Philosophisch-naturwissenschaftlichen Fakultät  
der Universität Bern

vorgelegt von

**Ramakrishna Ramisetty**

von Andhra Pradesh, India

2015

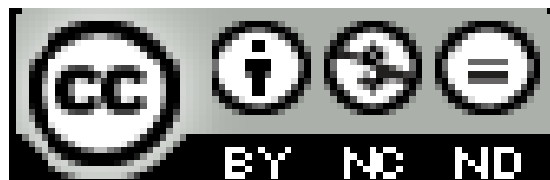
Leiter der Arbeit:

**Prof. Dr. Ingo Leya**

Physikalisches Institut, Universität Bern



Original document saved on the web server of the University Library of Bern



This work is licensed under a  
Creative Commons Attribution-Non-Commercial-No derivative works 2.5 Switzerland  
licence. To see the licence go to <http://creativecommons.org/licenses/by-nc-nd/2.5/ch/> or  
write to Creative Commons, 171 Second Street, Suite 300, San Francisco, California 94105,  
USA.

## Copyright Notice

This document is licensed under the Creative Commons Attribution-Non-Commercial-No derivative works 2.5 Switzerland. <http://creativecommons.org/licenses/by-nc-nd/2.5/ch/>

### You are free:

to copy, distribute, display, and perform the work

### Under the following conditions:



**Attribution.** You must give the original author credit.



**Non-Commercial.** You may not use this work for commercial purposes.



**No derivative works.** You may not alter, transform, or build upon this work.

For any reuse or distribution, you must take clear to others the license terms of this work.

Any of these conditions can be waived if you get permission from the copyright holder.

Nothing in this license impairs or restricts the author's moral rights according to Swiss law.

The detailed license agreement can be found at:

<http://creativecommons.org/licenses/by-nc-nd/2.5/ch/legalcode.de>

**A new Time-Of-Flight Mass Spectrometer (TOF-MS) for  
noble gas analysis**

Inauguraldissertation  
der Philosophisch-naturwissenschaftlichen Fakultät  
der Universität Bern

vorgelegt von  
**Ramakrishna Ramisetty**  
von Andhra Pradesh, India

Leiter der Arbeit  
**Prof. Dr. Ingo Leya**  
Physikalisches Institut, Universität Bern

Von der Philosophisch-naturwissenschaftlichen Fakultät  
angenommen.

**Bern, 08.07.2015**

**Der Dekan**  
**Prof. Dr. Gilberto Colangelo**



## **Dedicated to**

*This dissertation is dedicated to all my beloved **Teachers** those who enriched my knowledge...*

**Guru Brahma Guru Vishnu Guru Devo Maheshwara**

**Guru Sakshath Parambrahma Tasmai Shri Gurave Namaha**

*(The teacher is verily representative of Brahma (creator), Vishnu (preserver), Siva (destroyer); he creates, sustains the knowledge and destroys the weeds of ignorance. I offer all my efforts to those great teachers.)*





# Acknowledgments

First of all, I would like to thank my adviser **Prof. Dr. Ingo Leya** for giving me the opportunity and to write my PhD thesis. I am glad to say that Ingo Leya is wonderful PhD adviser and I inspired a lot by his extensive knowledge in physics and realistic thoughts in research. He provided cool atmosphere to work with free mind and encouraged me always towards the best. I never forget his support not only in research but also for my personal life. I always need, expect his wonderful guidance and support for my entire career.

My special thanks to Dr. Bernard Lavielle, CNRS Research Director from CENBG of University of Bordeaux for refereeing this work and he is the great inspiration for young experimental researchers like me. I am very lucky to have him as external referee.

I would like to thank Dominic Abplanalp for introducing to the EGT and his support. I also thank our wonderful technicians Patrick Enderli and Hans Erich for their great support at the machine and helped a lot me to finish my work. I cannot forget the help from the electronics department especially by Jürg Jost and Nussbaum Roland and thank you so much.

I would like to thanks to Prof. Dr. Peter Wurz for his support, very useful discussions and nice lectures which were helped me for better understanding the mass spectrometer and true inspiration to my mass spectrometric career.

I owe my thanks to Dr. André Bieler for introducing me to Python. My special thanks to Dr. Riedo Andreas, Hofer Lukas, and Meyer Stefan for their support and discussions.

My sincere thanks to Prof. Dr. Willy Benz for his support and inspired a lot from his interesting presentations.

I would like to thank Prof. Dr.N.Satyanarayana for his constant encouragement and Prof.Dr.S.V.S.Nageswara Rao for motivating towards research.

Further I owe many thanks to Dr. Thomas Smith for his great support and friendship. Our “bis milch pauses” were the one of the best times of PhD. Thank you so much for being with me and sharing all the things and also expect this forever. Also my special thanks to Peter Stephenson for his great support at all the time.

Many thanks to my Noble gas cosmochemistry group members Dr. Roth Antoine and Mészáros Marianna.

Many thanks to Dr. Vera Bhadra Rao, Dr.Nataraj, Sankar, and Pawan for their extensive support here in Bern.

I would like thank Geissbühler Urs and Borrini Gaetano for their great support for the software.

I would to thanks my former secretaries Graze and Amal for their great help at beginning of PhD and also many thanks to Gisela Herren, Weyeneth Katharina, Rothenbühler Tina, Brigitte Oggier for their effortless support at this office. My sincere appreciations to all the people in the physics institute individually.

My special thanks to the dearest friends Maraka.H, Bandaru.S, Sampath.SS, Ganisetty.S and also to Samatham.S, Endu.S for constant support in my life. My thanks to my uncle D.Saravana Kumar and family for their encouragement and support during my education.

I would like to thank my parents and family members for all their support for my education. Finally, I would to thanks my sweet wife for her great support, care, encouragement and this work would not have been possible without her patience. My wholehearted thanks to my little son Tanuj, he is new energy of my life and he never disturbed me during this work.

This work was funded by the Swiss National Science Foundation and the Kanton of Bern and thanks a lot for funding.

# Abstract

Noble gas analysis in early solar system materials, which can provide valuable information about early solar system processes and timescales, are very challenging because of extremely low noble gas concentrations (ppt). We therefore developed a new compact sized (33 cm length, 7.2cm diameter, 1.3 L internal volume) Time-of-Flight (TOF) noble gas mass spectrometer for high sensitivity. We call it as Edel Gas Time-of-flight (EGT) mass spectrometer. The instrument uses electron impact ionization coupled to an ion trap, which allows us to ionize and measure all noble gas isotopes. Using a reflectron set-up improves the mass resolution. In addition, the reflectron set-up also enables some extra focusing. The detection is via MCPs and the signals are processed either via ADC or TDC systems.

The objective of this work is to understand the newly developed Time-Of-Flight (TOF) mass spectrometer for noble gas analysis in presolar grains of the meteorites.

Chapter 1 briefly introduces the basic idea and importance of the instrument. The physics relevant to time-of-flight mass spectrometry technique is discussed in the Chapter 2 and Chapter 3 will present the oxidation technique of nanodiamonds of the presolar grains by using copper oxide. Chapter 4 will present the details about EGT data analysis software. Chapter 5 and Chapter 6 will explain the details about EGT design and operation. Finally, the performance results will be presented and discussed in the Chapter 7, and whole work is summarized in Chapter 8 and also outlook of the future work is given.



# Table of Contents

<b>Chapter 1 : Introduction.....</b>	<b>1</b>
<b>Chapter 2 : Time-of-flight mass spectrometry .....</b>	<b>3</b>
2.1 Introduction to time-of-flight mass spectrometry (TOF-MS) .....	3
2.1.1 Principle of TOF-MS.....	3
2.1.2 Linear TOF .....	5
2.1.3 Reflectron TOF.....	7
2.2 Electron Impact (EI) ion storage source.....	8
2.2.1 Electron Impact Ionization (EI).....	8
2.2.2 Ion Storage and Extraction .....	9
2.2.3 Extraction Pulser .....	10
2.3 Ion Detectors .....	10
2.3.1 Microchannel plates (MCP) .....	10
2.4 Data Acquisition Systems .....	13
2.4.1 Time to Digital Converters (TDC) .....	13
2.4.2 Analog to Digital Converters.....	13
<b>Chapter 3 : Oxidation of nanodiamonds.....</b>	<b>15</b>
3.1 Introduction .....	15
3.2 Oxidation of nanodiamonds using Copper-Oxide (CuO).....	15
3.3 Laboratory setup of EGT Combustor .....	16
3.4 Experimental Procedure .....	16
3.5 Experimental Results.....	18
3.5.1 Sample 1, CuO from Goodfellow®.....	18
3.5.2 Sample 2, CuO from Acros® .....	21
3.5.3 Sample 3, CuO from Elemental Micro Analysis® .....	22
3.5.4 Discussion .....	24
3.6 Conclusions .....	25
<b>Chapter 4 : EGT Data analysis .....</b>	<b>27</b>
4.1 Introduction to mass spectrometer software.....	27
4.2 EGT Data acquisition methods.....	27
4.2.1 Time to Digital Converter or Ion Counting mode (TDCs).....	27
4.2.2 Analog to Digital Converters (ADCs).....	28
4.3 EGT Data Analysis Software (EGT-DAS) .....	28
4.3.1 Introduction to the data analysis software .....	28

4.3.2	Software information and compatibility .....	29
4.3.3	Graphical User Interface of EGT-DAS .....	29
4.4	Introduction data handling .....	30
4.5	Peak area determination .....	34
4.5.1	Peak selection and baseline correction .....	34
4.5.2	Smoothing and Signal-To-Noise ratio calculation .....	36
4.5.3	Mass resolution.....	38
4.5.4	Peak Area Calculation .....	38
4.5.5	Monte Carlo integration (MCI) .....	38
4.5.6	Area calculation by peak fitting .....	39
4.5.7	Error Analysis.....	42
4.6	Output data file.....	42
<b>Chapter 5 : EGT-MS Design &amp; Development .....</b>		<b>43</b>
5.1	EGT-MS Introduction and motivation .....	43
5.2	EGT Design and characteristics .....	44
5.2.1	Ion Source.....	45
5.2.2	Drift tube & Reflectron .....	51
5.2.3	Detector .....	52
5.3	Pre-amplifier (Limiter) .....	53
5.4	Data acquisition system.....	53
5.5	MoRaMi Voltage control system .....	54
5.6	Vacuum and purification system and its control .....	54
5.7	Calibration gas and its control system.....	54
<b>Chapter 6 : EGT Operational Manual &amp; Troubleshooting Guide .....</b>		<b>57</b>
6.1	Pre-operational conditions.....	58
6.1.1	EGT Feedthrough connections .....	59
6.1.2	MoRaMi voltage connections.....	59
6.1.3	Pulser, Limiter, and filament connections .....	59
6.2.	EGT Start-Up procedure .....	60
6.3.	EGT Tuning.....	62
6.3.1	EGT Optimizer Manual.....	62
6.3.2	Manual Tuning .....	69
6.4.	Measurement procedure for Calibration gas .....	69
6.5.	Shutdown or Rest mode .....	71
6.6.	Trouble shooting guide of the EGT.....	72

<b>Chapter 7 : EGT Performance-Results &amp; Discussion.....</b>	<b>73</b>
7.1 Tuning results of EGT.....	73
7.1.1 Ion optical simulations results with SIMION.....	73
7.1.2 EGT optimizer tuning results .....	73
7.1.3 Manual tuning.....	74
7.1.4 Conclusions .....	75
7.2 EGT data analysis software (EGT-DAS) results.....	76
7.2.1 EGT-DAS Monte Carlo Integration (MCI) results.....	76
7.2.2 EGT-DAS EMG fit area results .....	78
7.2.3 Mass calibration .....	79
7.3 Pulser performance and storage characteristics.....	81
7.4 Measurements Methods and Results .....	83
7.4.1 ADC measurements and Results .....	83
7.4.2 TDC Measurements and Results .....	90
7.4.3 MCP Performance tests .....	91
7.4.4 Filament performance tests.....	92
7.5 Noble gas calibrations .....	94
7.5.2 Kr and Xe calibrations using the TDC card .....	98
7.5.3 Ar calibrations and dilutions .....	101
7.6 Mass Resolution of the whole mass range .....	107
<b>Chapter 8 : Summary &amp; Outlook .....</b>	<b>109</b>
<b>Appendix A .....</b>	<b>111</b>
A.1 Copper Oxide Combustion for Oxygen production.....	111
Appendix A.2: Amount of CuO for 10 mbar of oxygen .....	113
Appendix A.3: Amount oxygen required of oxidation.....	114
<b>Appendix B.....</b>	<b>115</b>
Appendix B.1: TDC hardware.....	115
Appendix B.2: ADC hardware .....	118
<b>Appendix C: Glossary .....</b>	<b>121</b>
<b>D: References .....</b>	<b>122</b>

## List of Tables

S.No.	Table Name	Page No.
1	<b>Table 2.1:</b> First ionization potentials of different elements (Radzig, 1985) and most commonly the electron beam is accelerated to energy of about 60 eV.)	9
2	<b>Table 2.2:</b> LSB values by resolution and reference voltage of ADC	14
3	<b>Table 3.1:</b> Oxygen desorption and absorption data for Sample 1 (GOODFELLOW, 99.99 % purity, 10 $\mu\text{m}$ mesh): The upper area (pink shaded) gives the oxygen pressure as a function of increasing heating temperature. The lower area (green shaded) gives the oxygen pressure as a function of decreasing temperature, i.e., while cooling.	20
4	<b>Table 3.2:</b> Oxygen desorption and absorption data. The upper area (pink shaded) gives the data for oxygen desorption as a function of increasing heating temperature and the lower area (green shaded) gives the oxygen pressure as a function of temperature during cooling.	22
5	<b>Table 3.3:</b> Oxygen desorption and absorption data. The upper (pink shaded) data area gives the data for oxygen desorption (increasing temperature) and the lower area (green shaded) gives the data for oxygen absorption (cooling).	23
6	<b>Table 3.4:</b> Total oxygen released at 860 <sup>0</sup> C from CuO samples with different grain sizes for two successive cycles.	25
7	<b>Table 4.1:</b> Information regarding ADC data acquisition settings in the data acquisition file.	33
8	<b>Table 5.1:</b> The technical details of the EGT are as mentioned in the.	45
9	<b>Table 5.2:</b> The basic characteristics of the used pulser (Montena <sup>®</sup> ).	49
10	<b>Table 6.1:</b> EGT general trouble shooting guide.	72
11	<b>Table 7.1(a):</b> Source voltages from SIMION ion optical simulations, EGT optimizer, and manual tuning for a 10 kHz pulse frequency.	74
12	<b>Table 7.1(b):</b> Reflectron voltages from SIMION ion optical simulations, EGT optimizer, and manual tuning for 10 kHz pulse frequency.	75
13	<b>Table 7.2:</b> Area with Monte Carlo Integration for known shapes: a triangle and a sinusoidal peak. The error in the MCI is decrease with increase in random numbers.	78
14	<b>Table 7.3:</b> EGT-DAS results for Kr isotopes on MCI.	78
15	<b>Table 7.4:</b> EGT-DAS results for Kr isotopes with EMG fitting function.	78
16	<b>Table 7.5:</b> Testing the Micro channel plates by measuring the strip current. The data show that the strip current is proportional to the applied voltage, indicating that the MCPs are working as expected.	91



## List of Figures

S.No.	Figure Name	Page No.
1	<b>Figure 2.1:</b> Ions with mass $m$ and charge $q$ are accelerated in potential difference $U$ towards the detector.	4
2	<b>Figure 2.2:</b> Linear TOF-MS, separation of different ions based on their mass with respect to flight time.	5
3	<b>Figure 2.3:</b> Schematic diagram of Linear-TOF representing different regions of ion trajectory.	6
4	<b>Figure 2.4:</b> Reflectron TOF, ions with same mass but having slightly starting velocities reach the detector simultaneously thanks to the focusing of the reflectron.	8
5	<b>Figure 2.5:</b> Schematic diagram of electron impact ionization.	9
6	<b>Figure 2.6:</b> A microchannel plate (MCP) cutaway view that explains the operational procedure of each channel. (Picture: Hamamastu (2006)).	11
7	<b>Figure 2.7:</b> Chevron (2-stage MCPs) and Z-stack (3-stage MCPs) configurations of MCPs.	12
8	<b>Figure 2.8:</b> (a) Side view of the Chevron operation of MCPs, MCP front and back are aligned with an angle (bias angle). The incident ion produces electron and that produces an avalanche of electron through the channel. This leads to higher gain. (b) Electron production and electron gain through the MCP channel (pore) (Source: Huber M.C.E., 2009).	12
9	<b>Figure 2.8:</b> Basic explanation of the time to digital converter (TDC). The dotted line in the upper panel is the threshold level or discriminator. The TDC only counts the signals which are above this threshold.	13
10	<b>Figure 2.9:</b> Pictorial representation of analog to digital conversation.	14
11	<b>Figure 3.1:</b> EGT spectrometer connected to the combustor. CuO furnace [1], oven with sample chamber, and CuO crucible [2], getters and charcoal for purification [3], calibration gas bottles [4], Edel Gas TOF MS [5], and vacuum system. Symbol ● shows full range pressure gauge or Pirani gauge and ○ shows the valve.	17
12	<b>Figure 3.2:</b> Laboratory setup of the combustor and the extraction line.	18
13	<b>Figure 3.3:</b> Oxygen desorption studies of Sample 1 for five different cycles. The data indicate significant oxygen release only at temperatures above 800°C. In the first cycle we produced 6.6 mbar of oxygen, 5.1 mbar in second cycle, 4.4 mbar in third cycle, 4.2 mbar in fourth cycle, and 4.1 mbar in fifth cycle. The maximum amount of oxygen slightly decreases over the course of the different cycles.	19
14	<b>Figure 3.4:</b> Oxygen absorption studies of Sample 1 for five different cycles.	19
15	<b>Figure 3.5:</b> Oxygen desorption and absorption data for the two heating cycles of sample 2. The data for cycle 1 shows that oxygen release starts at about 400°C and reaches a maximum pressure of 9.2 mbar. In cycle 2, oxygen release starts are about 800°C and a maximum pressure of 5.8 mbar is reached.	21

16	<b>Figure 3.6:</b> Oxygen desorption and absorption cycles for sample 3. The data show a consistent behavior in both cycles.	23
17	<b>Figure 3.7:</b> Oxygen loss % in each cycle for three different grain sized samples.	24
18	<b>Figure 4.1:</b> Gaussian peak shape (a); exponential decay tail (b); exponentially modified gaussian peak (c) (Picture taken from Chromatographic Integration Methods (Dyson, 1998))	28
19	<b>Figure 4.2:</b> The flow chart for the EGT_DAS gives basic information about the data analysis process.	31
20	<b>Figure 4.3:</b> Graphical user interface for the EGT-DAS program.	32
21	<b>Figure 4.4:</b> Plot of intensity versus time for a Kr-Xe calibration. The ADC data are for 40'000 data points taken every 0.5 ns with 60000 averagers.	33
22	<b>Figure 4.5:</b> Mass calibrated spectra for the time spectra shown in the upper panel.	34
23	<b>Figure 4.6:</b> Peak Selection on EGTDAS (a) Spectra of intensity as a function of time for Kr isotopes. (b) The same spectra but with intensity as a function of m/q (c) Selected <sup>84</sup> Kr peak.	35
24	<b>Figure 4.7:</b> First and second derivatives of Gaussian peak, both are positive after the peak starts and zero before. At the end of the peak first derivative (FD) is negative and second derivative (SD) is positive and then both are zero.	36
25	<b>Figure 4.8:</b> Original data (blue line), baseline (red line), and smoothed data (green line with dots) for the selected <sup>82</sup> Kr peak.	37
26	<b>Figure 4.9:</b> The calculation of the signal-to-noise-ratio (SNR), which is the ratio of the signal amplitude (S) to the noise level ( $\bar{X}_B$ ) (Agilent, 2011).	37
27	<b>Figure 4.10:</b> Hit and miss method for integrating an area under a curve.	38
28	<b>Figure 4.11:</b> Peak fitting with Gauss and EMG functions and area under the curve for <sup>82</sup> Kr and <sup>86</sup> Kr for MCI before smoothing, MCI after smoothing, gauss fit area and EMG fit area.	41
29	<b>Figure 5.1:</b> Engineering drawing of the EGT. Shown are all important parts of the ion-source, the reflectron and the detector with A) flange with the ion source and the detector with feedthroughs B) ion source C) getter D) reflectron, E) ion getter pump F) flange with reflectron feedthroughs G) ) turbo pump H) charcoal I) detector.	44
30	<b>Figure 5.2:</b> (a) View of the EGT ion source (b) schematic diagram of source electrodes. The dotted line is the ion optical axis.	45
31	<b>Figure 5.3:</b> (Upper) Electron current density emitted from a material as a function of temperature for several cathode materials (Wolf, 1995). (Lower) Saturation current density (solid line) and efficiency (dashed line) versus cathode temperature for tungsten (black) and lanthanum hexaboride (red).	46
32	<b>Figure 5.4:</b> EGT ion source with filament: (a) Filament position in the source on CF-63 flange, (b) filament holder (c) A lanthanum hexaboride cathode mounted on a ceramic base (white cylinder) from Kimball Physics (Kimball, 2015). (d) The LaB <sub>6</sub> crystal (lavender) mounted on a graphite base.	47

33	<b>Figure 5.5:</b> Typical parameters of a Kimball LaB <sub>6</sub> cathode (Kimball, 2015). (a) LaB <sub>6</sub> filament specifications (b) heating voltage vs heating current. (c) Temperature vs heating current (d) emission current vs heating current.	48
34	<b>Figure 5.6:</b> Front panel of the pulse generator from Montena <sup>®</sup> . PULSE OUT and SYNC OUT are for pulse and trigger signals. The back panel has three connections, one for ground, one for the bias voltage, and one for the high voltage power supply.	49
35	<b>Figure 5.7:</b> (upper panel) Rectangular pulse from the pulse generator. (Lower panel) (a) Pulse rise time of ~5 ns from 10% to 90 %; (b) Pulse width of ~2.5 ns; (c) Pulse fall time of ~80 ns.	50
36	<b>Figure 5.8:</b> (a) Reflectron of EGT (b) schematic view of reflectron electrodes.	51
37	<b>Figure 5.9:</b> Microchannel plates and detector setup.	52
38	<b>Figure 5.10:</b> Schematic view of detector configuration (a) Detector design of the first generation EGT (picture from Huber, 2011) (b) Detector design of the current version without any electronic components	52
39	<b>Figure 5.4:</b> Front view of the Agilent ADC card-Acqiris AP240.	53
40	<b>Figure 5.5:</b> Front panel view of the FastComTec <sup>®</sup> TDC with multi stop inputs. External trigger signal from pulse generator has to be connected to the START connection and spectrometer signal from the anode has to be connected to one of the STOP inputs.	54
41	<b>Figure 5.6:</b> Used MoRaMis systems for high and low voltage supply of the EGT.	55
42	<b>Figure 5.7:</b> (a) Schematic viewing of the combination calibration gas bottle and pipette combination. (b) Picture of a calibration bottles in the lab.	55
43	<b>Figure 6.1:</b> The key components of the EGT-MS detection system.	57
44	<b>Figure 6.2:</b> Vacuum systems of the EGT and the extraction line. T1, T2, and T3 are turbo molecular pumps, R1, R2, and R3 are recipient tanks, and IGP is the ion getter pump.	58
45	<b>Figure 6.3:</b> MInOS client window for the MoRaMi filament control.	60
46	<b>Figure 6.4:</b> Typical settings of the Acqiris-card (Instrument Control and Averager Settings).	61
47	<b>Figure 6.5:</b> ADC Live Waveform display. The user can also select the peak/portion by using the zoom option.	62
48	<b>Figure 6.6:</b> Schematic overview of the EGT lab configuration with the optimizer section.	63
49	<b>Figure 6.7:</b> The open “MInOS Client”.	64
50	<b>Figure 6.8:</b> The “EGT Optimizer” GUI and the command shell.	65
51	<b>Figure: 6.9:</b> The “EGT Optimizer” GUI (Quelle voltages) after loading the settings of “250microA_1kHz_Montena_PreAmp.opt”.	66
52	<b>Figure 6.10:</b> The “EGT Optimizer” GUI (Swarm Parameters).	67
53	<b>Figure 6.11:</b> Typical settings of the Acqiris-card (Instrument Control and Averager Settings).	68
54	<b>Figure 6.12:</b> The user interface of the Ionic <sup>2</sup> valve control software. A pop-up window will open after clicking on line 1. Each number (from 0 to 15) corresponds to an electro pneumatic valve.	70

55	<b>Figure 6.13:</b> Schematic diagram of the EGT with the calibration bottles.	71
56	<b>Figure 7.1:</b> Variation of the optimized backplane (QBP) voltage as a function of pulse frequency at a constant extraction grid voltage of -3.8 V.	76
57	<b>Figure 7.2:</b> Subtraction of interference peak to the $^{78}\text{Kr}$ by peak fitting.	79
58	<b>Figure 7.3: (a)</b> Result of the mass calibration for the measurement of Kr calibration gas. The Upper panel gives the intensity as a function of flight time and the lower panel, for the same spectra, the intensity as a function of mass.	80
59	<b>Figure 7.3: (b)</b> Result of the mass calibration for the measurement of Xe calibration gas. The Upper panel gives the intensity as a function of flight time and the lower panel, for the same spectra, the intensity as a function of mass.	80
60	<b>Figure 7.4: (a)</b> Pulse from the external pulse generator.	81
61	<b>Figure 7.4: (b)</b> Area vs pulse frequency for Kr isotopes. Area with respect to the frequency is decreasing with increase in pulse frequency for five spectra. This is due to integration time (data acquisition time) will decrease with increase in frequency.	82
62	<b>Figure 7.5:</b> Area of Kr isotopes for 10 minutes of acquisition time for all frequencies.	83
63	<b>Figure 7.6:</b> Storage capability in the electron impact storage ion source. The intensity versus the repetition frequency is plotted in counts per extraction pulse for Kr isotopes.	84
64	<b>Figure 7.7:</b> The Temporal behavior of the signal after every 20 minutes of acquisition time.	85
65	<b>Figure 7.8:</b> The dependence of the peak areas on the integration time for 1 kHz pulse frequency.	86
66	<b>Figure 7.9: (a)</b> Intensity as a function of number of accumulated spectra for 10 kHz pulse frequency.	86
67	<b>Figure 7.9: (b)</b> Signal to noise ratio (SNR) as a function of Number of accumulated spectra.	87
68	<b>Figure 7.9: (c)</b> mass resolution as a function of number of accumulated spectra.	87
69	<b>Figure 7.10: (a)</b> ADC spectra in averaging mode <b>(b)</b> ADC spectra in NSA mode with a threshold of -1 mV.	88
70	<b>Figure 7.11:</b> Signal intensities for Kr isotopes for averager mode and NSA mode on ADC card.	89
71	<b>Figure 7.12:</b> Signal intensities of Kr isotopes for different threshold voltage setting of the ADC card.	89
72	<b>Figure 7.13:</b> Signal area vs different offset voltage setting of the ADC card.	90
73	<b>Figure 7.14:</b> Effect of threshold on TDC measurements. From the threshold voltage 8 mV to 24 mV the signal height decreased with increase in threshold.	90
74	<b>Figure 7.15:</b> MCP operational diagram and strip current measurement.	92
75	<b>Figure 7.16: (a)</b> Signal size as a function of MCP bias voltage for old MCPs <b>(b)</b> and new MCPS	93

76	<b>Figure 7.17:</b> (a) Emission Current as a function of heating current for a LaB <sub>6</sub> filament from Kimball® (b) Laboratory performance of the filament.	94
77	<b>Figure 7.18:</b> Measurements of krypton calibration gas using the ADC data acquisition system. Mass dependent fractionation per mass unit for Kr isotopes. The isotopes ratios are normalized to <sup>86</sup> Kr.	96
78	<b>Figure 7.19:</b> Mass resolutions of Kr isotopes using ADC measurements. The average mass resolution for all measurements and all isotopes is in the range of 850.	96
79	<b>Figure 7.20:</b> FPMU for Xenon measurements using the ADC card. The minor isotopes of Xenon, <sup>124</sup> Xe and <sup>126</sup> Xe, were not detected in M1 and M3. The isotopic ratios are normalized to <sup>136</sup> Xe.	97
80	<b>Figure 7.21:</b> Mass resolutions of Xe isotopes using ADC measurements. The average mass resolution for all measurements and all isotopes is in the range of 900.	97
81	<b>Figure 7.22:</b> Measurements of krypton calibration gas using the TDC data acquisition system. The isotopes ratios are normalized to <sup>86</sup> Kr.	98
82	<b>Figure 7.23:</b> Mass resolution of Kr isotopes measured using the TDC data acquisition systems.	99
83	<b>Figure 7.24:</b> FPMU for Xe isotopic measurements using the TDC detection system. The isotopes ratios are normalized to <sup>136</sup> Xe.	100
84	<b>Figure 7.25:</b> Mass resolution for Xe isotope measurements using the TDC card	100
85	<b>Figure 7.26:</b> FPMU for Argon isotopes at 10 kHz pulse frequency and for 5 minutes acquisition time.	101
86	<b>Figure 7.27:</b> Mass fractionation for argon isotopes measured at 10 kHz pulse frequency and five minutes of acquisition time on the TDC.	102
87	<b>Figure 7.28:</b> Isotopic ratio <sup>40</sup> Ar/ <sup>36</sup> Ar for seven dilution steps. The black line is the theoretical ratio (~296); M1, M2, and M3 are for three measurements. The results are completely different for three measurements even though the voltage settings, acquisition time and pulse frequency are same.	103
88	<b>Figure 7.29:</b> Isotopic ratio for <sup>36</sup> Ar/ <sup>38</sup> Ar for seven dilution steps. The black line is the theoretical ratio (~5.32), M1, M2, and M3 are for three different measurements. The results are completely different for three measurements even though the settings are same.	103
89	<b>Figure 7.30:</b> An example for the multi peak problem and <sup>40</sup> Ar peak for different dilution steps.	104
90	<b>Figure 7.31:</b> Signal area versus dilution series for <sup>36</sup> Ar for different measurements.	105
91	<b>Figure 7.32:</b> Signal area versus dilution series for <sup>38</sup> Ar for different measurements.	105
92	<b>Figure 7.33:</b> Signal area versus dilution series for <sup>40</sup> Ar for different measurements	106
93	<b>Figure 7.34:</b> Signal intensity for the dilution series for Argon calibration gas at 10 kHz pulse frequency.	106
94	<b>Figure 7.35:</b> Mass resolution of EGT for mass range from 1 amu to 150 amu.	107



# Chapter 1 : Introduction

Exploring the origin of our Solar system including its association with the interstellar medium, the processes that transformed the cloud of dust and gas surrounding the nascent sun into the building blocks of planets, the geologic processes on those early planetesimals, and their accretion to form Earth and the other planets are of special interests to the scientific community. Understanding the chemical structure of early solar materials can tell us a great deal more than observations alone. There is now a whole space science discipline called "cosmochemistry" that involves studying what planets, meteorites, and stars are made of. It was the Swiss mineralogist Goldschmidt (1938) who first measured and compiled a wealth of chemical data on terrestrial rocks, meteorites, and individual phases of meteorites, which was then the foundation of modern cosmochemistry.

A branch of cosmochemistry that deals with the highly volatile elements He, Ne, Ar, Kr, and Xe, which gives potential information about early Solar system, is called "noble gas *cosmochemistry*". Noble gas *geochemistry* studies have also numerous applications such as understanding the history and evolution of planetary atmospheres, the flow pattern of hydrological systems by studying the noble gases in ground waters, geochronology, and others more. In cosmochemistry, understanding the origin and distribution of various noble gas isotopes reveals fundamental information about early stages of the solar system.

Noble gases (He, Ne, Ar, Kr, Xe, and Rn) belong to the last column of the Mendeleev's periodic table, implying they are chemically inert in contrast to the other elements. This distinct feature allows their primordial elemental and isotopic compositions on Earth and other planetary bodies to be determined without having to consider the additional complexities of chemical or biological influences. Any variation of elemental or isotopic ratios of the noble gases reflects either physical processes such as diffusion, adsorption, degassing, or effects of natural radioactivity. By using natural radioactivity noble gases provide possibilities to date geochemical fractionations that have been occurred since the beginning of the Solar system. These highly volatile elements provide fundamental information regarding Earth and the solar system and they are fantastic tools to investigate the origin of volatiles on the terrestrial planets. Variations in isotopic abundance can reveal information about the age and origin of terrestrial and geological samples and this isotopic analysis can be done by noble gas mass spectrometry. Noble gas mass spectrometry has been developing along with technological advances and achieving high precision and high sensitivity even for very low abundances.

In cosmochemistry, geology, and space science researchers deal with very small samples like, for example, pre-solar grains, cosmic dust, and mineral inclusions. For these kinds of applications, the instrument must be able to measure precisely and reliably. The developments in analytical techniques, especially mass spectrometry, allowed cosmochemists to perform detailed analyses of the isotopic abundances of elements within meteorites or other solar system materials. Various kinds of instruments were used to study the atmospheres and

surfaces of different Solar system objects, in that; mass spectrometers are one of the widely used instruments. Mass spectrometers have been associated for space applications for both in-situ and ground based space sample analysis. The logistical considerations of the space instruments like space and weight were lead to develop time-of-flight mass spectrometers. On other hand, geochemical and cosmochemical laboratories have been widely using sector-field mass spectrometers. Even though time-of-flight mass analyzers were used in 1950's their advancement was started in 1980's due to development in technology.

Sector field mass spectrometers and time-of-flight mass spectrometers are the two most commonly used spectrometers for noble gas measurements in space materials corresponding to meteorites and pre-solar grains. Noble gases in presolar grains of meteorites have been measured routinely since 1960's with sector field mass spectrometers. In sector field mass spectrometers, the mass analyzer consists of a magnet to separate ions based on their momentum, and the magnetic field is usually set that one type of ion reach the detector. Therefore, the magnetic field has to be adjusted for each mass to be analyzed. There are many practical problems with these instruments, relatedly loss of ions before detection, calibration problems, large space, and inept to measure all species in a single spectra. Various kinds of extraction techniques have been developed for noble gases and different ionizations procedures were introduced in noble gas mass spectrometry. The need of greater precision and high sensitivity to measure isotopic variations in low abundant samples in this field always give chance to develop new kind of instruments.

A new time-of-flight mass spectrometer was developed and a similar version was used for P-BACE (Polar Balloon Atmospheric Composition Experiment mission) for neutral gas analysis in atmosphere (Abplanalp, 2009), this design was further helped to develop another time-of-flight mass spectrometer for low concentration noble gases with high sensitivity (Huber, 2010). This special design of the EGT-MS is in such a way to overcome the problems faced in sector field mass spectrometers and to develop high sensitive time-of-flight mass spectrometers for noble gas cosmochemistry. New version this instrument was further developed with modifications in the detector and in the other parts.

This dissertation includes introducing the EGT-MS, the data analysis software for the EGT-MS, an operational manual for the EGT-MS, and a discussion of the performance studies of the mass spectrometer and also calibration studies for different noble gases. In addition to these, chapter 3 explains a procedure for the oxidation of the presolar nanodiamonds by using copper oxide.



# Chapter 2 : Time-of-flight mass spectrometry

## 2.1 Introduction to time-of-flight mass spectrometry (TOF-MS)

Time-of-flight mass spectrometry is a method of mass spectrometry in which ions of different masses are separated by the time-of-flight principle. In 1946 William Stephens presented for the first time the concept of a linear Time-Of-Flight Mass Spectrometer (TOF-MS) (Stephens (1946 and Cameron (1948)) when he published the first design and mass spectra for the linear TOF-MS in their laboratory. Wiley and McLaren published the linear TOF-MS design that later became the first commercial instrument (McLaren (1955)). Development of this technique is ongoing, and advances in areas such as ion optics and ion-detection hardware have pushed the mass resolution, sensitivity, and mass accuracy of TOF-MS to regimes that are appropriate for the identification of components of complex mixtures and also of low concentration elements in extremely small samples. The technique's intrinsic high ion transmission and capability to measure wide mass ranges without scanning either magnetic or electric field yields high sensitivity and fast spectral acquisition rates. Currently there is increasing interest in time-of-flight mass spectrometry that's results from the advent of new ionization methods, advancements in detection technology, and the wider use of compact mass spectrometers.

### 2.1.1 Principle of TOF-MS

Mass selection in TOF-MS is achieved by accelerating ions with different  $m/q$  (mass to charge) values to identical kinetic energies and allowing them to separate due to their mass-dependent velocities. Thus, ions with different  $m/q$  values reach the detector at different times. Ions with lower mass reach the detector faster than higher mass ions. This principle of separation-in-time is unlike the separation-in-space principle, which is used in magnetic sector field and quadrupole spectrometers. TOF mass spectrometers differ fundamentally from scanning instruments in that they involve temporally discrete ion formation and mass dispersion in the time domain rather than along a spatial axis. An electrostatic field accelerates the ions that formed inside the ion source to a kinetic energy of some keV. After leaving the source the ions pass a field-free drift region in which they are separated due to their  $m/q$  ratio. This takes place because at fixed kinetic energy ions with different  $m/q$  values are accelerated in the ion source to different velocities. Knowing the acceleration voltage and the length of the drift region, the  $m/q$  ratio can be determined by measuring the flight time.

In a simple case, an ion with a particular mass to charge ratio ( $m/q$ ) is accelerated in a potential difference  $U$ , attains electrical potential energy  $E_p$  and enters into the field-free drift region. In this region the initial potential energy of the particle is converted to kinetic energy  $E_k$ . After entering the flight tube (drift region) of length  $d$  the ion reaches the detector at time  $t$  (see Figure 2.1).

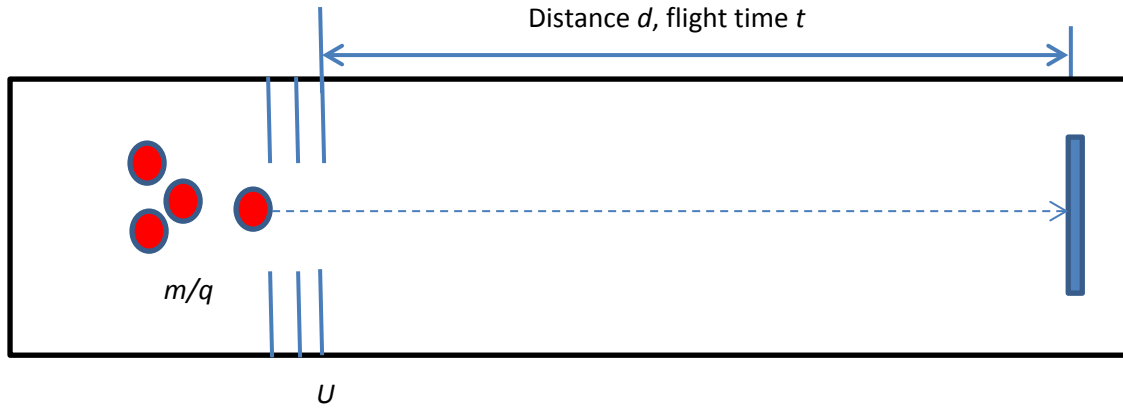


**Figure 2.1:** Ions with mass  $m$  and charge  $q$  are accelerated in potential difference  $U$  towards the detector.

Mathematically, the electrical potential energy of the ion in the potential  $U$  is

$$E_P = qU \quad (2.1)$$

The kinetic energy of the ion with mass  $m$  is

$$E_K = \frac{1}{2}mv^2 \quad (2.2)$$

where  $v$  is the velocity of the ion in the drift region. Using energy conservation gives:

$$E_P = E_K \quad (2.3)$$

$$qU = \frac{1}{2}mv^2$$

$$qU = \frac{1}{2}m\left(\frac{d}{t}\right)^2$$

(Since, velocity = distance over time for a constant velocity)

The time of flight of the ion is

$$t = \frac{d}{\sqrt{2U}} \sqrt{\frac{m}{q}} \quad (2.4)$$

$$\text{and } \frac{m}{q} = \frac{2U}{d^2} t^2 \quad (2.5)$$

$$m = \frac{2qU}{d^2} t^2 \quad (2.6)$$

By differentiating equation 2.6 with respect to time,

$$\frac{dm}{dt} = C (2 dt) \quad (2.7)$$

$$\text{where } C = \frac{4qU}{2d}$$

And from this equation one can write the mass resolution  $R$  as

$$R = \frac{\Delta m}{m} = \frac{\Delta t}{2t} \quad (2.8)$$

The time of flight of the ion is proportional to the square root of its mass to charge ratio. Consequently, assuming equally charged ions, the lighter ions arrive at the detector earlier than the heavier ions. These ions are effectively separated based on their respective masses. After being separated in the flight tube, the ions are detected by a charged particle detector, such as a micro-channel plate, and the mass spectrum is recorded as a function of flight time.

### 2.1.2 Linear TOF

The most commonly used time-of-flight mass spectrometers are linear and similar in design to the Wiley and McLaren (1955) model. This linear TOF-MS consists of an ion source that produces and focuses the ions in time and space onto the detector at the end of a field-free drift path. The ions move in only one direction from the ion source to the detector. Linear TOF-MS systems are simple to design but have lower mass resolution than other designs.

Figure 2.2 shows a simplified diagram of a linear TOF-MS. A sample gas consisting of atoms of three different masses is ionized and all ions are accelerated to the same kinetic energy. As discussed above, having the same kinetic energy lighter ions move faster than heavier ones and so the ions are separated by mass (assuming only single charged ions). The inset depicts the signal measured by the detector as a function of time and clearly shows the mass separation.

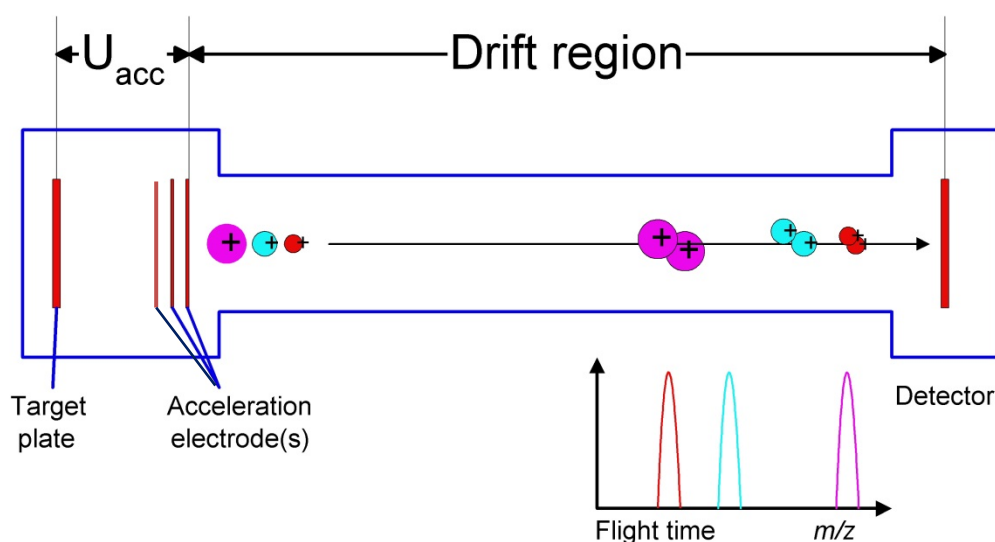


**Figure 2.2:** Linear TOF-MS, separation of different ions based on their mass with respect to flight time.

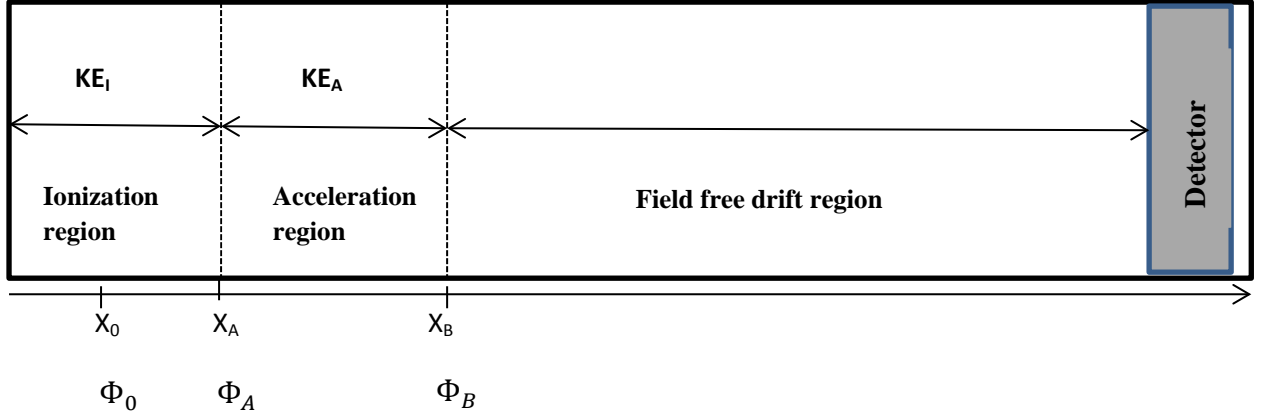


**Figure 2.3:** Schematic diagram of Linear-TOF representing different regions of ion trajectory

The actual kinetic energy of an ion leaving the ion source is equal to the sum of the initial kinetic energy ( $KE_{Ini}$ ), the kinetic energy ( $KE_I$ ) in the ionization region, and the kinetic energy ( $KE_A$ ) in the acceleration region:

$$KE_T = KE_{Ini} + KE_I + KE_A$$

$$KE_T = KE_{Ini} + q(\Phi_{Source} + \Phi_{Accel}) \quad (2.9)$$

Where  $\Phi_{Source} = \Phi_A - \Phi_0$

$$\Phi_{Source} = \Phi_B - \Phi_A$$

and the velocity of the ion at  $X_B$  is

$$v_B = \sqrt{\frac{2KE_T}{m}} \quad (2.10)$$

The total flight time  $t$  equals

$$t = t_0 + t_A + t_{Acc} + t_{drift} \quad (2.11)$$

where

$t_0$  = initial time delay (detector, electronics, cables, etc.)

$t_A$  = time to reach point  $X_A$

$t_{Acc}$  = travel time in acceleration region

$t_{drift}$  = travel time in drift region

$$t_{drift} = (t - t_0 - t_A - t_{Acc}) \quad (2.12)$$

With equation 2.2, 2.10, and 2.12 we can write

$$\frac{m}{q} = \left[ \left( \frac{KE_{Ini}}{q} + (\Phi_{Source} + \Phi_{Accel}) \right) \times \frac{2}{d^2} \times (t - t_0 - t_A - t_{Acc})^2 \right]$$

$$\frac{m}{q} = c \times (t - t')^2 \quad (2.13)$$

where

$c = \text{constant}$

$$t' = (t_0 + t_A + t_{Acc})^2$$

With the arrival times (the time of flight) of each ion ( $t$ ) and with the constants  $c$  and  $t'$  one can calculate mass to charge ratio.

### 2.1.3 Reflectron TOF

Mamyrin et al. (1973) developed a new type of TOF analyzer with high mass resolution, the reflectron time-of-flight mass spectrometer (R-TOF). In contrast to the linear TOF-MS, the ions in a reflectron TOF-MS will reverse their direction of motion, which increases the total flight path of the ions and consequently increases mass resolution. In addition, the reflectron also enables extra focusing. The reflectron is an ion optical device that reverses the travel direction of the ions in a mass spectrometer, i.e., the reflectron acts as an ion optical mirror by generating a repelling electrostatic field. The reflectron has two main purposes that enhance the resolving power of an instrument. First, the length of the flight path is increased, which increase the flight time of the ions, thereby resulting in a larger temporal separation between them. Second, the reflectron provides temporal focusing that can be exploited to reduce the arrival time distribution of the ions at the detector. The combination of greater flight time and a reduction in the arrival time distribution (decrease  $dt$ ) significantly increases mass resolution (resolution =  $t / 2dt$ ).

The reflectron is an isochronous ion optical element used to redirect an incoming ion beam at the end of the field free drift path using an appropriate the electrostatic field. Ions with higher kinetic energy penetrate deeper into the repelling field than lower energetic ions. Subsequently, the faster ions have a longer time of flight in the reflectron than slower ions. This effect compensates for the inverse behavior of the ions in the field free drift path. Therefore, ions with a specific energy distribution and the same  $m/q$  will reach the detector simultaneously. Thus the reflectron can produce time focus at the exit path.

The grid-free reflectron reduces the transmission losses and it has geometrical focusing properties that will enhance the sensitivity of the instrument. Figure 2.4 depicts the behavior of a simple reflectron system.

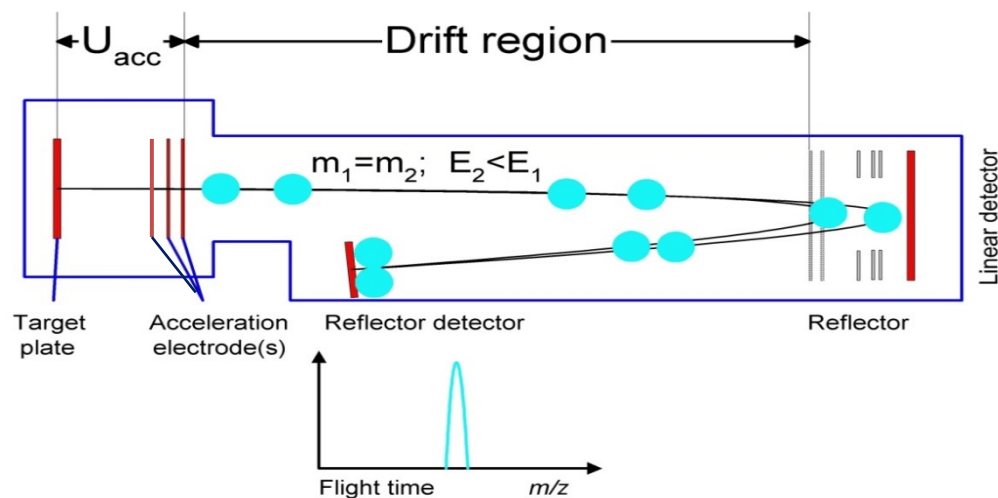


**Figure 2.4:** Reflectron TOF, ions with same mass but having slightly starting velocities reach the detector simultaneously thanks to the focusing of the reflectron.

## 2.2 Electron Impact (EI) ion storage source

The first step in mass spectrometry is the ionization of the sample. Different ionization techniques such as electron impact ionization, chemical ionization, laser ionization, thermal ionization, etc. can be used. The choice of the best ionization method depends on the type of the sample. For noble gases due to their high first ionization potential electron impact ionization is (EI) is the procedure of choice. Electron Impact (EI) ionization is one of the most suitable techniques analyzing volatile and semi-volatile species.

### 2.2.1 Electron Impact Ionization (EI)

Electron impact ionization is the oldest ionization technique. Dempster (1918) developed the first electron impact source and the technique was further improved by Nier (1947). This method ionizes volatilized atoms and molecules with a beam of electrons from a hot wire filament. The collision of an energetic electron with a target atom or molecule produces an ion by removing an electron. There is a minimum energy required for the ionization to happen, which is known as the ionization potential. Figure 2.5 is schematic diagram of the electron impact ionization process.

Depending on the energy of the primary electron further ionization may occur and the target particle may at the end be doubly or triply ionized. Ionization efficiency depends on the number of electrons available for ionization. The ionization potentials for different elements are given in Table 2.1.

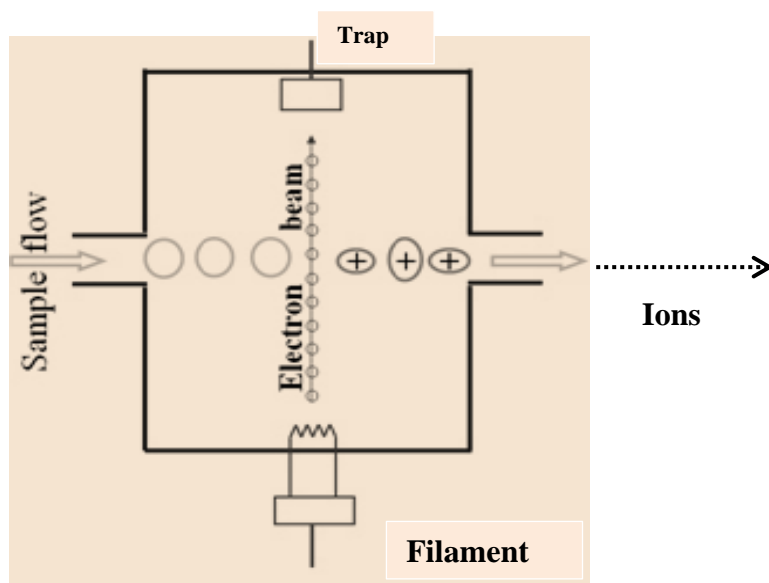


**Figure 2.5:** Schematic diagram of electron impact ionization

Element	Symbol	First ionization potential [eV]
Hydrogen	H	13.6
Helium	He	24.6
Carbon	C	11.3
Nitrogen	N	14.5
Oxygen	O	13.6
Neon	Ne	21.6
Argon	Ar	15.8
Krypton	Kr	14.0
Xenon	Xe	12.1

**Table 2.1:** First ionization potentials of different elements (Radzig, 1985) and most commonly the electron beam is accelerated to energy of about 60 eV.)

### 2.2.2 Ion Storage and Extraction

The ions produced in the ion source can be extracted into the analyzer using different techniques such as pulsed extraction, orthogonal extraction, and delayed extraction. The most common extraction technique is pulsed extraction, which was developed by Wily and McLaren (1955). In this technique, ions are extracted rapidly by a fast extraction pulse. However, there was no storage of the ions, i.e., only ions produced shortly before or at the time of the extraction pulse were measured. Thus in one extraction only very few ions reached the mass analyzer part, which results in a limited signal-to-noise ratio due to a small number of ions being extracted per extraction pulse. Consequently, the sensitivity of those types of instrument is relatively low. To improve on this and to increase sensitivity, a new kind of ion source, the ion storage source, was developed. The principle of this source is to store the continuously produced ions in a trap during the time between two extraction pulses, resulting in a distinctly higher number of ions extracted per pulse. In principle, ions can be trapped with electromagnetic fields. The trapping of ions with only electrostatic fields is often

done with a grid in the middle of the ion source, which has a slightly negative potential (relative to the backplane and the extraction grid). This configuration results in trapped ions oscillating back and forth through the grid and finally results in a fractionated loss of ions. At every oscillating cycle, the ions pass the grid in the middle and after a few times they might scatter at the wires. Assuming that the ions are in thermal equilibrium, high-mass ions are moving slower (and therefore oscillating slower) than low-mass ions (Grix, 1989). Storage of ions increases the efficiency of TOF mass spectrometers compared to non-storage sources due to duty cycle.

The ionization region should be field-free or nearly field-free during the storage phase in order to store a larger number of ions. If an electromagnetic field exists, the ions will accelerate and escape from the ionization region. The field of this region is given by the space charge of the electron beam, the space charge of the ions, and by the electrode potentials. By combining all these potentials the goal is to create a potential well and filling it up with ions. The ions should then be ejected into the acceleration region by applying an external pulse with a very fast rise time to the extraction grid (Abplanalp, 2010).

### **2.2.3 Extraction Pulser**

A high quality extraction pulser is crucial for ion storage sources since the temporal characteristics of the pulser, especially the turn-on-rise time and the pulse width, significantly affect the performance of the mass spectrometer. For example, if the turn-on-rise time is long, the extraction of all the ions out of the trap takes long, which compromise the mass resolution. Therefore, the turn-on-rise time should be as small as possible so that all ions at extraction grid feel the potential difference at the same time.

The quality of the pulser not only affects the mass resolution of the spectrometer as discussed above but also its sensitivity. This is because during the pulse there is no storage of ions and therefore the pulse width should be short. The pulse width (pulse-on-time) has to choose in such way that the signal produced by the declining pulser voltage should not interfere with the signals from the any mass. Usually this interference occurs at low masses  $^3\text{He}$  and  $^4\text{He}$ .

## **2.3 Ion Detectors**

### **2.3.1 Microchannel plates (MCP)**

Mass spectrometers can use many different types of ion detectors such as Faraday cups, Secondary Electron Multipliers (SEM), and microchannel plates. The choice of the detector depends on the required detection sensitivity, the required detection speed, and space available. Mass analysis based on time-of-flight requires an ion detector with a fast time response. Microchannel plates (MCPs) are suitable detectors for time-of-flight mass spectrometers and they have a response time in range 500 ps - a few nanoseconds. A microchannel plate is an array of miniature electron multipliers that are parallel oriented and is fabricated from a lead glass. The schematics are shown in Fig. 2.6. The aspect ratio of MCP channels is the ratio between the length and the diameter ( $L/d$ ) of each channel. An MCP with a higher aspect ratio provides higher gain and narrower pulse height distribution.



The maximum gain that can be recognized without significant ion feedback in a straight-channel MCP is of the order  $10^3$  to  $10^4$ . MCPs with small straight channels have only relatively low gain due to the effect of “ion feedback. The ion feedback effect within the microchannel plates (MCP) is caused by the growing electron avalanche as it is propagating through the MCP-channel. On its way through the channel the electrons hit the channel wall to extract more and more electrons. Due to an increasing electron avalanche atoms from residual gas or adsorbed atoms on the channel wall can be ionized. The ions then are accelerated back to the beginning of a straight channel by MCP bias voltage. These free, moving ions are called ion feedback, and it reduces the gain of MCPs. The ions striking the wall may also damage the channel. The positive ion feedback also produces noise which depends on the gain, pressure, nature of the residual gas and surface properties of the channel wall. The straight geometry of the microchannel is responsible for this. The ion feedback effect can be reduced by using shorter channels that are slightly tilted relative to the bias field-direction. Thus, the average free moving distance of electrons can be reduced and, therefore, the energy of the electrons at the collision is reduced, which in turn reduces the ionization of surrounding atoms.

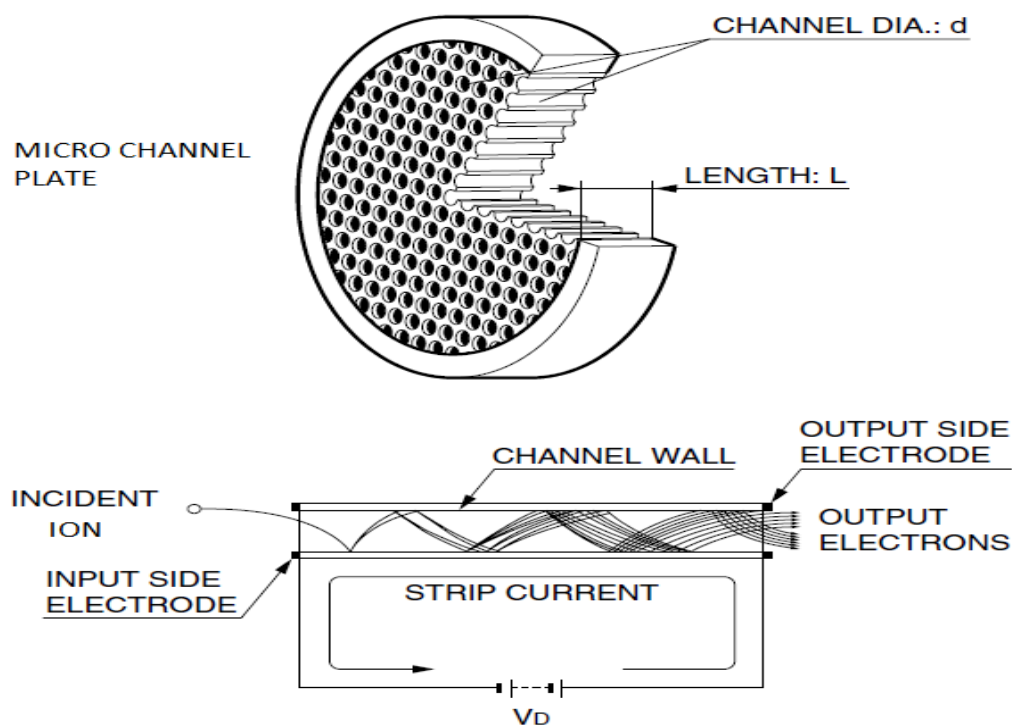


**Figure 2.6:** A microchannel plate (MCP) cutaway view that explains the operational procedure of each channel. (Picture: Hamamastu (2006))

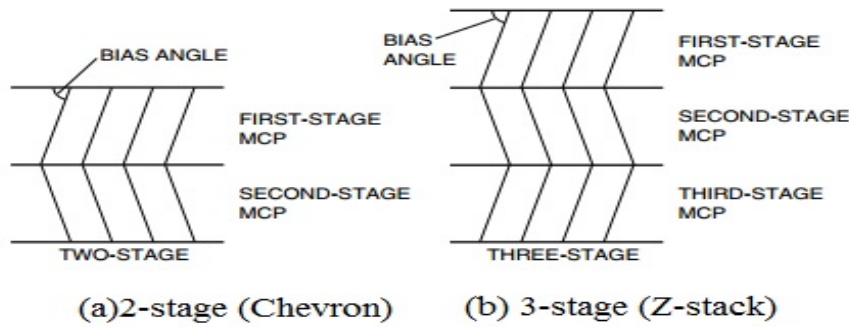


**Figure 2.7:** Chevron (2-stage MCPs) and Z-stack (3-stage MCPs) configurations of MCPs

Therefore the MCPs have a bias angle, and the optimum angle is in between  $5^\circ$  and  $15^\circ$ . It is advantageous to put two such MCPs in 'Chevron' configuration (Joseph, 1979), turned  $180^\circ$  along their axes with respect to each other which is also called V-stack, or three stage MCPs (Z-Stack configuration) to get better performance, since the feedback positive ions get trapped at the interface of the two plates. These combinations provide higher gain. Figure 2.7 shows Chevron and Z-stack configurations of MCPs and Figure 2.8 side view of operation of the Chevron configuration.

The anode is mounted behind the MCPs. It has electrodes that collect the electrons leaving the MCPs.

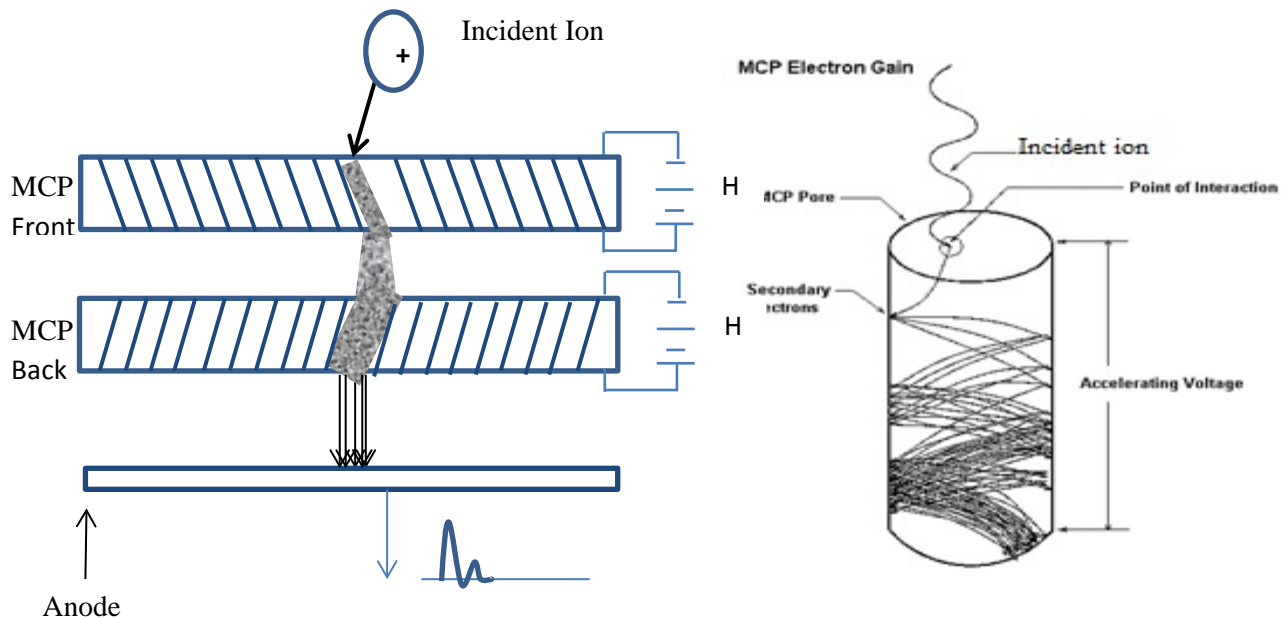


**Figure 2.8:** (a) Side view of the Chevron operation of MCPs, MCP front and back are aligned with an angle (bias angle). The incident ion produces electron and that produces an avalanche of electron through the channel. This leads to higher gain. (b) Electron production and electron gain through the MCP channel (pore) (Source: Huber M.C.E., 2009)

## 2.4 Data Acquisition Systems

A crucial part of a TOF-MS is pulse processing. This is usually done either by pulse counting or by fast digitization of the analog signal that is produced on the detector. Ion detection devices usually consist of a multi-stop time-to-digital converter (TDC) or an analog to digital converter (ADC).

### 2.4.1 Time to Digital Converters (TDC)

A TDC converts a signal into a digital representation of their time indices. Thus, TDCs are used when the important information is to be found in the timing of events. Typically, a TDC records the arrival times of ion events in binary format. This is usually followed by a discriminator, which sets the minimum accepted pulse amplitude. Therefore, TDCs only count amplitudes that exceed a preselected threshold. Measurements with very low gas concentrations have low ion currents and a TDC can be used to “count” the arrival times of individual ions (Figure 2.8). TDCs are most often used in applications where measurement events happen infrequently, because in TDC counting mode individual events cannot be distinguished from simultaneous events

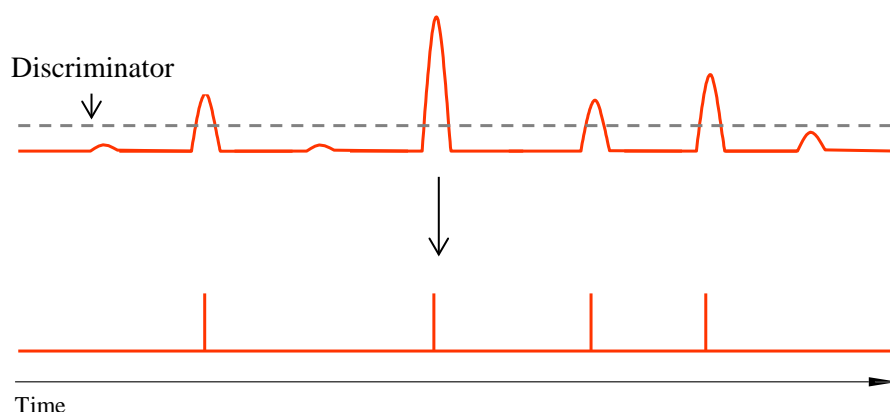


**Figure 2.8:** Basic explanation of the time to digital converter (TDC). The dotted line in the upper panel is the threshold level or discriminator. The TDC only counts the signals which are above this threshold.

Single ion events can be measure more accurately with time to digital converters in the time-of-flight mass spectrometry.

### 2.4.2 Analog to Digital Converters

An Analog to Digital Converter (ADC) is an electronic circuit that converts continuous analog signals into discrete digital values. The signal from the detector is digitized at a fixed sampling rate. The significant improvements in the speed and memory of these devices in recent years allow signals can be sampled at frequencies up to one or two GHz. The Analog to digital conversion is usually the digitization of time and discretization of the amplitude of the signal. Discretization of time is determined by sampling frequency. It is therefore required to define the sampling rate at which new digital values are sampled from the analog signal.

Secondly, the discretization of amplitude depends on the resolution of the ADC. The resolution of the converter indicates the number of discrete values it can produce over the range of voltage values. An n-bit ADC provides  $2^n$  discrete quantization levels corresponding to some specified analog input signal amplitude range. Resolution is expressed in bits. For example, the ADC encodes an analog input to one of 256 discrete values (0 to 255), which is 8-bit resolution.

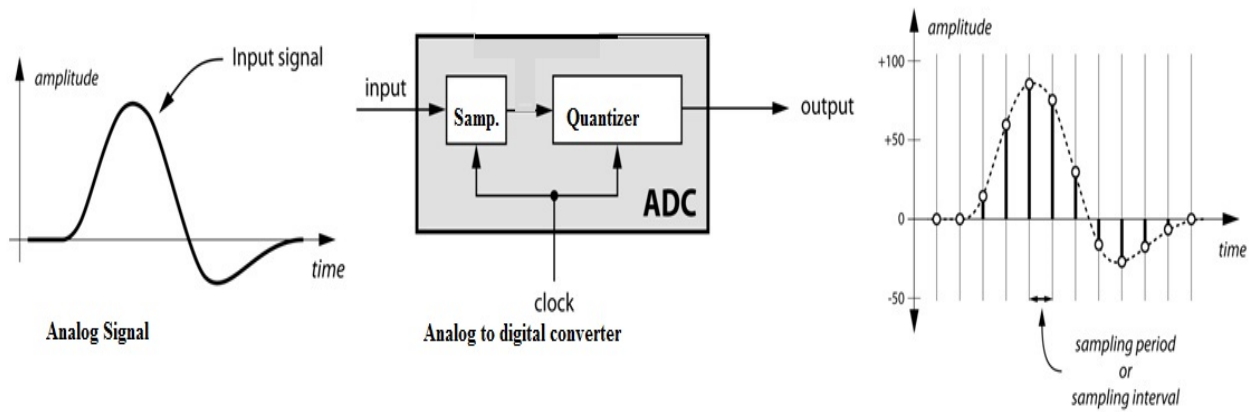


**Figure 2.9:** Pictorial representation of analog to digital conversation

The Figure 2.9 demonstrates the digitization concept, the analog signal is converted into digital signal in two steps, and first, sampling digitizes the time then the second step will be quantizer discretizes the amplitude. There are two ways to best improve the accuracy of analog to conversion, one is increasing the resolution which improves the accuracy in measuring the amplitude of the analog signal and second method is increasing the sampling rate which increases the maximum frequency that can be measured. Since one least significant bit (LSB) is equal to  $V_{REF} / 2^n$  ( $V_{REF}$  is full scale range), it stands to reason that better accuracy (lower error) can be realized if we did either (or both) of two things: (1) use a higher resolution converter and/or (2) use a smaller reference voltage. Table 2.2 LSB values by resolution and reference voltage of ADC. The problem with higher resolution (more bits) is the cost. Also, the smaller LSB means it is difficult to find a really small signal as it becomes lost in the noise, reducing signal to noise ratio (SNR) performance of the converter. The problem with reducing the reference voltage is a loss of input dynamic range. Again, we also can lose a small signal in the noise, causing a loss of SNR performance

$V_{REF}$ (Full scale)	Resolution (ADC bits)	1 LSB
1.00V	8	3.9062 mV
1.00V	12	244.14 $\mu$ V
2.00V	8	7.8125 mV
2.00V	12	488.28 $\mu$ V
4.00V	8	15.625 mV
4.00V	12	976.56 $\mu$ V

**Table 2.2:** LSB values by resolution and reference voltage of ADC

# Chapter 3 : Oxidation of nanodiamonds

## 3.1 Introduction

A major discovery in meteoritics and cosmochemistry was the finding that some primitive meteorites contain presolar material. Such presolar grains, which have been formed in stellar events outside and earlier of the solar system, gives crucial information not only on the stellar processes leading to the formation of presolar grains but also on processes and events in the early solar system itself. Nanometer-sized diamonds (average grain size ~3 nm) were the first presolar gains identified (Lewis *et al.*, 1987) and with up to 1500 ppm they provide the most abundant presolar material in meteorites. Abundance wise, the major types of presolar grains are nanodiamonds (~2-4 nm, ~1500 ppm), SiC (~ 0.1 to 10  $\mu\text{m}$ , ~30 ppm), graphite (~0.5 to 10  $\mu\text{m}$ , ~10 ppm), and also  $\mu\text{m}$  sized silicates (~200 ppm), and refractory oxides (~50 ppm) (e.g., Ott *et al.*, 2009).

Our plan originally was to separate and measure all noble gases in one set of presolar nanodiamonds. Typical presolar nanodiamonds have sizes in range 2–4 nm. A diamond with a diameter of 2.8 nm, the median of the size distribution, contains ~1,800 carbon atoms. However, there is only about one noble gas atom per one million diamonds (Daulton *et al.*, 1996). Since measurements of such low noble gas concentrations are technically very challenging, they require high sensitive noble gas mass spectrometers. This was one reason for us to develop the high sensitive Time-of-Flight noble gas mass spectrometer.

## 3.2 Oxidation of nanodiamonds using Copper-Oxide (CuO)

Extraction of noble gases out of presolar grains is challenging. A technique for the determination of the abundance and isotopic composition of carbon and nitrogen within organic compounds is described by Boyd *et al.* (1987, 1990). In this technique high-sensitivity static mass spectrometers are used. In addition, diamonds isolated from primitive carbonaceous meteorites have been analyzed by high resolution stepped combustion techniques to measure the C and N isotopic composition of the diamonds (e.g., Russel *et al.* 1996).

Stepped pyrolysis techniques were first introduced by Chang *et al.* (1974) for the isotopic analysis via dynamic mass spectrometry. Stepped combustion techniques, i.e., pyrolysis in the presence of oxygen, have been developed by Frick and Pepin (1981) and Lewis *et al.* (1983). However, while the early studies all measured dynamically, i.e., the measurement was performed while pumping the spectrometer, the analysis of sub-nanomole samples prohibits pumping the spectrometer while measuring the small gas amounts (Wright *et al.* 1988). The step combustion technique was further improved by Boyd *et al.* (1988) to reduce blank contributions, which is especially important for reliable measurements of sub-nanomol gas amounts. Carr *et al.* (1986) described a method for measuring nanomol levels of stable carbon isotopes by using a static mass spectrometer. For producing the oxygen they used copper oxide and the released oxygen then converted the carbon from the sample to CO<sub>2</sub>. In a very similar setup Wright *et al.* (1988) measured sub-nanomole levels of stable nitrogen isotopes.

Gray *et al.* (2007) developed a slightly different system for the analysis of nanomole-sized quantities of nitrogen and they developed a better understanding of analytical blank problems.

Verchovsky and coworkers (e.g., Verchovsky *et al.* 1997, 1998) analyzed presolar diamonds by stepped pyrolysis, stepped combustion, or a combination of both techniques. Going to temperatures up to 1450°C they achieved a low enough blank level and were able to analyze nanodiamond samples of a few  $\mu\text{g}$ . The amount of combusted carbon was estimated via the  $\text{CO}_2$  partial pressure. They found that the yield of carbon via  $\text{CO}_2$  is different for pyrolysis and combustion experiments. In addition, the oxygen they supplied for the bulk combustion set-up was not sufficient for a complete oxidation of the nanodiamonds. Since for normal pyrolysis set-ups there is only very little oxygen available for the oxidation of carbon, the release of gas usually requires long heating procedures, which in turn produces significant blank problems. At the University of Berne a special extraction line has been designed and built to extract noble gases from carbon-rich materials (Figure 3.1).

### 3.3 Laboratory setup of EGT Combustor

The laboratory system developed for the combustion of carbon-rich refractory material is shown in Figure 3.2. The extraction line for the combustion of refractory carbon-rich samples has a much simpler design than the set-ups used by Boyd *et al.* (1987, 1990) and Russel *et al.* (1996). The furnace for reducing the CuO and releasing the oxygen (label 1) consists of a Pt tube that is inside a stainless steel tube. While the stainless steel is the vacuum barrier, the Pt avoids any reactions between the (hot) CuO and the stainless steel. This oven-part is connected to the rest of the extraction line via valve number 7, which allows replacing the CuO and doing some first tests without venting/contaminating the rest of the extraction line. After the CuO is filled into the Pt-tube, the system is pumped down to a pressure of about  $10^{-9}$  mbar. To release remaining atmospheric surface contamination the crucible is heated to about 200°C for a few days. The detailed procedure is given in Appendix-A.1 and the stoichiometric calculations for the amount CuO needed to oxidize the carbon are explained in Appendix-A.2. The Pirani gauge directly connected to the sample chamber measures the pressure in the line. Due to the low background pressure in the line it is safe to assume that the measured pressure equals the oxygen partial pressure. We can roughly calculate the oxygen pressure required for fully oxidizing all nanodiamonds. Assuming a volume of about 500ml an oxygen partial pressure of about 4 mbar is needed to combust one mg of nanodiamonds. See also Appendix-A.3

### 3.4 Experimental Procedure

The basic idea of the newly developed combustion system is as follows: When CuO is heated to temperatures above 800°C it desorbs oxygen. Part of this oxygen is then used to oxidize the carbon-rich material, in our case, the nanodiamonds. After cooling the system back to room temperature, some of the oxygen reacts back with the Cu to CuO, thereby reducing the oxygen partial pressure in the line. Copper-oxide is used for desorption and absorption because it starts releasing oxygen already at ~800°C (higher temperatures would mechanically and structurally damage the extraction line). In addition, the possibility of the back-reaction reduces the partial pressure after noble gas release, which makes cleaning, gettering, and

separating the noble gases into different fractions easier. Note, larger amounts of oxygen can i) damage the filament, ii) damage the getters, and iii) compromise noble gas separation. For the set-up we filled a pre-calculated amount of CuO into the Pt tube, which was placed in the CuO furnace, evacuated the line, and pre-heated the system at 200°C for a few days. After this set-up we heated the CuO from 200°C to 860°C in steps of 50°C. Each temperature steps lasted at least 5 min. Note that heating above 860°C can cause damage of the extraction line. The release of oxygen, i.e., the dissociation of CuO, starts at about 800°C. A detailed description of the CuO loading and of the procedure to release the oxygen is given in Appendix 3.1.

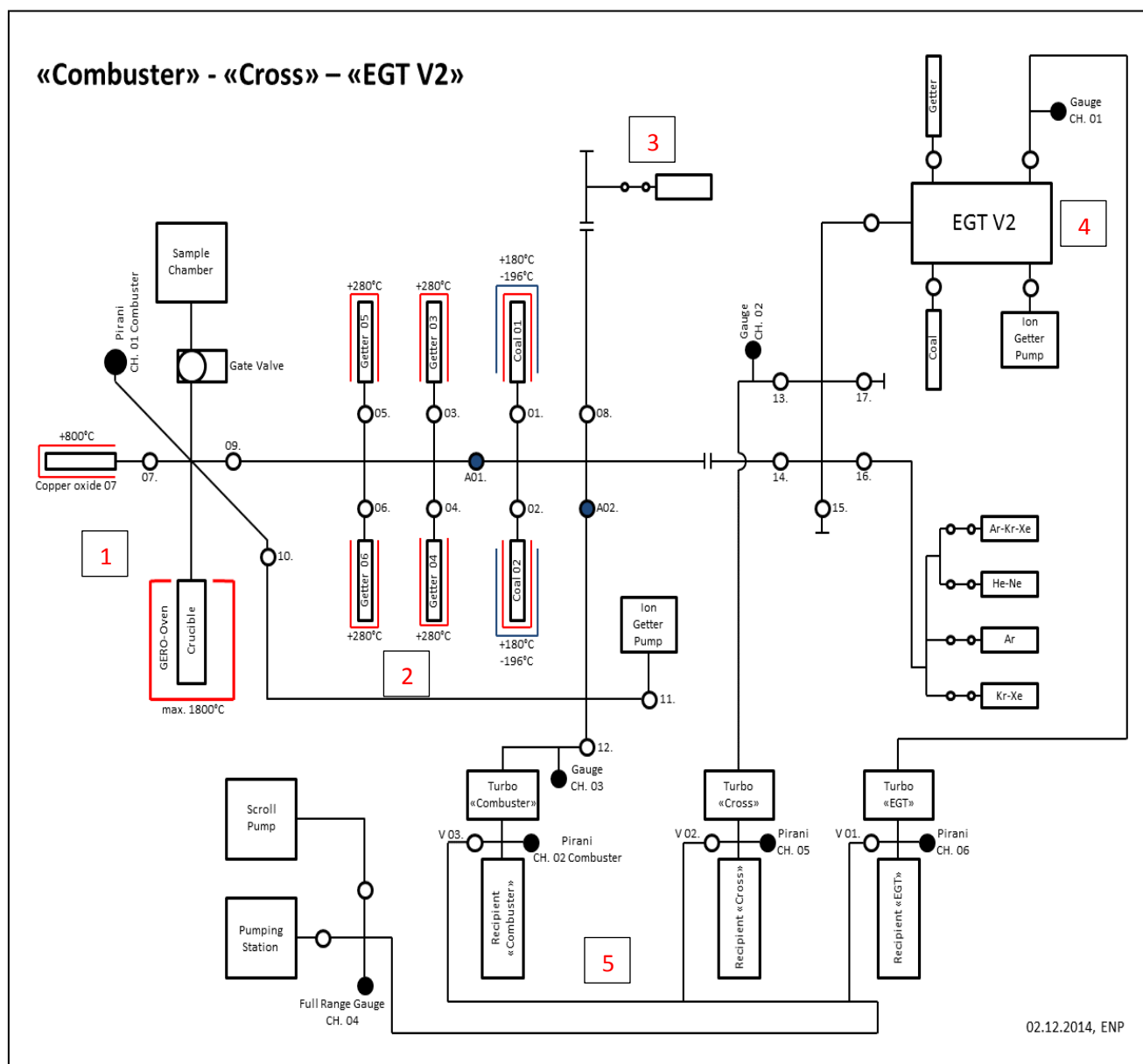


**Figure 3.1:** EGT spectrometer connected to the combustor. CuO furnace [1], oven with sample chamber, and CuO crucible [2], getters and charcoal for purification [3], calibration gas bottles [4], Edel Gas TOF MS [5], and vacuum system. Symbol ● shows full range pressure gauge or Pirani gauge and ○ shows the valve.



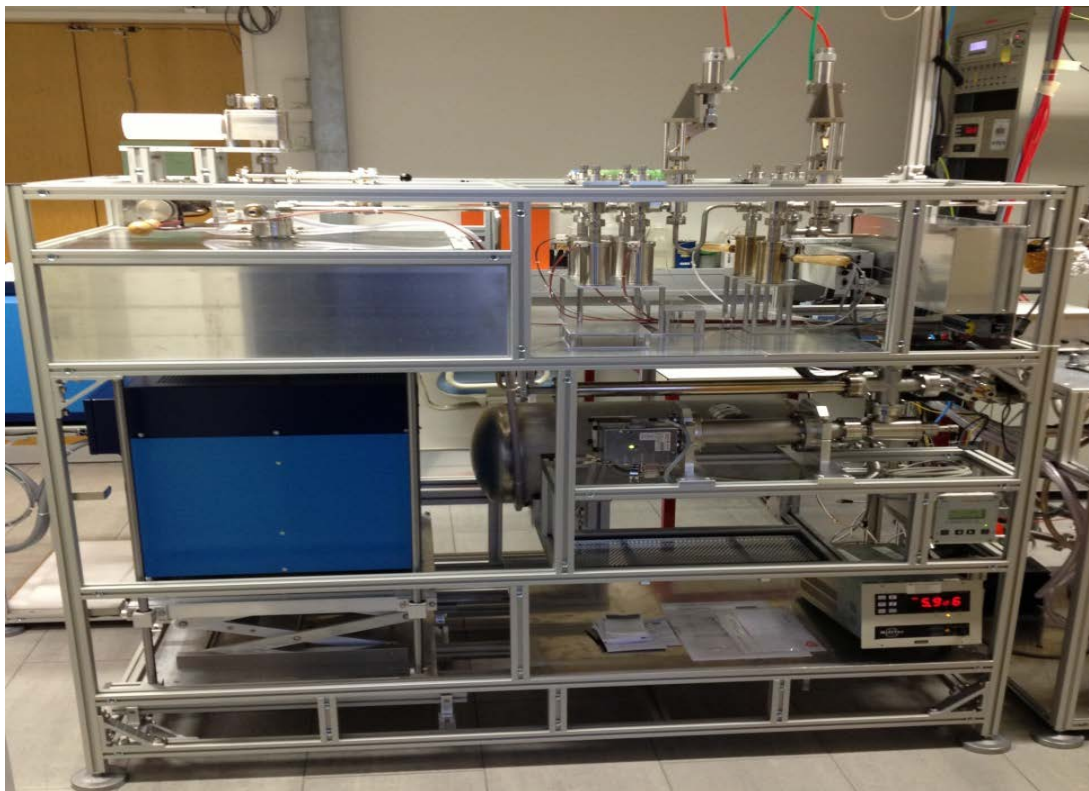


**Figure 3.2:** Laboratory setup of the combustor and the extraction line.

### 3.5 Experimental Results

We studied the thermal behavior of three different kinds of CuO with respect to oxygen release during heating and oxygen desorption during cooling. Both, release and desorption, is expected to depend on grain size (mesh) and purity of the copper oxide. Here we selected three different types, i) CuO from Goodfellow<sup>®</sup> (99.99 % purity, 10  $\mu\text{m}$  mesh, Sample 1), CuO from Acros<sup>®</sup> (99+% purity,  $\sim 10$  to 100  $\mu\text{m}$  mesh size, Sample 2), and iii) CuO from Elemental Micro Analysis<sup>®</sup> (99.9% purity, 0.1 to 0.5 mm grain size, Sample 3).

#### 3.5.1 Sample 1, CuO from Goodfellow<sup>®</sup>

The results for the step-wise heating experiment for sample 1 is shown in Figure 3.3. The five different lines correspond to five different but successive heating procedures. The general release pattern is for all five cycles similar; there is no release below 700°C. Release starts above 700°C but significant oxygen release only starts at about 850°C, i.e., at the maximum temperature in our set-up. One gram of CuO from Goodfellow<sup>®</sup> produces 6.6 mbar of oxygen at the first cycle, 5.1 mbar at the second cycle, 4.4 mbar at the third cycle, 4.2 mbar at the fourth cycle, and 4.1 mbar at the fifth cycle. The data therefore indicate that we lose about 30%, 16%, 5%, and 2% of oxygen after cycle 1, cycle 2, cycle 3, and cycle 4, respectively. The data therefore indicate that the back reaction, i.e., the oxidation of copper, is not quantitative. This is also shown in the lower panel of Figure 3.3 that shows how the pressure in the line evolves while cooling the CuO back to room temperature.



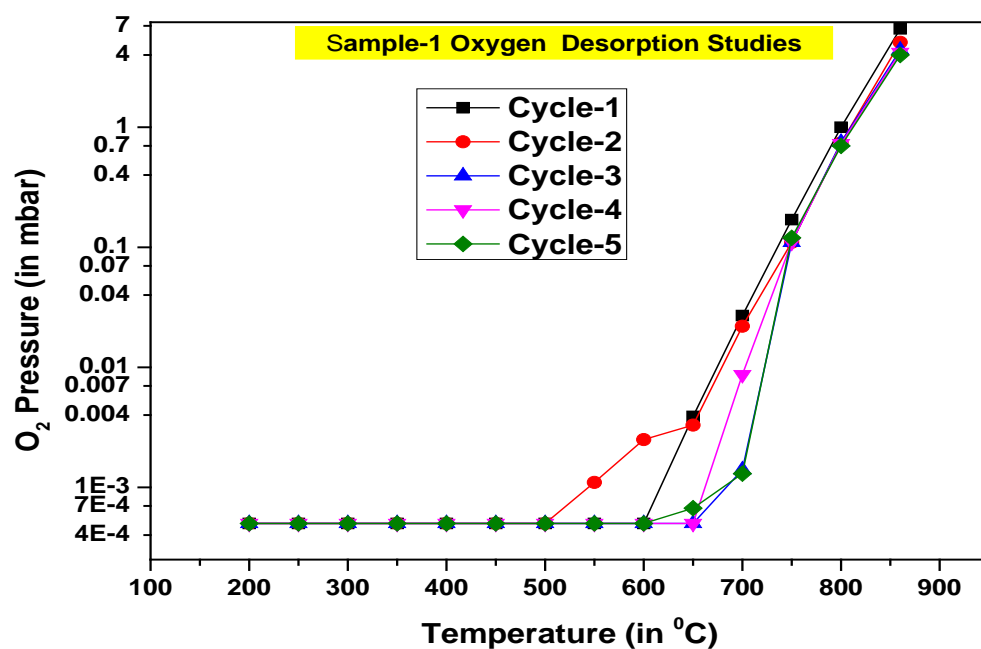


**Figure 3.3:** Oxygen desorption studies of Sample 1 for five different cycles. The data indicate significant oxygen release only at temperatures above 800°C. In the first cycle we produced 6.6 mbar of oxygen, 5.1 mbar in second cycle, 4.4 mbar in third cycle, 4.2 mbar in fourth cycle, and 4.1 mbar in fifth cycle. The maximum amount of oxygen slightly decreases over the course of the different cycles.

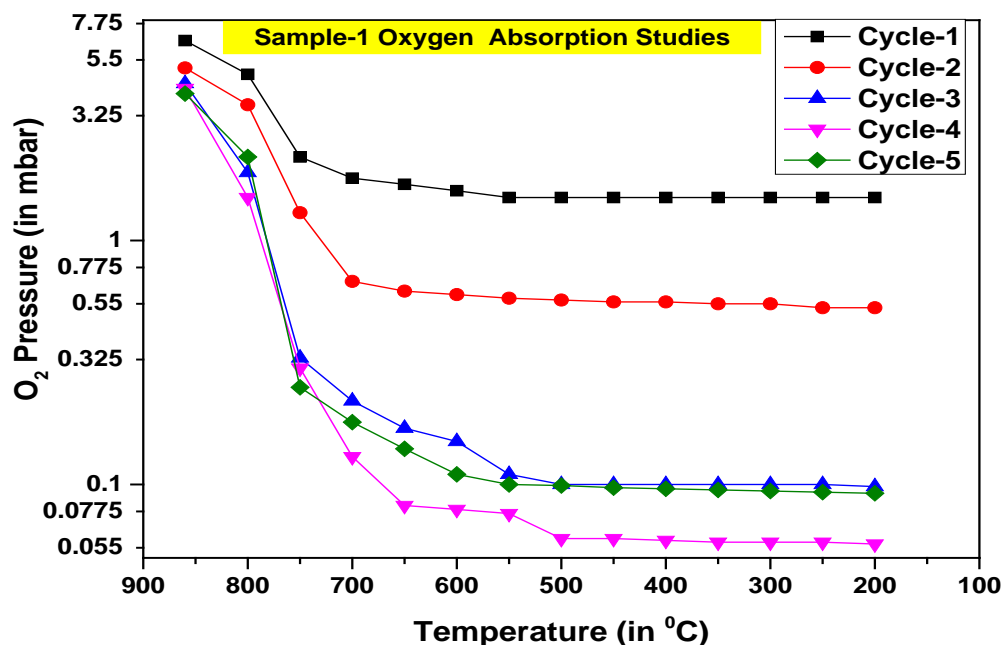


**Figure 3.4:** Oxygen absorption studies of Sample 1 for five different cycles.

Temperature (in °C)	Cycle-1 (in mbar)	Cycle-2 (in mbar)	Cycle-3 (in mbar)	Cycle-4 (in mbar)	Cycle-5 (in mbar)
<b>Oxygen Desorption Studies</b>					
200	< 5E-4	< 5E-4	< 5E-4	< 5E-4	< 5E-4
250	< 5E-4	< 5E-4	< 5E-4	< 5E-4	< 5E-4
300	< 5E-4	< 5E-4	< 5E-4	< 5E-4	< 5E-4
350	< 5E-4	< 5E-4	< 5E-4	< 5E-4	< 5E-4
400	< 5E-4	< 5E-4	< 5E-4	< 5E-4	< 5E-4
450	< 5E-4	< 5E-4	< 5E-4	< 5E-4	< 5E-4
500	< 5E-4	5E-4	< 5E-4	< 5E-4	< 5E-4
550	< 5E-4	0.0011	< 5E-4	< 5E-4	< 5E-4
600	5E-4	0.0025	< 5E-4	< 5E-4	5E-4
650	0.0039	0.0033	5E-4	5E-4	6.7E-4
700	0.027	0.022	0.0014	0.0087	0.0013
750	0.17	0.11	0.11	0.11	0.12
800	1	0.74	0.75	0.73	0.7
860	6.6	5.1	4.4	4.2	4
<b>Oxygen Absorption Studies</b>					
800	4.8	3.6	1.9	1.5	2.2
750	2.2	1.3	0.33	0.3	0.25
700	1.8	0.68	0.22	0.13	0.18
650	1.7	0.62	0.17	0.082	0.14
600	1.6	0.6	0.15	0.079	0.11
550	1.5	0.58	0.11	0.076	0.1
500	1.5	0.57	0.1	0.06	0.099
450	1.5	0.56	0.1	0.06	0.097
400	1.5	0.56	0.1	0.059	0.096
350	1.5	0.55	0.1	0.058	0.095
300	1.5	0.55	0.1	0.058	0.094
250	1.5	0.53	0.1	0.058	0.093
200	1.5	0.53	0.098	0.057	0.092

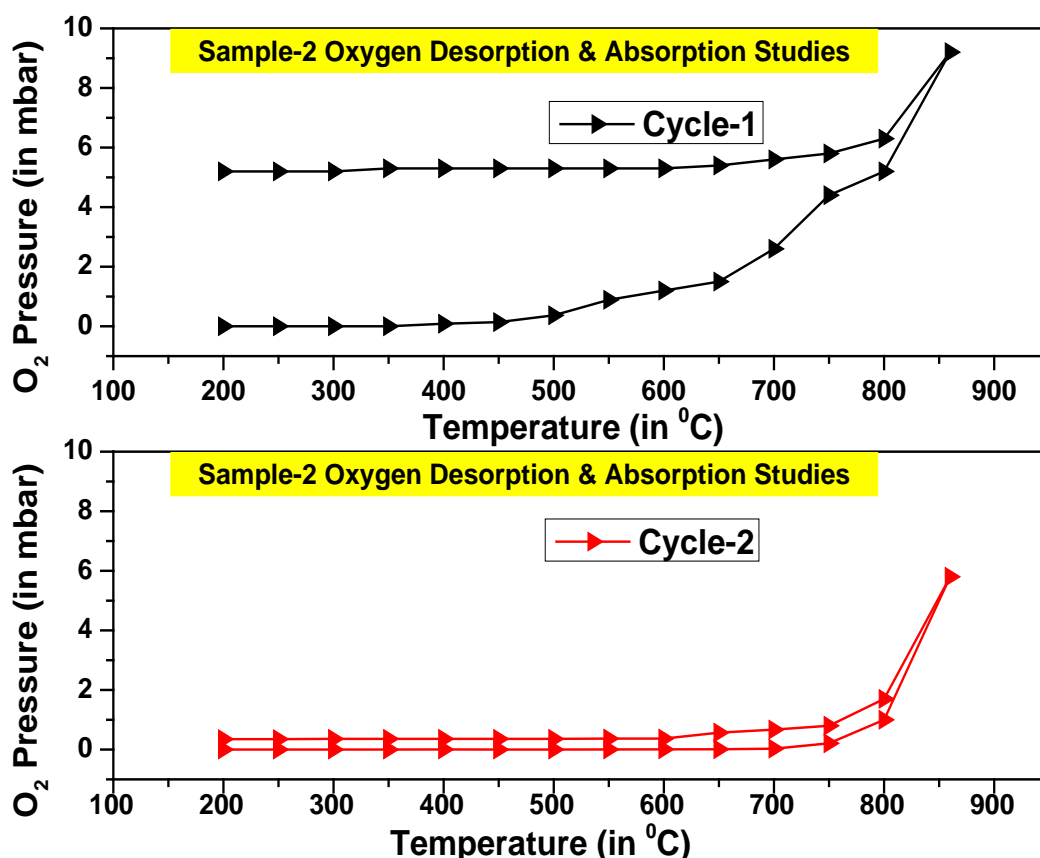
**Table 3.1:** Oxygen desorption and absorption data for Sample 1 (GOODFELLOW, 99.99 % purity, 10  $\mu\text{m}$  mesh): The upper area (pink shaded) gives the oxygen pressure as a function of increasing heating temperature. The lower area (green shaded) gives the oxygen pressure as a function of decreasing temperature, i.e., while cooling.

Figure 3.4 shows the evolution of the oxygen pressure as a function of temperature during cooling. The general trend is the same for all five cycles, the oxygen partial pressure drops significantly at about 700°C. However, at cycle 1, the pressure drops from 6.6 mbar to about 1.5 mbar, i.e., the back-reaction was by far not quantitative and about 30% of the oxygen stayed in the gas phases and finally had to be pumped away. Interestingly, the mass balance, though not perfect, is reasonable. Starting with 6.6 mbar and losing about 1.5 mbar through pumping would give, for the next cycle, a maximum pressure of about 5.1 mbar, which is identical to the pressure measured at the maximum in cycle 2. Considering now that at the end

of cycle 2 about 0.5 mbar of oxygen was still in the gas phase and had been pumped away, we only expect  $5.1 \text{ mbar} - 0.5 \text{ mbar} = 4.6 \text{ mbar}$  at the maximum of cycle 3, comparable to the measured pressure of 4.4 mbar. In the next round we expect  $4.4 \text{ mbar} - 0.1 \text{ mbar} = 4.3 \text{ mbar}$ . Again, the calculated value is very close to the measured value of 4.2 mbar. Finally, after cycle 4 about 0.05 mbar had been lost through pumping. With the maximum of 4.2 mbar measured in cycle 4 we expect about 4.15 mbar oxygen partial pressure at maximum, very similar to what has been measured, i.e., 4.0 mbar.

### 3.5.2 Sample 2, CuO from Acros®

The results of the two step-wise heating cycles of sample 2 (1 g CuO from Acros®, 99+% purity, ~10 to 100  $\mu\text{m}$  mesh size) are shown in Figure 3.5 and the data are given in Table 3.2. Note that sample 2 has a larger grain size than sample 1. This sample shows a different absorption and desorption pattern for the two different heating cycles. For the first heating cycle oxygen release started already at 450°C and we reached a maximum pressure of 9.2 mbar at 860°C. In the second cycle, oxygen release started much later, at about 800°C, and we reached a pressure of only 5.8 mbar. However, the mass balance is again reasonable. After cooling about 5.2 mbar of oxygen was still in the line in the first cycle and had been pumped.



**Figure 3.5:** Oxygen desorption and absorption data for the two heating cycles of sample 2. The data for cycle 1 shows that oxygen release starts at about 400°C and reaches a maximum pressure of 9.2 mbar. In cycle 2, oxygen release starts are about 800°C and a maximum pressure of 5.8 mbar is reached.

We therefore expect for the second cycle a maximum oxygen pressure of 4 mbar ( $9.2 - 5.2 = 4.0$ ), which is slightly less than measured by us, i.e., 5.8 mbar. Anyway, after the first heating cycle we lost about 50% of the oxygen. In the second cycle, however, the re-absorption was almost quantitative, i.e., 93%.

Temperature (in °C)	Cycle-1 (in mbar)	Cycle-2 (in mbar)	Temperature (in °C)	Cycle-1 (in mbar)	Cycle-2 (in mbar)
Desorption Studies			Absorption Studies		
200	< 5E-4	< 5E-4	860	9.2	5.8
250	< 5E-4	< 5E-4	800	5.8	0.8
300	< 5E-4	< 5E-4	750	5.6	0.67
350	5E-4	5E-4	700	5.4	0.57
400	0.088	0.0033	650	5.3	0.37
450	0.14	0.0021	600	5.3	0.37
500	0.37	0.0026	550	5.3	0.36
550	0.89	0.0042	500	5.3	0.36
600	1.2	0.0068	450	5.3	0.36
650	1.5	0.012	400	5.3	0.36
700	2.6	0.029	350	5.2	0.36
750	4.4	0.21	300	5.2	0.35
800	5.2	1	250	5.2	0.35
860	9.2	5.8	200	5.2	0.35

**Table 3.2:** Oxygen desorption and absorption data. The upper area (pink shaded) gives the data for oxygen desorption as a function of increasing heating temperature and the lower area (green shaded) gives the oxygen pressure as a function of temperature during cooling.

### 3.5.3 Sample 3, CuO from Elemental Micro Analysis®

The third sample is from Elemental Micro Analysis® (1 g, 99.9% purity, 0.1 to 0.5 mm grain size), which is among the maximum grain size of CuO available on the market. Table 3.3 gives the oxygen pressure as a function of temperature while heating (desorption) and cooling the sample (absorption). The data are plotted in Figure 3.6. Compared to the two samples studied before, sample 3 shows a consistent desorption and absorption pattern for the different heating cycles. It releases in both cycles 5.2 mbar of oxygen at the highest possible temperature of 860°C. Even more importantly, the studied CuO re-absorbs about 97% after the first heating and 99.5% after the second heating. Since the grain size for this sample is much larger than for the other two samples it seems that a larger grain size results in more consistent desorption and absorption pattern than smaller grain sizes. This is confirmed by our finding that for this type of CuO we found no indication for melting, which could be observed for the other two CuO types with finer grain size.

Temperature (in °C)	Cycle-1 (in mbar)	Cycle-2 (in mbar)	Temperature (in °C)	Cycle-1 (in mbar)	Cycle-2 (in mbar)
Desorption Studies			Absorption Studies		
200	< 5E-4	< 5E-4	860	5.2	5.2
250	< 5E-4	< 5E-4	800	0.17	0.49
300	< 5E-4	< 5E-4	750	0.17	0.062
350	5E-4	< 5E-4	700	0.17	0.047
400	0.015	< 5E-4	650	0.17	0.038
450	0.02	< 5E-4	600	0.17	0.032
500	0.023	< 5E-4	550	0.17	0.031
550	0.028	< 5E-4	500	0.17	0.029
600	0.032	5E-4	450	0.17	0.029
650	0.041	0.004	400	0.16	0.028
700	0.078	0.027	350	0.16	0.028
750	0.25	0.16	300	0.16	0.027
800	1	0.82	250	0.16	0.027
860	5.2	5.2	200	0.16	0.027

**Table 3.3:** Oxygen desorption and absorption data. The upper (pink shaded) data area gives the data for oxygen desorption (increasing temperature) and the lower area (green shaded) gives the data for oxygen absorption (cooling).

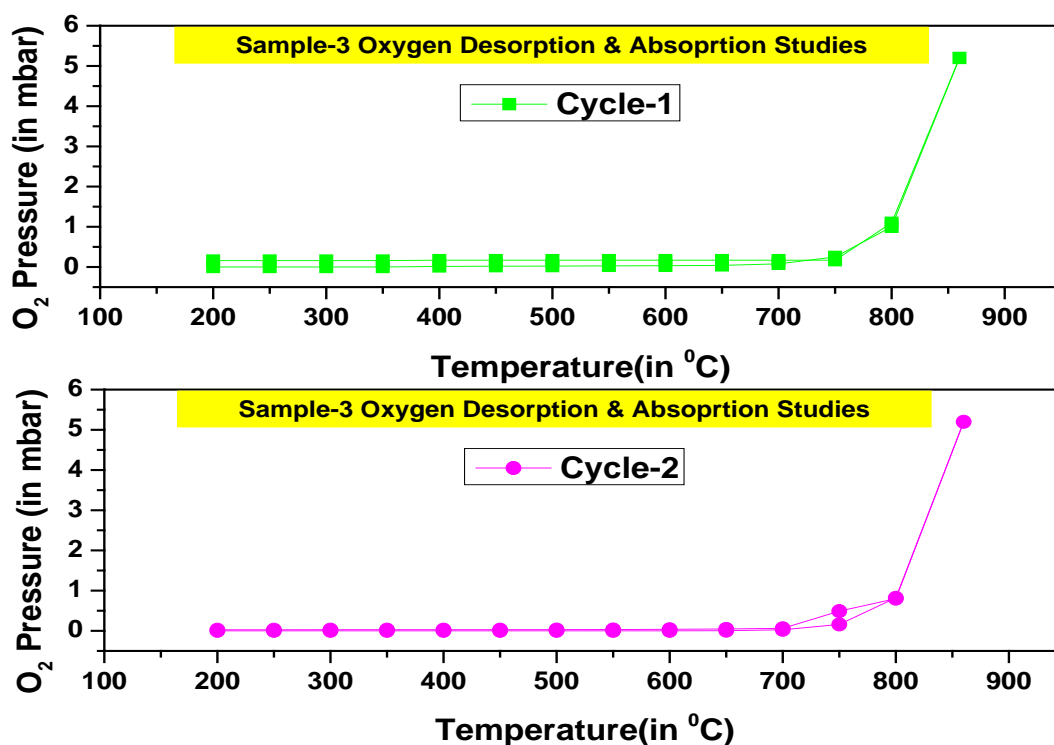


**Figure 3.6:** Oxygen desorption and absorption cycles for sample 3. The data show a consistent behavior in both cycles.

### 3.5.4 Discussion

As can be seen from the discussion above, desorption and absorption of oxygen depends on the grain size of the CuO. To remember, the basic idea of using CuO is that the released oxygen is used to oxidize the nanodiamonds but the left-over must be somehow removed. Ideally, the oxygen back-reacts with the Cu to reform CuO, the more oxygen back-reacts, the easier the rest of the noble gas separation and cleaning will be. To optimize desorption and absorption we therefore studied its dependence on grain size. For the three samples studied here the major difference is in their absorption behavior, not in their desorption behavior. For sample 2 (grain size of 10-100  $\mu\text{m}$ ) more than 50% of the oxygen was lost after the first heating due to insufficient absorption, making this type of CuO useless for our purpose. Sample 1 with the smallest grain size (10  $\mu\text{m}$ )<sup>1</sup> has shown consistent decrease in oxygen production due to loss in each cycle, which is probably due to partial melting of the upper layer, which reduces the efficiency of oxygen absorption. Partial melting of the upper layer was observed after the experiment and may be due to impurities in the sample. Oxygen loss in each cycle for three samples is shown in the Figure 3.7 and Table 3.4 shows the total oxygen released in first and second cycles from the three samples.

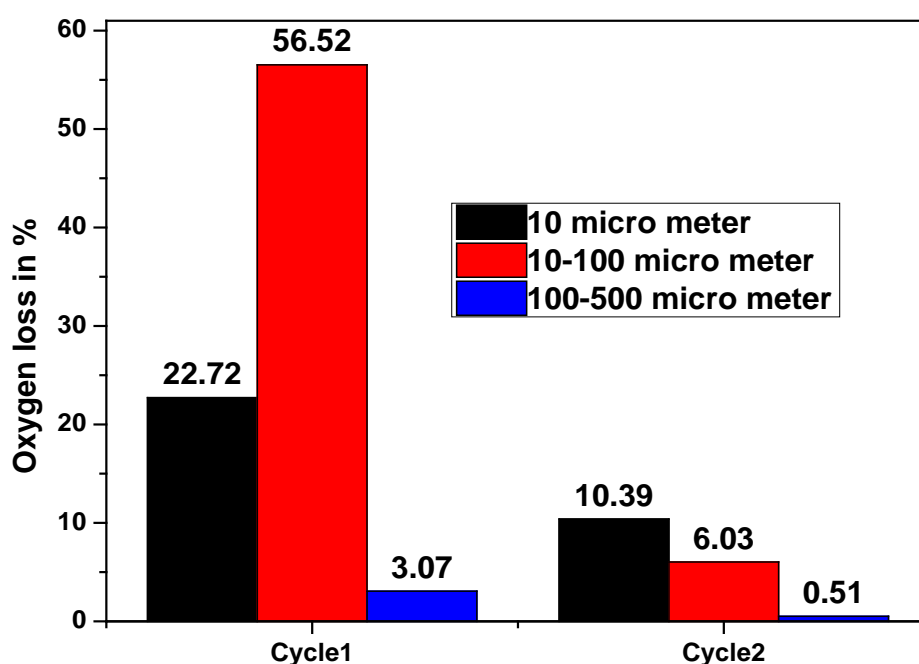


**Figure 3.7:** Oxygen loss % in each cycle for three different grain sized samples.

Sample 3, which has highest grain size, shows consistent desorption and absorption pattern in both the cycles. While cooling, it absorbed more than 99% of the released oxygen and it was not melted during heating.

Another important finding of the different heating experiments was that heating and cooling rates are important factors for both desorption and absorption efficiencies, at least for sample 1. A slow temperature increase of at least 15 min per 50<sup>0</sup>C produces more oxygen; especially in the temperature range 700<sup>0</sup>C-860<sup>0</sup>C. Similarly, a slow cooling rate of at least 50<sup>0</sup>C per 30

min in the temperature range 860<sup>0</sup>C-700<sup>0</sup>C will produce a higher absorption efficiency of oxygen.

Sample → Cycle ↓	CuO (10 μm ) Oxygen content	CuO (10-100 μm ) Oxygen content	CuO (100-500 μm ) Oxygen content
First	6.6 mbar	9.2 mbar	5.2 mbar
Second	5.1 mbar	5.8 mbar	5.2 mbar

**Table 3.4:** Total oxygen released at 860<sup>0</sup>C from CuO samples with different grain sizes for two successive cycles.

### 3.6 Conclusions

The CuO combustion studies produced initially 5.2 mbar to 9.2 mbar of oxygen at 860 <sup>0</sup>C, which would be sufficient for oxidizing carbonaceous material in meteorites. The absorption studies, i.e., the re-absorption of oxygen while cooling the CuO/Cu back to room temperature, indicates that a higher grains size and slow cooling rates increases the absorption efficiencies, i.e., reduces the amount of oxygen still in the line at the end of each heating cycle. However, more studies are needed to optimize the use of CuO for our combustion lines.





# Chapter 4 : EGT Data analysis

## 4.1 Introduction to mass spectrometer software

The noble gas mass spectrometers used so far in the institute are all sector field instruments, for which the signal is simply measured as a current on the top of a flat peak. Using proper calibrations, the current at peak maximum can directly be transferred to the number of ions and therefore to noble gas concentrations. The situation is different for Time-of-Flight instruments because for them the number of ions is proportional to the area of the signal, which is ideally a Gaussian peak. To properly handle the signals obtained from the TOF system we therefore developed a computer code able to handle different peak shapes, perform reliable baseline corrections, and enables uncertainty estimates.

## 4.2 EGT Data acquisition methods

A key instrumental aspect in TOF-MS is how to process the pulses from the detection system (MCPs). Thereby the major difficulty arises because any detection and data handling system must be very quick. For example, for our TOF- system a mass resolution of  $m/\Delta m = 1000$  requires that the individual signals are processed as fast as  $\sim 5$  ns. Typically this is usually done either by pulse counting (TDC) or by fast digitization of the analog signal (ADC). For the EGT we checked both data acquisition systems and found that each system has advantages and disadvantages (Guilhaus, 1995).

### 4.2.1 Time to Digital Converter or Ion Counting mode (TDCs)

A time-to-digital converter (TDC) measures the detector signal like binary values, i.e., the TDC counts the signal which is above a pre-selected threshold as '1' and below as '0', no matter how many ions are responsible for the signal. Consequently, the TDC gives no information about the number of ions. However, for proper using the TDC detection system the user has to carefully select the threshold voltage, which should cut all the electronic noise without cutting any signal.

In practice, ion counting devices usually based on multi-stop time to digital converters. Time to digital (TDC) digitization begins with a discriminator, which triggers when a particular signal level is reached. This signal is then registered by a counter, which records the flight time. After a small dead time ( $\sim 100$  ns), discriminator and counter are ready to record the next ion. TDC's sense either the onset of pulses (start event) or onset and decline of the pulse (start and stop event) and store the times of the start event or intervals between start and stop events.

The TDC digitizer used by us is the MCS6, a multiple event time digitizers from the company FASTCOM<sup>®</sup>. For proper usage an external starting pulse, which is given by the pulser, and the signals from the EGT detector are feed into the card, the latter is connected to one of the STOP inputs. Doing so, the EGT card records for each incoming stop event the specific time bin, which corresponds to the arrival time relative to START pulse. Specifications, features, and a TDC user manual (MCS6 user manual, 2012) are given in Appendix B.1.

## 4.2.2 Analog to Digital Converters (ADCs)

By using ADCs the detector signal is digitized at a fixed sampling rate, converting the voltage from the detector into a digital signal. For better dynamic range ADCs are usually used in so-called “sum averaging mode”, i.e., several spectra are digitized and the thus obtained results are summed together and stored into a memory. In contrast to TDC cards, using ADC cards it is possible to calculate the number ions that are detected in each interval. For a proper set-up of an ADC detection system impedance matching is required from the detector over the pre-amplifier to the ADC-card to avoid ringing effects.

The ADC card used here is an Agilent U1082A – Acqiris-High-Speed PCI Data Converter (AP240: 8-bit, 2 ch, 1 GHz, 1-2 GS/s), which is an 8 bit ADC system from Agilent®. Specifications and features of the EGT- ADC set-up procedure are explained in Appendix B.2.

## 4.3 EGT Data Analysis Software (EGT-DAS)

### 4.3.1 Introduction to the data analysis software

The TDC and ADC data acquisition systems (see above) produces output files with the extension \*.asc, \*.awd, and \*.dat. The data analysis software developed in this PhD, the EGT-DAS system, is able to work with all of those files. Ideally, the signals detected using either the TDC and/or ADC system should be of gaussian shape as shown in Figure 4.1. For real instruments, however, the signals are often not gaussian but instead have so-called modified gaussian shapes. Such modified Gaussians can best be described by a superposition of a gaussian distribution with an exponential curve (see Figure 4.1). Consequently, for getting proper data on peak areas the modified gaussian peak shapes must be fitted reliably, which is challenging. The rest of this section gives information about the software, the compatibility, and the user interface.

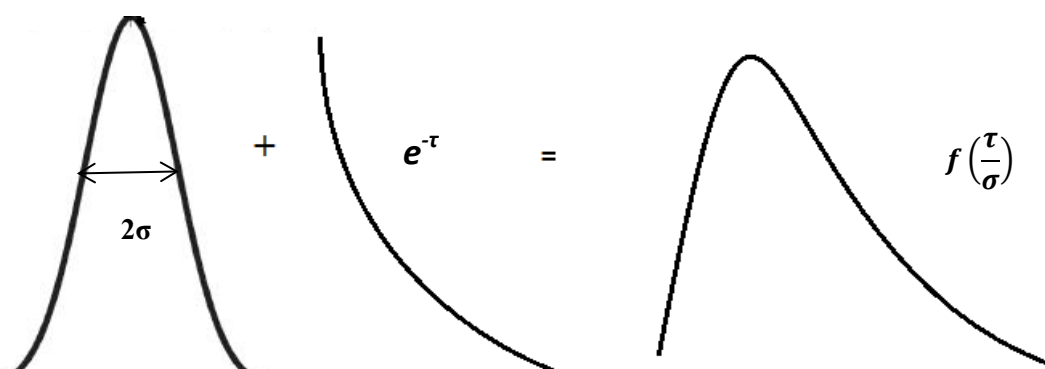


**Figure 4.1:** Gaussian peak shape (a); exponential decay tail (b); exponentially modified gaussian peak (c) (Picture taken from Chromatographic Integration Methods (Dyson, 1998))

### 4.3.2 Software information and compatibility

The coding of the EGT data analysis software EGT-DAS has been written in Python 2.7 and the graphical user interface has been designed using the Qt designer on a Windows 7 platform. After only minor adjustments, the program can also run under other operating systems like LINUX. The program can also run using a more recent version of Python, which is now available together with the Qt-designer in single package called “PythonXY”. Changing to the PythonXY-package is highly recommended for future changes because of its very useful library.

### 4.3.3 Graphical User Interface of EGT-DAS

The Graphical User interface (GUI) for the EGT-DAS software is optimized for noble gas analysis. However, the software can also be used for any other type of TOF measurements after only minor adjustments. The GUI is shown in Figure 4.3. Pressing the button “Load data” opens a pull-down menu allowing the user to load the data file, either from the EGT or from any other TOF instrument. In the next step the user can give some sample details that help compiling all information relevant for this measurement. Finally, the program automatically plots the intensity as a function of time on the upper panel graph. In the next step the user has to perform the mass calibration, i.e., the user has to enter the time of two known peaks for mass calibration. For higher accuracy of the mass calibration it is recommended that the selected peaks cover the entire range of masses the user is interested in. The principal of the mass calibration procedure, which is constant until the tuning of the instrument is changed, is explained in chapter 6. Briefly, the total flight time  $T$  of an ion through the instrument is given by (Cotter, 1993):

$$T = t_0 + \tilde{c} \left(\frac{m}{q}\right)^{\frac{1}{2}} \quad \text{--- (4.1)}$$

Where  $t_0$  takes into account any offsets from the experimental set-up, i.e., from the acquisition electronics, the detector or a possible delay in the extraction pulser. This leads to with  $c = \sqrt{\tilde{c}}$ :

$$\frac{m}{q} = \frac{(T-t_0)^2}{c} \quad \text{--- (4.2)}$$

Where  $m$  is the mass of the ion (amu/q),  $T$  its flight time,  $t_0$  the starting point for  $m = 0$ , and  $C$  is a constant factor depending on the set-up of the instrument (Scherer, 1999). The accuracy of the calibration can be improved by using more than two masses.

$$c = \frac{t_1 - t_2}{\sqrt{m_1} - \sqrt{m_2}} \quad \text{--- (4.3)}$$

$$t_0 = \frac{\sqrt{m_1} \cdot t_2 - \sqrt{m_2} \cdot t_1}{\sqrt{m_2} - \sqrt{m_1}} \quad \text{--- (4.4)}$$

The constants  $C$  and  $t_0$  can now be determined for two (or more) known values of  $m/q$  by using equations 4.3 and 4.4. Generally, the more known peaks are included into the evaluation

the better are the results. The quality of the mass calibration is also increased by using species that lie on opposing ends in the mass spectrum. The quality of a mass calibration is determined by the relative deviation  $\delta m$  of the measured mass to the tabulated values and calculated by

$$\delta m = \frac{m_{tab} - m_{meas}}{m_{tab}} \quad \text{--- (4.5)}$$

Where  $m_{tab}$  is the theoretical value and  $m_{meas}$  is the mass determined using the calibration. After the mass calibration, the plot of intensity versus  $m/q$  is shown on the lower panel of the GUI after pressing the button “mass plot”. In the next step the user has to select the peak of interest, which can be done using the mouse and selecting the time span in the first panel. After selecting the peak of interest the program shows the starting and end points of the selection, the position of the peak center, and the peak height on a display window. After having checked that the peak selection is reliable in term of baseline correction (see below), the user presses the button “EGT FIT” to obtain the results of the selected peak, i.e., peak center, the background corrected peak amplitude, and the full width at half maxima. In addition, the program calculates the mass resolution and the signal-to-noise ratio. The main result, however, which is the net-area under the peak, is calculated via three different methods. First, is assumed that the peak has a gaussian shape and a gaussian function is fitted through the (background corrected) data. Second, an exponential modified gaussian function (EMG) is used for fitting. Third, the area is determined using Monte Carlo integration techniques (MCI). The results for each selected peak can be exported into a text-file by pressing the button “exports results“. Note, the current version of the GUI also consists of additional buttons labeled with the names of the noble gas isotopes. Unfortunately, the buttons are not yet programmed but the goal is that pressing the button with automatically select the peak of this isotope and the program will perform all the peak selection and fitting procedures automatically. A flow diagram of the EGT-DAS program is given in Figure 4.2.

#### 4.4 Introduction data handling

While pre-handling the data is not necessary in our EGT-DAS program, we have to distinguish whether the measurements have been done using the ADC or the TDC card. In general, the data obtained using the ADC card are more difficult to handle and to interpret. The reasons are as follows. First, measurements done using the ADC card produce – depending on the acquisition setting - often more than one spectra/file and/or folder for each measurement. In contrast, measurements using the TDC card produce only one data file. Second, data measured using the ADC card often suffer from electronic noise and a proper background correction is necessary. In contrast, the noise is electronically eliminated via the threshold and discrimination option of the TDC system, which therefore enables an almost background free measurement. However, no matter the differences, both types of spectra can be handled with the EGT-DAS program using the same GUI set-up.

Flow chart of EGT Data analysis Software

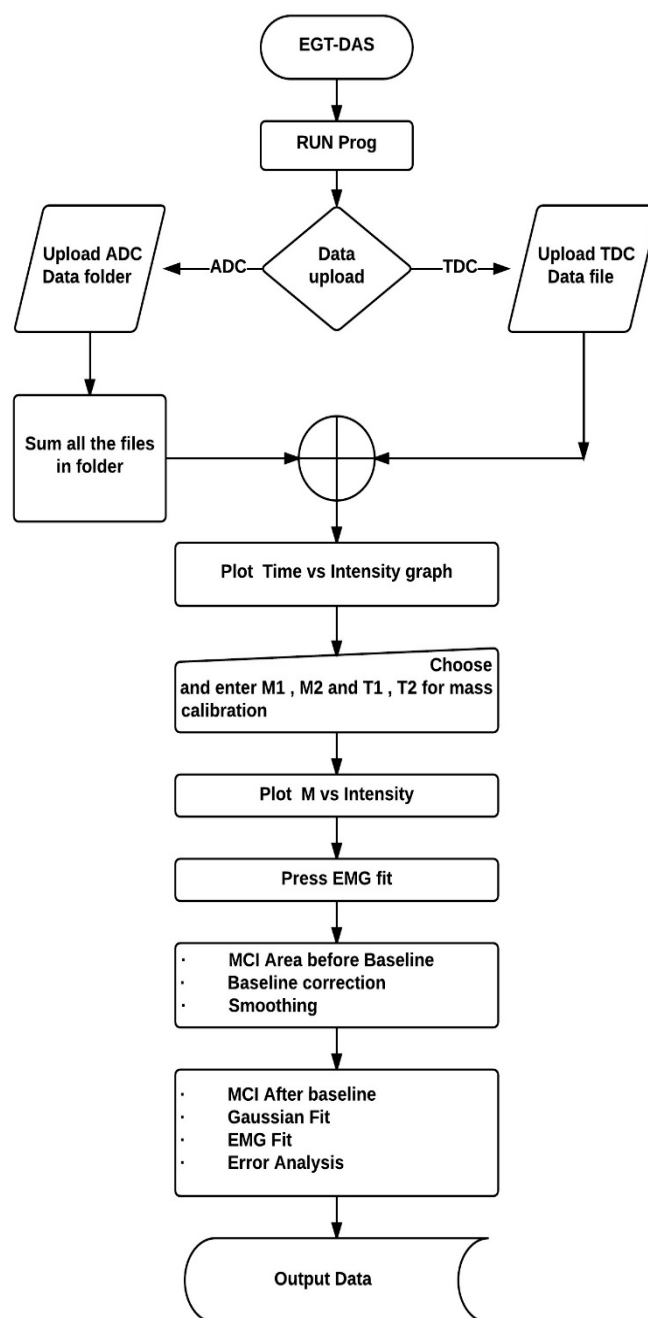


**Figure 4.2:** The flow chart for the EGT-DAS gives basic information about the data analysis process

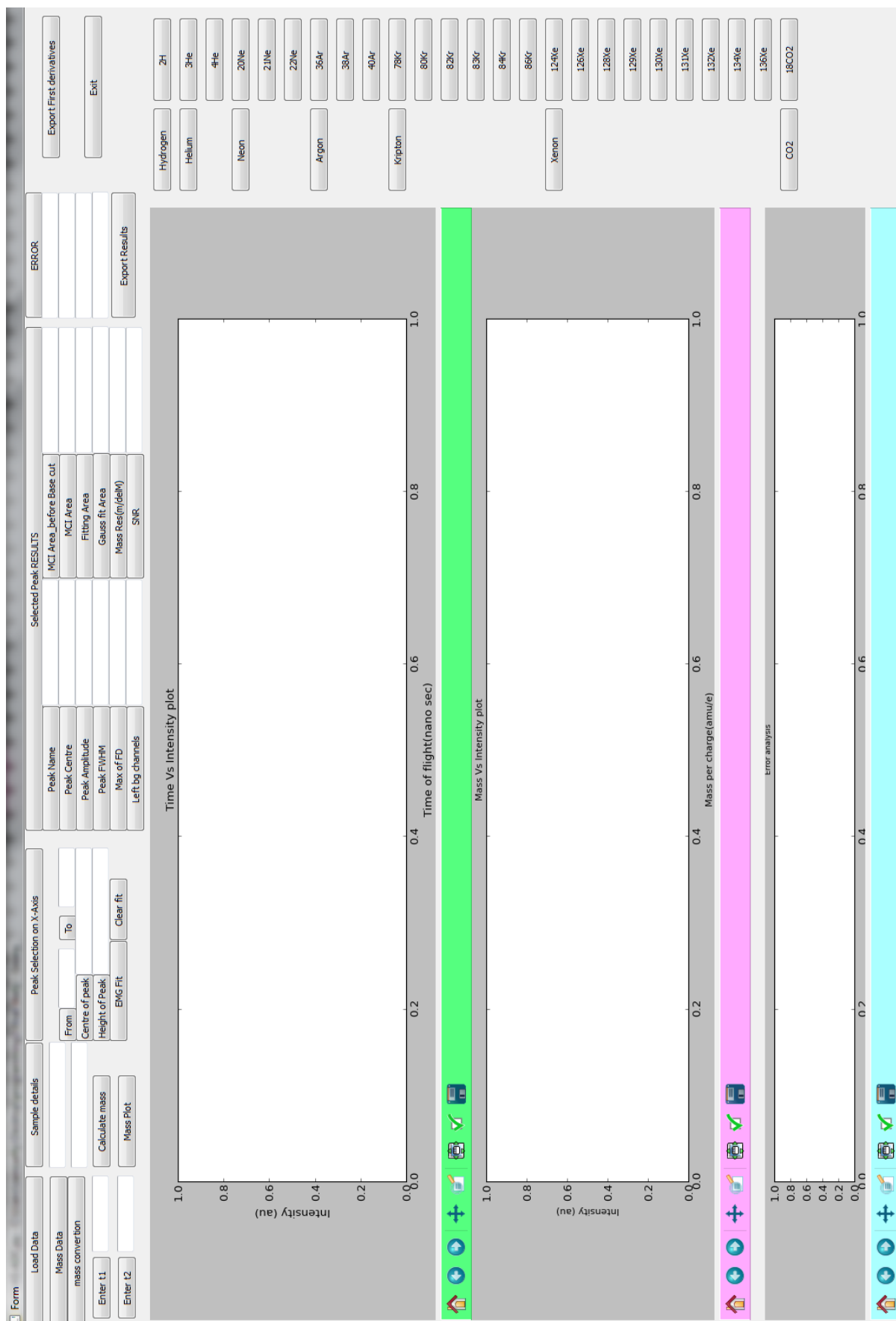


**Figure 4.3:** Graphical user interface for the EGT-DAS program

Using the ADC card for data analysis multiple files are summed together and plotted as intensity versus time diagrams (Fig. 4.4., upper panel) and – after mass calibration - as intensity versus mass diagrams (Figure 4.5, lower panel). An ADC data files consist of 40'000 data points. With a sampling rate of 0.5 ns a spectrum is 20  $\mu$ s. Note that with this sampling rate the heaviest Xe isotopes reach the detector after about 14  $\mu$ s). In the measurement set-up used by us we produce mass spectra from mass zero up to mass 500 amu. For our data handling procedures, however, we limit the mass spectra to masses lower than 200 amu. Note that the averaging mode of the ADC card itself produces averages of the individual spectra, called waveforms. An example of such an averaged version, where 60'000 individual waveforms are summed together, are shown below Figure 4.4. With the used 1 kHz pulse frequency, averaging 60'000 spectra then takes 1 minute of acquisition time. Each output data file produced by the ADC card contains information regarding settings (Table 4.1). The first line gives the path of the data file, the second line gives the acquisition date and time, the third lines gives the number of data acquisitions (the ADC card recalls each acquisition as a sample). Line number five gives the time range, i.e., the 0.5 ns sampling time. With such settings, i.e., 0.5 ns sampling time and 40'000 number of samples we cover a total measurement time per spectra of 20  $\mu$ s.

1	# c:\Users\ramisetty\Desktop\AcqirisRun_2014-12-11T12-22-36\AP240 Ch1 2X_1.awd
2	# Date: 2014-12-11T12:23:37
3	# Number of samples: 40000 S (40.0 KS)
4	# Time increment: 5.00000000e-10 s (500 ps)
5	# Gain: -1.95312500e-04 V/LSB (-195 $\mu$ V/LSB)
6	# Offset: 2.40000000e-02 V (24.0 mV)
7	# Number of waveforms per average: 60000 Waveforms
8	# Trigger delay (in samples!): 0.00000000e+00 S (0.00 S)0

**Table 4.1:** Information regarding ADC data acquisition settings in the data acquisition file.

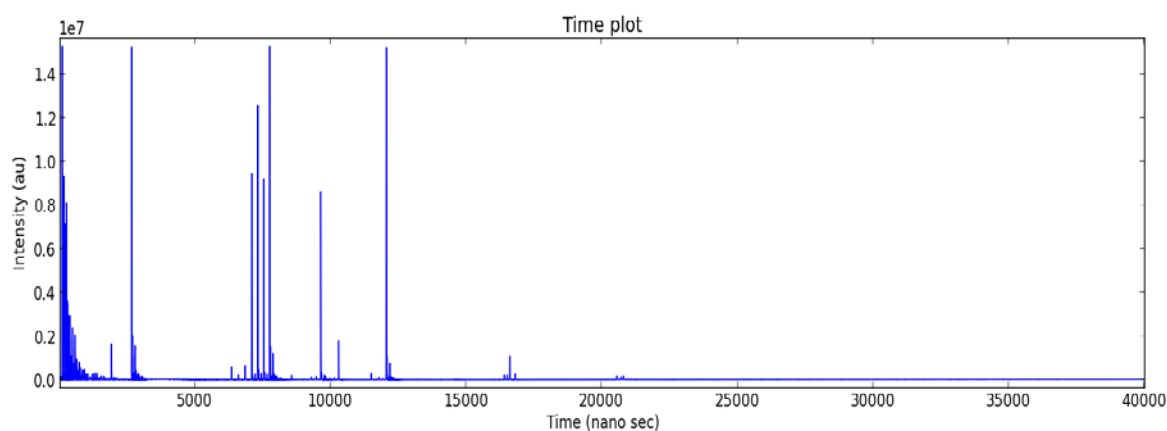


**Figure 4.4:** Plot of intensity versus time for a Kr-Xe calibration. The ADC data are for 40'000 data points taken every 0.5 ns with 60000 averagers.

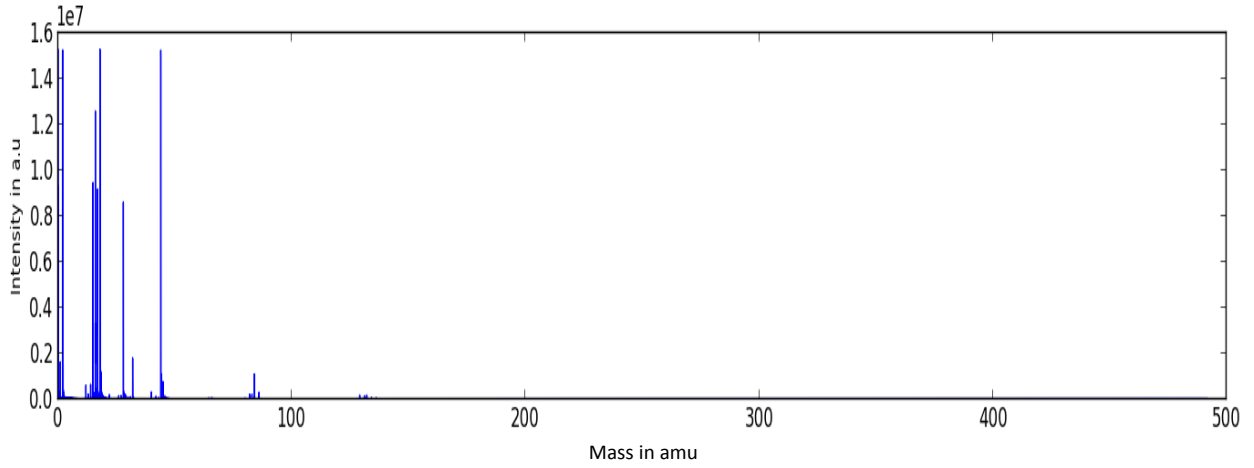


**Figure 4.5:** Mass calibrated spectra for the time spectra shown in the upper panel.

As mentioned above, the header includes information on measurement date, number of acquired samples, the sampling interval (given by the time increment of 0.5 ns), the gain of the acquisition card (Gain), and the Offset, which is chosen by user. In addition, the header gives the number of waveforms per average and the trigger delay. With such information the conversion of the voltages to the digital value scan is done according to (see also Acqiris acquisition card manual, Acqiris Manual, AP240):

$$voltage = Gain * \left( \frac{data\ values}{Number\ of\ waveforms} - 128 \right) - offset \quad --- (4.6)$$

Based on the thus determined voltage and with the input impedance of  $R = 50\ \Omega$  we can calculate the ion current and therefore the ratio of the ion current relative to the gas amount, which is the sensitivity of the spectrometer.

## 4.5 Peak area determination

### 4.5.1 Peak selection and baseline correction

The span selection of a Kr spectrum before mass calibration is shown in the upper panel of Figure 4.6(a), the corresponding mass spectrum is given in the middle panel in Figure 4.6 (b), and the selected  $^{84}\text{Kr}$  peak is as shown in the lower panel (Figure 4.6(c)).

After having selected the region of interest, data obtained using the ADC card need to be corrected for electronic noise, which gives the baseline in the spectrum. Here we use a simple numerical technique for the baseline correction of the selected peak, which is based on first and second order derivatives (Glynn, 2007). The procedure, which gives the left ( $X_L$ ) and right ( $X_R$ ) limits of the peak, is graphically explained in Figure 4.7.

Briefly, the peak is defined by positive values that are continuously increasing from the beginning to center of the peak. Coming from the low mass side, first and second derivatives are zero or close to zero until the peak starts, then both derivatives show positive data points that increase with time or  $m/q$ . At the end of the peak of the high mass side the first derivative is negative and second derivative is positive and both become zero again (Figure 4.7) (Shulamit Levin, 1997). With this technique the start and the end of the peak can be determined, which is needed to define the background. After having established where the



peak is, i.e., the region covered by the peak, the rest of the selected region is assumed to be baseline that needs to be corrected for. Thereby the baseline under the peak is determined from the baseline left (and right) of the peak. This is done using a best linear fit from  $X_L$  to  $X_R$ . Note, this technique only gives a reliable baseline for peaks where the baseline of the high and the low mass side of the peak is similar. In cases where the baseline is different on both sides of the peak, alternative and more sophisticated baseline fitting procedures must be used.

Note, for proper baseline correction the selected area should cover at least 20 points to the left of the starting position of the peak.

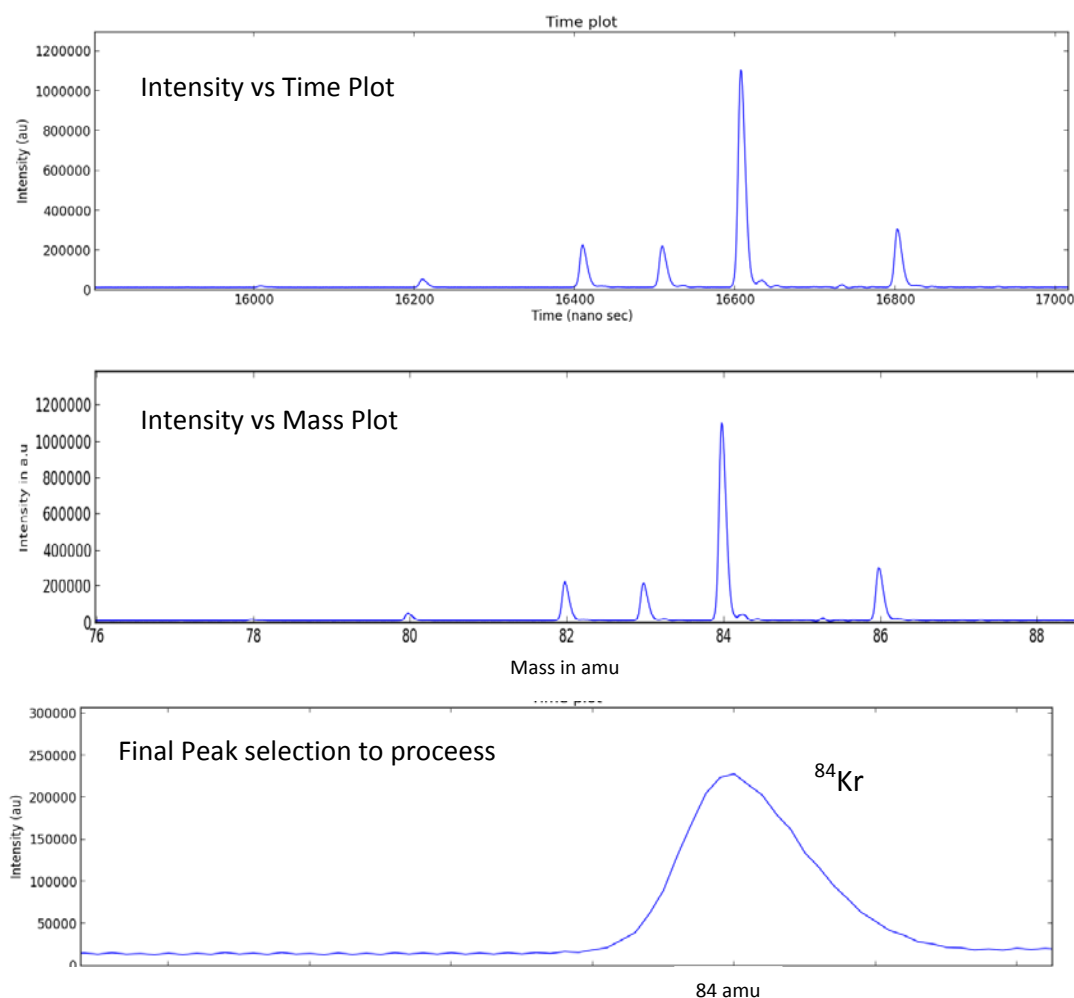


**Figure 4.6:** Peak Selection on EGT-DAS (a) Spectra of intensity as a function of time for Kr isotopes. (b) The same spectra but with intensity as a function of  $m/q$  (c) Selected  $^{84}\text{Kr}$  peak.

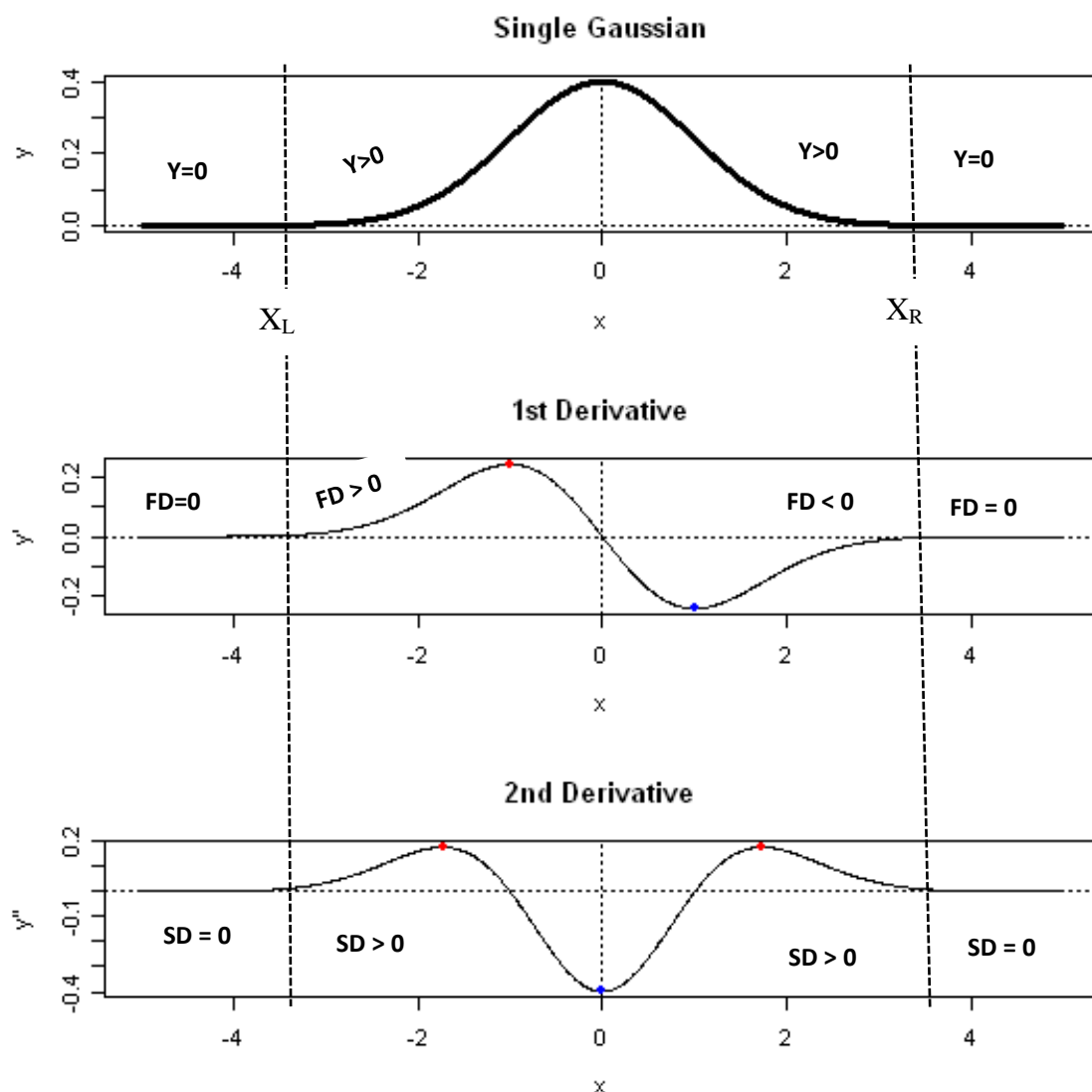


**Figure 4.7:** First and second derivatives of Gaussian peak, both are positive after the peak starts and zero before. At the end of the peak first derivative (FD) is negative and second derivative (SD) is positive and then both are zero.

#### 4.5.2 Smoothing and Signal-To-Noise ratio calculation

The background corrected data are then smoothed using a lower degree Savitzky Golay filter (Golay, 1964), which is a smoothing technique without disturbing the original signal. A very important parameter describing the quality of a measurement set-up is the signal to noise ratio (SNR), which is a measure how much larger the signal is compared to the noise. A large signal-to-noise ratio indicates that the signal is much larger than the noise, which is an indication of a reliable measurement.

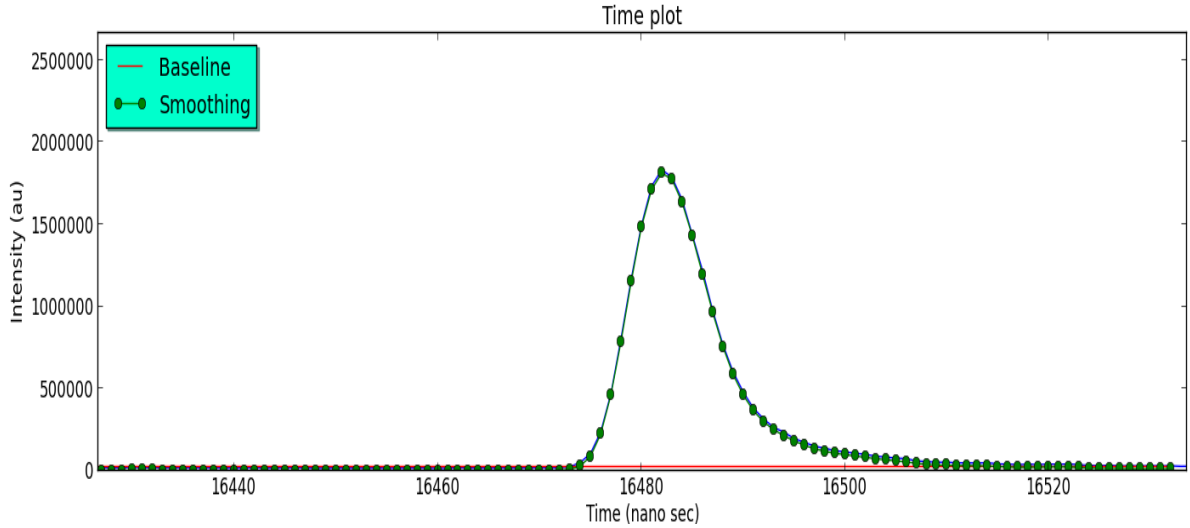


**Figure 4.8:** Original data (blue line), baseline (red line), and smoothed data (green line with dots) for the selected  $^{82}\text{Kr}$  peak.

Here we calculate the SNR by making use of the fact that the noise level on the signal should be the same as in-between signals, i.e., that the noise is mass independent (at least in limited mass ranges). Note, the noise can be reduced by using longer acquisition times and/or by summing and averaging more spectra. Doing so, the reduction of the noise and therefore the increase in SNR is proportional to the square root of the acquisition time and/or the number of spectra that are averaged. The EGT-DAS program calculates the SNR for every peak automatically after subtracting the baseline according to:

$$\frac{\text{Signal amplitude}}{\text{noise base}} = \frac{S}{(\bar{X}_B)} \quad \text{--- (4.7)}$$

Here the signal amplitude is the peak height after baseline subtraction and the noise base is the mean value of the baseline.

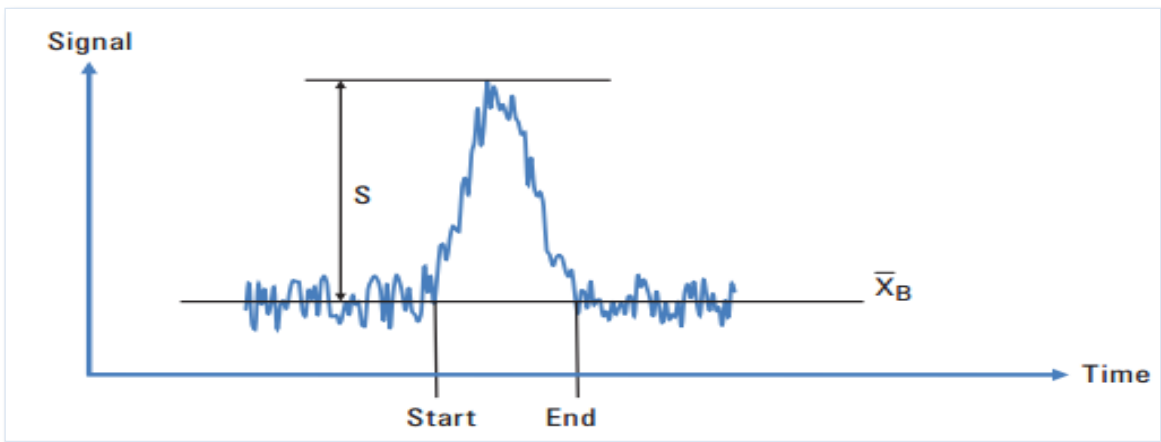


**Figure 4.9:** The calculation of the signal-to-noise-ratio (SNR), which is the ratio of the signal amplitude ( $S$ ) to the noise level ( $\bar{X}_B$ ) (Agilent, 2011).

### 4.5.3 Mass resolution

The mass resolution is mathematically defined as

$$\frac{m}{\Delta m} = \frac{t}{2 \cdot \Delta t} = \frac{\mu_t}{2 \cdot FWHM} \quad \text{--- (4.8)}$$

where  $t$  is the time-of-flight,  $\mu_t$  is the center of the peak, and  $\Delta t$  is the full-width at half maximum (FWHM), which is experimentally determined from the time spectrum.

### 4.5.4 Peak Area Calculation

After peak finding, definition of the background, baseline subtraction, and smoothing the EGT-DAS software calculates the area under the peak by using three different methods, i) numerical Monte Carlo integration (MCI), ii) fitting a gaussian shape to the peak, and iii) fitting an exponentially modified gaussian shape to the peak. Below the three different methods are explained in some detail.

### 4.5.5 Monte Carlo integration (MCI)

For the EGT-DAS program we use the so-called “dart method” also known as “hit and miss method” (Langtangen, 2012).

Consider a geometric region  $G$  in the plane and a surrounding bounding box  $B$  with geometry  $[x_L, x_H]$  and  $[y_L, y_H]$ . One way of computing the area of  $G$  is to draw  $N$  random points inside  $B$  and count how many of them,  $M$ , lies inside  $G$ , i.e., under the peak. The area of  $G$  is then the fraction  $M/N$  times the area of  $B$ ,  $(x_H - x_L) \times (y_H - y_L)$ .

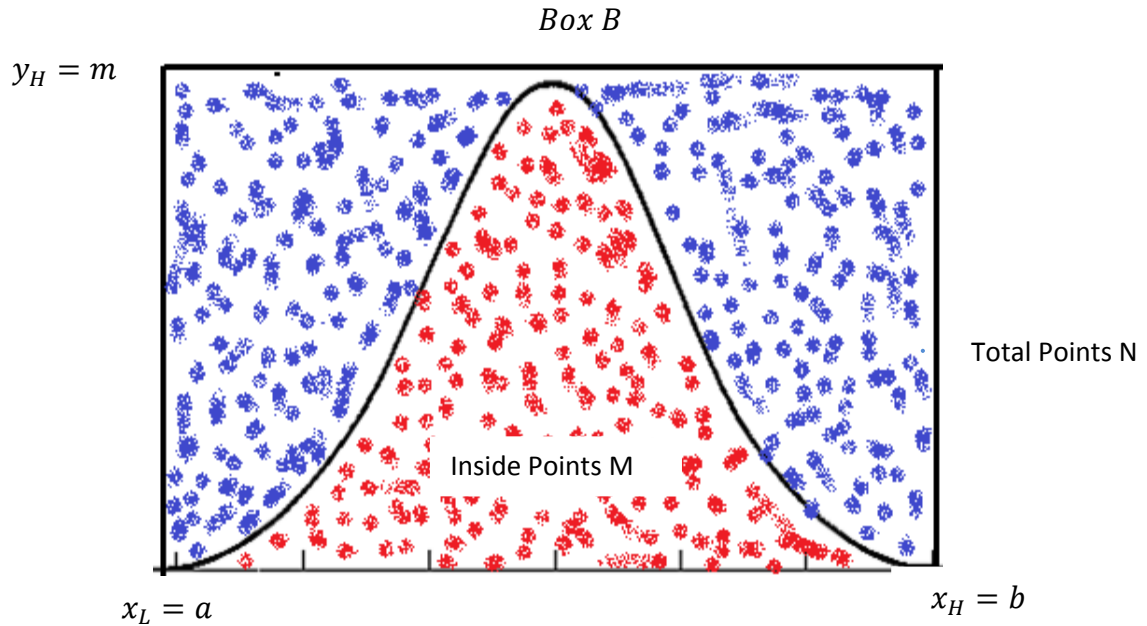


**Figure 4.10:** Hit and miss method for integrating an area under a curve. Random numbers are produced within the  $x$ - $y$  limits and are compared to the curve  $f(x)$ . All random numbers are

shown as blue dots. The points under the curve are shown by the red dots. The fraction of hit points under the curve with respect to the total number of random points in the total selected area gives the area under the curve, i.e. the area or integral is then given by:

$$Area = \frac{M}{N} \times m \times (b - a) \quad \text{--- (4.9)}$$

Where  $M$  = number points under the curve

$N$  = total number of random points

$m$  = maximum of  $f(x)$  in the limits of  $a$  and  $b$

$a, b$  = left and right limits of  $x$

In our case, after selecting a peak, the MCI will determine the area as given in eqn. 4.9. The MCI part of the code has been validated for different shapes of known area (triangle, semicircle) and with different amounts of random numbers. In addition, the MCI part has been done for peaks before and after smoothing.

### Monte Carlo Error Analysis:

The accuracy of Monte Carlo methods only depends on the sample size of the random numbers  $N$ ; the uncertainty is proportional to  $N^{1/2}$ . Note, the uncertainty is independent on the dimension of the integration, i.e., the accuracy of the integral only depends on the number of trials. The variance of the data is given by

$$Var(f) \equiv \frac{1}{N} \sum_{i=1}^N (f(i) - \bar{f})^2 \quad \text{--- (4.10)}$$

And by Central Limit Theorem, the error of the integral is

$$Error(I) = \sqrt{\frac{Var(f)}{N}} \quad \text{--- (4.11)}$$

Here  $f(i)$  is the value of the function at interval  $i$ , in our case it is the data measured at time step  $i$ . The term  $\bar{f}$  is the mean value of the data. The EGT-DAS program determines the peak areas usually by using between  $10^4$  and  $10^5$  random numbers for integration. The result of the MCI is the area and the uncertainty for each selected peak.

### 4.5.6 Area calculation by peak fitting

The EGT produces gaussian or almost gaussian peaks. Those being only “nearly gaussian” can best be described using the exponentially modified gaussian shapes. The EGT-DAS program can fit both types, i.e., gaussian or EMG to the data. For fitting the program uses the Scipy optimizer’s *fmin* ( ) function, that is based on a downhill simplex algorithm. The initial parameters needed for fitting are automatically calculated from the measured peak data. The gaussian function used for fitting is defined as:

$$f_{Gaussian}(x) = \frac{A}{\omega\sqrt{2\pi}} \exp\left(-\frac{1}{2}\left(\frac{x-x_c}{\omega}\right)^2\right) \quad \text{--- (4.12)}$$

The exponentially modified gaussian (EMG) is a gaussian function extended by an exponential term that describes the tail of the peak (see also section 4.3.1). The exponentially modified gaussian (EMG) function is defined as (Dyson, 1998):

$$f_{EMG}(x) = \frac{B}{2t_0} \exp\left(\frac{\omega^2}{2t_0^2} - \left(\frac{x-x_c}{t_0}\right)\right) * \left[1 + \operatorname{erf}\left(\frac{1}{\sqrt{2}}\left(\frac{x-x_c}{\omega} - \frac{\omega}{t_0}\right)\right)\right] + y_0 \quad \text{--- (4.13)}$$

Where  $y_0$  is the offset from the y-axis

$B$  is the Area under the peak

$x$  is the time step

$x_c$  is the center of the data set

$w$  is the width of the function

$t_0$  is the modification factor

The EMG function with respect to the amplitude is written as:

$$f(x) = y_0 + \frac{A}{t_0} \exp\left[\frac{1}{2}\left(\frac{\omega}{t_0}\right)^2 - \frac{x-x_c}{t_0}\right] \int_{-\infty}^z \frac{1}{\sqrt{2\pi}} \exp\left(-\frac{y^2}{2}\right) dy \quad \text{--- (4.14)}$$

Where  $z = \frac{x-x_c}{\omega} - \frac{\omega}{t_0}$

$y_0$  is the offset from the y-axis

$A$  is the amplitude of the data set

$x$  is the time step

$x_c$  is the center of the data set

$w$  is the width of the function

$t_0$  is the modification factor

However, equation 4.12 is a normal probability integral; its error function is given by:

$$\int_{-\infty}^z \frac{1}{\sqrt{2\pi}} \exp\left(-\frac{y^2}{2}\right) dy = \frac{1}{2} + \frac{1}{2} \operatorname{erf}\left(\frac{z}{\sqrt{2}}\right) \quad \text{--- (4.15)}$$

Here  $\operatorname{erf}(z)$  represents the error function (Dyson, 1998)

$$\operatorname{erf}(z) = \frac{2}{\sqrt{2\pi}} \int_0^z \exp(-u^2) du \quad \text{--- (4.16)}$$

Therefore, the final equation in terms of amplitude can be written as:

$$f(x) = y_0 + \frac{A}{t_0} \exp\left[\frac{1}{2}\left(\frac{\omega}{t_0}\right)^2 - \frac{x-x_c}{t_0}\right] \left(\frac{1}{2} + \frac{1}{2} \operatorname{erf}\left(\frac{z}{\sqrt{2}}\right)\right) \quad \text{--- (4.17)}$$

In the program, we are using this function for peak fitting. The initial parameters are  $y_0$  from the baseline correction,  $A$  from the maxima of the selected data,  $X_c$  from the center of the peak. Also the initial value of the FWHM, here  $w$ , is determined from the experimental data. For all these data the peak fitting procedure will return best fitted parameters. The result of the peak fitting is as shown in Figure 4.11

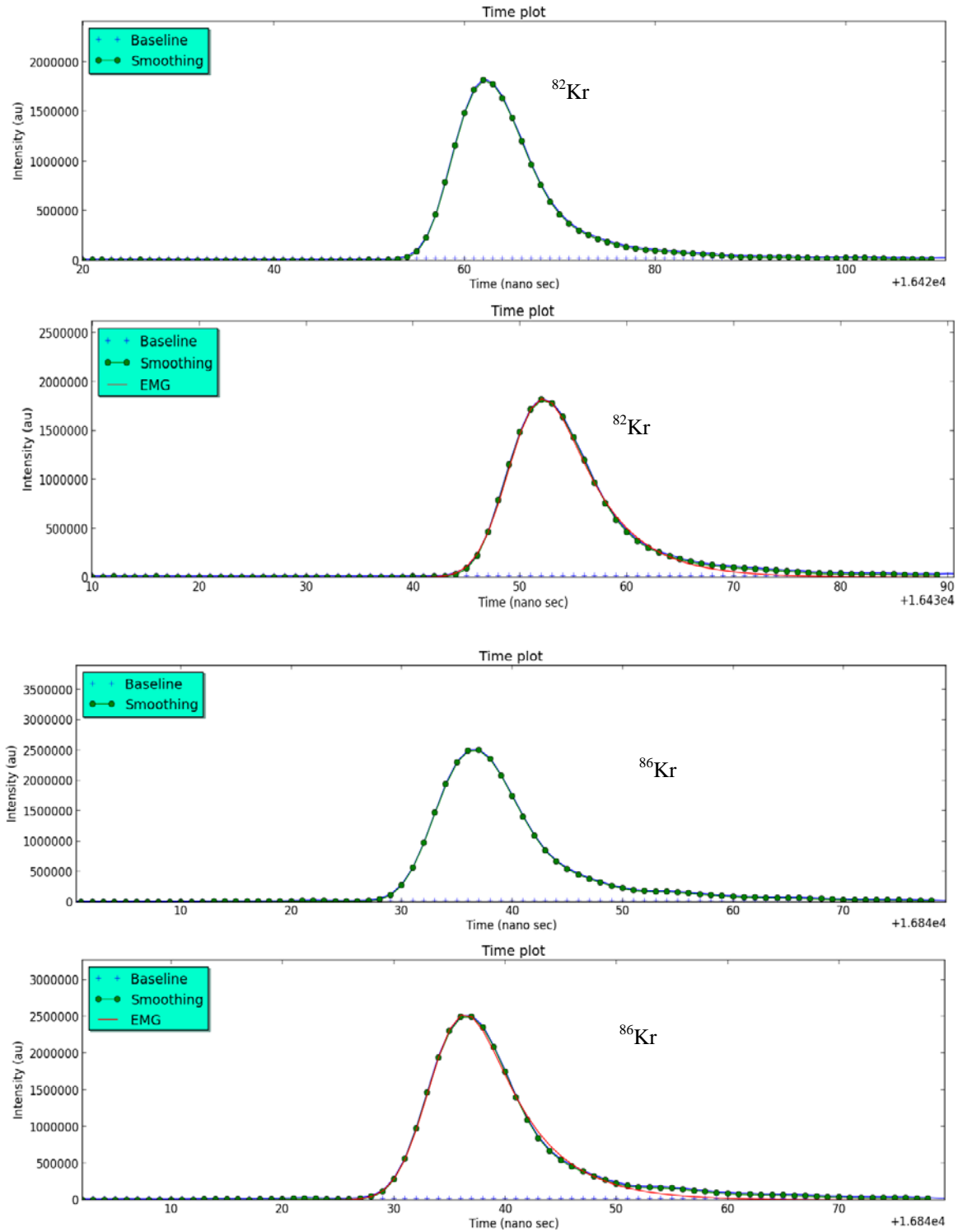


**Figure 4.11:** Peak fitting with Gauss and EMG functions and area under the curve for  $^{82}\text{Kr}$  and  $^{86}\text{Kr}$  for MCI before smoothing, MCI after smoothing, gauss fit area and EMG fit area.

#### 4.5.7 Error Analysis

Physically the peak area is determined by the number of electrons counted in a certain time interval. Consequently, each signal in each time follows a gaussian distribution (Bevington, Robinson, 2003). Therefore the area and its uncertainty can be calculated using:

$$\sigma_{Tot} = \sqrt{\sigma_{BG}^2 + \sigma_{MCI}^2}$$

or

$$\sigma_{Tot} = \sqrt{\sigma_{BG}^2 + \sigma_A^2}$$

Where  $\sigma_{BG}^2 = \text{variance of background calculation}$

$\sigma_{MCI}^2 = \text{error in Monte carlo integration}$

$\sigma_A^2 = \text{variance of total area calculation}$

#### 4.6 Output data file

After a successful calculation of peak areas and uncertainties the user can store the results in a text-file that can later be opened by, e.g., EXCEL®. Currently the output file contains sample details, peak limits, peak heights, FWHM values for all peaks, SNR, Mass resolution, the areas obtained using MCI, areas obtained using a gaussian fit, and the areas obtained by fitting an EMG. For all areas the uncertainties are also given.



# Chapter 5 : EGT-MS Design & Development

## 5.1 EGT-MS Introduction and motivation

Measurements of trace elements or isotopic abundances are of considerable interest in cosmochemistry and would not only allow an assessment of the abundances of elements and isotopes in the solar system but would also give information on transformation mechanisms of planetary material. Spectroscopic methods (gamma ray spectroscopy, X-ray spectroscopy, etc.) have been used for a long time in for elemental analysis but they have many disadvantages such as low sensitivities and difficulty in spectroscopic data interpretation. On the other hand, approaches like mass spectrometry provide precise and accurate measurements of trace elements and isotopic abundances. For several decades, sector field instruments became very popular for cosmochemistry and geochemistry but there are several disadvantages. Old types of sector field mass spectrometers were only able to measure one isotope per time. Recently, multi-collector sector field instruments became popular, but also faced problems, such as the ability to measure only one noble gas at a time, the difficulty calibrating different detectors, and an increase in volume, which decreases the efficiency of the system. However, Mass spectrometry continues to prove to be a very reliable, robust, and flexible analytical technique, ensuring that its use will continue to help investigating the universe, especially, time-of-flight (TOF) mass spectrometry is considered as one of the most important analytical technique with miniature high sensitive features, and also the time-of-flight mass spectrometers became popular due to recent advancements in technology, which can avoid the above mentioned difficulties in the sector field instruments. Several miniature time-of-flight mass spectrometers were developed for space applications including the RTOF mass spectrometer of the ROSINA instrument onboard the ROSETTA mission (Balsiger, 2007) but no significant development of time-of-flight (TOF) mass spectrometry for laboratory noble gas measurements all isotopes. The TOF instruments in the noble gas laboratories are using pulsed laser systems in ionization which are highly efficient but they are highly specialized (for example, the RELAX system in Manchester (Xe isotopes) and for the newly developed Kr spectrometer in Bordeaux) i.e. they are limited to one type of noble gas. To overcome the limitations mentioned above a new time-of-flight mass spectrometer is developed, which is based on RTOF (Balsiger et al. 2007). This works with electron impact ionization couple with ion trap and then the ions are extracted from the trap by using a high voltage extraction pulser into drift region followed by reflectron. The reflectron enhance the mass resolution. This design allows to measure all types of noble gases (He, Ne, Ar, Kr, and Xe). This new compact high sensitive design of time-of-flight mass spectrometer call it as Edel Gas Time-of flight Mass Spectrometer (EGT-MS). Another similar time-of-flight mass spectrometer for stratospheric chemical composition measurements was used for the P-BACE (Polar Balloon Atmospheric Composition Experiment) mission by Abplanalp (2009). With several modifications in EGT-MS design, leads to develop a new miniature high sensitive mass spectrometer for very low concentrations of noble gases in meteorites at the University of Bern.

Noble gas analysis in cosmochemistry often needs high sensitive mass spectrometers. For such kind of applications, a miniature high sensitive noble gas mass spectrometer has been developed, which contains a well optimized compact electron impact ion storage source (Abplanalp, 2010), a grid-free reflectron, and a well-designed detector. More details about the design and characteristics of the EGT-MS are described and discussed later in this chapter.

## 5.2 EGT Design and characteristics

The basic modules of the Edel Gas Time-of flight Mass Spectrometer (later called EGT-MS, here after EGT-MS will refer as EGT) are the electron impact ion storage source, the reflectron time-of-flight analyzer, and the microchannel plate detection system. The engineering diagram of EGT is shown in Figure 5.1

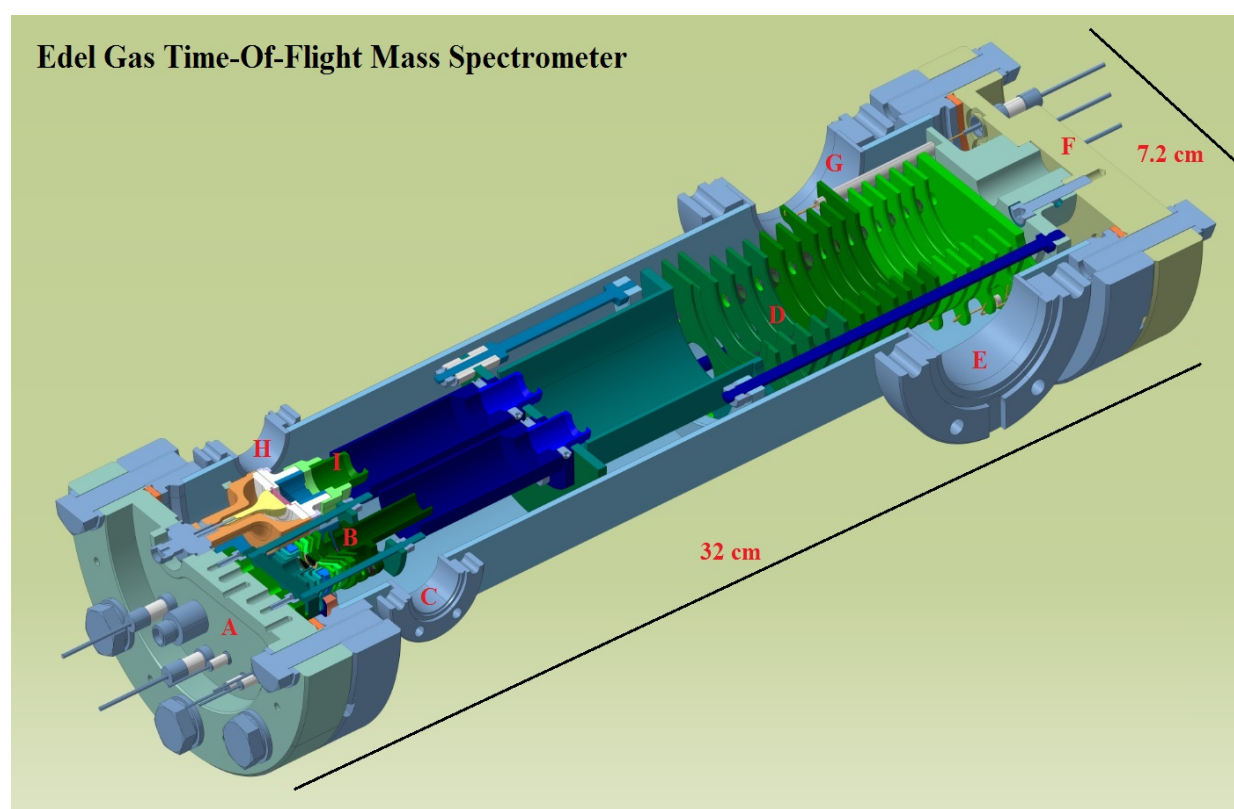


**Figure 5.1:** Engineering drawing of the EGT. Shown are all important parts of the ion-source, the reflectron and the detector with A) flange with the ion source and the detector with feedthroughs B) ion source C) getter D) reflectron, E) ion getter pump F) flange with reflectron feedthroughs G) ) turbo pump H) charcoal I) detector

The primary design of the EGT has undergone various changes and improvements (Huber, 2011). Further modifications in the connection of the turbo pumps and the detection system led to the present version. This new EGT has no electronic parts and a reduced volume due to improvements of the pumping connections. Its dimensions are 32 cm length, 7.2 cm of inner diameter, and a volume of 1.3 L. EGT physical details and operational parameters are given the Table 5.1.

EGT Physical Parameter	
EGT weight	~2.0 kg
Length	33.0 cm
Diameter	7.2 cm
EGT Operational Parameter	
Base pressure	$\sim 10^{-10}$ mbar
Filament Heating current	~1.25 A
Detector voltages	~2100 V for both (<2400V)
Pre-amp(Limiter) Gain	1
Pre-amp(Limiter) clipping voltage	5 V
Pulser voltage	~485 V
Bakeable Temperature	~300° C

**Table 5.1:** The technical details of the EGT are as mentioned in the.

### 5.2.1 Ion Source

The primary module of the EGT is an electron impact ion storage source. It is a small gridless electron impact ion source coupled with a trap as shown in Figure 5.2(a) and 5.2(b). The electrons produced by a hot LaB<sub>6</sub> filament move perpendicular to the ion optical axis towards the electron trap. On their way to the trap they ionize the neutral atoms/molecules and the thus produced ions are stored in a small potential well created by the space charge of the electron beam. The difference between a non-storage, continuous extraction ion source and a storage ion-source is explained in chapter 2. The ion source consists of several electrodes (as shown in Figure 5.2. (b)), which guide the electrons and ions to increase the performance. The EGT source has two slots for two filaments. The ions will be extracted into the acceleration region towards the time-of-flight drift region by applying a high negative potential at the extraction grid. In the acceleration region, ions are accelerated by applying high voltages to the lenses, which also focuses the ion beam

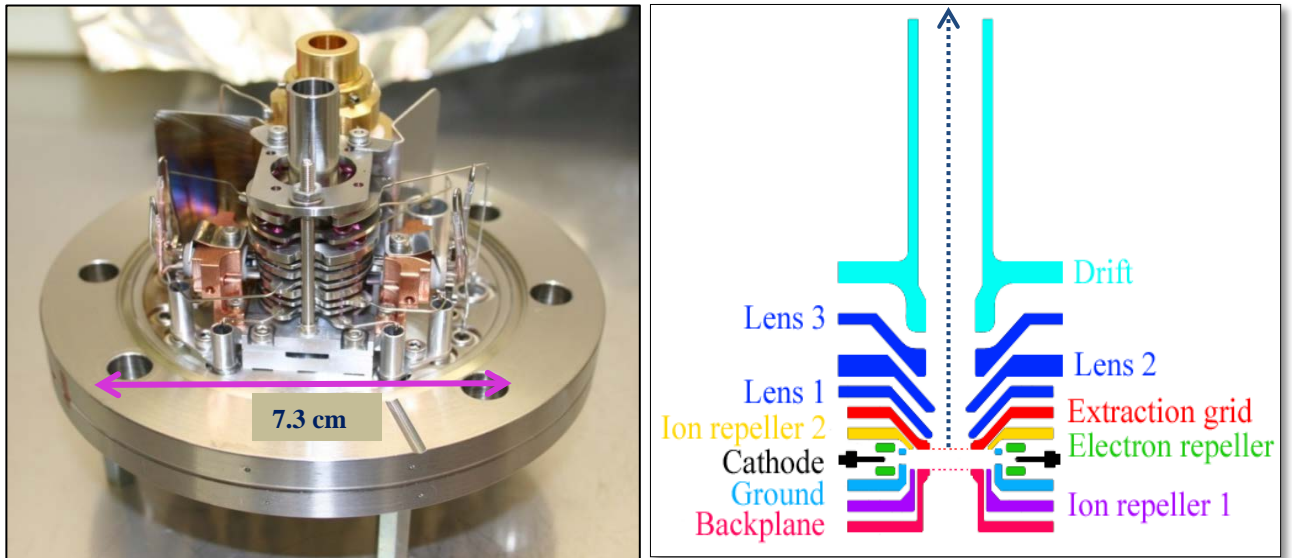


**Figure 5.2:** (a) View of the EGT ion source (b) schematic diagram of source electrodes. The dotted line is the ion optical axis.

### a) Filament:

The basic component in an electron impact ion source is the filament. In our EGT, it is a Lanthanum Hexaboride Cathode ( $\text{LaB}_6$ ) from Kimball<sup>®</sup>.  $\text{LaB}_6$  filaments give a greater brightness (higher current density), lower energy spread, and a longer lifetime than standard tungsten filaments. The rate of electron emission from any surface is material and temperature dependent. The current density and efficiency for various cathode materials are shown in Figure 5.3. The rate at which ions are produced depends on the electron current and the ionization cross-section of the considered species.

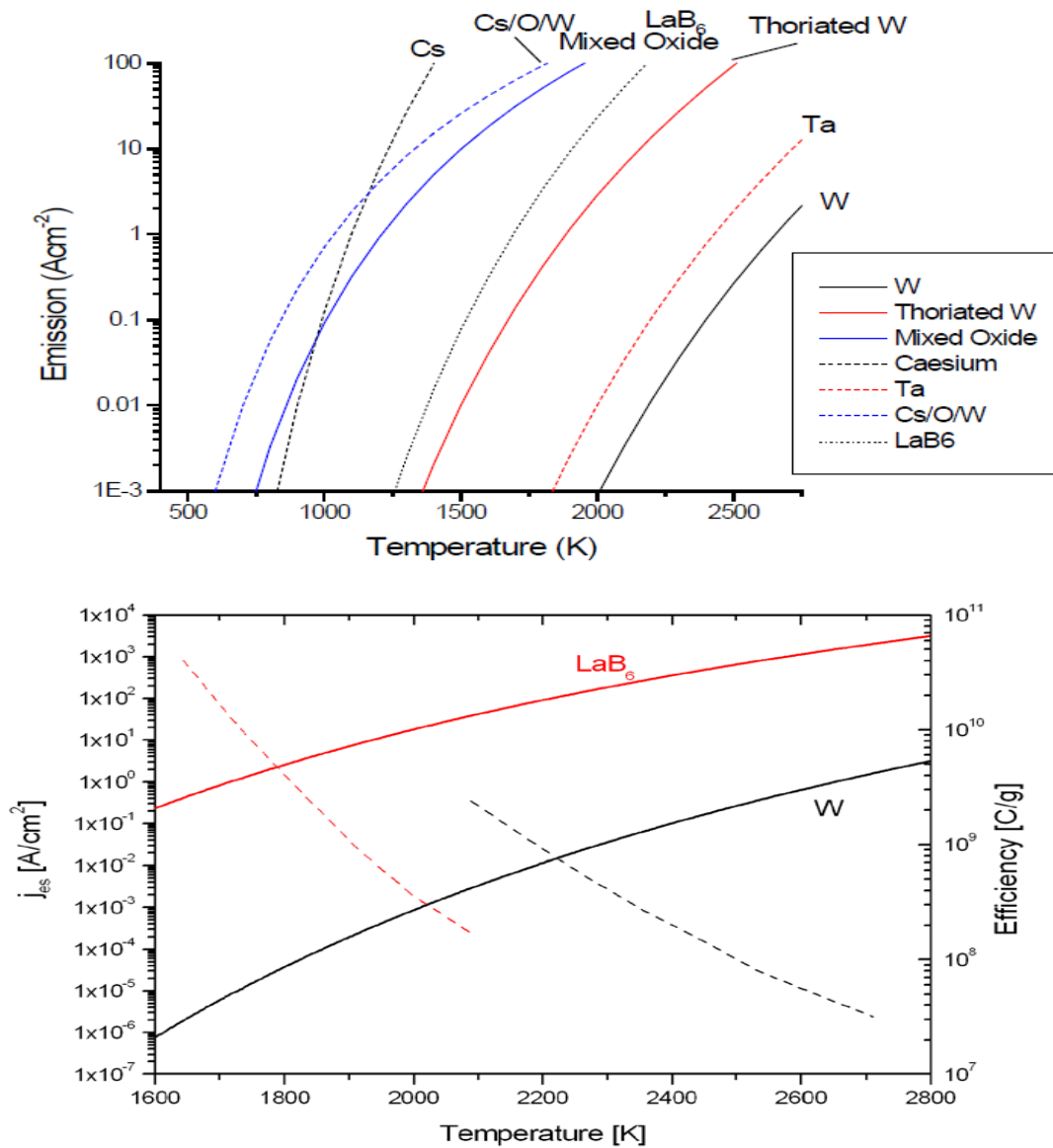


**Figure 5.3:** (Upper) Electron current density emitted from a material as a function of temperature for several cathode materials (Wolf, 1995). (Lower) Saturation current density (solid line) and efficiency (dashed line) versus cathode temperature for tungsten (black) and lanthanum hexaboride (red).

For ion storage and extraction, the position of the filament and the direction of the electron beam are very important parameters, which can be better adjusted using  $\text{LaB}_6$  filaments compared to tungsten filaments, since for the latter the position of the electron emission is uncertain when switching on and off the heating current and it can even change over time. The  $\text{LaB}_6$  cathode is mounted on a graphite base in a small and well defined area. The EGT has two slots for two filaments but at the moment only one filament is in operation, the filament slot and the filament position are shown in Figure 5.4. The specifications and different characteristics of the used  $\text{LaB}_6$  filament are shown in Figure 5.5. The filament set-up and startup procedures can be found in Kimball (2015). Filament emission and heating currents are optimized for an efficient performance of the ion source and we are using a heating current of about 1.25 A, to have a constant regulated emission current of 250  $\mu\text{A}$ . The operating voltage is 2 V and the cathode should operate at a pressure of lower than  $10^{-8}$  mbar. The heating current should not exceed 2 A, because the lifetime of the cathode is significantly reduced due to evaporation of the crystal if the heating current is in the range  $\sim 2$  A. The performance of the filament for different emission currents are discussed later in the results chapter. The filament should be installed carefully without any deformation since the position of the electron beam strongly depends on the exact position of the filament in the source. Due to electron beam deformation during ion extraction by the high voltage pulse, the electrons often reach not the other side of the ion source, i.e., the electron trap. Hence regulating the trap current as a measured of electron emission does not work reliable. We therefore regulate directly measured emission current.

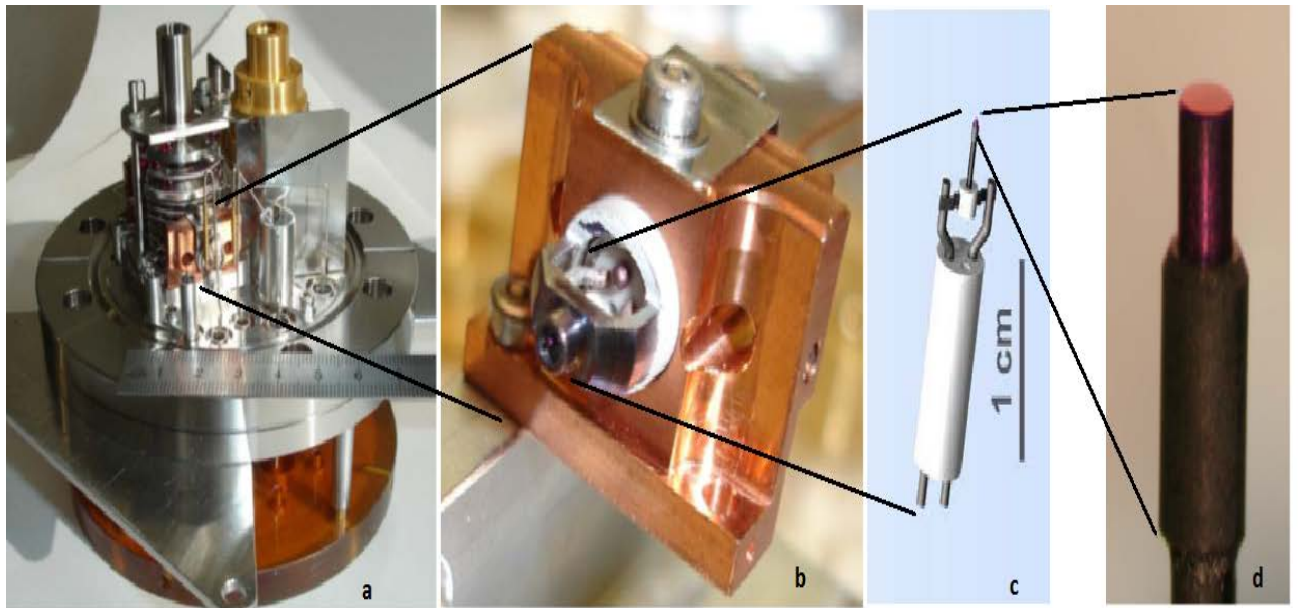
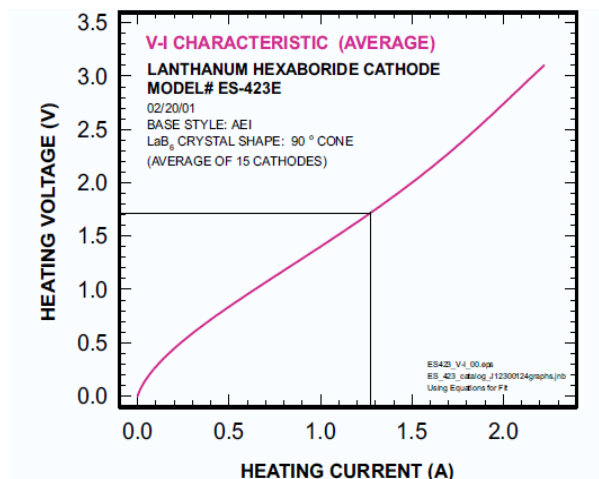


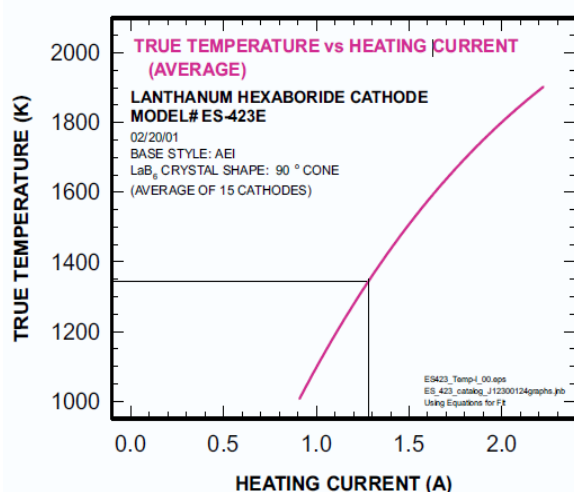
**Figure 5.4:** EGT ion source with filament: (a) Filament position in the source on CF-63 flange, (b) filament holder (c) A lanthanum hexaboride cathode mounted on a ceramic base (white cylinder) from Kimball Physics (Kimball, 2015). (d) The  $\text{LaB}_6$  crystal (lavender) mounted on a graphite base.



ES-423E	
CATHODE MATERIAL	Lanthanum Hexaboride ( $\text{LaB}_6$ ) single crystal
CATHODE SHAPE	Cone with 90° sides and microflat tip
MICROFLAT SIZE	Standard: 0.015 mm dia., larger or smaller available
HEATER	Single piece carbon rod
EMISSION AREA	$1.7 \times 10^{-6} \text{ cm}^2$ standard microflat, excluding sides
HEATING CURRENT	1.7A to 2.1A
CATHODE LOADING	20-30A/cm <sup>2</sup> recommended High loadings result in reduced lifetime
WORK FUNCTION	2.69 eV
OPERATING TEMP	approx. 1700-1900K
ENERGY SPREAD	approx. 0.4 eV
LIFETIME	Thousand plus hours with medium currents, good vacuum
VACUUM LEVEL	$10^{-7}$ torr or better, recommended
POWER SUPPLY CAPABILITY	Voltage regulated power supply recommended, 4 V, 3 A



Standard microscopy styles include: 90-15, 90-20, 60-06



Typical performance;  
data for guidance only.

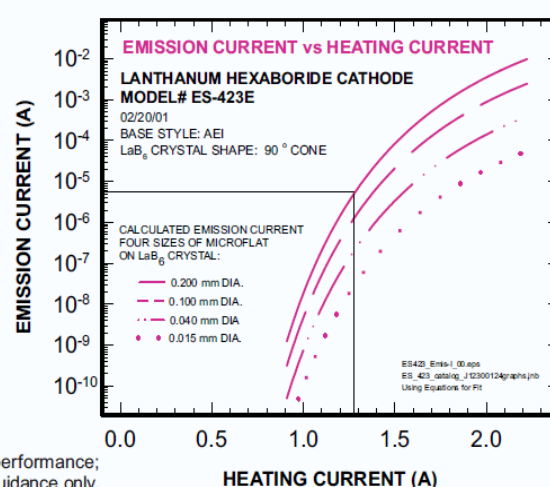


**Figure 5.5:** Typical parameters of a Kimball  $\text{LaB}_6$  cathode (Kimball, 2015). (a)  $\text{LaB}_6$  filament specifications (b) heating voltage vs heating current. (c) Temperature vs heating current (d) emission current vs heating current.

The upper left table of Figure 5.5 shows the technical details of the filament, the upper right figure shows the variation of heating voltage with respect to the heating voltage of the filament, the left lower figure gives the information about filament temperature versus heating current and the right lower plot shows the emission current versus heating current for filament of different diameters. We are using the filament at 1.3 A of heating current for 250  $\mu\text{A}$  of emission current and the heating current below 1400 K.

### b) High frequency pulse generator:

Another important component of an ion storage source is the extraction pulser because the temporal properties (turn-on rise time, turn-off rise time, and pulse width) of the extraction pulser significantly affect the performance of a TOF system (see chapter 2). The extraction pulser is connected to the extraction grid and extracts ions periodically from the storage region (close to the source). Thanks to the high voltage of the pulse relative to any of the source voltages, the ions are accelerated into the drift region. The rectangular pulse generator

used by us is based on an ultrafast solid state switch from Montena<sup>®</sup>. The repetition frequency and the duration of the time base can manually be adjusted.



**Figure 5.6:** Front panel of the pulse generator from Montena<sup>®</sup>. PULSE OUT and SYNC OUT are for pulse and trigger signals. The back panel has three connections, one for ground, one for the bias voltage, and one for the high voltage power supply.

The pulser can be operated continuously, from 0 V to -600 V, and up to 10 kHz frequency with a maximum pulse width of 2.5  $\mu$ s.

The detailed specifications of the pulser are listed in Table 5.2

Specification	Condition
Maximum pulse amplitude	20 V to 600 V (adjustable)
Repetition frequency	~10 kHz (adjustable)
Turn-on-rise time	< 5 ns
Turn-off-rise time	~80 ns
Pulse width time	~2.5 $\mu$ s (adjustable)

**Table 5.2:** The basic characteristics of the used pulser (Montena<sup>®</sup>).

The back panel of pulser has three connections, one for the bias voltage, one for ground, and one for the high voltage supply.

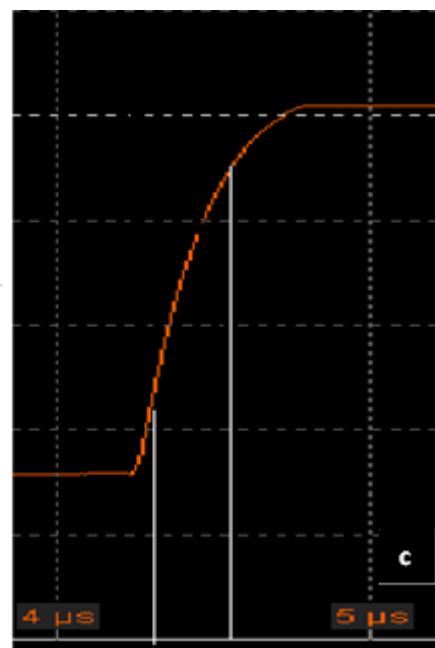
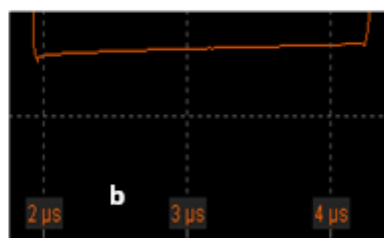
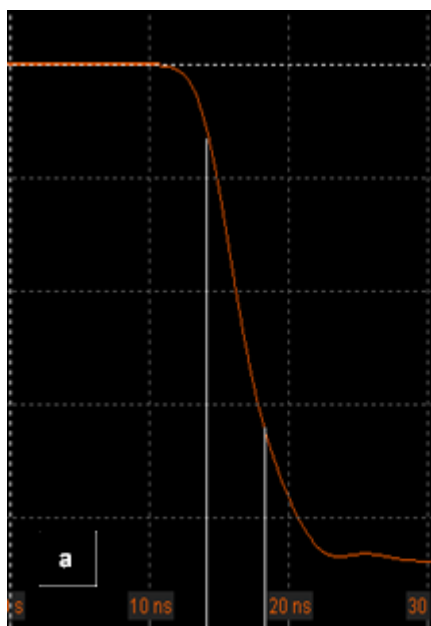
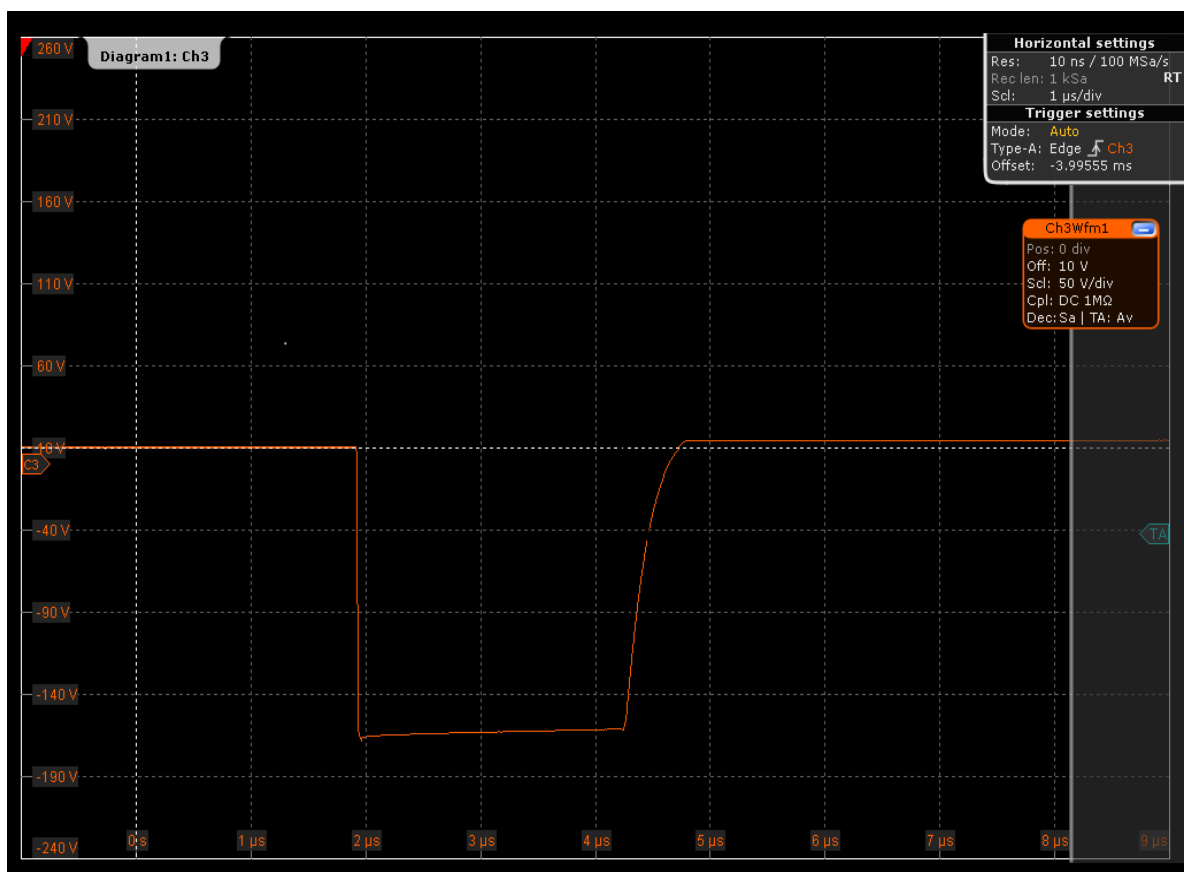


**Figure 5.7:** (upper panel) Rectangular pulse from the pulse generator. (Lower panel) (a) Pulse rise time of  $\sim 5$  ns from 10% to 90 %; (b) Pulse width of  $\sim 2.5$   $\mu$ s; (c) Pulse fall time of  $\sim 80$  ns.



### c) Source Electrodes:

The ion source has a total of 18 feedthroughs; the schematic diagram of the electrodes is shown in Figure 5.2(b). Considering the electrodes, the back plane and the extraction grid are very important to create the potential depression needed to store the ions. Abplanalp (2010) has explained the effect of these voltages on the potential well and also on the ion storage region. The ion source has two ion repellers, which direct the ions into the storage space. The source also has two electron repellers, which guide the electron beam for optimizing the ion efficiency. Filament, ion repeller, electron repeller, back plane, extraction grid, and ground electrodes are all connected low voltage feedthroughs ( $\pm 100$  V). The remaining electrodes are connected high voltage feedthroughs (up to 5000 V). The storage region is connected to the acceleration region; which consists of three electrostatic lenses (lens 1, lens 2, and lens 3). High voltages ( $-1000$  V to  $-5000$  V) are applied in order to accelerate the ions into the drift region. These voltages have to be carefully tuned to achieve good focusing of the ion beam.

### 5.2.2 Drift tube & Reflectron

At the beginning of the drift region all ions in the same charge state acquire the same energy and they start moving into the field-free drift region. However, ions with different masses have different kinetic energies and will therefore have different velocities, which temporarily separates them. At the end of the drift tube the ions enter the reflectron where they are reflected. After this turnaround they travel back towards the detector. The grid-free reflectron consists of 16 stainless steel rings with different shapes and potentials, carefully adjusted to focus the ions spatially and energetically on the detector.

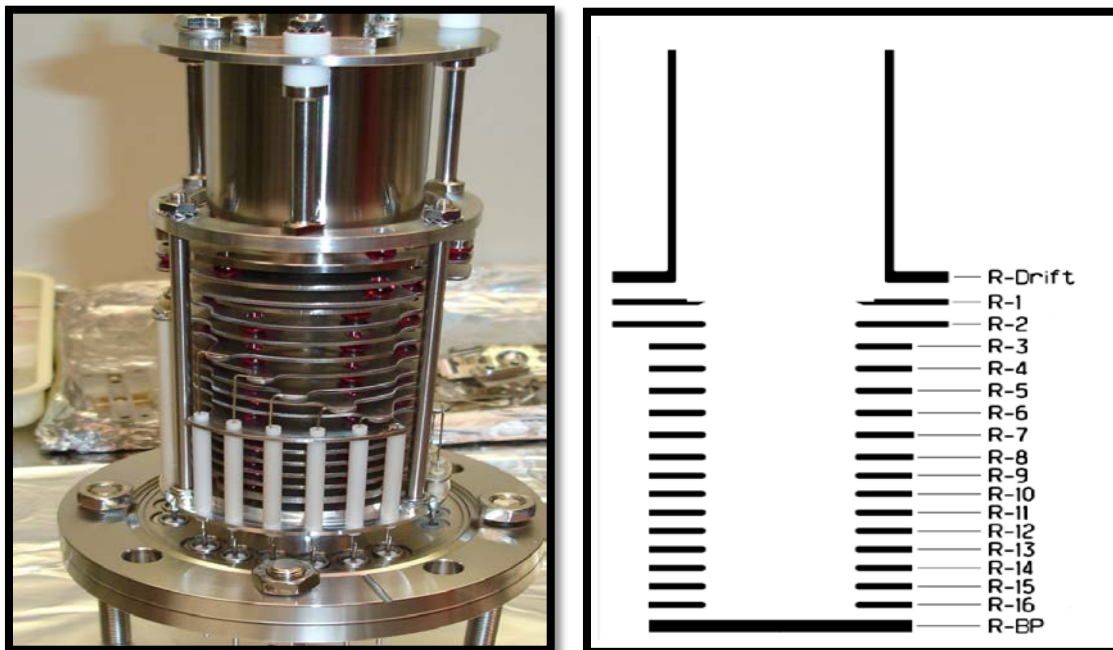


**Figure 5.8:** (a) Reflectron of EGT (b) schematic view of reflectron electrodes.

### 5.2.3 Detector

The detector setup is especially designed and built for this instrument. It is characterized by a very small volume, it is bakeable to 250°C, and connected to a 50  $\Omega$  impedance matched gold plated anode. For detection we use microchannel plates (MCP) from Photonis<sup>®</sup>, which offer longer life time, relatively higher gain, and lower dark currents than other commercially available MCP. They also provide the highest L/d ratio currently available on the market for a high gain in chevron configuration.

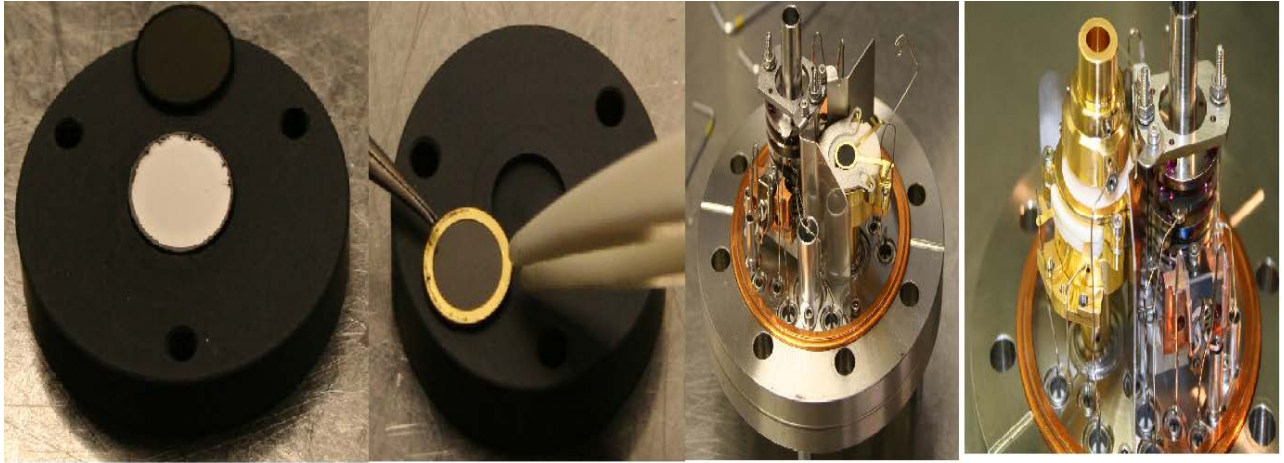


**Figure 5.9:** Microchannel plates and detector setup.

The detector design of the first EGT generation is as shown in Figure 5.10(a). It was set up with electronic components in a RC-circuit and zener diodes to reduce ringing and to control the voltage of the detector back side. The used MCPs had a 40:1 aspect ratio. In contrast, the present design comes without any electronic components and the MCPs have a 60:1 aspect ratio, which produces more gain and also controls ion feedback.

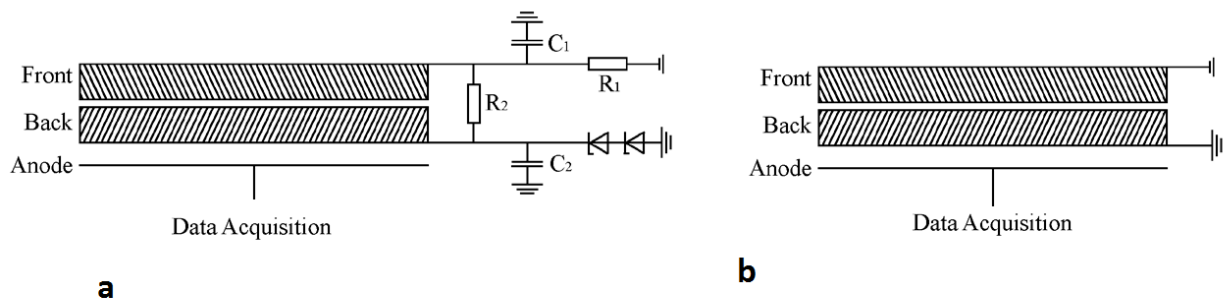


**Figure 5.10:** Schematic view of detector configuration (a) Detector design of the first generation EGT (picture from Huber, 2011) (b) Detector design of the current version without any electronic components.

Another important part of detector set up is the design of the anode and the connection to the standard 50  $\Omega$  transmission line. The anode is a 1 mm thick gold plated stainless steel disk with a diameter of 11 mm. At the center of the anode, a 1 mm thick wire is directly welded

and straight-line connected to a high-frequency sub-miniature-version A (SMA) vacuum feed-through. The signal line is completely shielded to ensure a 50  $\Omega$  impedance matching, which is needed for a clean pulse shape and no ringing (Abplanalp, 2009).

### 5.3 Pre-amplifier (Limiter)

A custom made pre-amplifier is placed in between the anode and the data acquisition system to protect the latter from high voltage signals. The 1 GHz voltage clamp preamplifier with gain of 1 has a very fast recovery time after voltage saturation. Two stages of clamping diodes are used to limit high voltage peaks. Due to this set-up, high voltage peaks are clamped while small voltage peaks are unchanged. It is actually a “limiter”, because it cuts/limits signals larger than 5 V using the clamper circuit. The limiter is needed to protect the ADC and TDC cards from too high voltage signals since their maximum input voltage is  $\sim 5$  V. This circuit also reduces the internal noise generated during the signal transmission by impedance (Pre-amp EGT, 2011)

### 5.4 Data acquisition system

As described above, the EGT has two data acquisition systems: An analog to digital converter (ADC) and a time to digital converter (TDC).

The ADC card used by us is from Agilent® (Figure. 5.4). It is a two channel, 8 bit card with ultra-fast real time sampling and transfer rate (up to 1-2 GS/s) and a full scale from 50 mV to 5 V. Hardware and software installation procedures are described in Agilent Acqiris (2012).. The connection ‘INPUT 1’ is the connection to the spectrometer anode signal and ‘TRIGGER IN’ is connected to the external trigger. The maximum signal amplitude should not exceed 5 V, otherwise the signal will damage the ADC card. To avoid this problem we are using the voltage limiter (see section 5.3). The ADC card can be used in different modes but we are using mostly the averaging mode. More details can be found in Appendix 4.A.



**Figure 5.4:** Front view of the Agilent ADC card-Acqiris AP240.

The used TDC card is an ultra-fast multiple event time digitizer from FastComTec®. It is able to measure multiple events in up to 6 input channels with a time resolution of 100 ps. The sweep count rate is up to 2 GHz. (MCS6, 2012). The spectrometer signal and the external trigger signal are connected to the STOP and START inputs, respectively. The output signals of the TDC are transferred to the computer via high speed USB ports. The TDC card can be used in “Endless mode” without dead time or in “stop after sweep mode” with a fixed dead time of 96 ns.

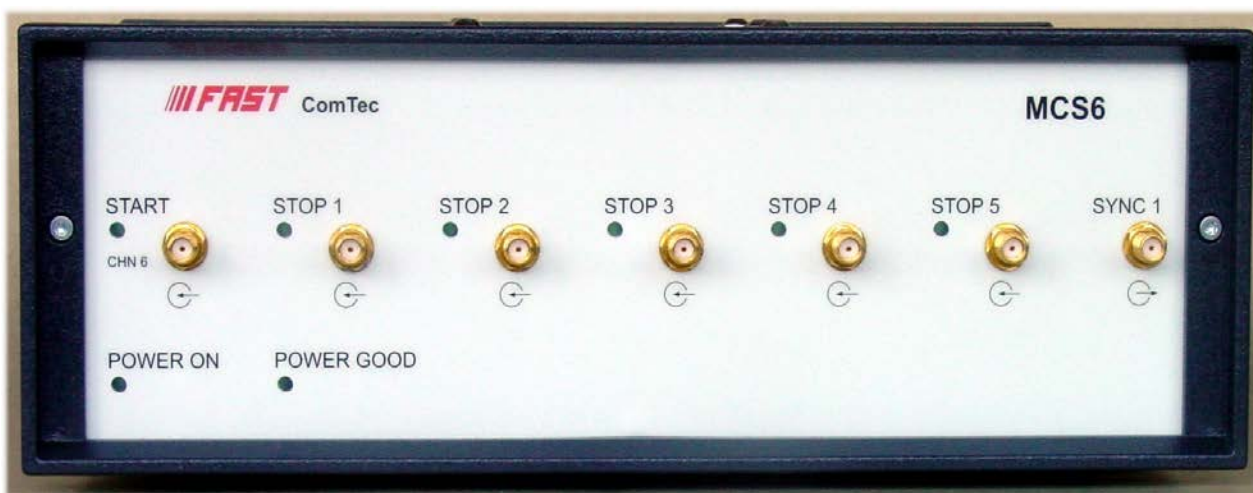


**Figure 5.5:** Front panel view of the FastComTec<sup>®</sup> TDC with multi stop inputs. External trigger signal from pulse generator has to be connected to the START connection and spectrometer signal from the anode has to be connected to one of the STOP inputs.

### 5.5 MoRaMi Voltage control system

All the voltages to the EGT are controlled by custom made voltage control systems called MoRaMi (Modular Rack Measurement Instrument). Two separate MoRaMIs are built, one for low voltages and one for high voltages. The low voltage MoRaMi can supply voltages in the range -100 V to +100 V. In a final version an external -500 V module for a pulser and a filament control unit are also planned. Currently, the control filament for the EGT is via an external supply. The high voltage MoRaMi can deliver voltages up to -5000 V. Both MoRaMIs can either be operated via computer control or manually.

### 5.6 Vacuum and purification system and its control

The EGT has an ultra-high vacuum pumping system with turbo molecular pumps, ion getter pumps, together with charcoal and getter purification systems. The vacuum system of the new EGT has been improved compared to the earlier version by reducing unnecessary volume.. The Turbo pumps, which are from Pfeiffer Vacuum<sup>®</sup> (model High pace 80), are connected to the EGT with a CF-40 flange. The turbo pumps are connected to pre-vacuum tanks. On the opposite side of the EGT an ion getter pump is connected via a CF-40 flange. A charcoal trap and a getter are connected to the EGT via CF-16 flanges.

### 5.7 Calibration gas and its control system

The determination of the mass fractionation factors and the sensitivity of the EGT is done using so-called calibration gases, which are stored in 2 liter bottles. By using a well calibrated pipette, a small fraction of the gas is taken out of the bottle (usually in the range of permil or less of the total amount in the bottle, see Figure 5.7), which is then measured using exactly the same procedure as for the samples. The calibration bottles were filled and cross-calibrated at ETH in Zurich. For the EGT there are three calibration bottles, of for He-Ne, one for Ar, and



one for Kr-Xe. The valves of the calibration bottles are automatic and can be operated using the (self-made) Ionic<sup>2</sup> software.

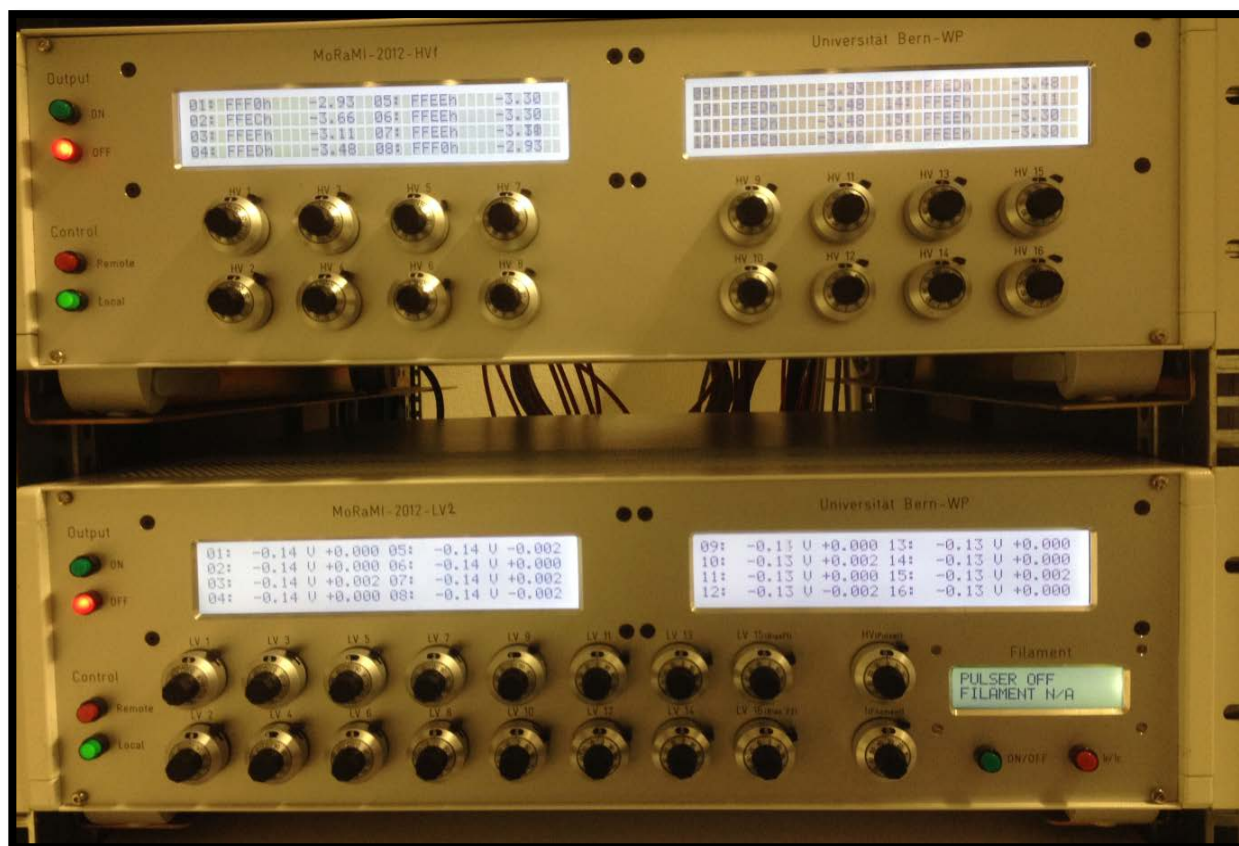


**Figure 5.6:** Used MoRaMis systems for high and low voltage supply of the EGT.

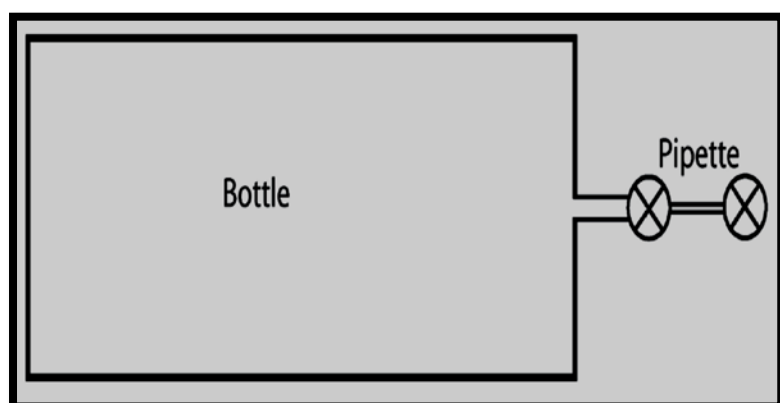


**Figure 5.7:** (a) Schematic viewing of the combination calibration gas bottle and pipette combination. (b) Picture of a calibration bottles in the lab.



## Chapter 6 : EGT Operational Manual & Troubleshooting Guide

A simple overview of the laboratory set-up of the EGT is shown in Figure 6.1. The EGT is connected to a sophisticated vacuum system, an extraction system either for melting of samples in vacuum or combusting samples under oxygen partial pressure, calibration bottles, and the electronic supply and control system (MoRaMi).

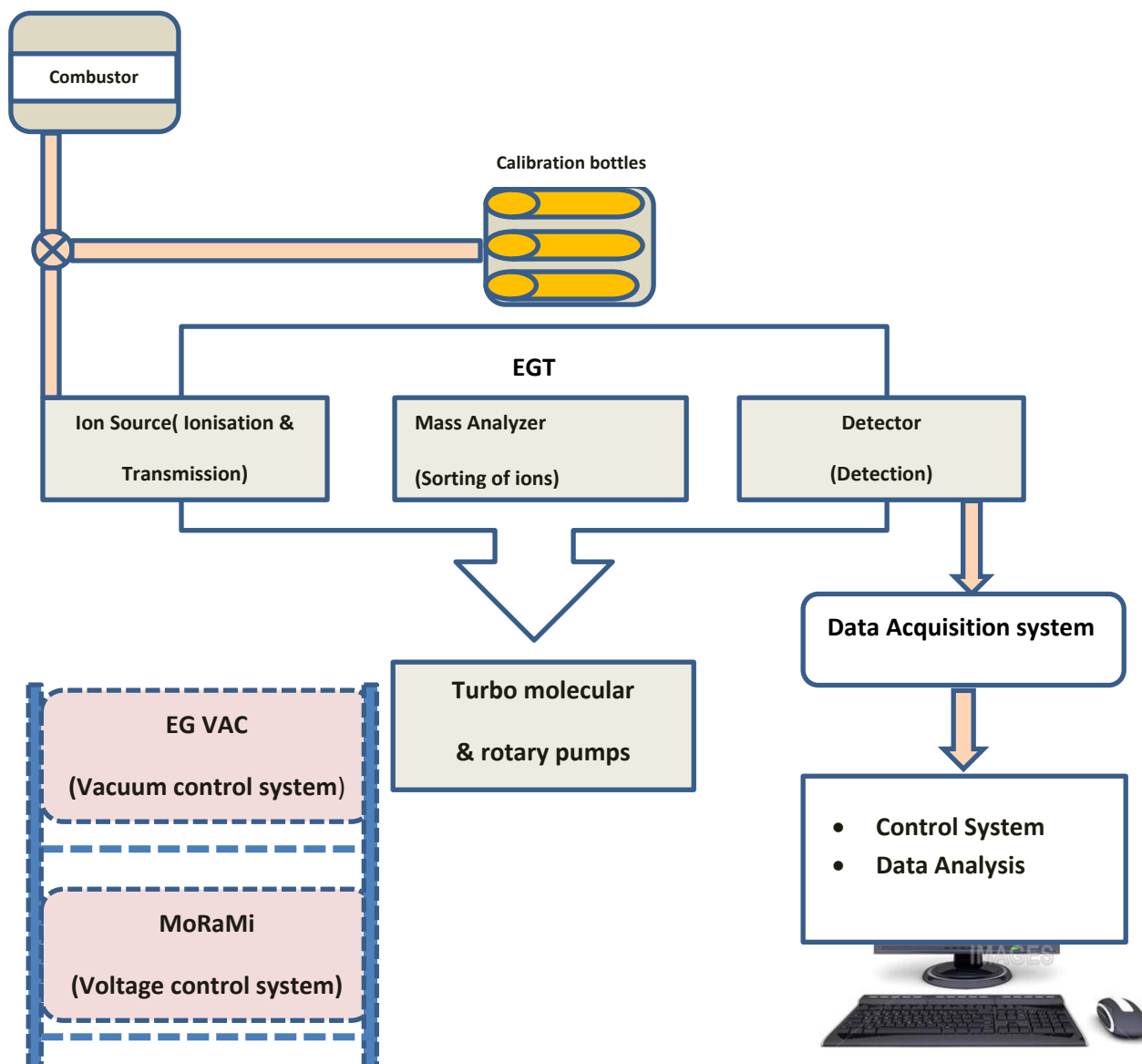


**Figure 6.1:** The key components of the EGT-MS detection system.

## 6.1 Pre-operational conditions

The pre-operational conditions for the EGT in terms of vacuum, electronic connections, and control system are very similar to other noble gas mass spectrometers. The EGT has a very efficient and safe vacuum system and is equipped with turbo molecular pumps from Pfeiffer Vacuum® and ion getter pump from Varian®. The extraction system and the mass spectrometer have separated pump systems and can both be pumped separately with either the turbo molecular pump and/or the ion getter pump. A schematic drawing of the vacuum system is shown in Figure 6.2.

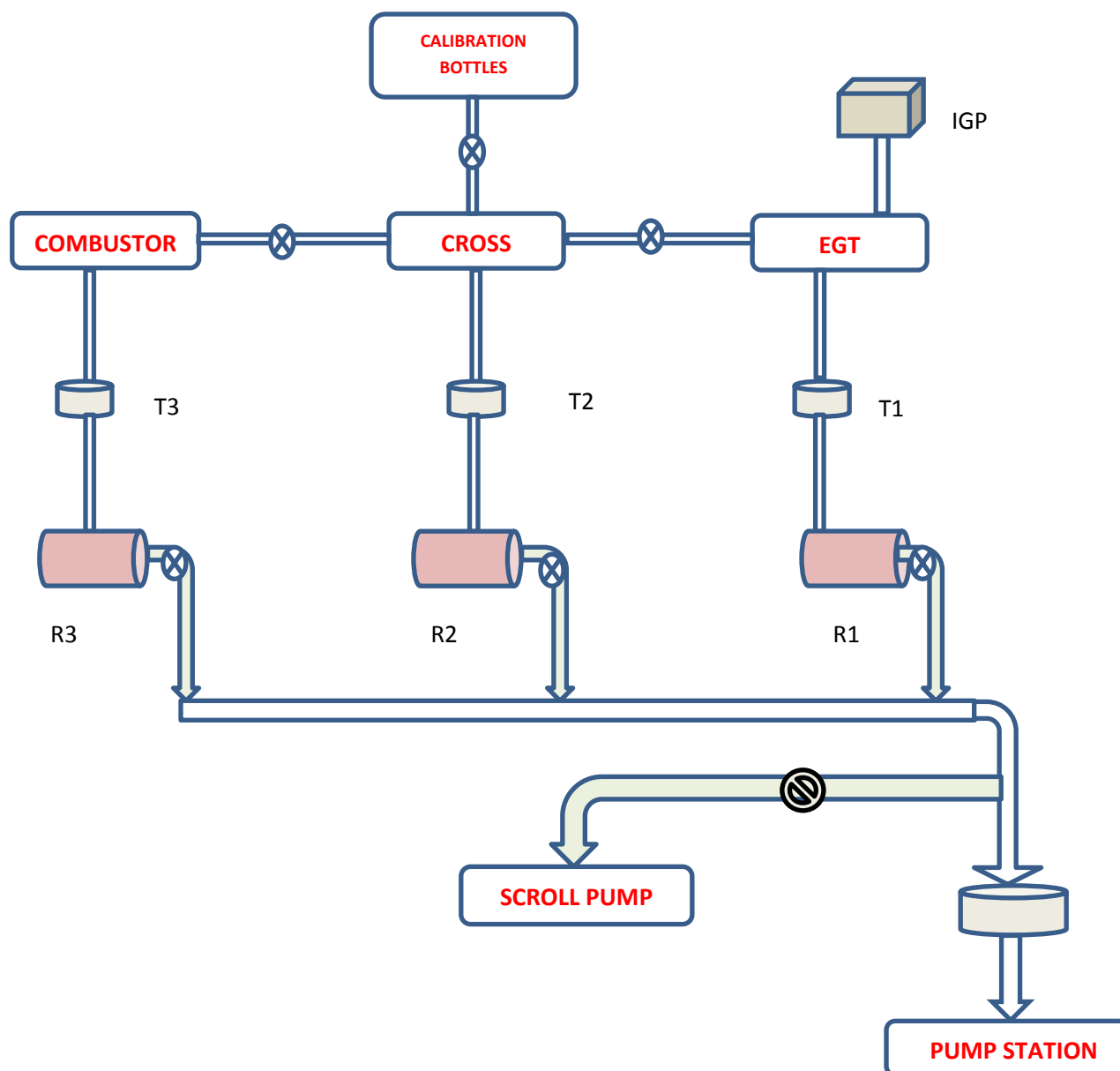


**Figure 6.2:** Vacuum systems of the EGT and the extraction line. T1, T2, and T3 are turbo molecular pumps, R1, R2, and R3 are recipient tanks, and IGP is the ion getter pump.



### **6.1.1 EGT Feedthrough connections**

The EGT has 36 electronic connections, all connected to the inside of the spectrometer via feedthroughs. Proper grounding of the entire system is crucial because otherwise the high noise level makes proper measurements impossible.

### **6.1.2 MoRaMi voltage connections**

The EGT is equipped with a voltage supply and control device called MoRaMi (Modular Rack Measurement Instrument). The MoRaMi currently used is able to control and handle unwanted charging effects at electrodes and therefore supplies very stable voltages. For the EGT two MoRaMi systems are used, one for high voltages and another one for low voltages. In addition, an old MoRaMi instrument is used for filament control. After proper connections of all cables, first, the low voltages are set (use low increments of about 5 V per step only). After having set the low voltages one has to slowly and carefully ramp up the high voltages. The best procedure is to ramp up all voltages simultaneously to avoid discharging effects. After the lowest (high) voltage is reached, stop with this voltage but increase all the other voltages until the final value of the second lowest is reached, fix the second lowest (high) voltage and continue like this. Next, set up the pulser and the filament control. The user can also set the voltages using the EGT computer.

### **6.1.3 Pulser, Limiter, and filament connections**

In the next step the pulser is connected to the power supply and as an external trigger to the data acquisition system (ADC, TDC). The pulser also delivers the grid voltage to the ion source. The typical voltage is in the range  $\sim -485$  V. The pulse frequency can be chosen to be in between 1 kHz and 10 kHz. The pulse width for the used pulser is 2.2  $\mu$ s. More information on the Pulser is given in section 5.3.

Since the ADC and TDC detection systems used by us both have upper limits of maximum input voltages of 5 V, we use a so-called voltage limiter between the exit of the detection system and the ADC or TDC card, which cuts all voltages larger than 5 V and therefore saves the ADC and/or TDC card from overcharging. The limiter is matched to the 50  $\Omega$  of the rest of the detection system (series connection) and therefore reduces the signal by a factor of 2. Finally, the user can start heating the filament by opening the MInOS Client software and entering the IP address for Host name, the system name (egt), and the password (moon). The set-up of the EGT allows for two filaments, usually we work with filament 1 and regulate the heating current to obtain a stable emission current. The emission current is slowly increased to 250  $\mu$ A (in steps of about 10  $\mu$ A) to avoid heating currents of more than 2 A, which would significantly shorten the lifetime of the filament.

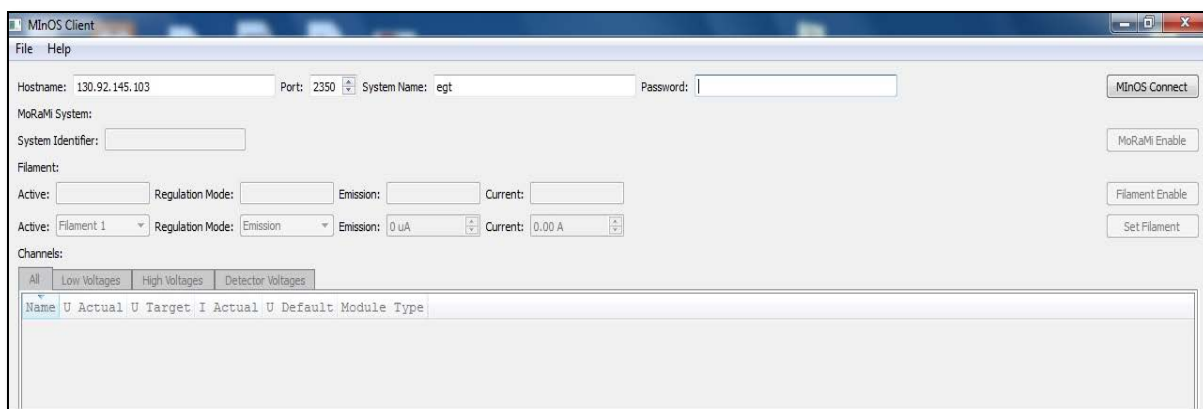


**Figure 6.3:** MInOS client window for the MoRaMi filament control.

## 6.2. EGT Start-Up procedure

- Switch the MoRaMi low voltages on
- Set all low voltages (in small steps)
- Switch the MoRaMi for high voltages on
- Set all high voltages, starting from the lowest value to the highest value (100 V steps), except the detector.
- Switch the pulser on, set the pulser voltage
- Set the pulse frequency and the pulse width
- Switch on the old MoRaMi instrument for filament control
- Open the MInOS client software on the EGT-Windows desktop computer
- Enter Hostname: 130.92.145.103 (IP of MoRaMi)
- Enter Port: 2350
- Enter System Name: egt
- Enter Password: moon
- Click on “MInOS Connect”
- “System Identifier “ shows the name of the MoRaMi
- Click on “MoRaMi Enable”
- Enable “Filament”
- Select “Filament 1” to Active and set “Emission“ to “Regulation Mode”
- Set the emission current (if new ramp up slowly)
- If the pressure is good and all the voltages are set, ramp the detector voltages on the high voltage MoRaMi slowly up
- Set detector back to 600 V and detector front to 2700V (difference between front and back should not exceeds 2400 V).
- If the anode is connected to an oscilloscope, the user can see the mass spectrum. If there is no oscilloscope, use the ADC or TDC card.

The next requirements for proper measurements are proper ADC or TDC settings. The settings for the ADC card should be as shown in Figure 6.4. Details are given in Appendix B.1 and B.2 and more information can be found in (Agilent Acqiris, 2010). With the settings

as discussed an individual spectra (called waveform) should be seen (Figure. 6.5). Check section 6.2 for “Troubleshooting” if no spectra can be seen

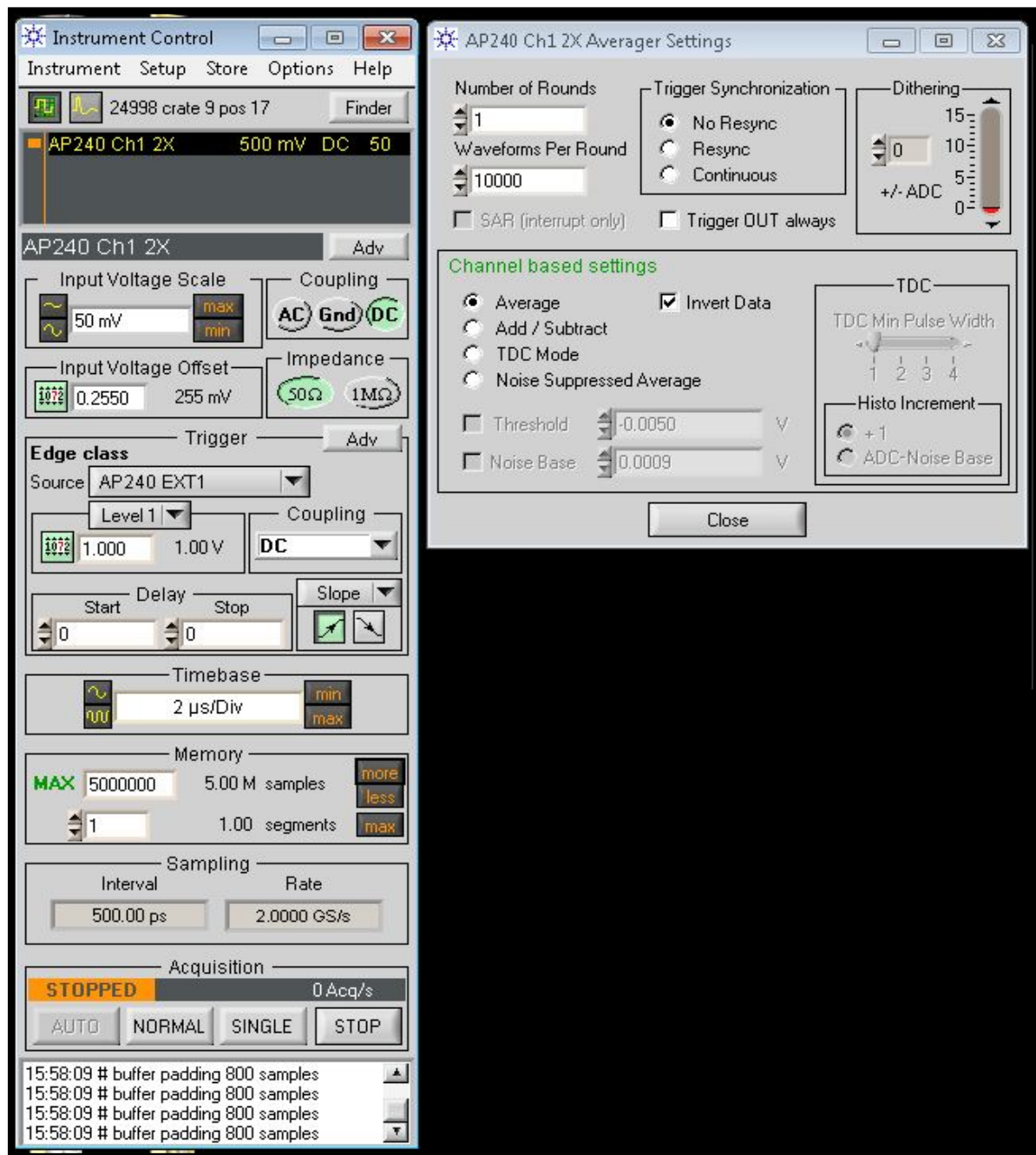


**Figure 6.4:** Typical settings of the Acqiris-card (Instrument Control and Averager Settings)

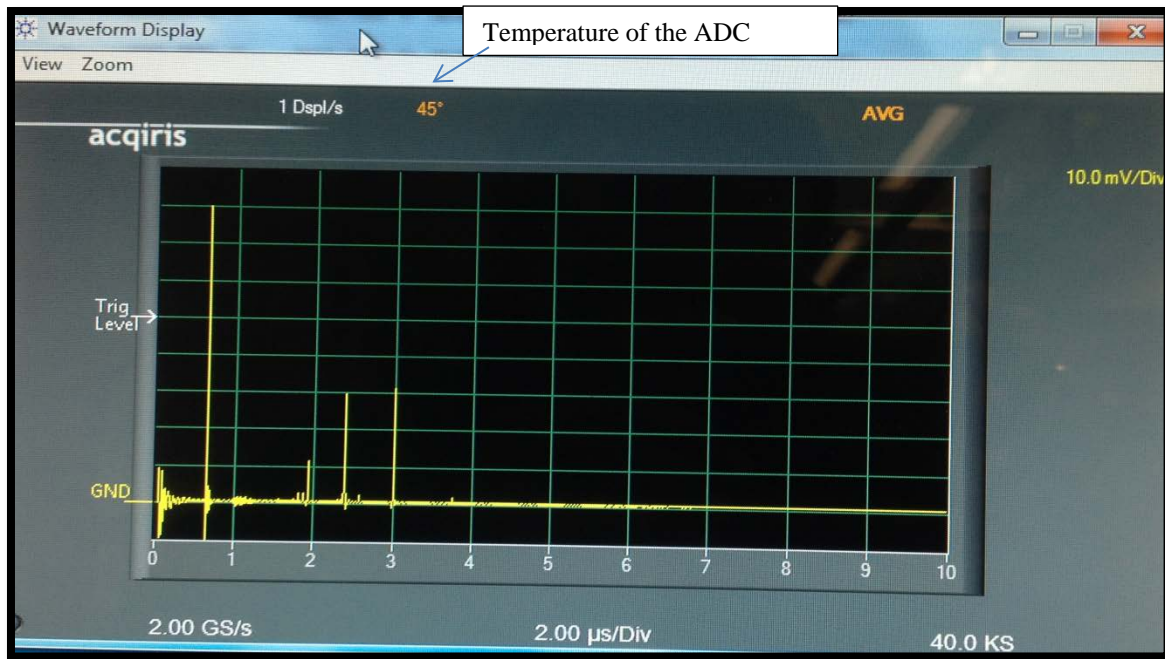


**Figure 6.5:** ADC Live Waveform display. The user can also select the peak/portion by using the zoom option.

### 6.3. EGT Tuning

After observing peaks on the oscilloscope or the ADC/TDC card the spectrometer can be tuned for optimal performance, i.e., maximum sensitivity, symmetric peaks, and high mass resolution. Tuning can be done either manually or via computer control, the latter is based on a particle swarm algorithm (Bieler, 2012). In brief, the optimizer runs with data acquired from the Agilent Acqiris ADC card. The program uses different combination of voltages – within a pre-selected range – and determines peak parameters for all of the different settings. After the optimization the user can choose the best voltage settings, i.e., the setting that gives the best peak parameters. Some details of the optimization program are given below.

#### 6.3.1 EGT Optimizer Manual

##### Introduction

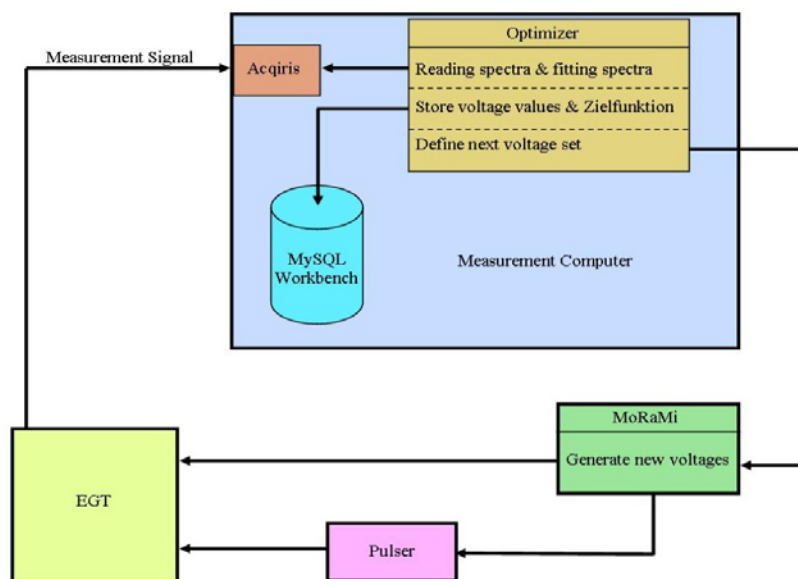
This section only guides through the optimizer operation; the details of the algorithm are described in Bieler (2012).

Figure 6.6 gives an overview of the most important (electronic) parts of the EGT lab configuration with special emphasis on the optimizer. The signal is acquired by the ADC Acqiris-card (Agilent AP240). The optimizer reads out the signal, creates a Gaussian fit of the biggest peak in the defined area, determines the corresponding “Zielfunktion”, and stores the voltage settings as well as other information on a MySQL workbench. Finally, a new voltage set is defined for the next iteration. The MoRaMi sets the new voltages and the EGT is ready for the next iteration step.

## Sequence of Operations

The password of the measurement computer is: “*quieta3*”.

- 1) Check the pressure in the analyzer part: In order to avoid damages of the MCP’s and cathodes, the pressure must be **lower than  $10^{-7}$  mbar**.
- 2) The Anode cable (SMA) must be connected to the Acqiris-card.
- 3) Open the “*Agilent AcqirisLive*” program.
  - a) Choose the settings (Digitizer/Averager, channels, acquisition times, offset, ...)  
The settings of the Acqiris-card can also be changed later
- 4) Open the “*MInOS Client*” (Fig. 6.7), which enables the communication between the Computer and the MoRaMi.
  - a) Hostname: xanthus.unibe.ch  
Port: 2350  
System Name: egt  
Password: moon  
System Identifier: MoRaMi M46-1003
  - b) Activate “MInOS Connect”, activate “MoRaMi Enable”. Wait until all voltages are set  
Check the detector voltages; the difference between “MCP-front” and “MCP-back” should not exceed 2400 Volts.
  - c) At the menu bar of the MInOS Client > File open > load target values: choose the selected start set of voltages (e.g., “250muA\_1000Hz”.txt).
  - d) Activate “Filament Enable”, choose the active Filament (1 or 2), choose the regulation mode (Emission or Current), and the emission (or current) value. Activate “Set Filament”. The pressure in the spectrometer increases.



**Figure 6.6:** Schematic overview of the EGT lab configuration with the optimizer section.

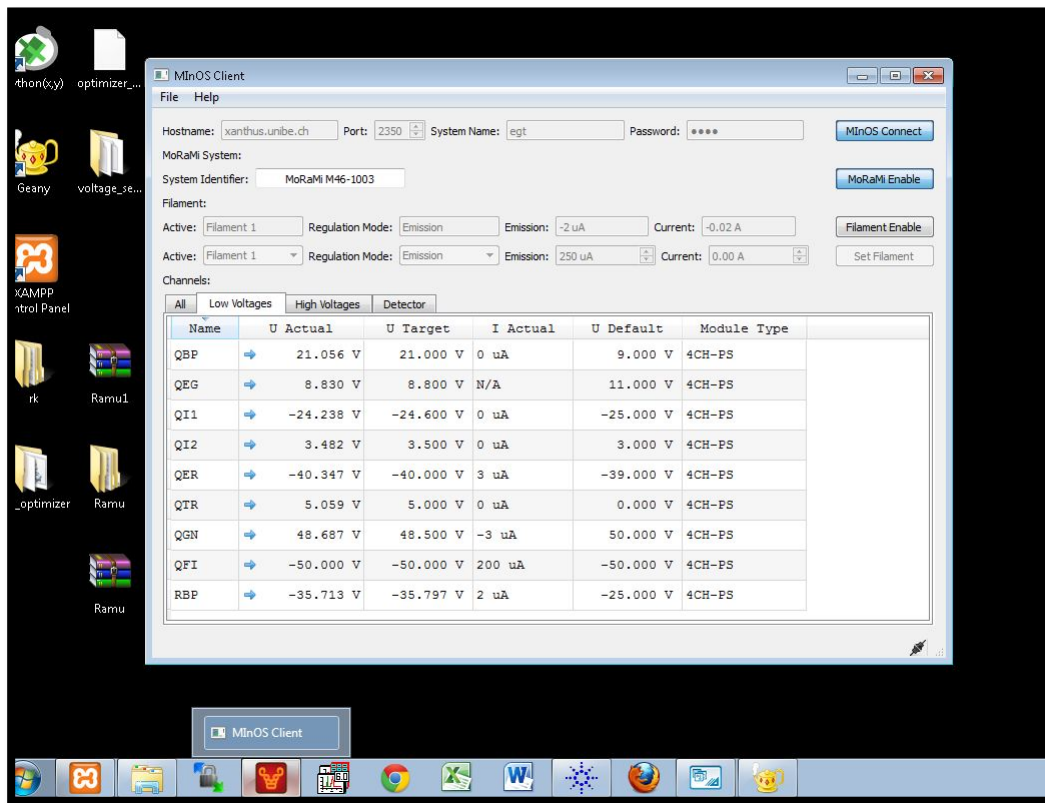


**Figure 6.7:** The open “*MinOS Client*”.

5) Montena Pulser: Switch “POWER ON” and press the blue “PULSE ON” button.

a) Choose the repetition frequency of the pulser and the pulse length (with an oscilloscope or – more challenging – with the Acqiris-card). Note that every change of the repetition frequency also requires an adjustment of the voltages, especially of the QEG and QBP voltages!

6) Switch on the power supply of the preamplifier (if used). **Attention: The preamplifier limits the peak height and might therefore affect the optimization procedure for large signals!**

\*\*\*\*\*

**At this point, the EGT is principally ready to use for measurements.**

\*\*\*\*\*

7) Open the “*XAMPP Control Panel*” (on the Desktop).

a) Start “*Apache*” and “*MySQL*” (if necessary).

8) Open the “*Geany*” compiler (on the Desktop).

a) Open “*egt\_optimizer\_functions.py*” (Folder: “*egt\_optimizer*” on the desktop) and click on “Ausführen”.



- b) Open “egt\_optimizer\_a.py” (Folder: “egt\_optimizer” on the desktop) and click on “Ausführen”. The GUI “EGT Optimizer” and the command shell are now running (Fig. 6.8).

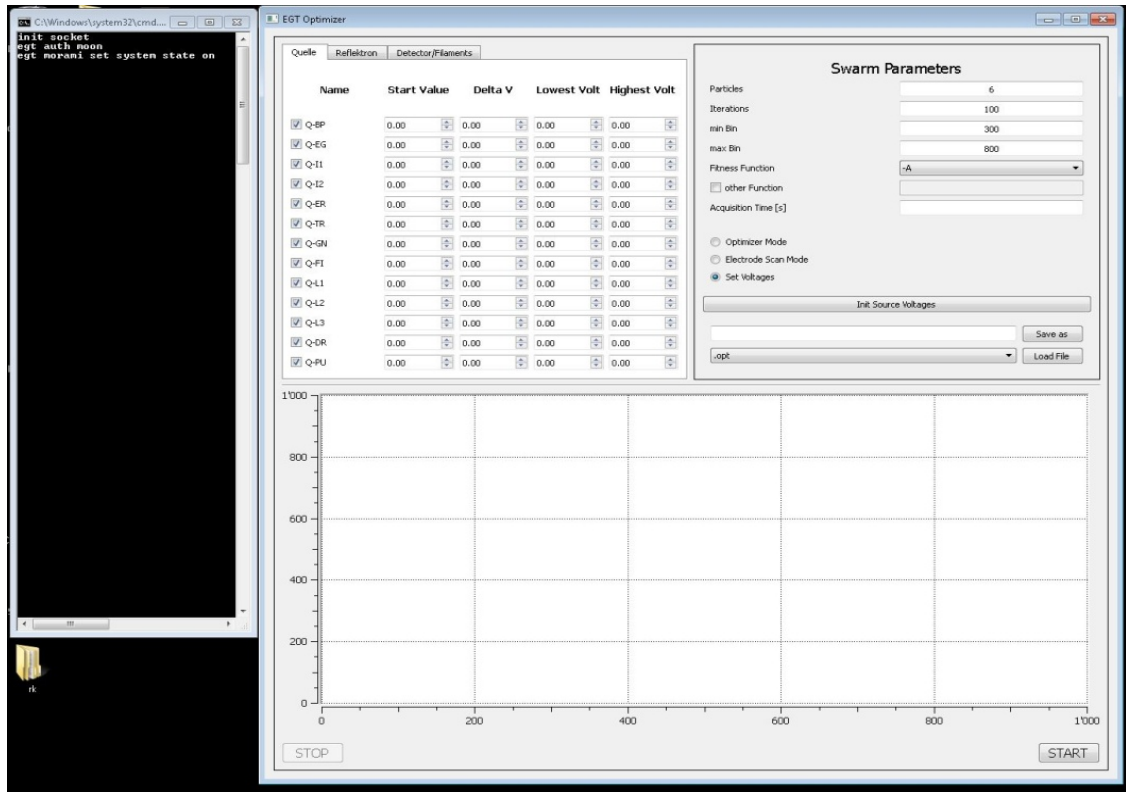


**Figure 6.8:** The “EGT Optimizer” GUI and the command shell.

- 9) For some optimizations it might be useful to choose the initial voltage settings (e.g., “250microA\_1kHz\_Montena\_PreAmp.opt”, see Fig. 6.9). Otherwise the user can also define all voltages and their ranges manually (in “Quelle” and “Reflekttron”).
- a) **Disable in every case “Q-ER” and “Q-FI”** (see Fig. 6.9, red circles). Otherwise, these two voltages will also be varied, which can result in an uncontrolled pressure increase and/or a complete suppression of the electron emission. By clicking “START” the voltages are set by the MoRaMi.
- b) Note that neither the filament settings nor the detector settings are part of the optimization procedure. These values therefore have to be set manually in the “MInOS Client”.
- c) Define the Swarm Parameters (see Fig. 6.10):
- Particles:** Should be set to about half the value of the electrodes to be optimized. For example, the user should choose 10 particles if 20 voltages are to be optimized.
- Iterations:** 100 or more, depending on the settings and the number of voltages to be optimized.
- min Bin and max Bin:** Defines the (time) area in which the biggest peak will be fitted and optimized. One *Bin* is equivalent to the sampling interval of the Acqiris-card. For example, for a sampling rate of 2 GS/s one *Bin* corresponds to 500 ps.

**Fitness Function:** Defines to function that is optimized, e.g., “ $-A/\sigma$ ”. It is useful to try different “fitness functions” to obtain the best results. (Here  $A$  is amplitude and  $\sigma$  is full width half maxima)

**Acquisition Time [s]:** Defines the waiting time (in seconds) of the optimizer between two loops. As a result of the relatively slow voltage ramping of the MoRaMi an “Acquisition Time” of 30 s works well if a real acquisition takes 10 seconds (e.g., 10000 waveforms with a 1 kHz pulse repetition frequency).

d) Choose the “Optimizer Mode”.

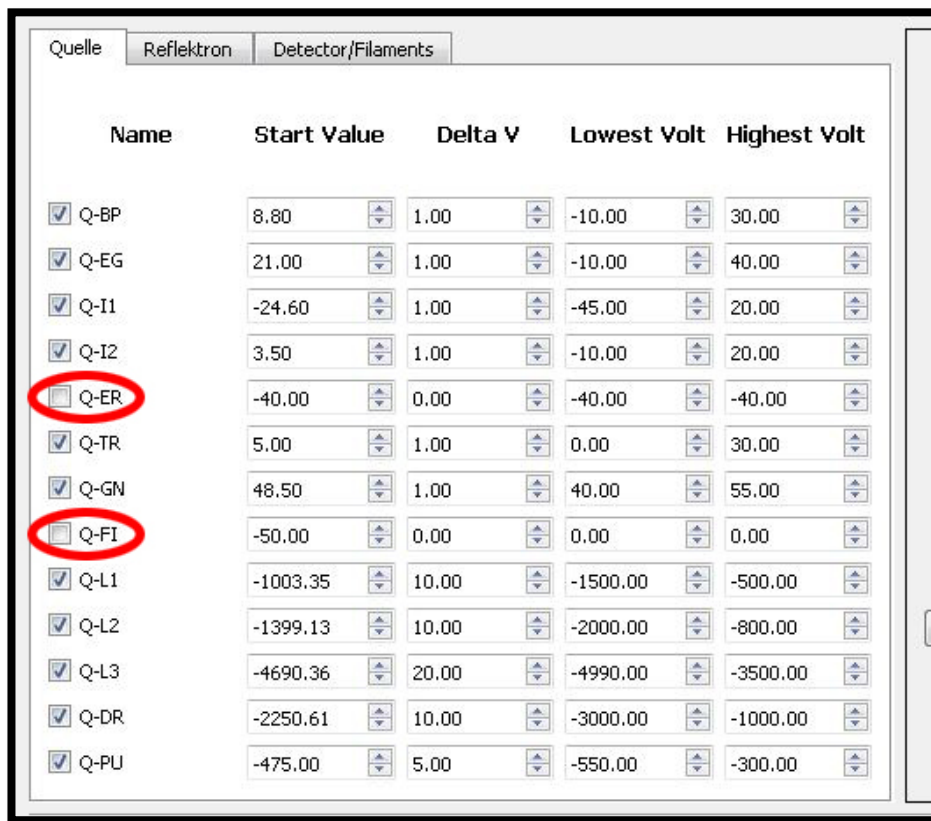


**Figure: 6.9:** The “EGT Optimizer” GUI (Quelle voltages) after loading the settings of “250microA\_1kHz\_Montena\_PreAmp.opt”.

10) In the desktop folder “egt\_optimizer” there are two subfolders called “log” and “spectra”; both must be empty before a new optimization is started.

11) Depending on the settings of the optimizer and the pulse repetition rate, the user has to adjust the Acqiris-card settings. In general:

(a) Averagers

-Two converters per channel (2 GS/s)

-Averager settings: see Fig. 6.11.

The number of waveforms per round is depending on the pulse frequency.

Invert Data has to be enabled!

-Instrument control settings: see Fig. 6.11.



The Input Voltage Scale must be adapted to the measurement conditions. Attention: the peaks may increase during the optimization process, therefore don't choose the scale too small!

The offset has to be adjusted to Input Voltage Scale (typical: 5 mV – 15 mV cut off)

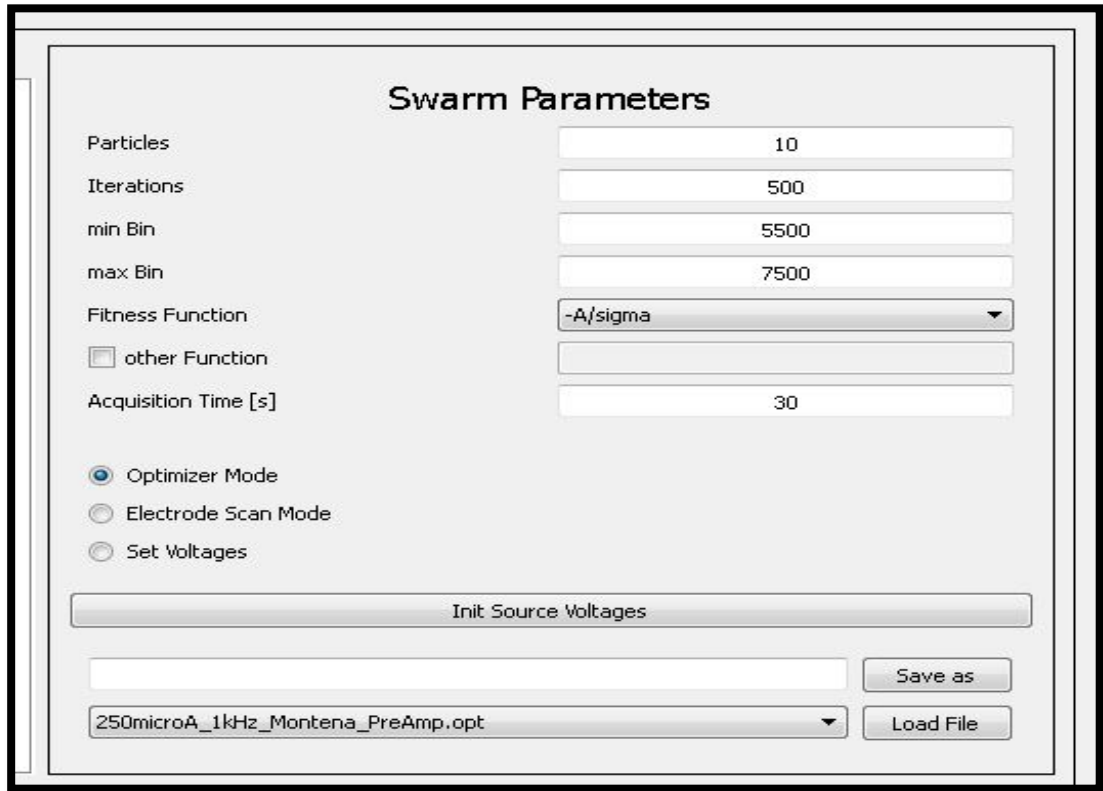


**Figure 6.10:** The “EGT Optimizer” GUI (Swarm Parameters).

(b) Choose “Store” > “AutoStore”:

*Destination folder:* For example

“c:\Users\abplan\Desktop\egt\_optimizer\spectra”

*Number of waveforms to be stored*

-Max total samples memory [MB]

-Select “Raw ADC values”

- push “ok” [ Appendix B.2 explains more details about the settings]

12) Start the data acquisition of the Acqiris-card and wait at least one full acquisition time. Then push “START” on the “EGT Optimizer” GUI.

**The optimizing process is now running!**

The progress of the optimizer is visible in real time on the command shell as well as on the “EGT Optimizer” GUI. If any problems occur, information can be found on the command shell.

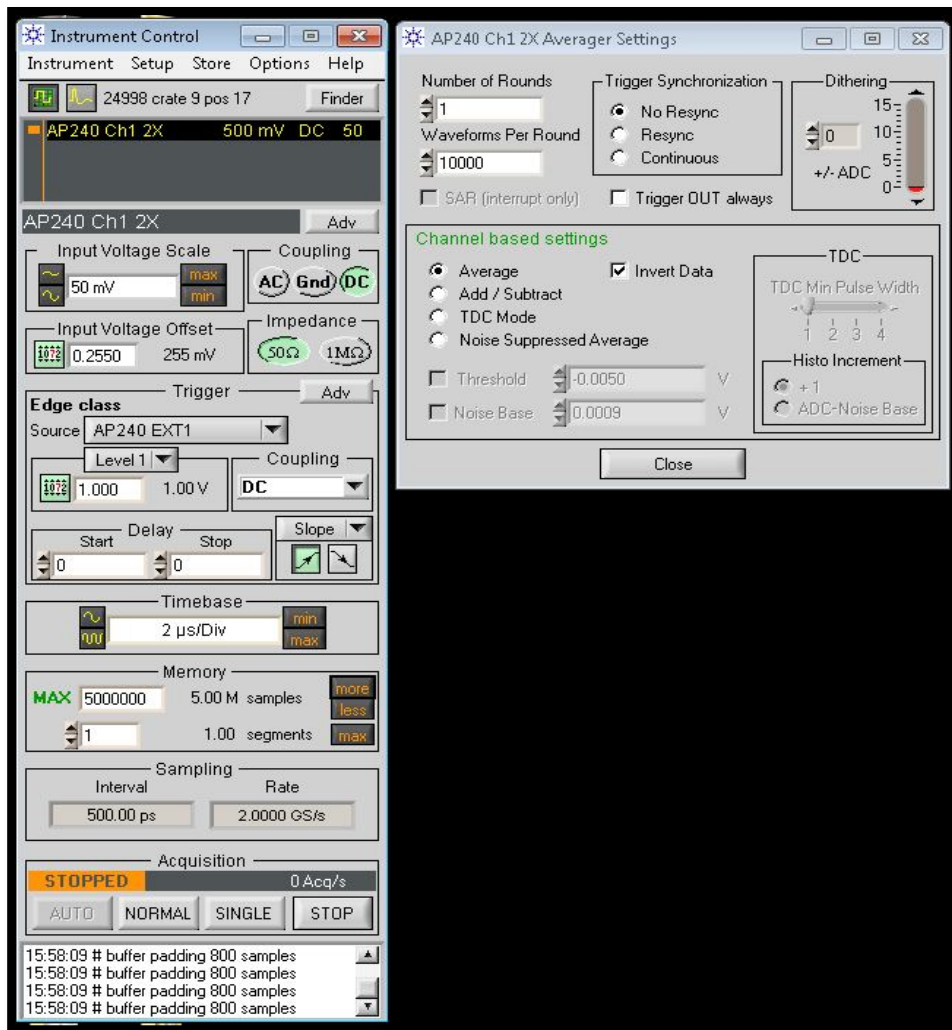


**Figure 6.11:** Typical settings of the Acqiris-card (Instrument Control and Averager Settings).

\*\*\*\*\*

**You can abort the optimizing process at any time by closing the command shell and stop the data acquisition (Acqiris-card)!**

\*\*\*\*\*

13) The plots for peak fitting of each optimization cycle are visible in real time in the folder “log” (in the “egt\_optimizer” folder).

14) Open the “MySQL” workbench:

In general, the user can select “egt-optimizer”, otherwise:

```
-host_var = 'localhost'          (port: 3306)
-user_var = 'root'               (name: egt-optimizer)
-pw_var = 'optimizer'
-db_var = 'optimizer_db'
```

a) Select “optimizer\_db”.

Choose “edit” > “preferences” > “sql editor” > set “Limit Rows Count” to the max. Value (99999).

- b) Select the “*overview*” menu: By double clicking on “*jobs*”, all iterations are listed (with target functions and amplitudes, etc.). You can sort them and identify the best solution (job\_id).

Select again the “*overview*” menu, and by a right mouse click on the “*voltages*” you can select “*Select Rows – Limit 99999*”. Therefore you are able to get the voltages of the best solution. The numbering of the electrodes is given by the electrode order in the “*EGT Optimizer*” GUI!

\*\*\*\*\*

- **The cathode should be active for at least 60 minutes before an optimization is started.**
- **In case of an Ethernet connection failure, restart the measurement computer.**

### 6.3.2 Manual Tuning

Manual tuning is an easy but time consuming process. The first step of the tuning is the optimization of the ion source for high intensities. In the second step the reflectron is tuned for good peak shapes. A rough guide through the procedure is given below:

- First, set all voltages to the SIMION voltages
- Start the tuning procedure with the backplane and the extraction grid voltages, which both significantly influence the peak intensities. A good tuning for these two voltages will affect the position of the electron beam and therefore will affect the potential well for trapping the ions
- Do not change much or only change little (and very carefully) the voltages of the electron repeller and the filament. Always control the heating current and the pressure in the spectrometer while changing these two voltages.
- The tuning parameters depend on the pulse frequencies, especially for the backplane voltage.
- Ion repeller voltages are very important for trapping the ions and therefore for the sensitivity.
- Reflectron voltages affect the peak shape. Proper voltages of these electrodes will give very good peak shapes, i.e., symmetric peaks; especially RBP, R15, and R16 are showing a large influence on the tuning.
- Drift voltage affects the mass resolution

More details about tuning the voltages will be given in chapter 7.

### 6.4. Measurement procedure for Calibration gas

EGT has three calibration bottles; one for lighter noble gases He-Ne, one for Ar, and one for Kr-Xe. All bottles can be operated electronically. A schematic drawing is given in Figure 6.13. The operational procedure for a calibration is:

- Close valve 13, 14, and the EGT inlet (13 goes to pump, 14 is connected to the combustor line, and for safety close the EGT inlet)

- Close 16 also while Ar calibration ( for multiple dilutions)
- Click on the “valve control” in the old MoRaMi instrument (it enables automatic valve control via the computer)
- Open the **Ionic<sup>2</sup>** software window (see Figure 6.12)
- Click on run line 1, it will show a small pop up window with numbers from 0 to 15 (be careful with gas bottle valve numbers, Kr-Xe are connected to valves 2 and 3; Ar is connected to valves 4 and 5)
- For Kr-Xe, first click on 2, which open the backside valve of the pipette. Wait for 20 s and click again on 2. Carefully check if valve 2 is closing. Now there is some calibration gas in the pipette.
- Wait for 20 s, click on 3, which will open the front side valve of the pipette. Wait for 20 sec and click again on 3. Again, carefully check is valve 3 is closing. Now the gas expands into the selected volume.
- Now, close the EGT pump valve and slowly open the EGT inlet valve. The gas will expand into EGT. Close the gas inlet valve after 2 or 3 minutes. Start the measurements.

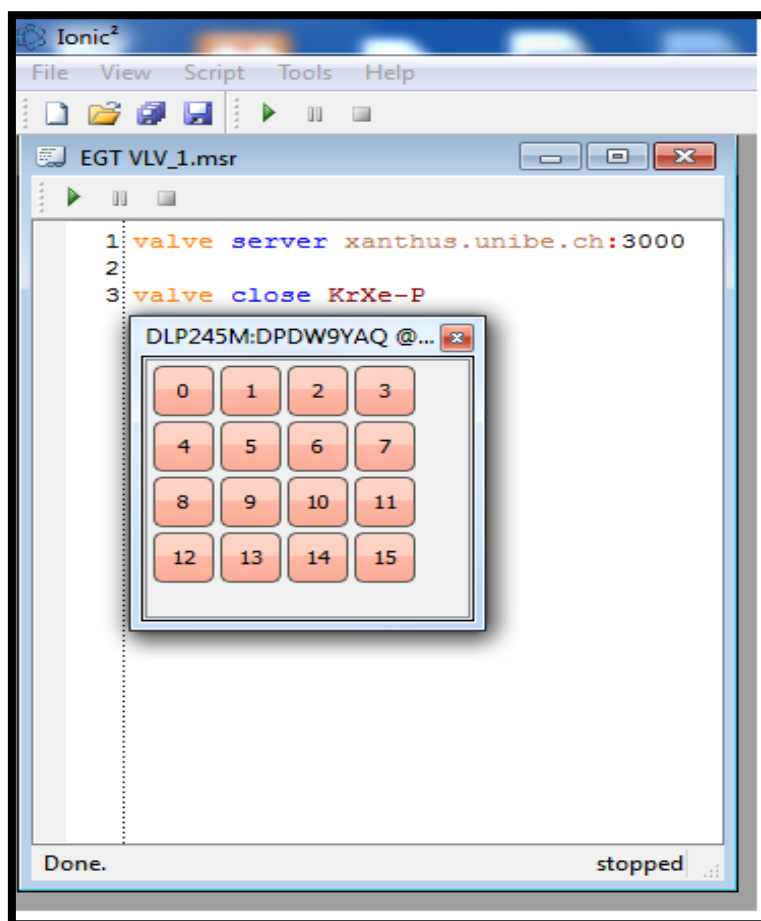


**Figure 6.12:** The user interface of the **Ionic<sup>2</sup>** valve control software. A pop-up window will open after clicking on line 1. Each number (from 0 to 15) corresponds to an electro pneumatic valve.

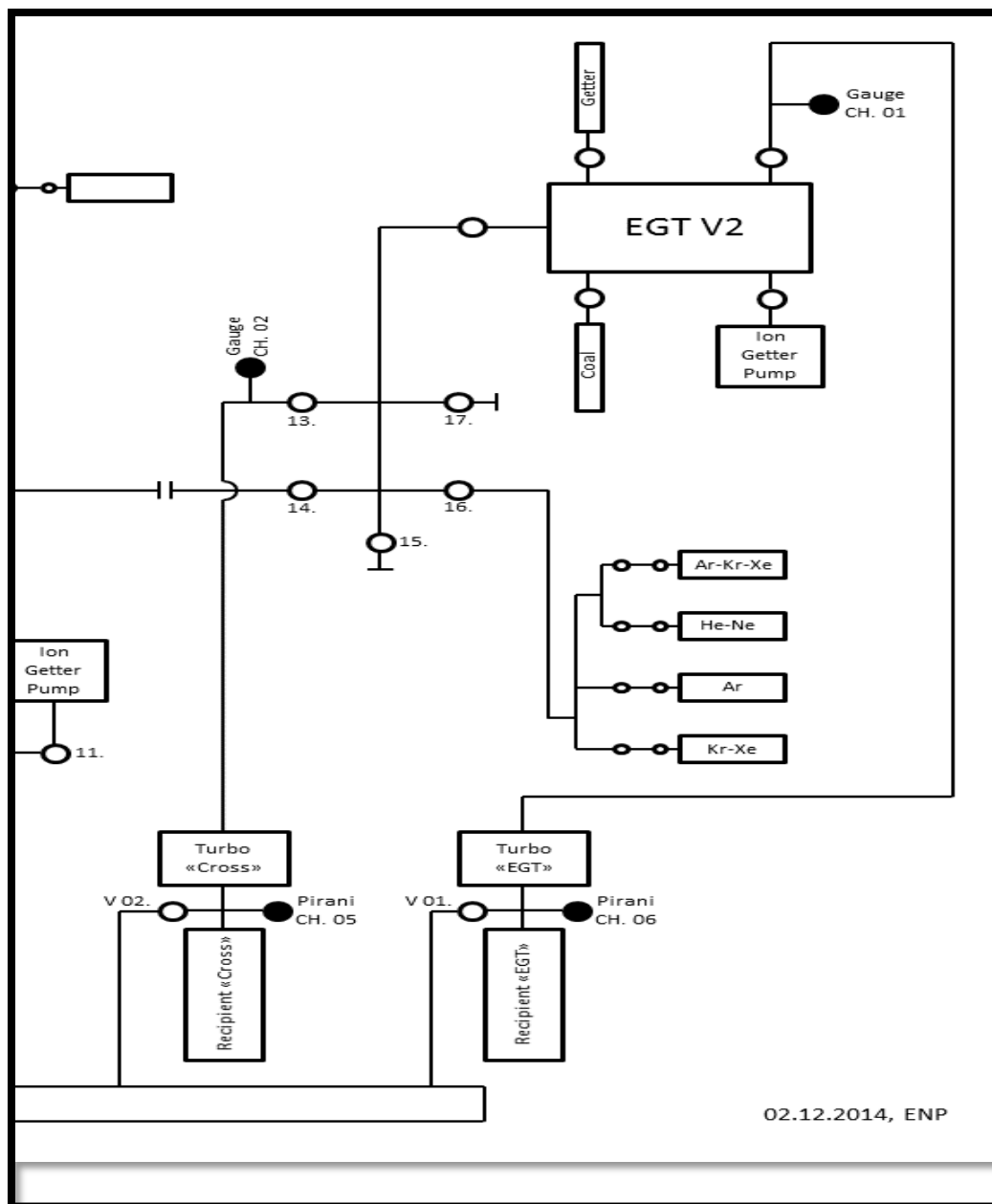


**Figure 6.13:** Schematic diagram of the EGT with the calibration bottles.

### 6.5. Shutdown or Rest mode

The EGT should be in night or rest mode when there are no measurements. The procedure is as follows: Switch from turbo pump and to ion getter pump. Decrease for safety the detector front potential to -2000V. For a complete shutdown of the EGT, first turn off the filament, the pulser and all low voltages. Finally, slowly ramp down all high voltages to zero and switch off all MoRaMi instruments.

## 6.6. Trouble shooting guide of the EGT

General trouble shooting guide for the EGT is as in below Table 6.1.

Problem	Possibilities	Solution
No Signal	1. False connections , voltage failure	<ul style="list-style-type: none"> <li>• Check electrical connections</li> <li>• Check power supplies</li> </ul>
	2. No ions	<ul style="list-style-type: none"> <li>• Check filament emission</li> <li>• Check detector resistance and strip current</li> <li>• Check pulse generator</li> <li>• Retuning</li> </ul>
	3. Acquisition system	<ul style="list-style-type: none"> <li>• Check ADC / TDC parameters, like threshold limits, ...</li> </ul>
High base pressure	1. Vacuum Pumps	<ul style="list-style-type: none"> <li>• Check turbo pumps</li> </ul>
	2. Leak	<ul style="list-style-type: none"> <li>• Check leaks at joints , gasket problems, ...</li> </ul>
Less sensitivity	1. Filament function	<ul style="list-style-type: none"> <li>• Filament emission current</li> <li>• Filament misalignment</li> </ul>
	2. MCP function	<ul style="list-style-type: none"> <li>• Low gain of the MCP due to treatment and/or aging</li> <li>• Preamp function</li> <li>• Clean connections at the outside</li> </ul>
	3. Tuning	<ul style="list-style-type: none"> <li>• Adjust ion source voltages</li> </ul>
Noise	1. Periodic noise	<ul style="list-style-type: none"> <li>• Check the radiation from ambient instruments</li> </ul>
	2. Non periodic	<ul style="list-style-type: none"> <li>• Grounding system</li> </ul>
	3. Ringing	<ul style="list-style-type: none"> <li>• Adjust reflectron voltages</li> </ul>

**Table 6.1:** EGT general trouble shooting guide.

## Chapter 7 : EGT Performance-Results & Discussion

The EGT has undergone various performance tests during the course of optimization and calibration for different parameters like mass fractionation, mass resolution, sensitivity, detection limits, and dynamic range; the results are discussed in this chapter.

### 7.1 Tuning results of EGT

Tuning is the primary step of optimization for any mass spectrometer in order to achieve the best performance. The EGT consists of 36 individual adjustable voltages and it is necessary and important to set up all of them for an optimal performance. Here we present three different kinds of tuning results; first, the best voltage settings for the EGT from SIMION ion optical simulations, second, tuning results from the specially coded EGT optimizer software, and finally results from manual tuning.

#### 7.1.1 Ion optical simulations results with SIMION

SIMION models are usually the starting point for the development of an ion optical instrument. This program numerically models electrostatic (and magnetic) fields as boundary value problems of the partial differential Laplace equation. Optimization of the instrument geometry and the applied electrode voltages can be done. SIMION ion optical simulations for the EGT are described by Abplanalp et al (2010) and Huber et al. (2011). The voltage settings from SIMION are given in Table 7.1(a) and 7.1(b).

#### 7.1.2 EGT optimizer tuning results

The data from SIMION are a good starting point for the setup of the real instrument. However, there are always a few limitations and shortcomings of simulations compared to real instruments. For example, SIMION 8.0 does not consider space charging effects. The lack of specific features in the used software and/or approximations done by the modelers always leads to performance differences between simulation and real instruments. However, the ion optical simulations are often used as a starting point for voltage settings on the actual instrument and fundamental behavior can be understood and visualized much easier within a model. For best performance, however, the real instrument must be tuned. As described in the previous chapter we used special software developed for the auto tuning of TOF mass spectrometers developed by Bieler (2012). Using this software, the EGT is optimized for 10 kHz pulse frequency, -2100 V detector bias voltages (detector front at -2700 V and detector back at -600 V), and assuming an exponentially modified gauss (EMG) function as peak shape. The thus obtained tuning results are tabulated in Table 7.1(a) and (b).

### 7.1.3 Manual tuning

Manual tuning of the EGT is tedious but important job to check the optimizer tuning results. The manual tuning done for single ion peaks of less concentration isotopes - at both low and high masses - with the help of the oscilloscope is explained in section 6.4. The performance of the EGT is very sensitive to small changes in the voltages. Therefore manual tuning has to be done carefully. Important results and observations are explained below.

Tuning the ion source voltages are the most important for peak shape and intensity as these voltages are responsible for ion production, ion storage, and ion beam acceleration towards the drift region. First, set the filament to the chosen emission current (~250 micro amps), which produces the electron beam. It turned out that the voltage settings of the EGT strongly depends on the pulse frequency. Note that this was not expected from the SIMION modeling results. However, the potential depression for ion storage depends on the source voltages and the peak shape depends on the ion extraction time, which is loosely related the pulse frequency. The most relevant voltage for ion source optimization is the back plane potential, which increases with increasing repetition frequency (Figure 7.1). For the other source voltages there is no or only a very minor dependence on the pulse frequency.

<b>Pin N° TOF 2</b>	<b>Name TOF 2 / Cable</b>	<b>SIMION Voltage [V]</b>	<b>EGT OPT. Voltage[V]</b>	<b>Manual tuning Voltage[V]</b>
<b>1</b>	Backplane	+8.60	+9.31	+8.14
<b>2</b>	Ion-Rep1	-24.60	-37.3	-43.40
<b>3</b>	Gnd	+48.50	+68.4	+55.50
<b>4</b>	El-Rep	-40.00	-42.60	-42.60
<b>5</b>	Fil 1A	-50.00	-55.80	-55.80
<b>6</b>	Fil 1B	-50.00	-55.80	-55.80
<b>7</b>	Fil 2A	+5.00	-5.5	+5.00
<b>8</b>	Fil 2B	+5.00	-5.5	+5.00
<b>9</b>	Ion-Rep2	+3.50	+4.5	-11.00
<b>10</b>	Extr.Grid/Pulser (SMA)	+18.9 / -555	+10.00/485	-3.8/-485
<b>11</b>	Lens 1	-1003.35	-1033.00	-1021.00
<b>12</b>	Lens 2	-1399.13	-1311.00	-1248.00
<b>13</b>	Lens 3	-4690.36	-4923.00	-4850.00
<b>14</b>	Drift	-2250.61	-2189.00	-2275.00
<b>15</b>	Detector Back	-600.00	-600.00	-600.00
<b>16</b>	Detector Anode (SMA)	---		---
<b>17</b>	Detector Front	-2700.00	-2700.00	-2700.00
<b>18</b>	Drift	-2250.61		-2275.00

**Table 7.1(a):** Source voltages from SIMION ion optical simulations, EGT optimizer, and manual tuning for a 10 kHz pulse frequency.



The influence of the filament emission current on the tuning was tested for by optimizing the EGT for filament emissions currents in the range 0  $\mu\text{A}$  to 300  $\mu\text{A}$

<b>Pin N° TOF 2</b>	<b>Name TOF 2 / Cable</b>	<b>SIMION Voltage [V]</b>	<b>EGT OPT. Voltage[V]</b>	<b>Manual tuning Voltage[V]</b>
<b>1</b>	Backplane	-32.73	-70.00	-68.25
<b>2</b>	R16	-213.74	-230.00	-223.00
<b>3</b>	R15	-250.12	-277.00	-330.00
<b>4</b>	R14	-670.92	-672.00	-700.00
<b>5</b>	R13	-992.31	-986.00	-915.00
<b>6</b>	R12	-699.83	-560.00	-710.00
<b>7</b>	R11	-1945.49	-1952.00	-1950.00
<b>8</b>	R10	-1473.19	-1528.00	-1470.00
<b>9</b>	R9	-1983.22	-1780.00	-1980.00
<b>10</b>	R8	-1301.98	-1278.00	-1305.00
<b>11</b>	R7	-2250.61	-2189.00	-2275.00
<b>12</b>	R6	-2250.61	-2189.00	-2275.00
<b>13</b>	R5	-4950.01	-4768.00	-4900.00
<b>14</b>	R4	-4950.01	-4768.00	-4900.00
<b>15</b>	R3	-4950.01	-4768.00	-4900.00
<b>16</b>	R2	-4950.01	-4768.00	-4900.00
<b>17</b>	R1	-2250.61	-2189.00	-2275.00
<b>18</b>	Drift	-2250.61	-2189.00	-2275.00

**Table 7.1(b):** Reflectron voltages from SIMION ion optical simulations, EGT optimizer, and manual tuning for 10 kHz pulse frequency.

#### 7.1.4 Conclusions

The results from the ion optical simulations obtained via the SIMION software are slightly different from the manual tuning results. For a proper judgement of the optimizer software more tests are needed. The results from the manual tuning show that some of the source voltages, especially the back plane voltage (QBP), unexpectedly depends on the pulse frequency and therefore has to be adjusted each time the pulse frequency is changed. The QBP slightly increases with increasing pulse frequency, as shown in the Figure 7.1. This

explains the number ions stored in particular time interval between two consecutive pulses are more in the case of wider potential-well created between back plane and extraction grid.

The drift voltage is another important voltage that affects the performance of the mass spectrometer and special focus should be put on it while optimizing the spectrometer. Note, the drift voltage should not be lower than the detector front voltage; otherwise the electrons produced at the grid located in front of the detector may cause unwanted signals on the low mass side, i.e., at earlier times, than the main signal. The reflectron voltages are especially important for high mass resolution and symmetric peak shapes and both can be achieved by gradually increasing the reflectron voltages from R1 to “reflectron back” and to avoid any discontinuities.

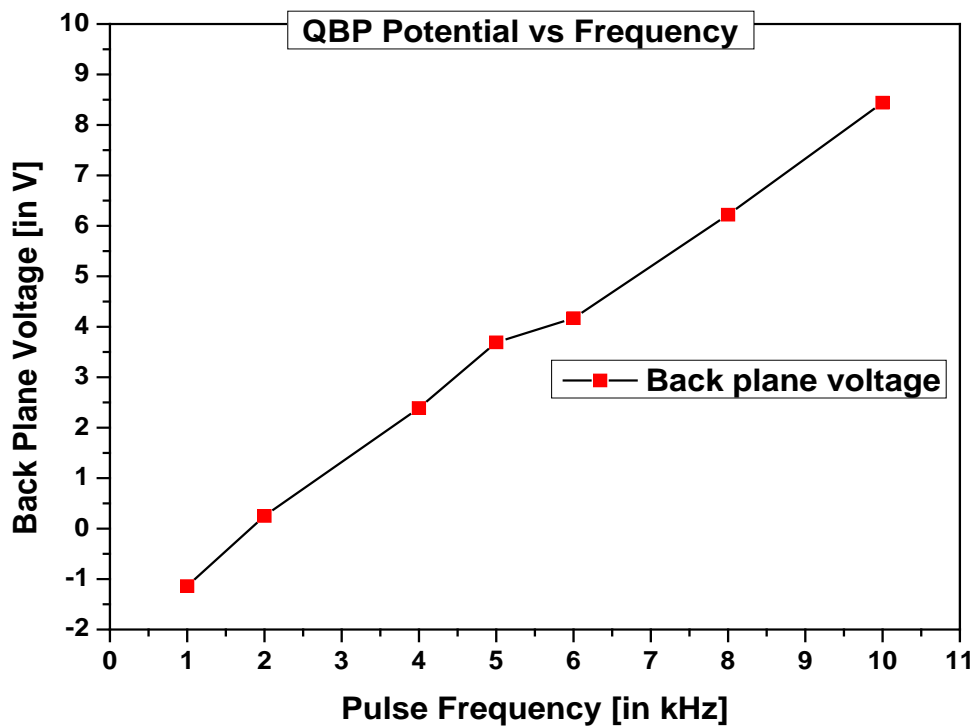


**Figure 7.1:** Variation of the optimized backplane (QBP) voltage as a function of pulse frequency at a constant extraction grid voltage of -3.8 V.

## 7.2 EGT data analysis software (EGT-DAS) results

### 7.2.1 EGT-DAS Monte Carlo Integration (MCI) results

The EGT-DAS software code has been developed to analyze EGT spectra. One of the main purposes is to find the area under the peak. As described earlier a very powerful method is Monte Carlo integration (MCI), which is therefore implemented in the code. We tested the MCI part using easy to analytically calculate shapes like triangles and sinusoidal waves. The results are given below.

**(a) Area of a triangle:**

The area of a right-angled triangle with base 30 and height 75 is 1125. The results obtained using MCI and different number of random numbers are given in Table 7.2. It can be seen that MCI with lower numbers of random numbers results is more scattering for the results of the determined peak. Consequently, higher numbers of random numbers should be chosen for proper integration. For this study we always used  $10^5$  or  $10^4$  random numbers, which is a compromise between scattering and calculation time and gives uncertainties in the range 1%. The negative relative error in the triangle area calculations is due to excess area (35) of MCI calculation which is due to extra portion covered in the plot and it is included to the error. The MCI value will be more accurate by subtracting this portion.

Area of Triangle	MCI Area with $10^3$ Random Numbers	% Error
1125	1136 $\pm$ 41.87	-0.97778
1125	1137 $\pm$ 54.59	-1.06667
1125	1162 $\pm$ 55.37	-3.28889
1125	1195 $\pm$ 74.04	-6.22222
1125	1171 $\pm$ 41.87	-4.08889
Area of Triangle	MCI Area with $10^4$ Random Numbers	% Error
1125	1131 $\pm$ 40.73	-0.53333
1125	1137 $\pm$ 37.98	-1.06667
1125	1129 $\pm$ 40.24	-0.35556
1125	1134 $\pm$ 40.24	-0.8000
1125	1141 $\pm$ 60.42	-1.42222
Area of Triangle	MCI Area with $10^5$ Random Numbers	% Error
1125	1156 $\pm$ 36.97	-2.75556
1125	1145 $\pm$ 37.05	-1.77778
1125	1142 $\pm$ 35.94	-1.51111
1125	1142 $\pm$ 40.50	-1.51111
1125	1150 $\pm$ 36.57	-2.22222
Area of Triangle	MCI Area with $10^6$ Random Numbers	% Error
1125	1142 $\pm$ 35.20	-1.51111
1125	1148 $\pm$ 35.47	-2.04444
1125	1139 $\pm$ 35.47	-1.24444
1125	1140 $\pm$ 35.75	-1.33333
1125	1141 $\pm$ 35.62	-1.42222
Area of Sine wave	MCI Area with $10^3$ Random Numbers	% Error
0.4597	0.4530 $\pm$ 2.1E-2	1.457
0.4597	0.4566 $\pm$ 1.9E-2	0.674
0.4597	0.4548 $\pm$ 2.0E-2	1.066
0.4597	0.4670 $\pm$ 2.3E-2	-1.588
0.4597	0.4604 $\pm$ 2.1E-2	-0.152
Area of Sine wave	MCI Area with $10^4$ Random Numbers	% Error
0.4597	0.4562 $\pm$ 7.8E-3	0.761
0.4597	0.4561 $\pm$ 7.5E-3	0.783
0.4597	0.4562 $\pm$ 3.7E-3	0.761
0.4597	0.4577 $\pm$ 0.8E-3	0.435
0.4597	0.4544 $\pm$ 8.1E-3	1.153

Area of Sine wave	MCI Area with 10 <sup>5</sup> Random Numbers	% Error
0.4597	0.4497±7.7E-3	2.175
0.4597	0.4516±2.1E-3	1.762
0.4597	0.4501±2.3E-3	2.088
0.4597	0.4509±3.6E-3	1.914
0.4597	0.4512±4.1E-3	1.849
Area of Sine wave	MCI Area with 10 <sup>6</sup> Random Numbers	% Error
0.4597	0.4505±6.0E-4	2.001
0.4597	0.4510±7.5E-4	1.893
0.4597	0.4514±4.3E-4	1.806
0.4597	0.4504±6.7E-4	2.023
0.4597	0.4516±3.7E-4	1.762

**Table 7.2:** Area with Monte Carlo Integration for known shapes: a triangle and a sinusoidal peak. The error in the MCI is decrease with increase in random numbers.

(b) Area of a sinusoidal peak:

$$\int_0^1 \sin(x)dx = 1 - \cos(1) = 0.4597$$

Area of a Sinusoidal peak with limits 0 to 1 for different random numbers for Monte Carlo Integration is shown in the above table (Table 7.2) with percentage error with respect to the theoretical value. Here also the error is around 2 % and is relatively high for one million random numbers.

## 7.2.2 EGT-DAS EMG fit area results

Isotope	Theoretical Ratio(*Kr/ <sup>86</sup> Kr)	MCI Ratio(*Kr/ <sup>86</sup> Kr ± Δ)	Relative Error
<sup>78</sup> Kr	0.0202	0.0212±2.1E-3	-4.9395
<sup>80</sup> Kr	0.1317	0.1310±3.8E-3	0.5406
<sup>82</sup> Kr	0.6693	0.6629±7.4E-3	0.9520
<sup>83</sup> Kr	0.6641	0.6607±1.6E-3	0.5161
<sup>84</sup> Kr	3.2947	3.1970±1.8E-3	2.9667

**Table 7.3:** EGT-DAS results for Kr isotopes on MCI.

Isotope	Theoretical Ratio(*Kr/ <sup>86</sup> Kr)	EMG Ratio(*Kr/ <sup>86</sup> Kr ± Δ)	Relative Error
<sup>78</sup> Kr	0.0202	0.0201±2.1E-3	0.38700
<sup>80</sup> Kr	0.1317	0.1318±3.8E-3	-1.91947
<sup>82</sup> Kr	0.6693	0.6735±7.4E-3	-0.63202
<sup>83</sup> Kr	0.6641	0.6519±1.6E-3	1.84045
<sup>84</sup> Kr	3.2947	3.2210±1.8E-3	2.24094

**Table 7.4:** EGT-DAS results for Kr isotopes with EMG fitting function.

Another option determining peak areas in the EGT-DAS program is fitting an EMG curve through the measured data. Both approaches, EMG fitting and MCI, give very similar results, as it is demonstrated for the results of the Kr calibration measurement (Table 7.3 and Table 7.4). The Kr isotopic ratios are calculated with the relative error between theoretical ratio with respect to  $^{86}\text{Kr}$  and MCI ratios in Table 7.3. The relative error is close to zero except for  $^{84}\text{Kr}$ . The Table 7.4 presents the data for the EMG fitting ratios and their errors. Here, in MCI results the lighter isotopes of the Kr i.e.  $^{78}\text{Kr}$  is having higher ratio than theoretical ratio and also more than EMG ratio ratios, this is due to interference of hydrocarbons( $\text{C}_6\text{H}_6$ ) at mass 78 with the  $^{78}\text{Kr}$  make additional peak and this has corrected via peak fitting method (Figure 7.2) Mass fractionations values calculated for MCI and EMG and the relative error between these two are close to each other; the differences are in the range of ~1% or less except for  $^{78}\text{Kr}$  due to interference.

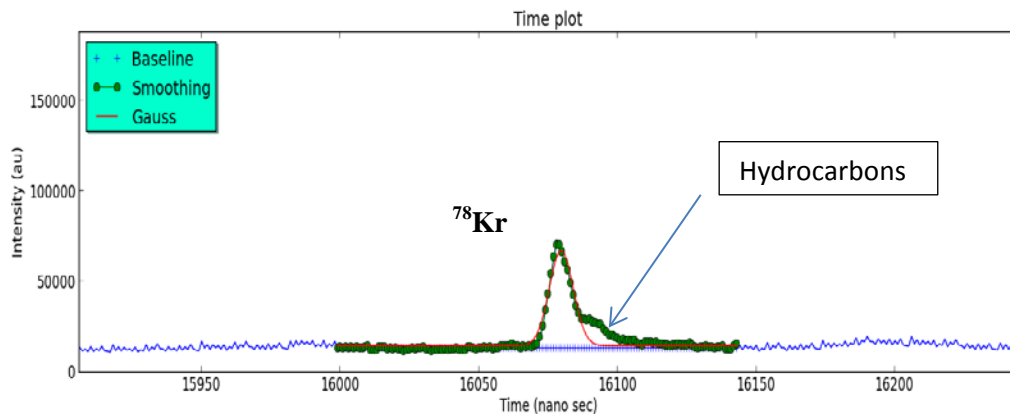


**Figure 7.2:** Subtraction of interference peak to the  $^{78}\text{Kr}$  by peak fitting.

### 7.2.3 Mass calibration

The mass calibration for a TOF mass spectrometer is given by:

$$m = \left( \frac{t - t_0}{C} \right)^2 \quad \text{---7.1}$$

The constant  $C$  and the time offset  $t_0$  can be determined by identifying two known masses,  $m_1$  and  $m_2$ , and their time-of-flight  $t_1$  and  $t_2$  in the TOF spectrum by

$$C = \frac{t_1 - t_2}{\sqrt{m_1} - \sqrt{m_2}} \quad \text{---7.2}$$

and

$$t_0 = \frac{\sqrt{m_2} \cdot t_1 - \sqrt{m_1} \cdot t_2}{\sqrt{m_2} - \sqrt{m_1}} \quad \text{---7.3}$$

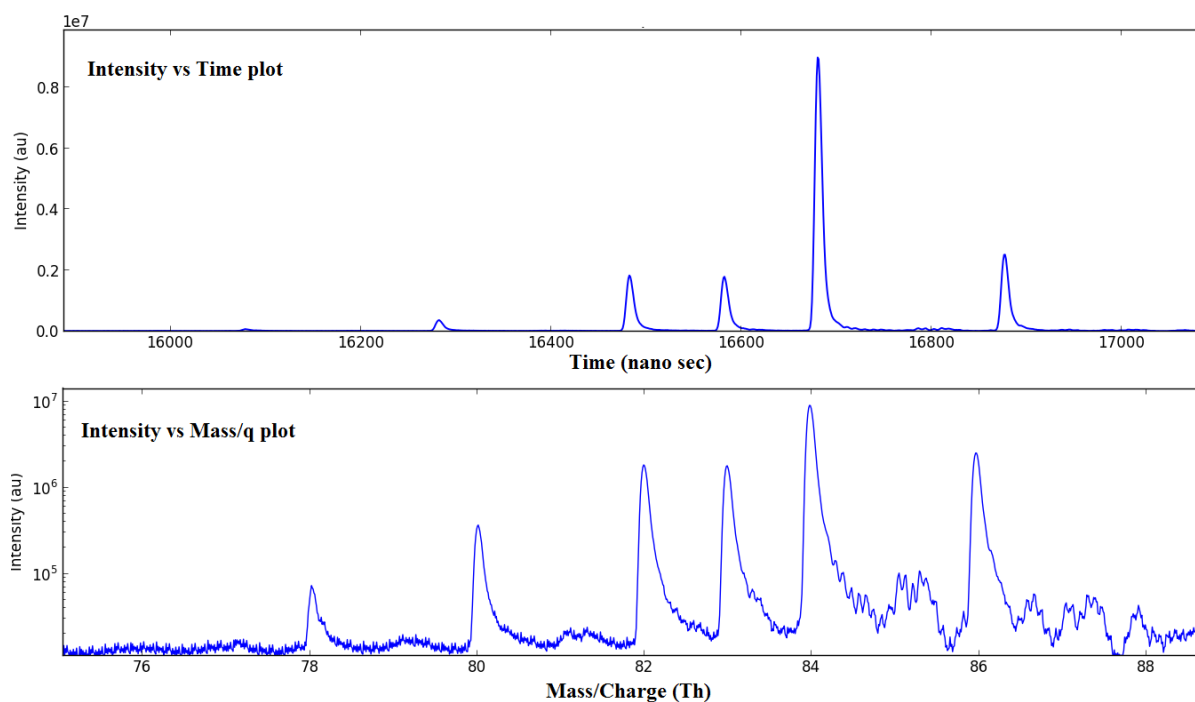


**Figure 7.3: (a)** Result of the mass calibration for the measurement of Kr calibration gas. The Upper panel gives the intensity as a function of flight time and the lower panel, for the same spectra, the intensity as a function of mass.

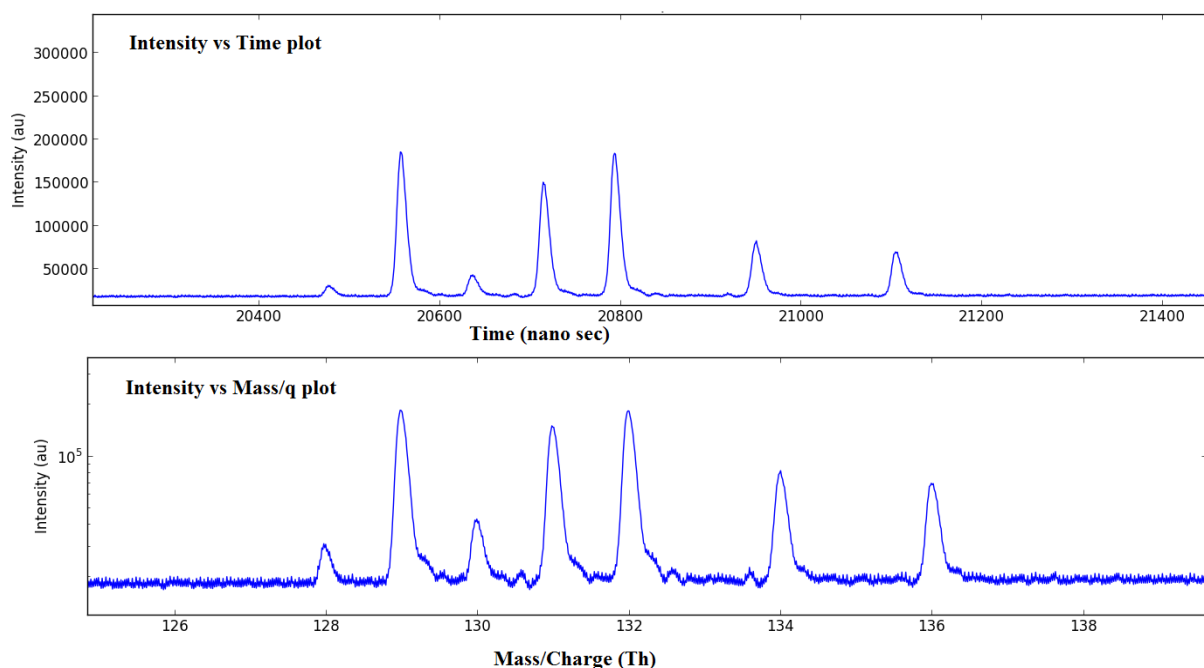


**Figure 7.3: (b)** Result of the mass calibration for the measurement of Xe calibration gas. The Upper panel gives the intensity as a function of flight time and the lower panel, for the same spectra, the intensity as a function of mass.

On the GUI of the EGT-DAS program the user has to select two known isotopic peak times in order to calculate  $C$  and  $t_0$  for each spectrum and then enter the mass calibration section. If the spectrometer is well tuned and settings are constant, the mass calibration will remain stable and constant for all spectra. Note that the mass calibration will be more accurate if  $m_1$  and  $m_2$  are relatively widely separated. In the EGT-DAS code the masses 2 amu ( $H_2$ ) and 44 amu ( $CO_2$ ) can be used for mass calibration. After entering the peak centre of the chosen peaks on the GUI and pressing the buttons “Enter  $t_1$ ” and “Enter  $t_2$ ” followed by pressing the button “calculate mass”, the intensity versus mass plot will be displayed in the lower panel of the GUI. An example for the measurement of Kr and Xe isotopes are shown in Figure 7.3(a) and 7.3(b).

### 7.3 Pulsar performance and storage characteristics

The Rectangular pulse generator is biased with the extraction grid of the ion source and the pulse characteristics are pre-tested before starting the experiment. The key parameters of the pulser are given below and the pulse is as shown in Figure 7.4(a).

- Can be used up to 10 kHz with pulse voltage of 500 V
- Pulse on time is 2.2  $\mu s$
- Pulse rise time is  $\sim 5$  ns (10 % to 90 %)
- Pulse fall is less  $\sim 80$  ns

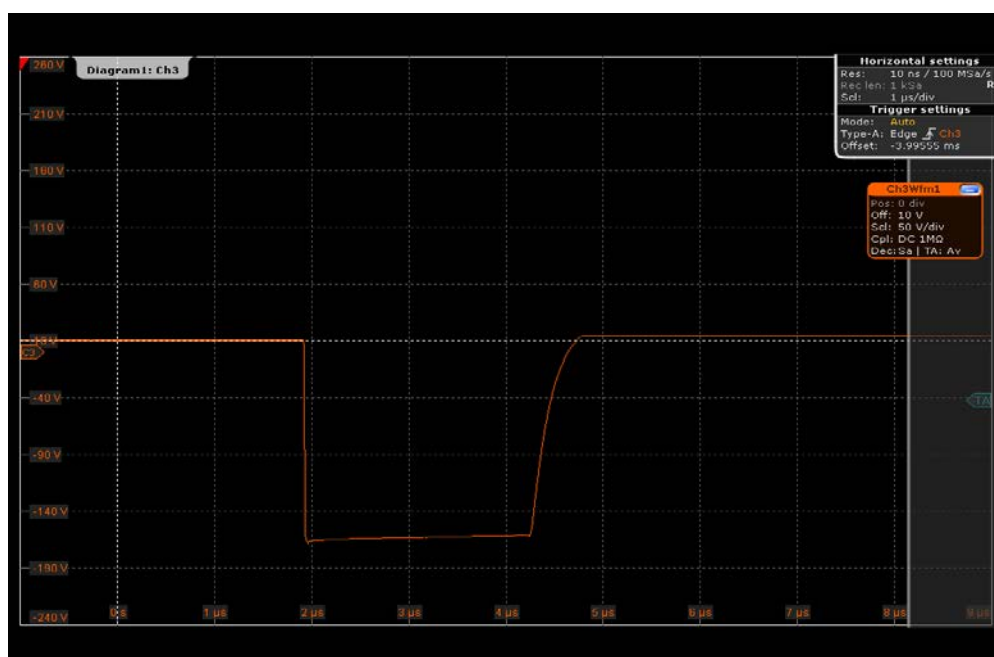


**Figure 7.4:(a)** Pulse from the external pulse generator.

The EGT performance tests have been done for different pulse frequencies from 1 kHz to 10 kHz all at a pulse height of -485 V and a pulse width of 2.2  $\mu s$ . Note that pulse height and pulse width are adjustable parameters. In contrast, pulse rise time and pulse fall time are fixed and cannot be changed.

### Storage characteristics:

The ion storage or ion trap capability of the electron impact ion source is directly related to the pulse frequency. Maximum storage capability is reached just if the potential depression formed by the ion source is compensated, i.e., filled, by the produced and stored ions. Further ion production ends in an overflow of the source, which simply produces some extra noise but no proper signals because there is no defined start time. In general, higher frequencies give shorter storage times and therefore less risks of overflowing the ion trap. Also, with a lower pressure in the spectrometer the ion trap will not fill as quickly. For testing this dependence krypton calibrations have been done for different frequencies, i.e., for different trapping times, and the results are shown in Figure 7.4(b). The area decreases with increasing pulse frequency, i.e., decreasing trapping time. This plot is for the measurements for 5 spectra at all frequencies, that means for 1 kHz pulse frequency and with 60000 averager on ADC takes 5 minutes of acquisition time, for 2 kHz frequency it is 2.5 minutes and so on. The area is decreased with decrease in trapping (increase in frequency) time and also lighter isotope  $^{78}\text{Kr}$  become negligible amount with higher frequencies, however longer measurement time can detect more amount of lighter isotopes at higher frequencies.

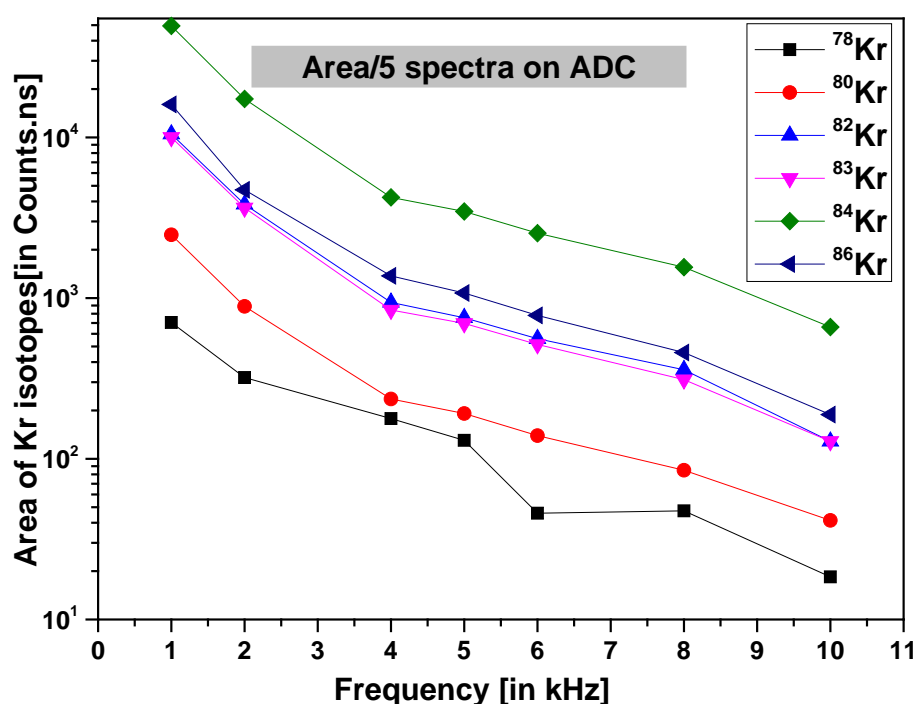


**Figure 7.4 :( b)** Area vs pulse frequency for Kr isotopes. Area with respect to the frequency is decreasing with increase in pulse frequency for five spectra. This is due to integration time (data acquisition time) will decrease with increase in frequency.

Figures 7.5 showed the storage characteristics of the ion source for Kr calibration gas for same data acquisition time at all frequencies. The measurements done for 10 minutes of acquisition at 1 kHz, 2 kHz, 5 kHz and 10 kHz pulse frequencies and the area under each isotopes increases due to the number cycles are more in the case of higher frequencies in



given time. Large integration times at higher frequencies are perfectly suitable for small concentration gas measurements.

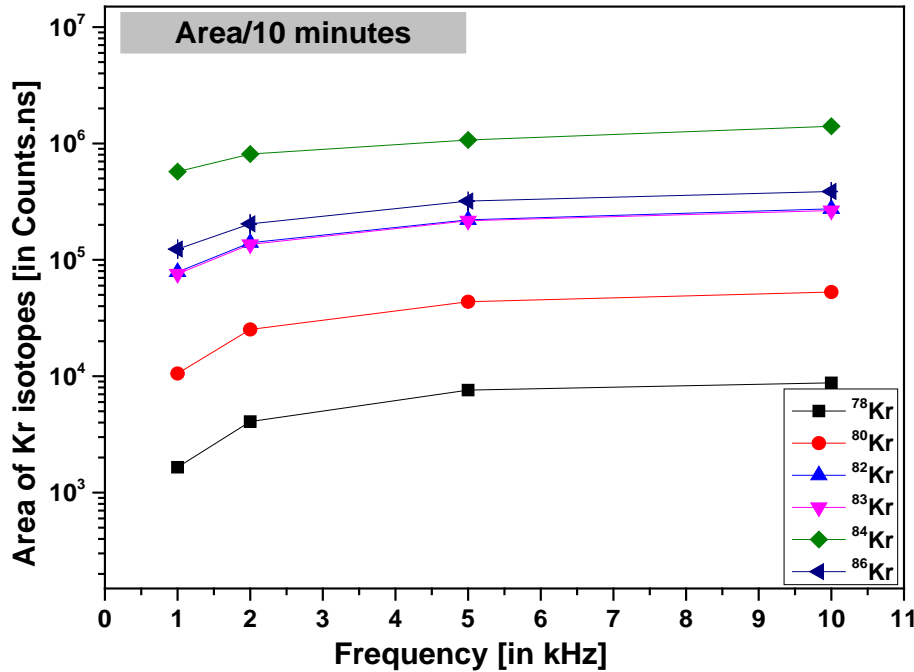


**Figure 7.5:** Area of Kr isotopes for 10 minutes of acquisition time for all frequencies.

For the same results of these number counts per pulse are decreasing with increase in pulse frequency. The Figure 7.6 shows the number of counts detected per extraction pulse versus repetition frequency (i.e. available storage time) for different isotopes of Kr. This shows the number counts are decreasing with high repetition rates since less storage time. Another important characteristic of static mass spectrometers temporal behavior is given in the Figure 7.7. This plot shows the decrease in the signal for every 20 minutes of data acquisition time, and the signal is decreased nearly 12 % for all isotopes of Kr except <sup>84</sup>Kr. This is due to loss of sample in the form of ions and may be continuous pumping but it is very low.

## 7.4 Measurements Methods and Results

### 7.4.1 ADC measurements and Results

The measurements with the ADC data acquisition system are done using the averaging mode. The results, i.e., the peak intensities depend on the integration time and number of accumulated spectra. Optimized settings for those parameters are needed to measure low intensity peak, like, e.g., <sup>78</sup>Kr, <sup>124</sup>Xe, and <sup>126</sup>Xe. Figure 7.8 shows the effect of the integration time on the peak area for integration times from one minute to 4 minutes for a pulse frequency of 1 kHz. As expected, for a fixed pulse frequency, more integration time means more accumulated spectra and therefore larger signals. For example, the number counts will be approximately double in the case of two minutes integration time than one minute integration time.

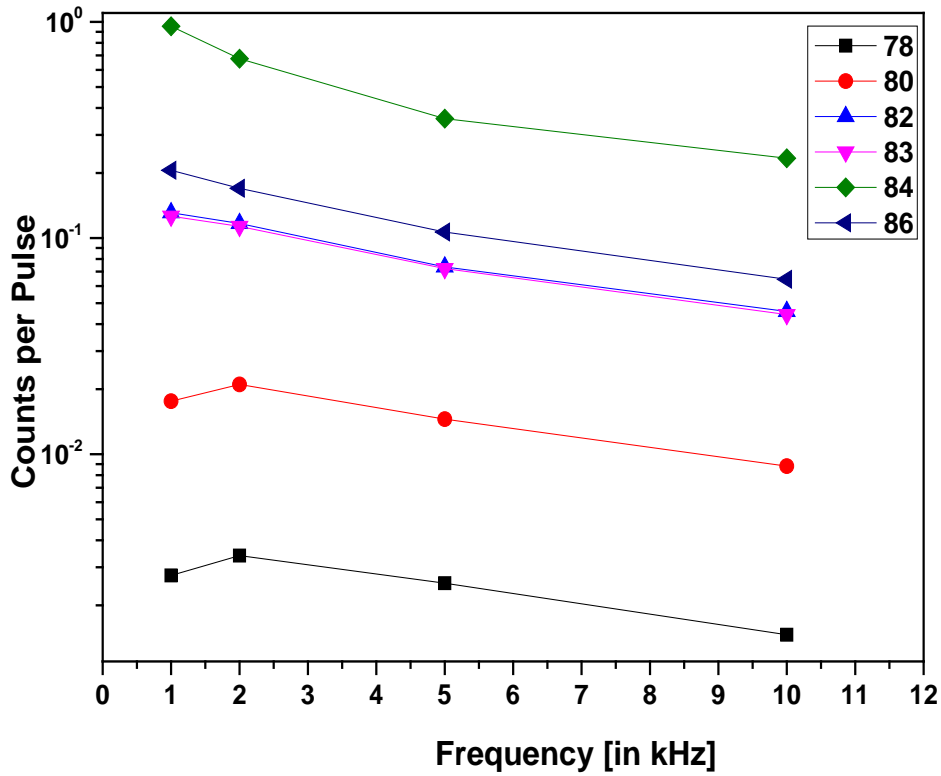


**Figure 7.6:** Storage capability in the electron impact storage ion source. The intensity versus the repetition frequency is plotted in counts per extraction pulse for Kr isotopes.

Figure 7.9(a) shows the influence of the number of accumulated spectra on the peak area for 10 kHz pulse frequency. The plot shows that the peak area increases with the number of accumulated spectra, which is very similar to the influence of the integration time on the peak area discussed above. Figure 7.9 (b) shows for the same data the signal to noise (SNR) ratio and the mass resolution as a function of number of accumulated spectra. The SNR ratio scatters but does not show a trend with the number of accumulated spectra, this is due to variation in signal and noise in the same proportion. In contrast, the mass resolution mass resolution is slightly decreasing with increasing accumulation of spectra due to more time spread for the peak and it is as shown in the Figure 7.9 (c).

The ADC card used by us has different kinds of data acquisition modes; averager mode, noise suppressed accumulation mode (NSA) and TDC mode. The standard measurement mode is the averaging mode. Another important data acquisition mode is the noise suppressed averaging (NSA) mode. In this mode, the ADC works with a threshold and it excludes signals that are lower than a given threshold and thereby increases the SNR ratio. If the signal is a rare event sitting on top of a noisy baseline, the averaging process will reduce the random noise. However, to enhance the averager's ability to detect such signals in the presence of synchronous noise, the averagers allow the user to set a threshold that has to be exceeded for each data value to be entered into the sum. The threshold should be set above (above for positive signals and below for negative signal) the level of the noise. With the same other settings of the ADC card the results with and without noise suppression are compared in Figure. 7.10. In NSA mode the signal intensities are higher than the signals produced in averaging mode since for each trigger and in each time bin, if the data value exceeds the

threshold then the threshold minus the base value will be added to the sum. An important note for the NSA mode is that the threshold value has to be chosen carefully to avoid losing any signals. The Figure 7.11, which compares the Kr signals and the Kr isotope ratios for a calibration gas measured in averaging and NSA mode. The data shows at least 1 to 2 orders of magnitude difference for NSA and averager mode for the same number of data acquisition settings (five minutes of integration time, 60000 averagers and 10 kHz frequency). The variation of signal with respect to the threshold voltage on NSA mode is as shown in the Figure 7.12. Surprisingly this shows very less threshold (-1 mV) and thereafter it starts cutting the signal.

In the averager mode the signal value calculated by averaging the total number of acquisitions but in the case of NSA mode it is only the signals which are more than the threshold value. For example if there are for acquisitions with number of counts 1, 2, 4, 6, 2, in the averager mode the final value is 3 (sum divided by 5) but in the case of NSA mode with the threshold limit of 3, the final result is 5, because only two acquisitions are more than the threshold limit (i.e. sum divided by 2). Hence the signal in the case of NSA is larger than averager mode.

In NSA mode the chosen threshold voltage is an important parameter and must be set carefully to reduce the baseline noise but not loosing any signal. The optimised threshold voltage has to be found using the pulse amplitude analysis. Since the signals from the MCP are negative, the threshold voltage was increased from 0 mV to -35 mV. The data indicate that the minimum threshold voltage possible, i.e., the voltage that do no cut any signal is only around -1 mV.

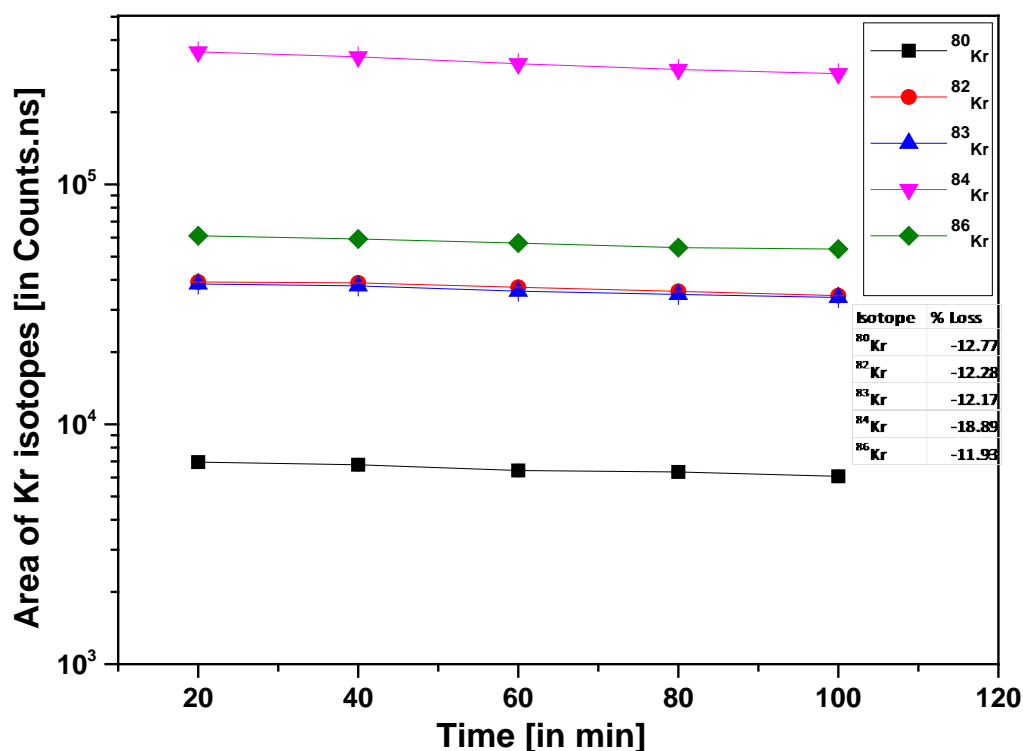


**Figure 7.7:** The Temporal behavior of the signal after every 20 minutes of acquisition time.

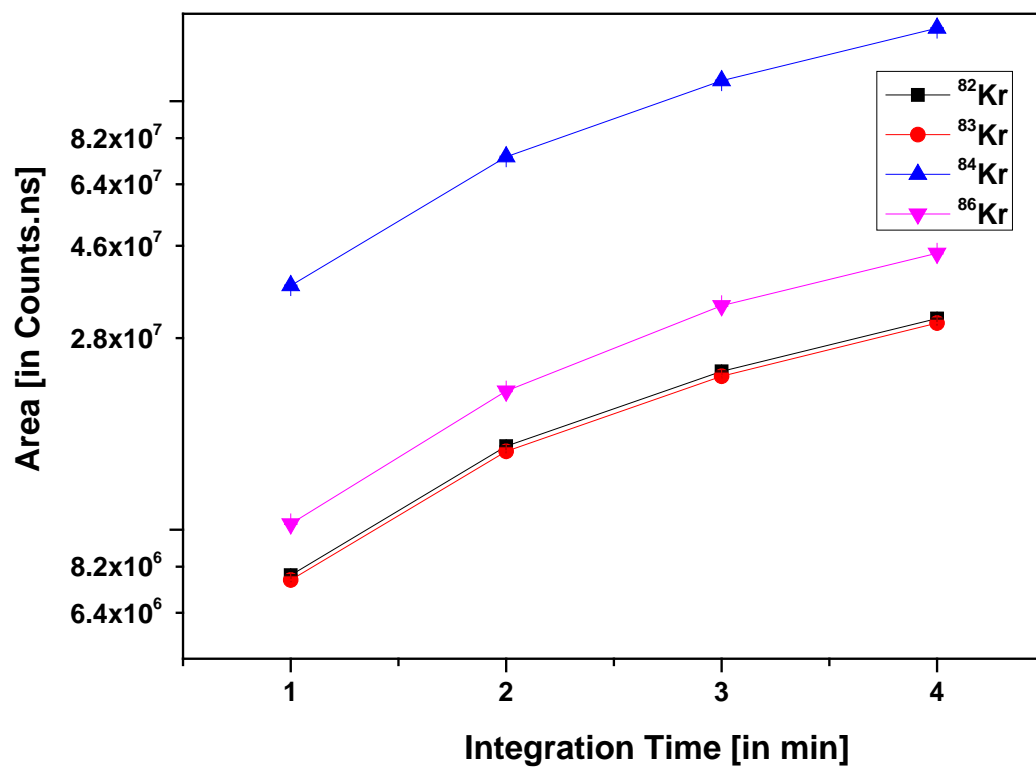


**Figure 7.8:** The dependence of the peak areas on the integration time for 1 kHz pulse frequency.

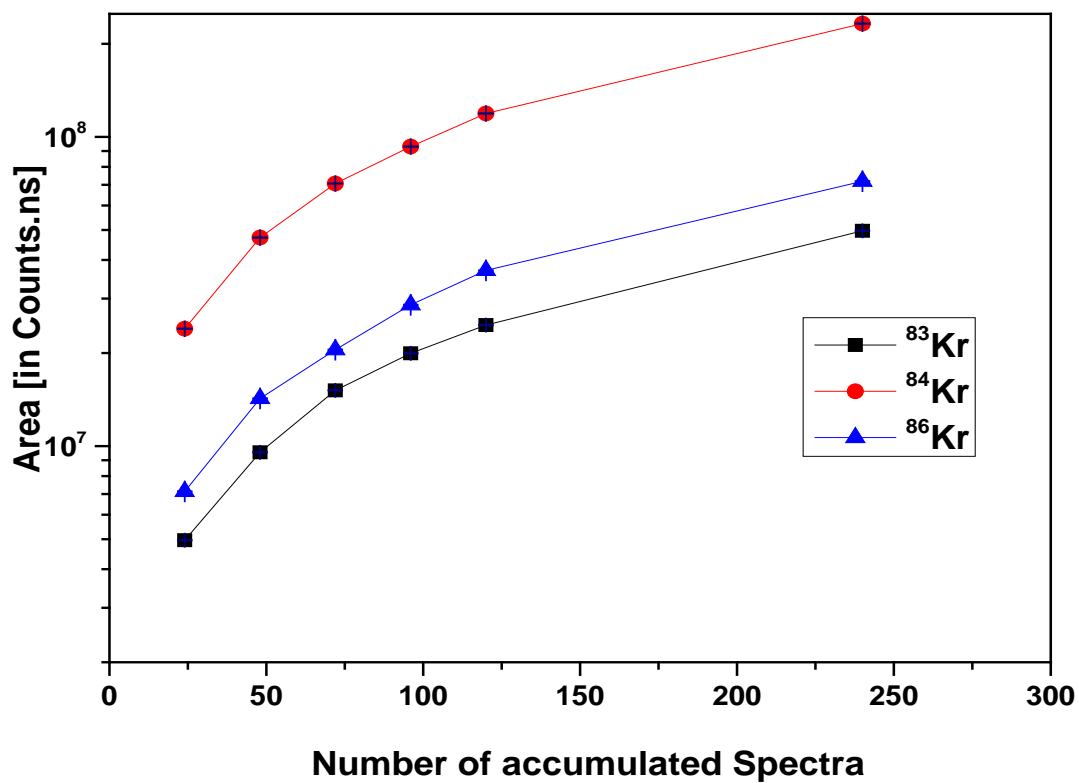


**Figure 7.9:** (a) Intensity as a function of number of accumulated spectra for 10 kHz pulse frequency.

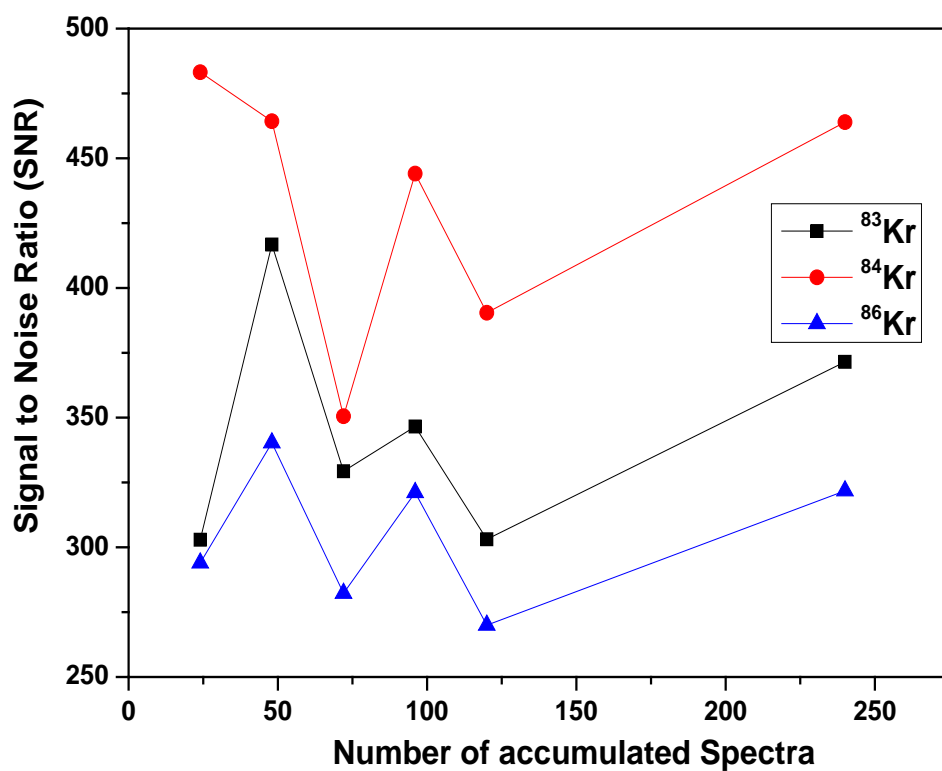


**Figure 7.9: (b)** Signal to noise ratio (SNR) as a function of Number of accumulated spectra.

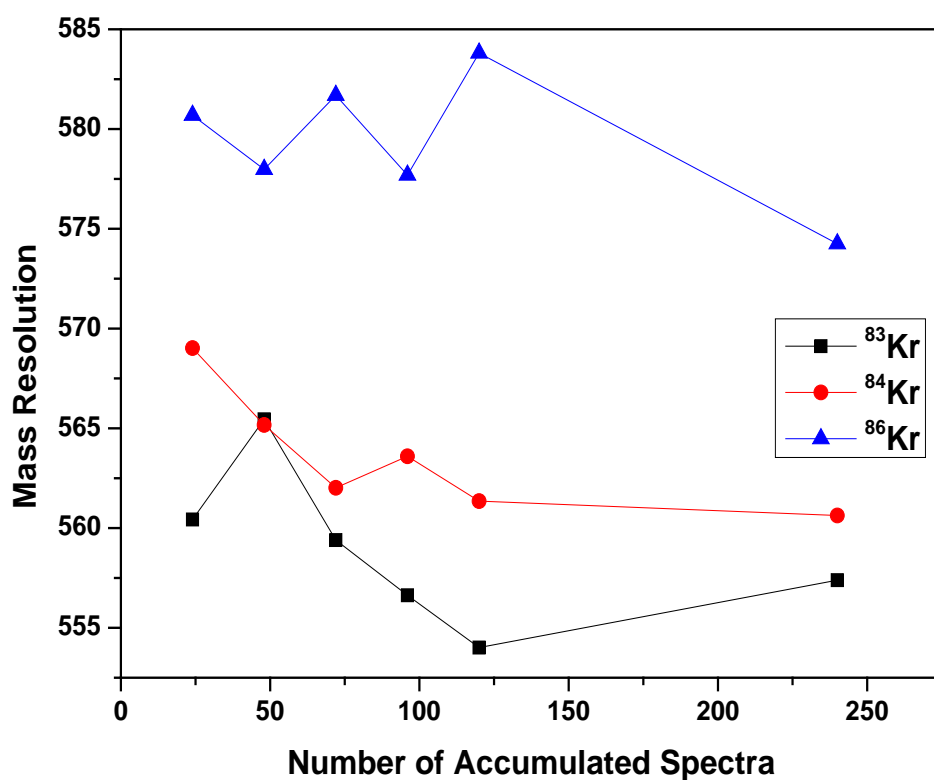


**Figure 7.9: (c)** mass resolution as a function of number of accumulated spectra.

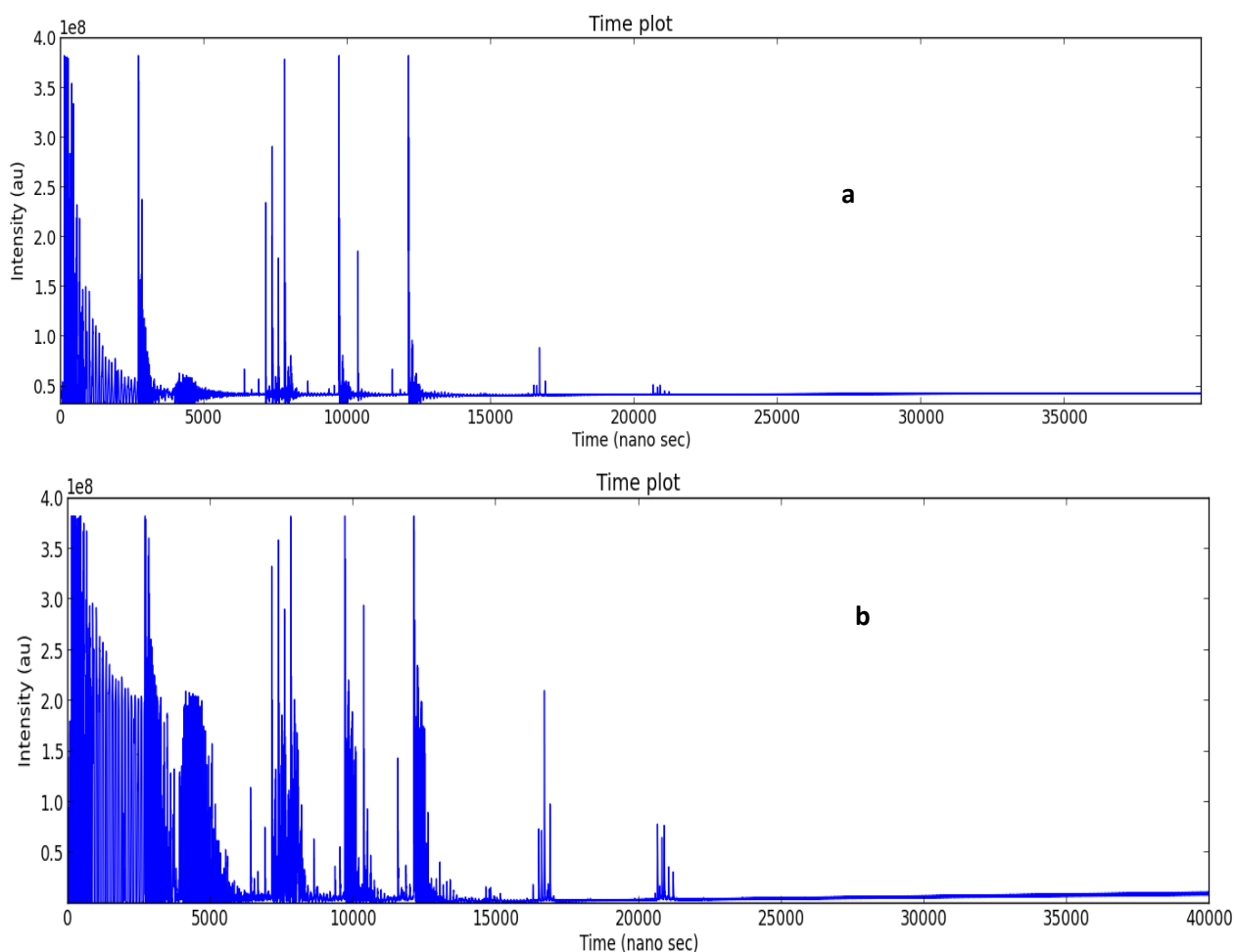


**Figure 7.10:** (a) ADC spectra in averaging mode (b) ADC spectra in NSA mode with a threshold of -1 mV

Another important parameter for ADC measurements is full scale and offset. The full scale should be set that all important peaks are covered and none of them is cut. The zero offset position automatically starts in the middle of the full scale and it has to be adjusted in order to get proper spectra. Figure 7.13 shows the influence of the chosen ADC offset on peak intensities (areas). With a set full scale of 200 mV we varied the offset from 96 mV to 105 mV. The results clearly show that the peak areas are constant up to an offset of 99 mV. Similarly for 50 mV full scale the offset should be less than 24 mV and for 100 mV full scale it should be less than 49 mV to avoid signal loss. At higher offset, one starts cutting some part of the signal, which results in decreasing peak areas. Consequently, to avoid any signal losses, which would also result in strange isotope fractionation pattern, the offset value should always be always less than half of the full scale. The threshold voltage variation at the beginning is showing unusual trend; i.e. from 4 mV to 8 mV it is increasing where it should be constant or decrease. After 8 mV of threshold decrease in the peak area shows that the discrimination cuts the signal.

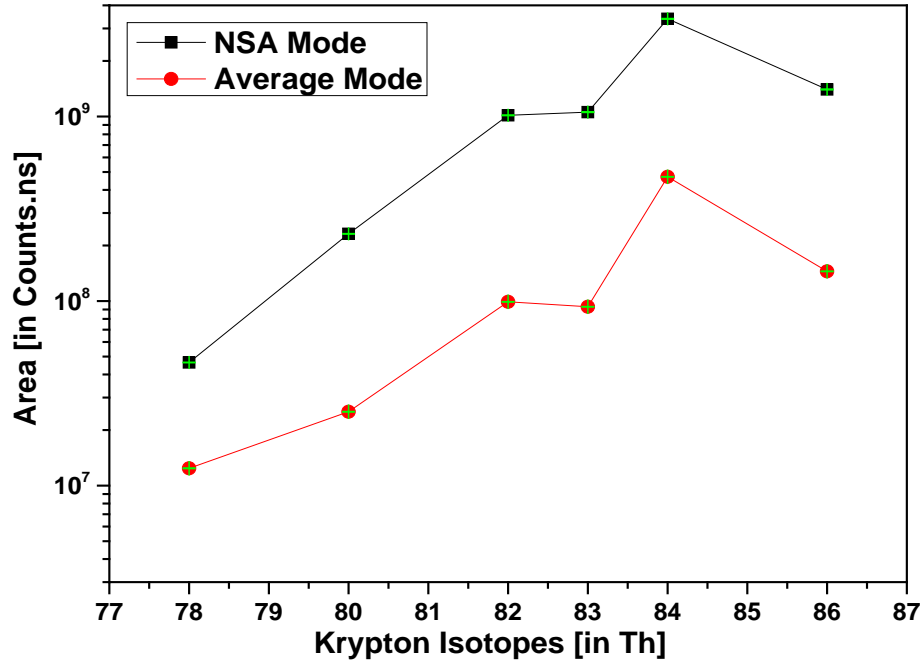


**Figure 7.11:** Signal intensities for Kr isotopes for averager mode and NSA mode on ADC card.

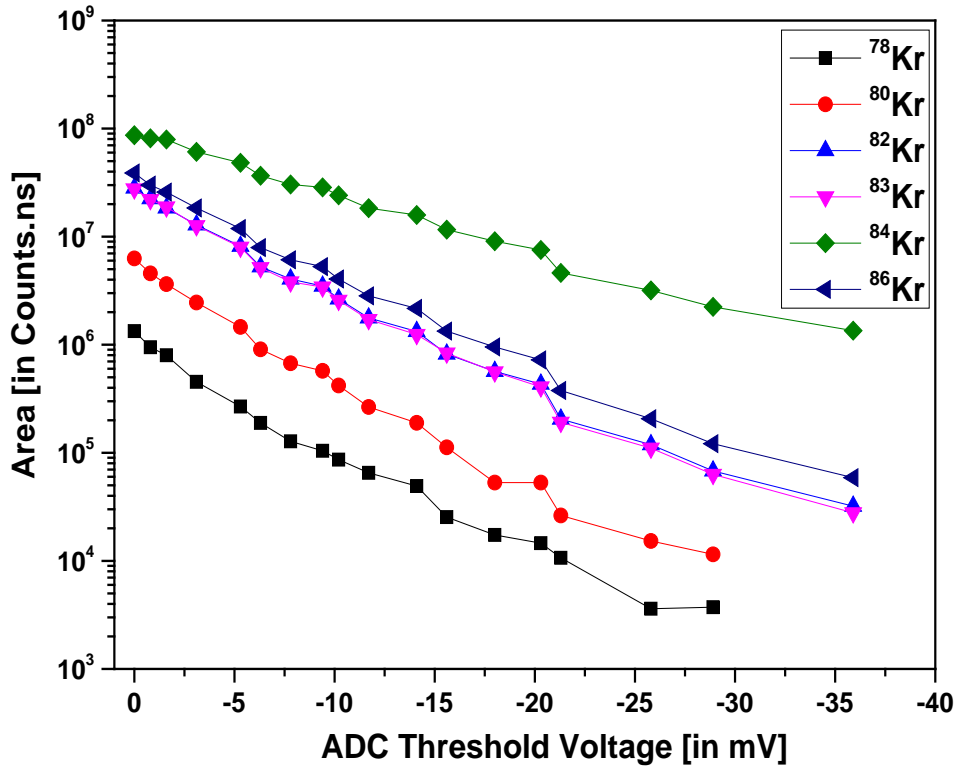


**Figure 7.12:** Signal intensities of Kr isotopes for different threshold voltage setting of the ADC card.

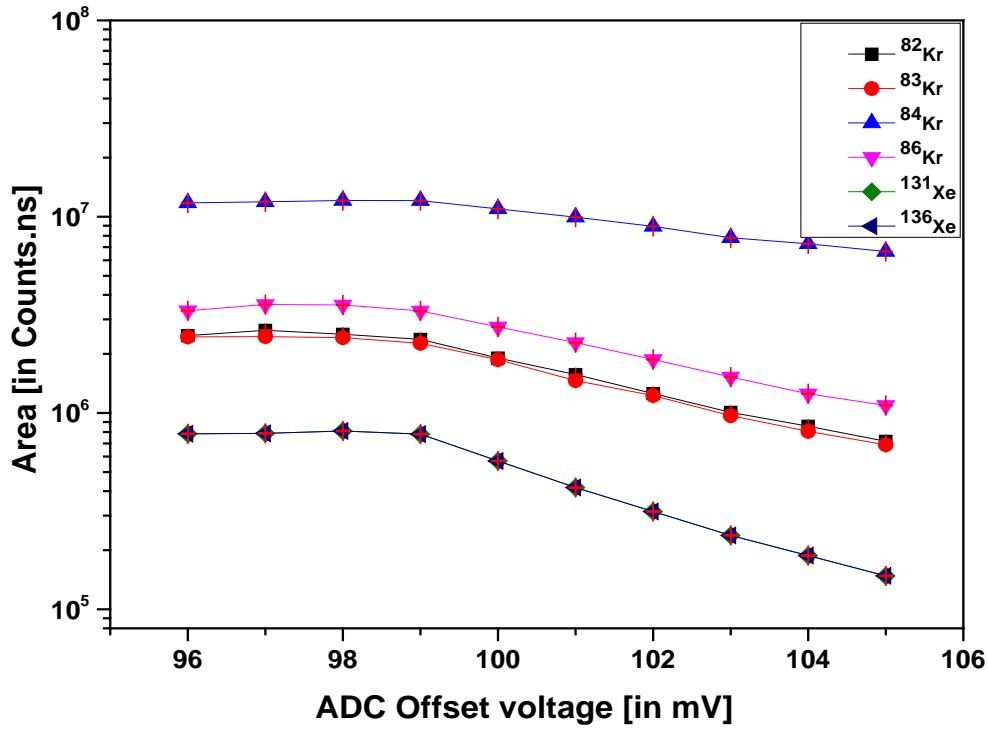


**Figure 7.13:** Signal area vs different offset voltage setting of the ADC card.

#### 7.4.2 TDC Measurements and Results

As discussed above, TDC measurements count signal above a preselected threshold and they are therefore completely different from ADC measurements. The effect of the threshold is as shown in Figure 7.14. Threshold value for EGT is around -8 mV.

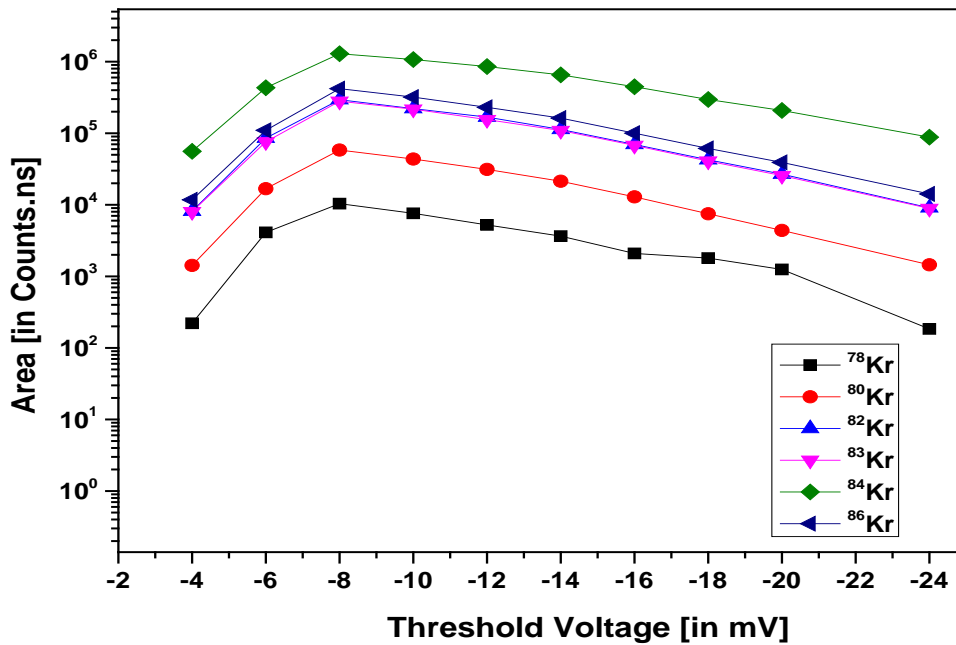


**Figure 7.14:** Effect of threshold on TDC measurements. From the threshold voltage -8 mV to -24 mV the signal height decreased with increase in threshold.



### 7.4.3 MCP Performance tests

The first step for checking if MCPs are working properly is checking the strip current ( $I_{strip}$ ) in the MCP circuit. The strip current is the current flowing along the channel wall when a voltage is applied between the front and back side of the MCP. The current can be measured by connecting the MCP-front with a high voltage power supply and MCP-back to the ground. The strip current can then be measured in between MCP-back and ground via

$$I_{strip} = \frac{V}{R_{Front} + R_{Back}}$$

where  $R_{Front}$  ,  $R_{Back}$  are the resistances of front MCP and back MCP respectively and V is the potential difference between two MCPs. (see the Figure 7.15)

$V_{back}$ (Volts)	$V_{front}$ (Volts)	Bias voltage ( $\Delta V$ ) in Volts	Strip current ( $\mu A$ )
-100	0	100	0.47
-200	0	200	0.65
-300	0	300	0.75
-400	0	400	0.91
-500	0	500	1.23
$V_{back}$ (Volts)	$V_{front}$ (Volts)	Bias voltage ( $\Delta V$ ) in Volts	Strip current ( $\mu A$ )
0	-100	100	2.50
0	-200	200	3.15
0	-300	300	3.20
0	-400	400	3.50
0	-500	500	3.68

**Table 7.5:** Testing the Micro channel plates by measuring the strip current. The data show that the strip current is proportional to the applied voltage, indicating that the MCPs are working as expected.

For a quick examination of MCPs one can also measure the resistance of each MCP and compare them with given values. However, such a measurement is relatively difficult. The strip current measurement circuit is shown in the Figure 7.15 below.

#### MCP life time:

Typically, MCP gain decreases by ~20 % when the total accumulated charge reaches one Coulomb. The total accumulated charge in the MCP can be measured by the current flowing through the MCP times the total time of accumulation. For example, on an average 10  $\mu A$  of current flows in the MCPs for 100 hours then a total charge of 3.6 C is accumulated.

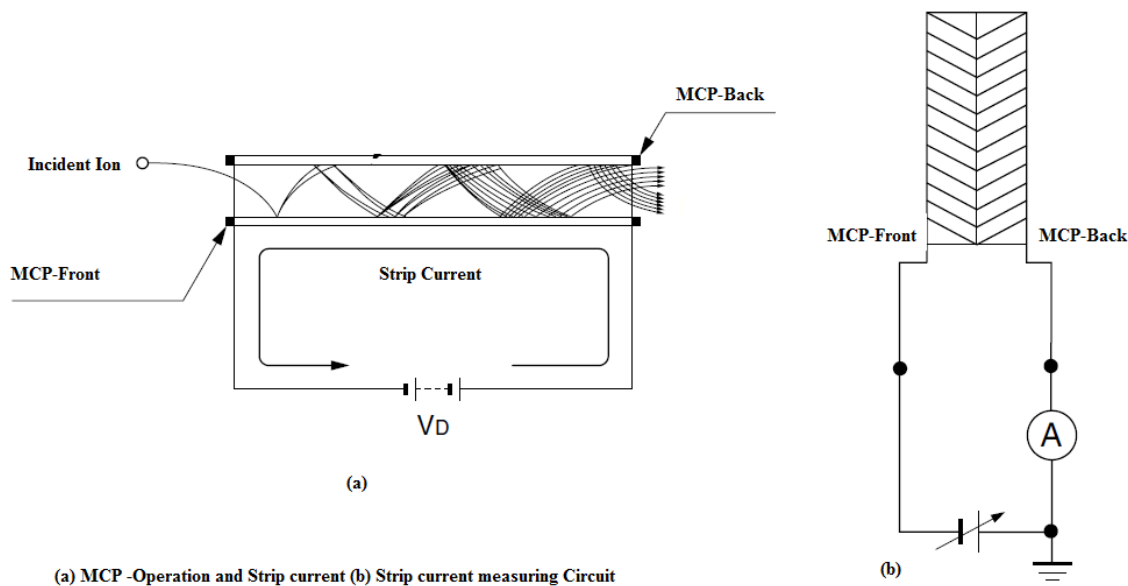


**Figure 7.15:** MCP operational diagram and strip current measurement.

#### Signal size as a function of MCP Voltage:

The MCPs are tested for different voltages to determine the optimal voltage settings. Applying voltages differences from 1800 V to 2300 V between the detector front and back for new and old MCPs gives the results shown in Figure 7.16(a) and 7.16(b). The difference in the performance between new and old MCPs is due to the decrease in gain caused by charge accumulation over time (see above). Theoretically, the optimal voltage setting for the detector is given by lowest voltage for which the signal size is no longer increasing, i.e., the beginning of a plateau. In Figure 7.16(a) it can be seen that such a plateau starts at about 2100 V, though the trend is only weak. Note, applying more than 2400 V between detector front and back or more than 1200 V for each MCP will significantly reduce the lifetime of the MCPs or even destroy them.

#### 7.4.4 Filament performance tests

##### Filament resistance:

The filament Resistance is measured before starting the experiment as 2.2  $\Omega$  for filament 1 and 2.3  $\Omega$  for filament 2. Both values are close to the value of  $\sim 2 \Omega$  given from the company.

##### Filament Emission Current:

Filament emission current is set to 250  $\mu\text{A}$  and in an ideal case the electron beam should reach the opposite electrode. In our instrument, however, the electron beam is scattered in the ion source. Hence the sum of the currents at all other source electrodes should be equal to the selected and regulated emission current. These currents have been measured with an ampere meter and sum is  $\sim 240 \mu\text{A}$ , i.e., very close to the total emission current.

## Filament Heating Current Vs Emission current:

For the EGT the LaB<sub>6</sub> Filament emission current is regulated by the heating current. Figure 7.17 shows the plot of the emission current as a function of the heating current. The left side shows the characteristics given in the manual and the right side shows the measured laboratory performance.

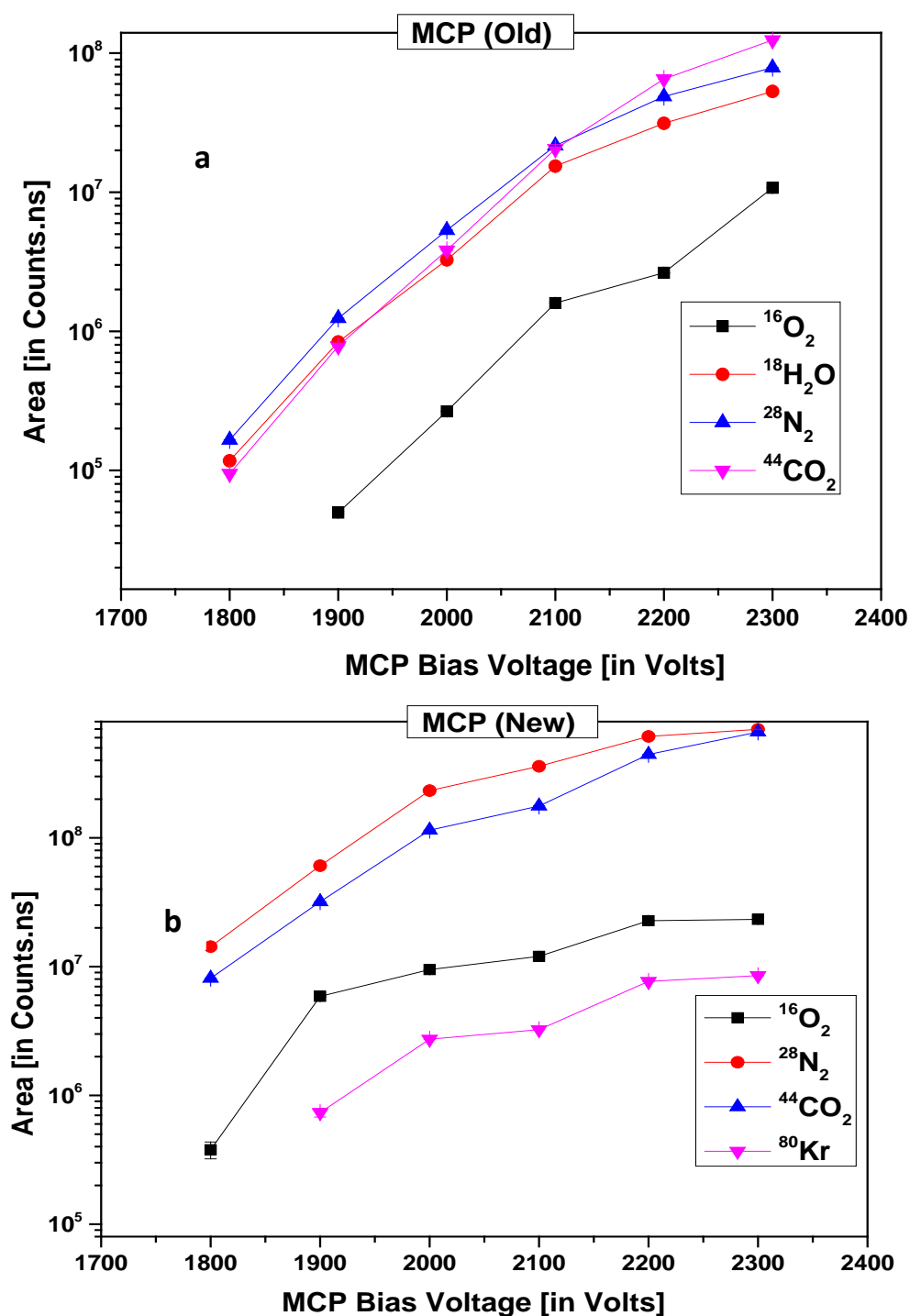


**Figure 7.16:** (a) Signal size as a function of MCP bias voltage for old MCPs (b) and new MCPS

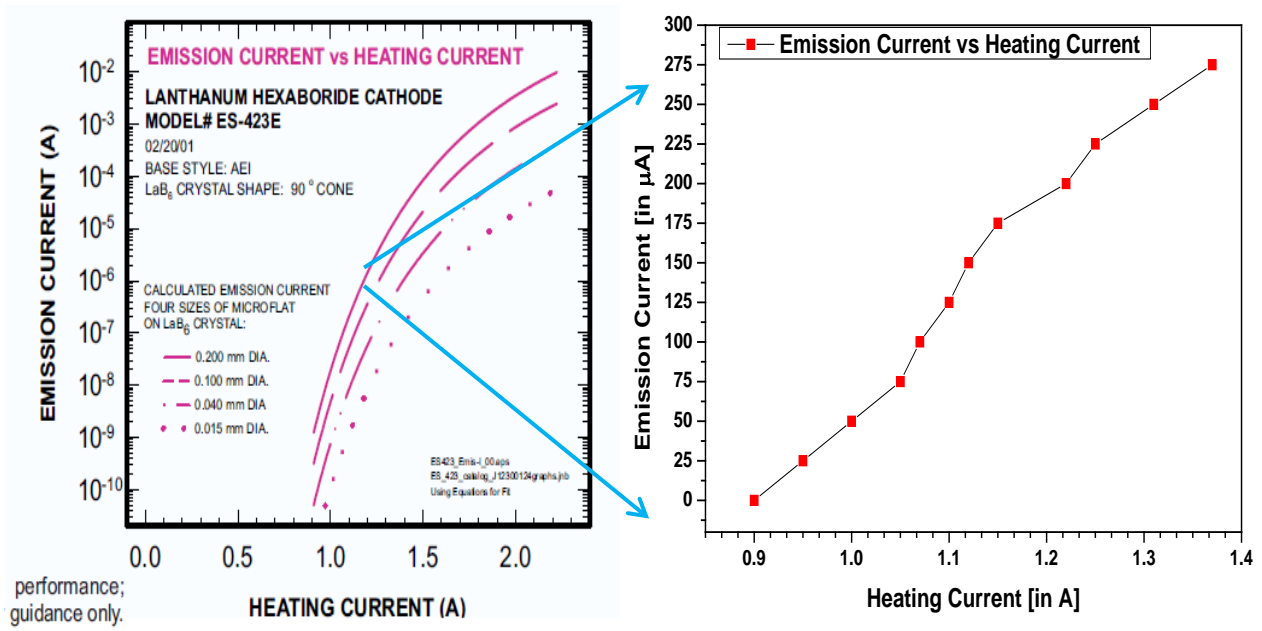


**Figure 7.17:** (a) Emission Current as a function of heating current for a LaB<sub>6</sub> filament from Kimball® (b) Laboratory performance of the filament.

## 7.5 Noble gas calibrations

The EGT is calibrated using Ar, Kr, and Xe standards, which are all of atmospheric isotopic composition. For quantitative noble gas measurements the sensitivity of the mass spectrometer must be known. In addition, the performance of a mass spectrometer can also be estimated by studying the instrumental mass fractionation. Both ADC and TDC measurements were used for calibrations.

### Mass dependent fractionation per unit mass:

The ideal mass spectrometer should have the same performance independent on the sample gas amount (linearity) and should also have the same sensitivity for all isotopes of the same element. However, for real instruments the sensitivity is different for different isotopes of the same element, an effect calls instrumental mass fractionation. This performance difference of mass spectrometer is due to the higher velocities of lighter isotopes than heavier once. Lighter isotopes preferentially fractionate more than heavier isotopes. This difference fractionation leads to different detection efficiencies which are called as mass-dependent fractionation. The mass dependent fractionation per unit mass (FPMU) is mathematically formulated as

$$\text{Fractionation Per Mass Unit} = FPMU_j^i = \frac{\left[ \frac{\left( \frac{i}{j} \right)_{\text{measured}} - \left( \frac{i}{j} \right)_{\text{standard}}}{\left( \frac{i}{j} \right)_{\text{standard}}} \right]}{\text{mass}_i - \text{mass}_j} \times 100\%$$

This is usually expressed as percent per mass unit and should be zero or close to zero for all isotopic ratios. It is appropriate to discuss the performance of a mass spectrometer in terms of FPMU because we are usually measuring isotopic ratios.

### 7.5.1 Krypton-Xenon Calibrations using the ADC

Kr-Xe calibration bottle attached with EGT usually releases  $2 \times 10^{-10} \text{ cm}^3$  STP per calibration. This section describes the ADC and TDC measurements of Kr-Xe calibration gases.

#### (a) Kr-calibration measurements using the ADC card:

- **Isotopic mass fractionation of Kr**

The instrumental mass fractionation per mass unit (FPMU) of the EGT for Kr isotopes has been determined in five measurements using the ADC data acquisition system with 60000 averages at 10 kHz pulse frequency and for five minutes of integration time. The results are plotted in Figure 7.18.

The FPMU for Krypton isotopes for  $^{80}\text{Kr}$ ,  $^{82}\text{Kr}$ ,  $^{83}\text{Kr}$  are relatively constant and in the range of 1%. For  $^{84}\text{Kr}$ , however, the FPMU is much larger and highly variable, though there is no possibility of interference this is unclear. Since  $^{78}\text{Kr}$  is small compared to the other peaks and therefore difficult to measure using the full scale on the ADC card.

- **Kr detection Sensitivity**

The detection sensitivity of the EGT for Kr isotopes is given by the minimum Kr isotopic signal that is detectable, which depends on the settings of the data acquisition system. For the above measurements the best detection sensitivity is  $2.7 \times 10^{-14} \text{ cm}^3$  STP for one minute of measurement. The detection sensitivity will increase with integration time, since the area will increase with increase in integration time.

- **Mass resolution**

The mass resolution for the Kr isotope measurements discussed above is shown in Figure 7.19. The mass resolution is around 850, which is slightly higher than the mass resolution expected from the simulations (~700).

#### (b) Xe -calibration measurements using the ADC card:

- **Isotopic mass fractionations of Xe**

Each calibration out of the Xenon bottle also contains  $2 \times 10^{-10} \text{ cm}^3$  STP of gas. The mass fractionation per unit mass with respect to the heaviest Xe isotope  $^{136}\text{Xe}$  is plotted in Figure 7.20. The results show huge variations in FPMU for the different measurements. In addition, the minor isotopes like  $^{124}\text{Xe}$  and  $^{126}\text{Xe}$  could not be detected with the used ADC setting. Note that small signals can easily be lost using the full scale or a high threshold.  $^{130}\text{Xe}$  shows some inconsistency which is unclear for some measurements. The other isotopes show a lower and more consistent pattern in FPMU of around 1%.

- **Xe detection sensitivity**

The sensitivity for Xe isotopes is  $\sim 9.01 \times 10^{-14} \text{ cm}^3$  for one minute of integration time and 10 kHz pulse frequency.

- **Mass resolution**

The mass resolution for Xe isotopes is about ~900; which is slightly higher than for Kr isotopes and also higher than the value from the SIMION theoretical simulations. The results are shown in the Figure 7.21

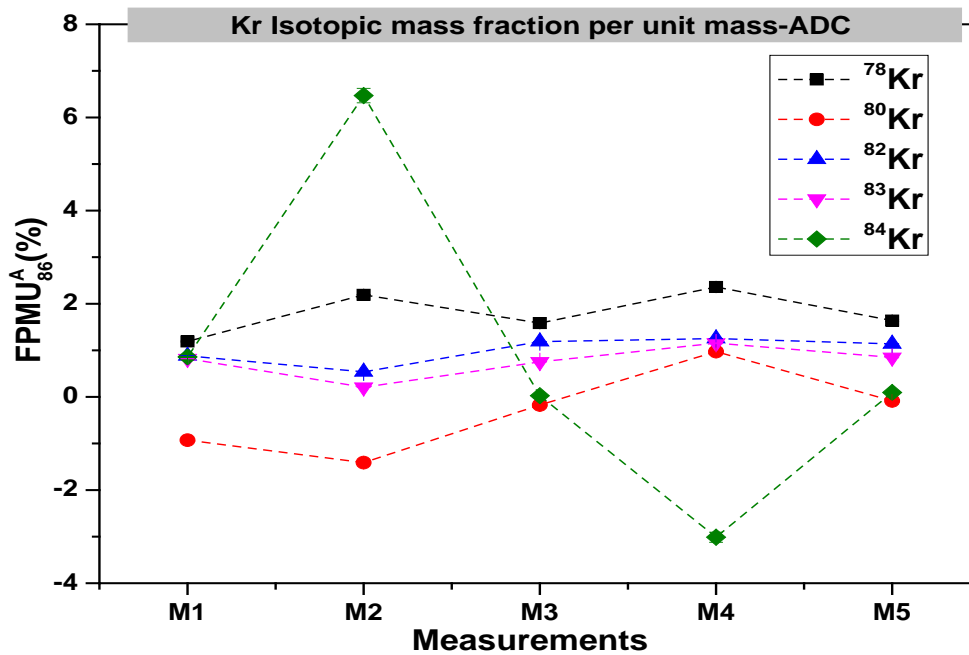


**Figure 7.18:** Measurements of krypton calibration gas using the ADC data acquisition system. Mass dependent fractionation per mass unit for Kr isotopes. The isotopes ratios are normalized to <sup>86</sup>Kr.

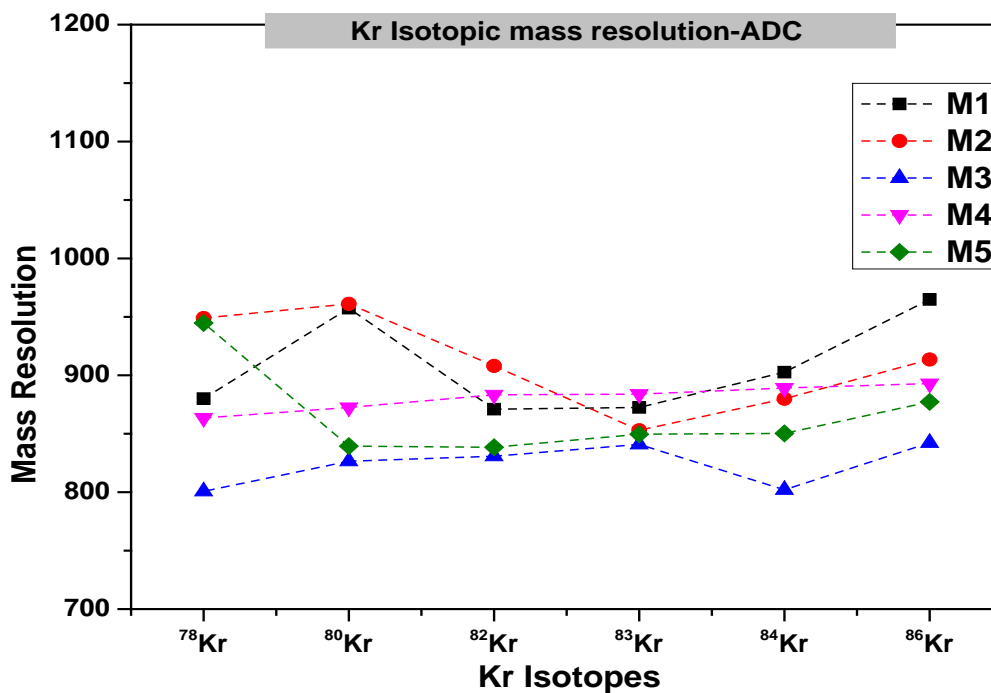


**Figure: 7.19** Mass resolutions of Kr isotopes using ADC measurements. The average mass resolution for all measurements and all isotopes is in the range of 850.

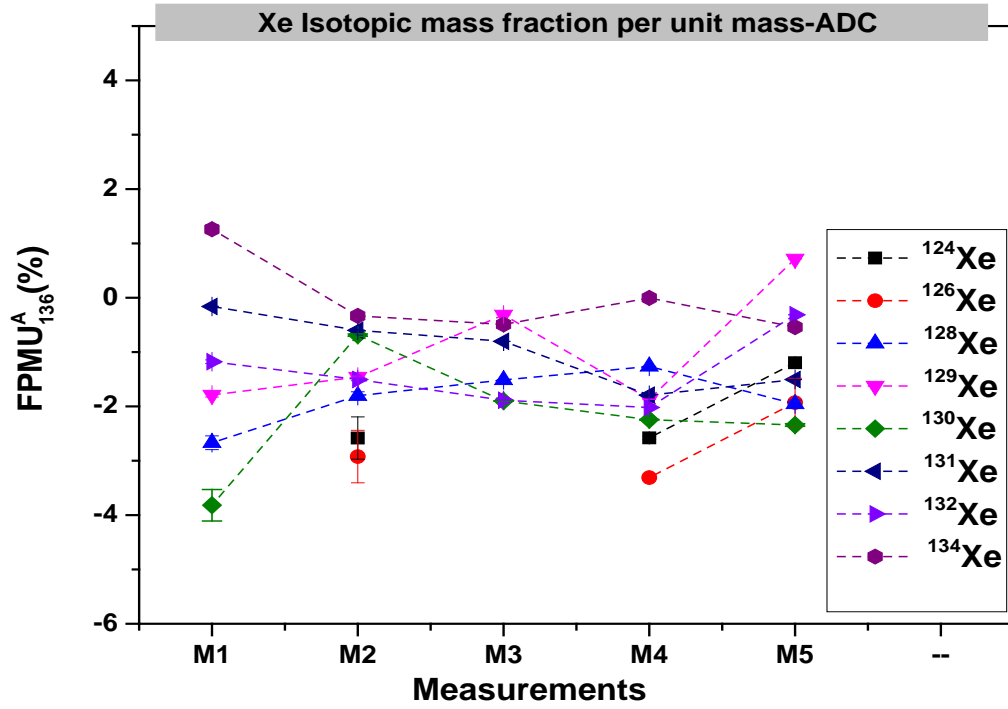


**Figure 7.20:** FPMU for Xenon measurements using the ADC card. The minor isotopes of Xenon,  $^{124}\text{Xe}$  and  $^{126}\text{Xe}$ , were not detected in M1 and M3. The isotopic ratios are normalized to  $^{136}\text{Xe}$ .

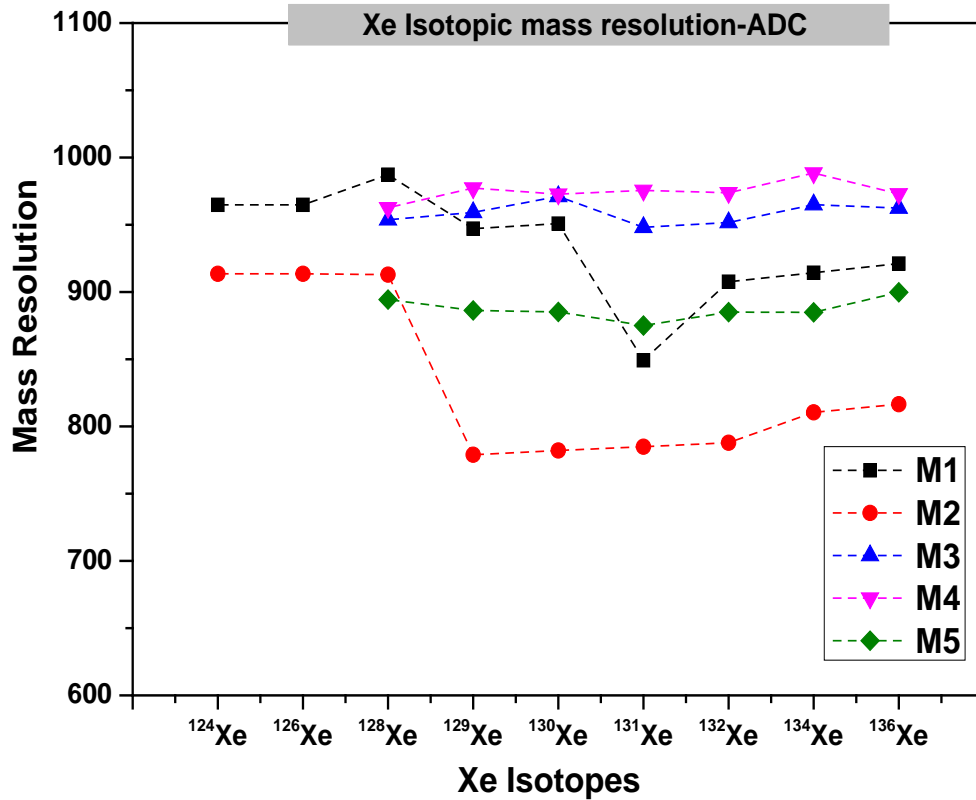


**Figure: 7.21** Mass resolutions of Xe isotopes using ADC measurements. The average mass resolution for all measurements and all isotopes is in the range of 900.

## 7.5.2 Kr and Xe calibrations using the TDC card

### (a) Kr calibrations measurements using the TDC card:

The measurements of the Kr-Xe calibration gas have been done using the FastComTec® time to digital converter. The results are given in this section.

- **Isotopic mass fractionations of Kr**

The FPMU for Krypton isotopes measured using the TDC card in five minutes of acquisition time and 10 kHz pulse frequency are shown in Figure 7.22. Most of the results are more consistent than the data obtained using the ADC measurements. An exception is  $^{84}\text{Kr}$ , even though the  $^{84}\text{Kr}$  peak is similar to the other peaks and no possible interference exists at this mass. For all measurements the  $^{84}\text{Kr}/^{86}\text{Kr}$  ratio is much higher than atmospheric. If there are more than one ion per pulse then it is not possible to detect them with the TDC, but the  $^{84}\text{Kr}$  is having higher ratios than atmospheric which means there is an extra source of ions with the same mass.

- **Kr detection sensitivity**

The detection sensitivity for Kr isotopes is  $\sim 1.5 \times 10^{-14} \text{ cm}^3$  STP for one minute of acquisition time and at 10 kHz pulse frequency.

- **Mass resolution**

Using the TDC card the mass resolution for Kr isotopes is about 1200 (Figure. 7.23), i.e., significantly higher than the mass resolution obtained using the ADC card. The mass resolution using TOF technology depends on the time resolution of the used converter. Since TDC has more resolution (100 ps) than ADC (500 ps).

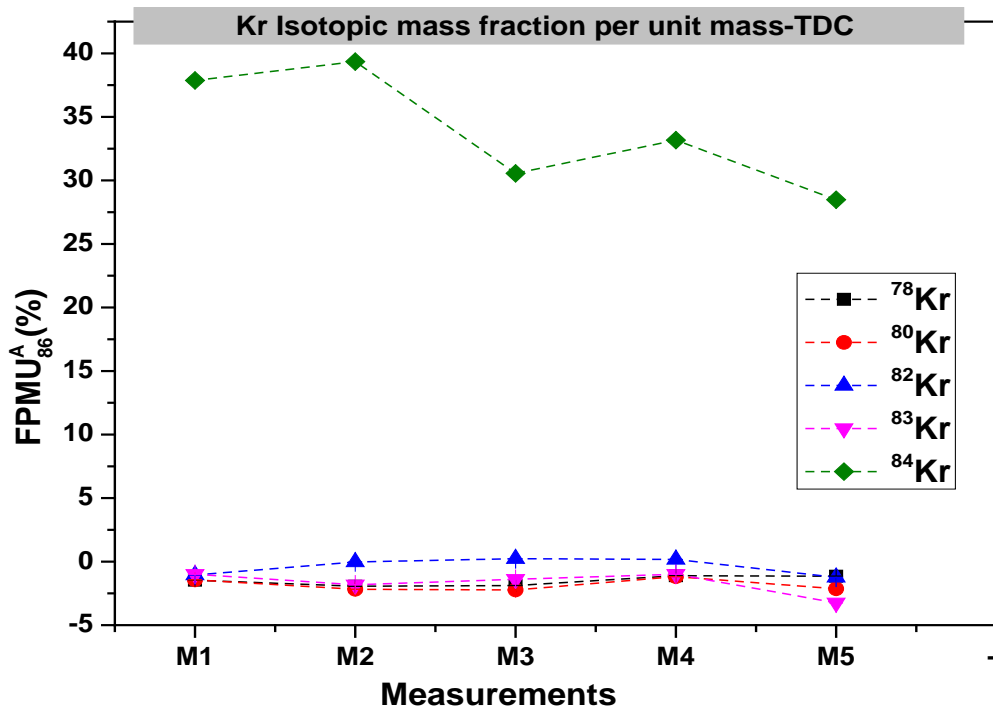


**Figure 7.22:** Measurements of krypton calibration gas using the TDC data acquisition system. The isotopes ratios are normalized to  $^{86}\text{Kr}$ .



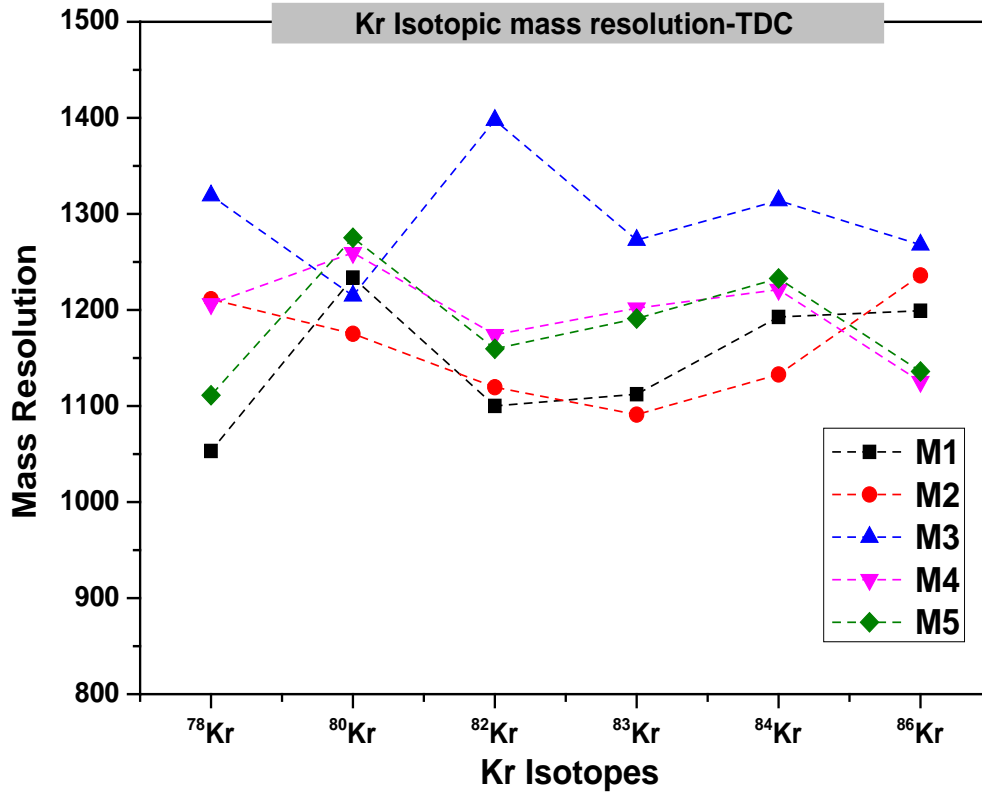


**Figure 7.23:** Mass resolution of Kr isotopes measured using the TDC data acquisition systems.

**(b) Xe-calibration measurements using the TDC card:**

- **Xe isotopic mass fractionations**

In contrast to the measurements using the ADC card, all Xe isotopes could be measured using the TDC card, including the minor isotopes which could not be measured using the ADC card. With a threshold of one mV, 10 kHz pulse frequency, and five minutes of acquisition time the FPMU values are in the range 1% (Figure 7.24).

- **Xe detection sensitivity**

The detection sensitivity for Xe isotopes is around  $3.7 \times 10^{-14} \text{ cm}^3 \text{STP}$  for one minute of acquisition time, 0.85 mV of threshold and 10 kHz pulse frequency.

- **Mass resolution of Xe isotopes**

The mass resolution for Xe isotopes is around 1200 (Figure. 7.25), i.e., again higher than for the ADC card and higher than calculated using the SIMION optical model. The full width half maxima is less in the TDC measurements than ADC due to more time resolution of TDCs.

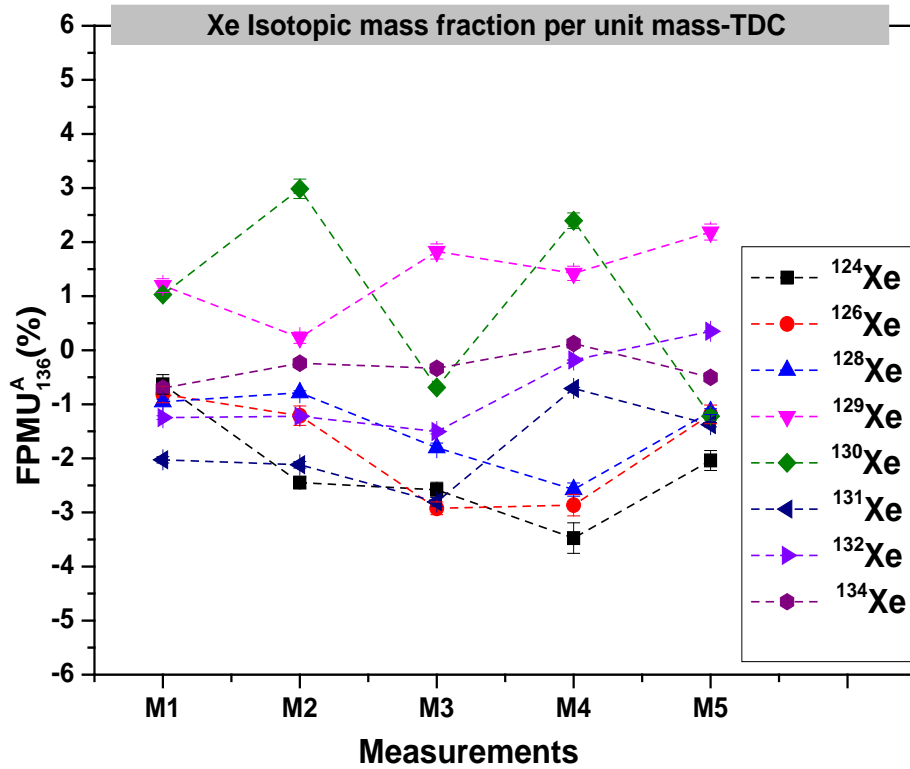


**Figure 7.24:** FPMU for Xe isotopic measurements using the TDC detection system. The isotopes ratios are normalized to  $^{136}\text{Xe}$ .

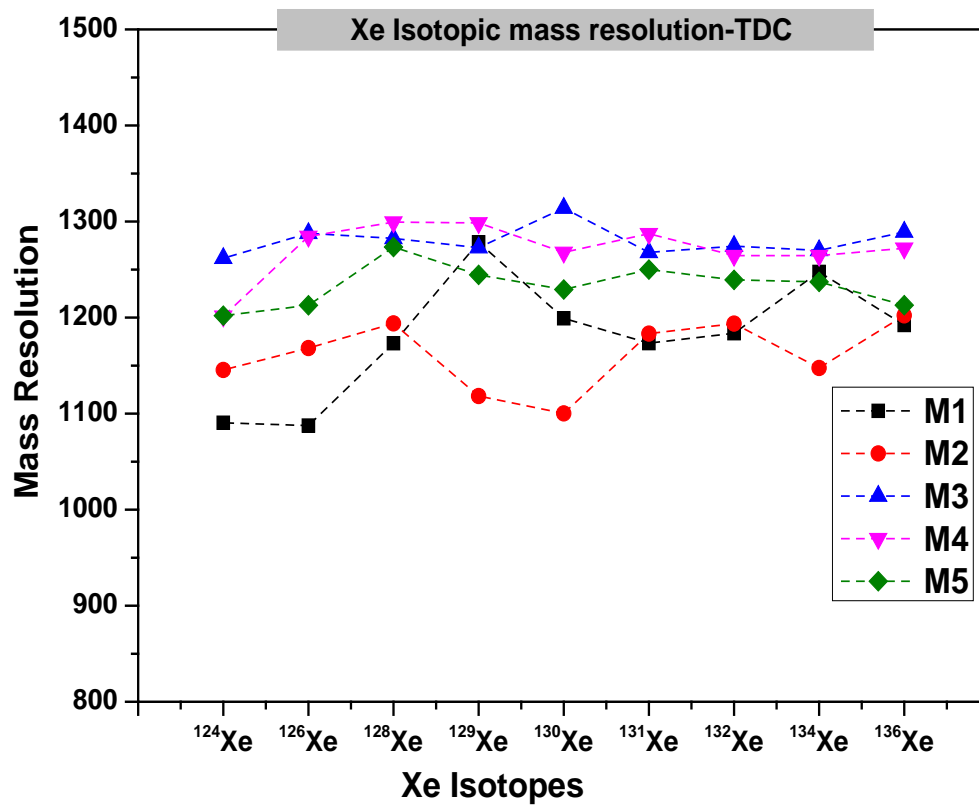


**Figure 7.25:** Mass resolution for Xe isotope measurements using the TDC card

### 7.5.3 Ar calibrations and dilutions

Extensive Ar calibration measurements have been performed to estimate mass fractionation and sensitivity. Each (undiluted) calibration is  $4 \times 10^{-7} \text{ cm}^3 \text{ STP}$  of Ar with atmospheric isotopic composition.

#### (a) Ar calibration measurements using the ADC card:

The Ar measurements clearly indicate that the EGT has some difficulties measuring Argon. It is difficult to measure  $^{38}\text{Ar}$  on a large full scale like 500 mV or 1000 mV, which is required to simultaneously measure the large  $^{40}\text{Ar}$  signal. On other hand it is difficult to impossible to measure  $^{40}\text{Ar}$  on small full scale like 50 mV or 100 mV. The measurements discussed now have been done on the large full scale and the results for FPMU are plotted in Figure 7.26. The FPMU values are in the reasonable range of 1% for  $^{40}\text{Ar}/^{36}\text{Ar}$ . However the mass fractionation for  $^{36}\text{Ar}/^{38}\text{Ar}$  scatters widely, most likely due to the small signal of  $^{38}\text{Ar}$ . The mass resolution for Ar is around 700 and the detection sensitivity is  $\sim 7 \times 10^{-13} \text{ cm}^3 \text{ STP}$  for one minute acquisition time at 10 kHz frequency. Even with the dilutions of Ar calibration gas shows the same behavior.

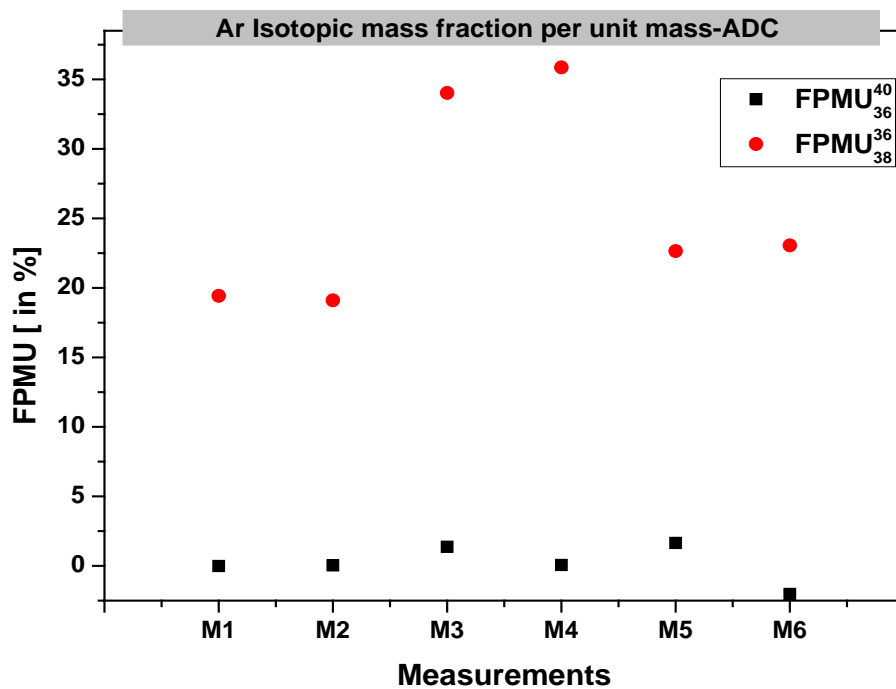


**Figure 7.26:** FPMU for Ar isotopes at 10 kHz pulse frequency and for 5 minutes acquisition time.

#### (b) Ar calibration measurements using the TDC card:

The Argon measurements done using the TDC system show even more unexpected results than the measurements on the ADC system. The results for FPMU are shown in Figure 7.27. The data scatter widely and especially the data based on  $^{40}\text{Ar}$  are difficult to explain.

Note that  $^{40}\text{Ar}$  is not a proper peak but has multiple side peaks. This will be discussed in the next section. However, the results show huge mass fractionations for both  $^{36}\text{Ar}/^{38}\text{Ar}$  and  $^{40}\text{Ar}/^{36}\text{Ar}$  ratios.

**(c) Ar-dilution measurements:**

Ar dilution measurements have been done to test the linearity of the EGT for different gas amounts and also to understand and solve the problems we had with the Argon measurements on the ADC and TDC card (see above). However, also in the Argon dilution series the  $^{40}\text{Ar}/^{36}\text{Ar}$  and  $^{36}\text{Ar}/^{38}\text{Ar}$  ratios are far from atmospheric, indicating massive and therefore unreliable isotopic fractionation. The data are shown in Figures 7.28 and 7.29.

The multi peak problem is as shown in the Figure 7.30 for successive dilutions of Ar calibration gas. These kinds of problems may occur in the TDC measurements due to dead time effects and this has also tested for some measurements. However the primary results showed no effect on peak shapes even with dead time and no dead time, and the technical problems with TDC delayed further experiments; therefore more tests have to perform on this. The less ratios of  $^{40}\text{Ar}$  to  $^{36}\text{Ar}$  is showing less value of  $^{40}\text{Ar}$  and it may be due to multiple ions of  $^{40}\text{Ar}$  are reaching at the same time were not able to count on TDC.

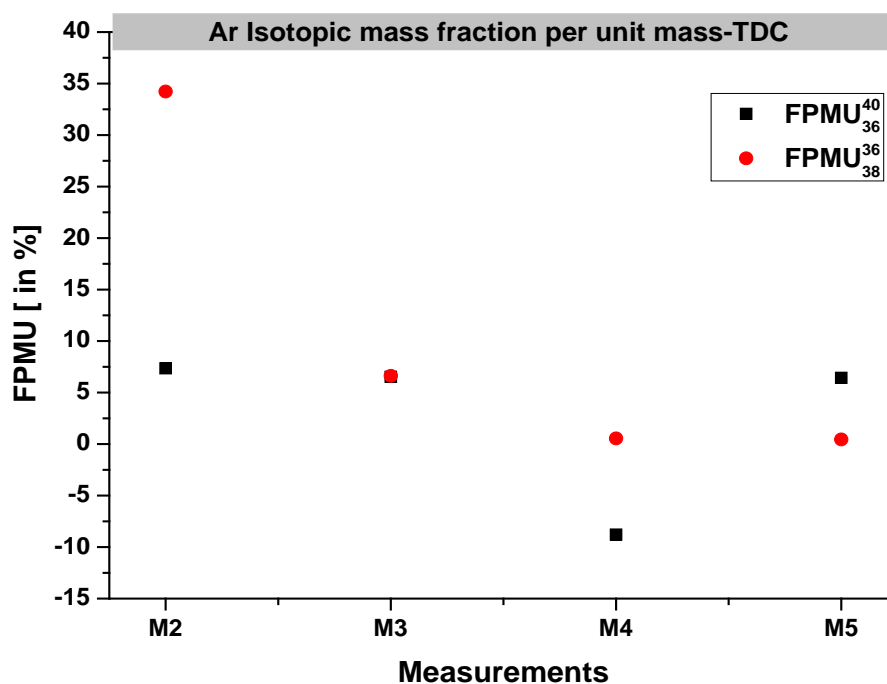


**Figure 7.27:** Mass fractionation for argon isotopes measured at 10 kHz pulse frequency and five minutes of acquisition time on the TDC.

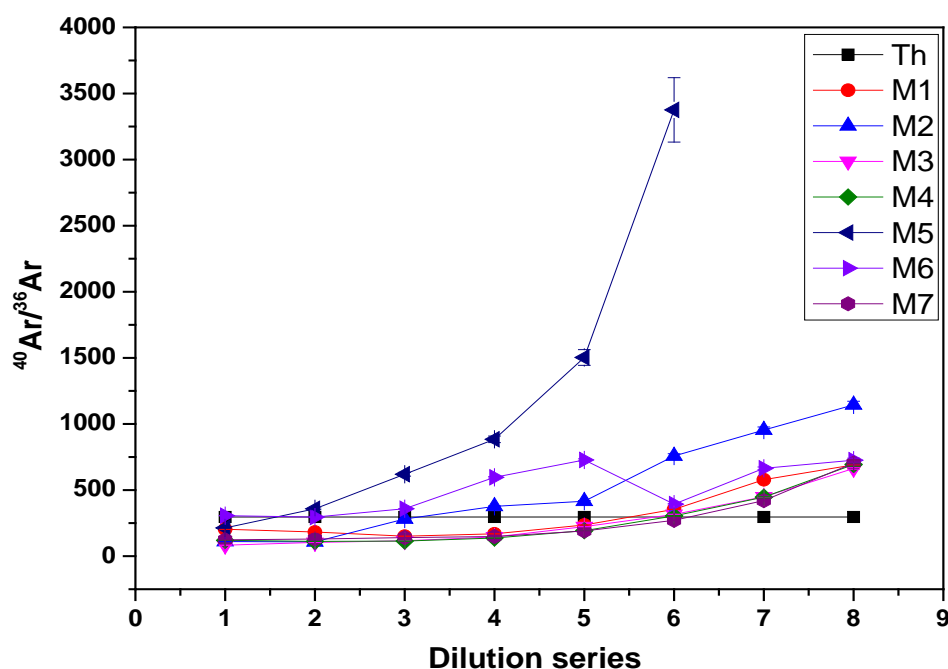


**Figure 7.28:** Isotopic ratio  $^{40}\text{Ar}/^{36}\text{Ar}$  for seven dilution steps. The black line is the theoretical ratio ( $\sim 296$ ); M1, M2, and M3 are for three measurements. The results are completely different for three measurements even though the voltage settings, acquisition time and pulse frequency are same. M4 to M7 are for different voltage settings but for the same time.

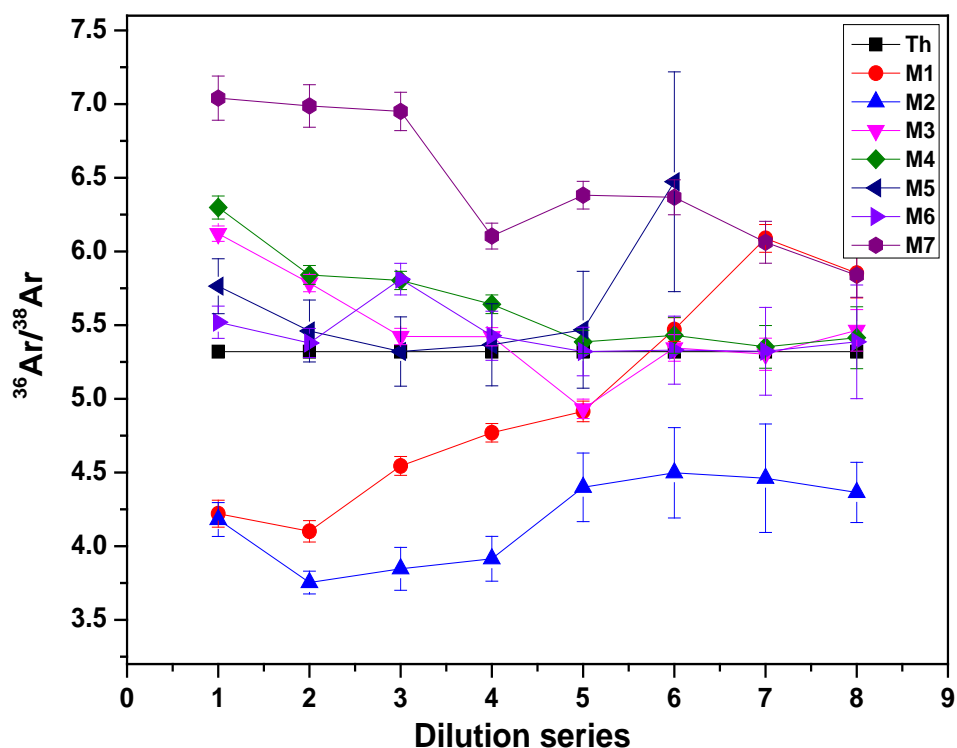


**Figure 7.29:** Isotopic ratio for  $^{36}\text{Ar}/^{38}\text{Ar}$  for seven dilution steps. The black line is the theoretical ratio ( $\sim 5.32$ ), M1, M2, and M3 are for three different measurements. The results are completely different for three measurements even though the settings are same. M4 to M7 are for different voltage settings but for the same time.

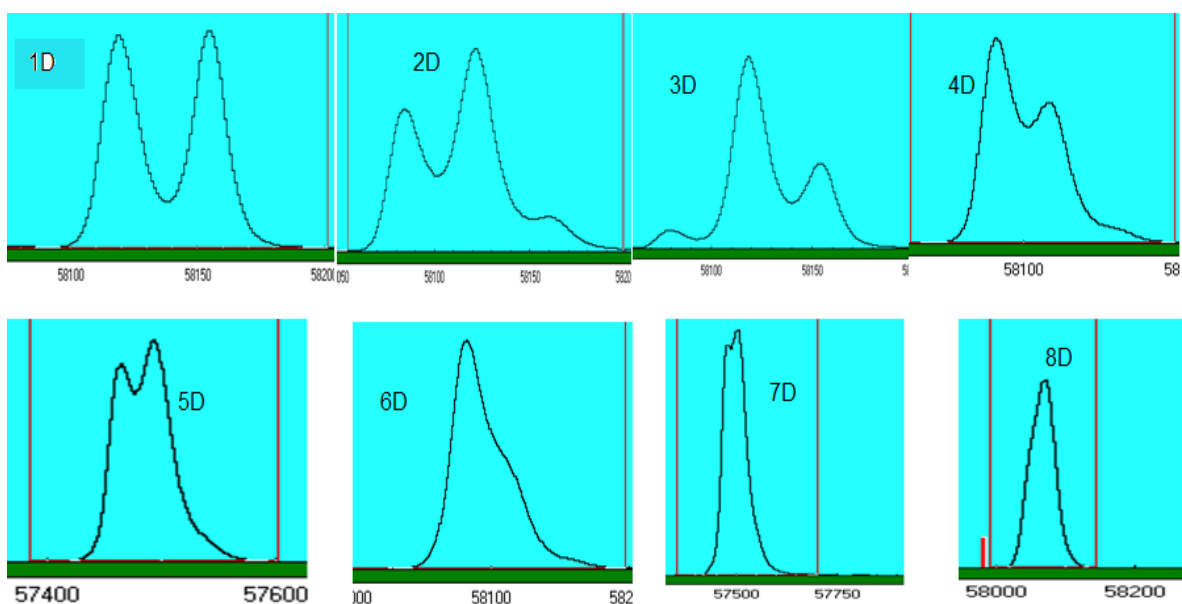


**Figure 7.30:** An example for the multi peak problem and  $^{40}\text{Ar}$  peak for different dilution steps.

The individual isotopic signal for different dilutions series are shown in the Figures 7.31, 7.31 and in 7.32.  $^{36}\text{Ar}$  and  $^{38}\text{Ar}$  have nearly common trend for all the dilutions but  $^{40}\text{Ar}$  shows several trends for different dilutions which is due to multi peak issues. The signal area is decreased with dilution steps in the case of  $^{36}\text{Ar}$  and  $^{38}\text{Ar}$  isotopes which is understandable due to loss of gas in each dilution, however the slopes are not same. The measurement four is showing increase at the beginning due to mistake in the measurement.

On other hand  $^{40}\text{Ar}$  area with respect to the dilution series shows various trends, the area is calculated by fitting for central peak of multiple peaks expect in the measurement 6 where it is the sum of the all multiple peak areas, which is different trend on the plot. This is done due to the central peak has only 2 ns or less than 2 ns pulse width, whereas the other all peaks are 3.8 ns pulse width. If we see the width of all multiple peaks it is around 3.8 ns. However the isotopic ratios are not comparable with the atmospheric ratios.

#### **Linearity behavior of the EGT:**

Argon dilution measurements are also used to study the linearity of the mass spectrometer, i.e., the sensitivity for different gas amounts. Figure 7.34 shows the signal intensity for the different dilution steps, i.e., for different gas amounts. . The signal area with respect to the dilution series for  $^{36}\text{Ar}$ ,  $^{38}\text{Ar}$  and,  $^{40}\text{Ar}$  are shown that the slopes for  $^{36}\text{Ar}$  and  $^{38}\text{Ar}$  are close but not same. The slope for  $^{36}\text{Ar}$ ,  $^{38}\text{Ar}$  and  $^{40}\text{Ar}$  are -0.25, -0.18 and -0.04 respectively. Even though the slopes for  $^{36}\text{Ar}$  and  $^{38}\text{Ar}$  also close but not same, on other hand the slope for  $^{40}\text{Ar}$  is completely different. However more tests are needed with different gas dilutions and for different frequencies to confirm or disproof linearity.

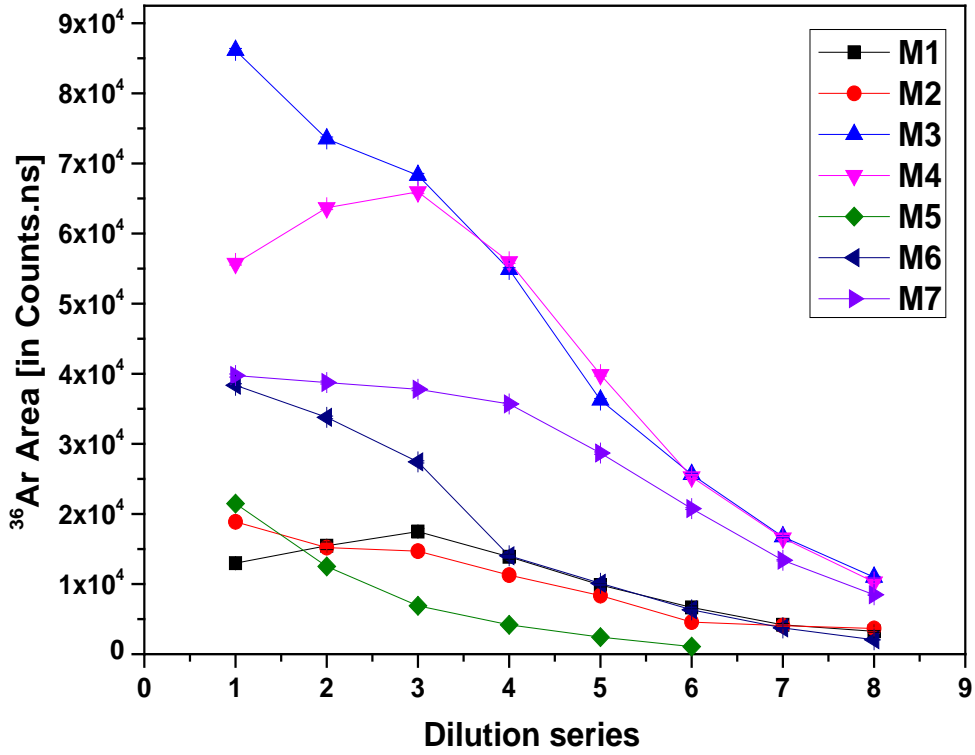


Figure 7.31: Signal area versus dilution series for  $^{36}\text{Ar}$  for different measurements.

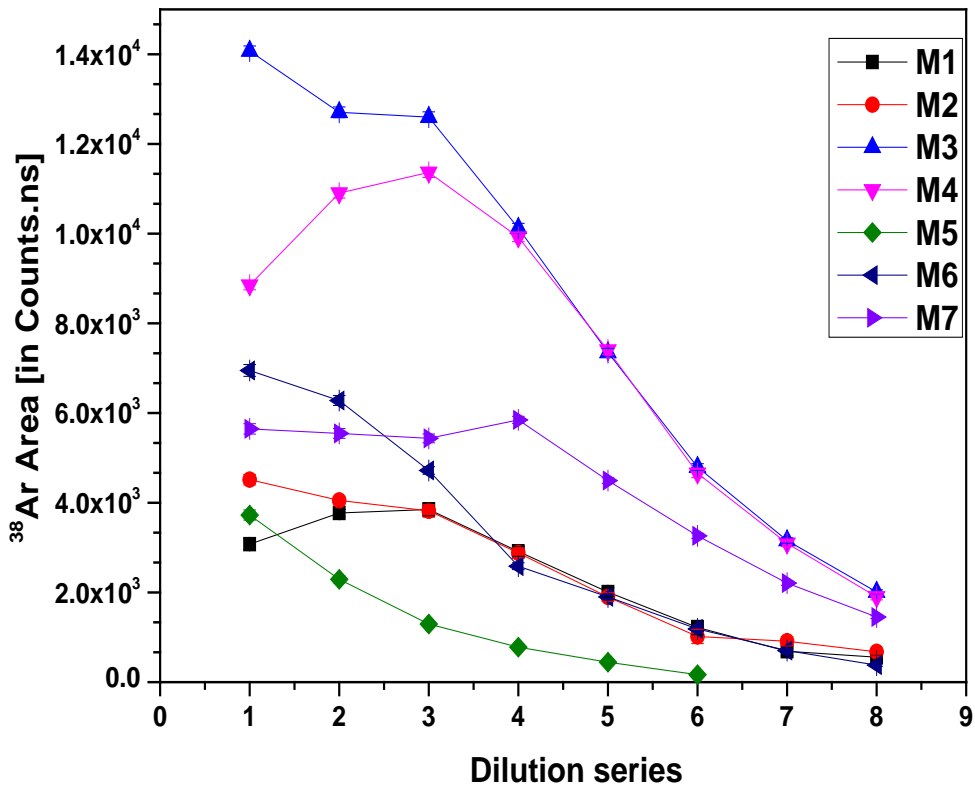


Figure 7.32: Signal area versus dilution series for  $^{38}\text{Ar}$  for different measurements.

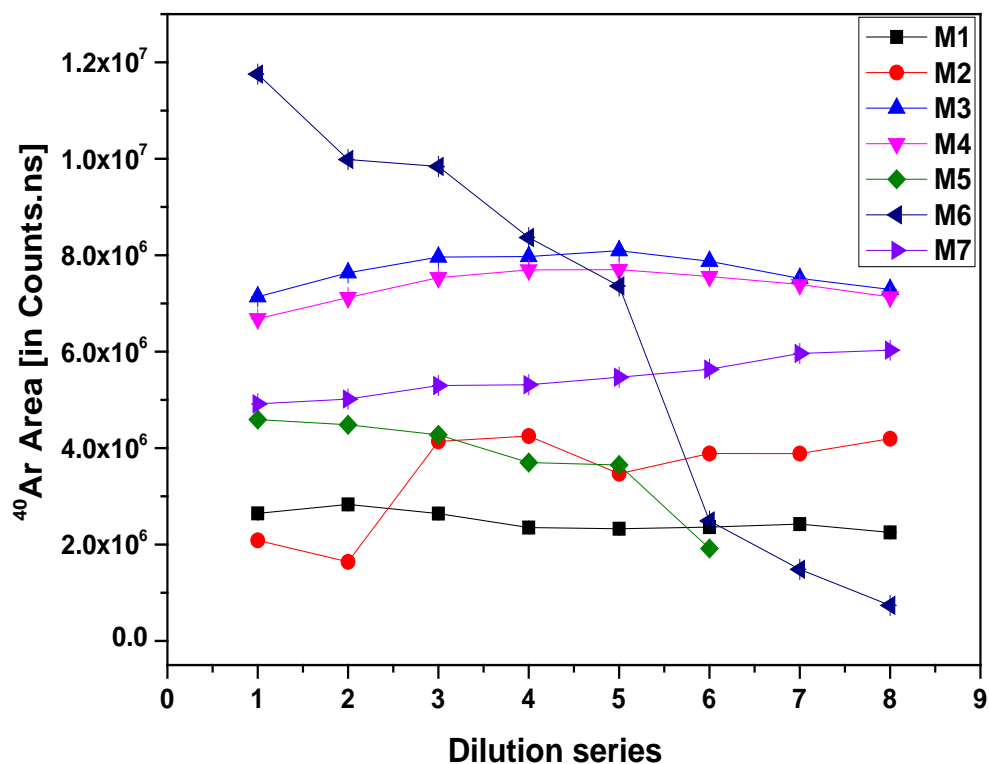


Figure 7.33: Signal area versus dilution series for  $^{40}\text{Ar}$  for different measurements

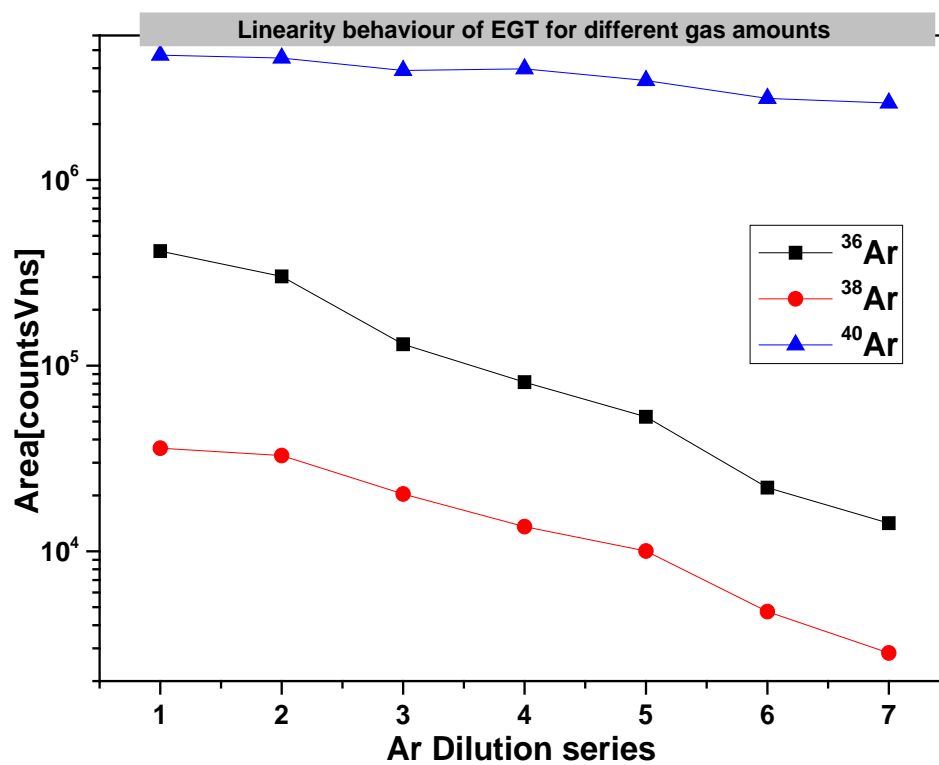
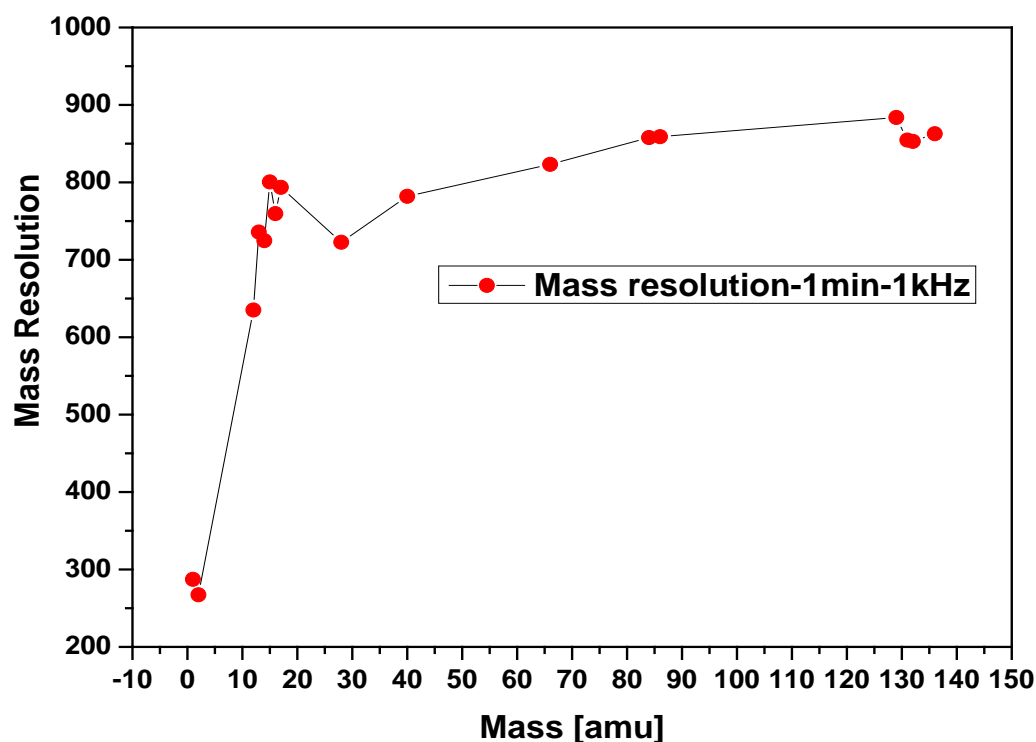


Figure 7.34: Signal intensity for the dilution series for Argon calibration gas at 10 kHz pulse frequency.



## 7.6 Mass Resolution of the whole mass range

Mass resolution at the FWHM-level of the EGT for the whole mass range is measured using the ADC acquisition is shown in the Figure 7.27 for one minute of data acquisition and 1 kHz pulse frequency: it increases and saturates ~850 and this value is more than the mass resolution in the simulations (~700). The dip in the plot mass 28 amu is due to interference with other peaks make it wider peak than usual.



**Figure 7.35:** Mass resolution of EGT for mass range from 1 amu to 150 amu.



## Chapter 8 : Summary & Outlook

### Summary:

The primary goal of the EGT was to achieve a high sensitivity and measuring all noble gas isotopes with a high accuracy. However various technical problems delayed the progress and understanding the performance of the instrument took much longer than anticipated. Nevertheless, some results of this PhD are unexpected and are difficult to understand and to interpret.

First, the mass resolution of the instrument is  $\sim 1000$ , which is higher than the mass resolution determined in the simulations ( $\sim 700$ ). In addition, the mass resolution depends on the data acquisition system; using the TDC data acquisition system the mass resolution is higher than by using the ADC data acquisition system.

Second, the EGT can either be tuned manually or by using the optimizer software, both approaches give essentially the same results. For tuning, the optimal setting for the backplane voltage in the source depends on the pulse frequency, which must be considered for optimal performance. Consequently, a change in the pulse frequency requires at least some re-tuning. Peak shape and peak symmetry mostly depend on the drift voltage and the reflectron voltages R15 and R16.

Third, strange and unexpected results are obtained for the mass fractionation per mass unit (FPMU), which is an important parameter for a discussion of instrument performance and reliability of the measurements. The results depend not only the type of gas measured but also on the data acquisition system used. The results obtained with the ADC system are different for Ar, Kr, and Xe isotopes. For Kr calibration the FPMU is  $\sim 1\%$ , except for  $^{84}\text{Kr}/^{86}\text{Kr}$  where it is higher. For Xe isotopes it was difficult measuring the minor isotopes, however, for the isotopes that could be measured the FPMU was also in the range  $1\%$ . Measuring Argon isotopes was difficult because setting the scale to properly measure  $^{38}\text{Ar}$  overloads the signal on  $^{40}\text{Ar}$  and if the scale is set to properly measure  $^{40}\text{Ar}$ , the  $^{38}\text{Ar}$  signal is hardly any larger than the background noise.

An improvement for the measurement of Krypton and Xenon isotopes could be achieved by using the TDC detection system. The FPMU values were smaller and more constant for the different isotope ratios, except  $^{84}\text{Kr}/^{86}\text{Kr}$ , and also the minor isotopes could be measured. However, besides the better performance for Kr and Xe, measurements using the TDC card show unexpected and not understood fractionation pattern for Argon isotopes. In addition, the peak shape depends on the gas amounts and has in worst case a double or triple peak structure.

Fourth, the detection sensitivities for Kr and Xe are  $\sim 10^{-14} \text{ cm}^3 \text{ STP}$ . For Argon the detection sensitivity is  $\sim 10^{-13} \text{ cm}^3 \text{ STP}$ , which is in all cases at least one order of magnitude lower than expected.

In addition to the EGT performance tests, in the third chapter of this dissertation the oxidation of nanodiamonds by using copper oxide is discussed and first results and tests for different grains sizes of copper oxide are given. The copper oxide with larger grain size will release sufficient oxygen for oxidation of any organic material while heating and will re-absorb more than 90% via cooling.

### **Outlook:**

Since one of the reasons for the unexpectedly low sensitivity of the EGT could be the reduced gain of the already used MCPs and preliminary tests showed - for the now replaced MCPs - that there is indeed an increase in gain, we anticipate an improve in overall performance of the EGT. We hope that the detection sensitivity can also be improved using better settings of the ADC and TDC cards and these will also improve the results for the FPMU. In addition, using a higher bit ADC detection system, e.g., 10 bits compared to 8 bits, would significantly improve the detection sensitivity for minor isotopes. By Studying dead-time effects introduced by the MCPs and also by the TDC detection system we might understand better the multiple peak problems for  $^{40}\text{Ar}$  measurements. Overall, the optimizer results of future tests, with the stable power supplies and new MCPs will increase the performance of the EGT in the future.

## Appendix A

### A.1 Copper Oxide Combustion for Oxygen production

The separated nanodiamonds have to be oxidized to CO and/or CO<sub>2</sub>. During this process the noble gases are released. Note that released of noble gases from refractory carbon phases without oxidizing them is extremely difficult and requires extremely high temperatures and long extraction times. In the combustor, Copper (II) oxide (CuO) is used as the source of oxygen.

#### Procedure:

Step 1: The pressure in the combustor should be in the range  $10^{-9}$  mbar before starting the combustion.

Step 2: Valve 9 should be closed and valves 1, 2, 3, 4, 5, 6, 7, and 10 should be open (see the Figure Ap.3.1 below).

Step 3: Heat the CuO up to 200°C (increase temperatures slowly in 50 °C per 5 minutes), observe the pressure variation in the Pirani gauge (CH-1). T Pirani gauges starts reading pressures above  $5 \times 10^{-4}$ ; for lower pressures it shows under range (ur-under range). Heating and pumping should last at least two days to release all residual/dirt gases. Wait for a constant pressure in the combustor in the  $\sim 10^{-9}$  mbar.

Step 4: When the pressure in the combustor is  $\sim 10^{-9}$  mbar, close the valve 10 (the other valves stay in the same position)

Step 5: close getter valves 3, 4, 5, and 6 to protect the getters from the high oxygen pressures.

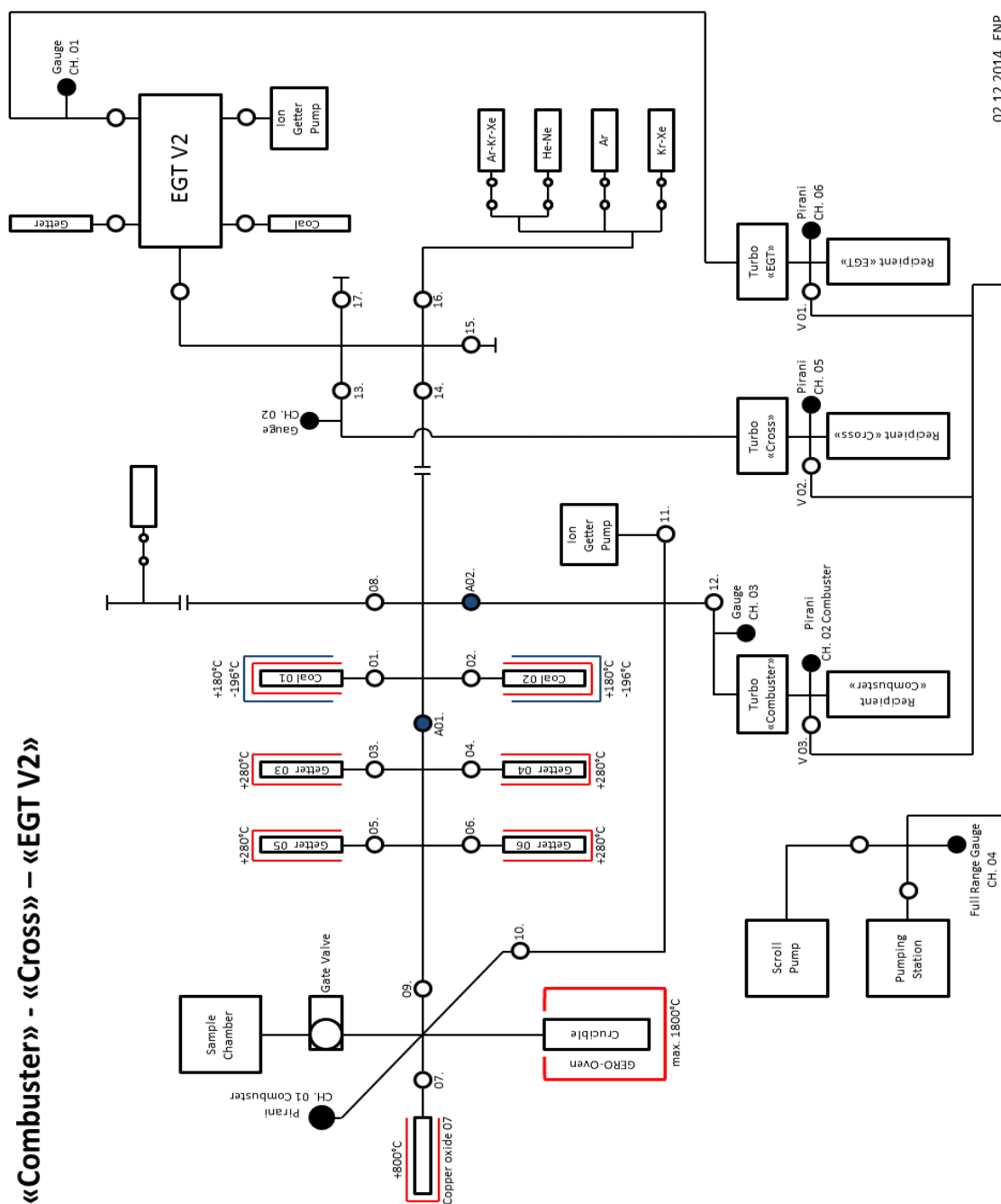
Step 6: Heat CuO crucible to 860°C in 50°C steps (use channel 7 on the control unit. Do not go beyond 900 °C. Check the pressure reading of the Pirani gauge (channel 1)

Step 7: Cool down the CuO crucible from 860 °C to 200 °C in 50 °C steps.

Step 8: Open valve 10 to pump the remaining oxygen with the turbo pump.

Step 9: Open the valves 3, 4, 5, and 6 and pump the getters

## «Combuster» - «Cross» – «EGT V2»



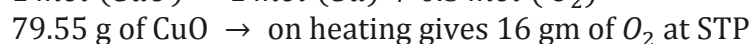
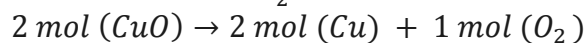
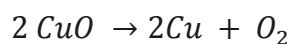
02.12.2014, ENP

Figure Ap-3.1: Schematic diagram of the combustor and the EGT

## Appendix A.2: Amount of CuO for 10 mbar of oxygen

The stoichiometry of this reaction: How many grams of CuO is required for producing 10 mbar of O<sub>2</sub> in a volume of 500 ml?

Sol:



\*\*\*\*\*

# 1 mol of gas fills - at standard temperature and pressure (STP) - a volume of 22.4 l  
therefore

0.5 mol of O<sub>2</sub>-gas fills at STP a volume of 11.2 l

\*\*\*\*\*

79.55 g of CuO gives 11.2 l of oxygen at 1 atm pressure, therefore 3.55 g CuO gives 0.5 l of O<sub>2</sub> at 1 atm pressure.

3.55 g → 500 ml at 1 atm = 1.01325 bar

500 ml at 1 atm = 1.01325 bar

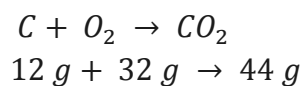
Therefore,

0.0355 g → 500 ml at 0.0101325 bar (~ 10 mbar)

Therefore we need about 35.5 mg for about 10 mbar of O<sub>2</sub>

### Appendix A.3: Amount oxygen required of oxidation

Oxygen (pressure) required for oxidize 1 mg of nanodiamonds in 500ml of oven chamber. ?



Therefore, we need 2.6 mg of O<sub>2</sub> to fully oxidize 1 mg of carbon, 1 mol of gas at STP fills a volume of 22.4 l (22400 ml), therefore 32 g of O<sub>2</sub> fills at STP a volume of 22.4 l. Consequently, 2.6 mg, the amount required to oxidize the carbon, corresponds to  $8.1 \times 10^{-5}$  mol  
With

$$\begin{aligned}PV &= nRT \\P &= \frac{nRT}{V}\end{aligned}$$

$$(R = 0.082 \text{ L atm K}^{-1} \text{ mol}^{-1})$$

$$P = \frac{8.1 \times 10^{-5} \times 0.082 \times 300}{0.5}$$

$$\begin{aligned}&= 398 \times 10^{-5} \text{ atm} \\&= 4.03 \text{ mbar}\end{aligned}$$

i.e., ~4.03 mbar of O<sub>2</sub> is required to oxidize 1 mg of nanodiamonds in a volume of 500 ml.



# Appendix B

## Appendix B.1: TDC hardware

TDC-MCS6 hardware installation procedure is available in **MCS6 user manual, (2012)**, and the drivers and firmware is available from the FastCamTec® website.

### TDC Software settings for measurements:

1. Open MCS6 software on the desktop, it opens mcs6 GUI window (MPANT-MCS6) as shown in Figure 4.A.1 if everything is connected and power is on; otherwise it shows a pop-up message “MCS6 not found or device drivers are not installed”.

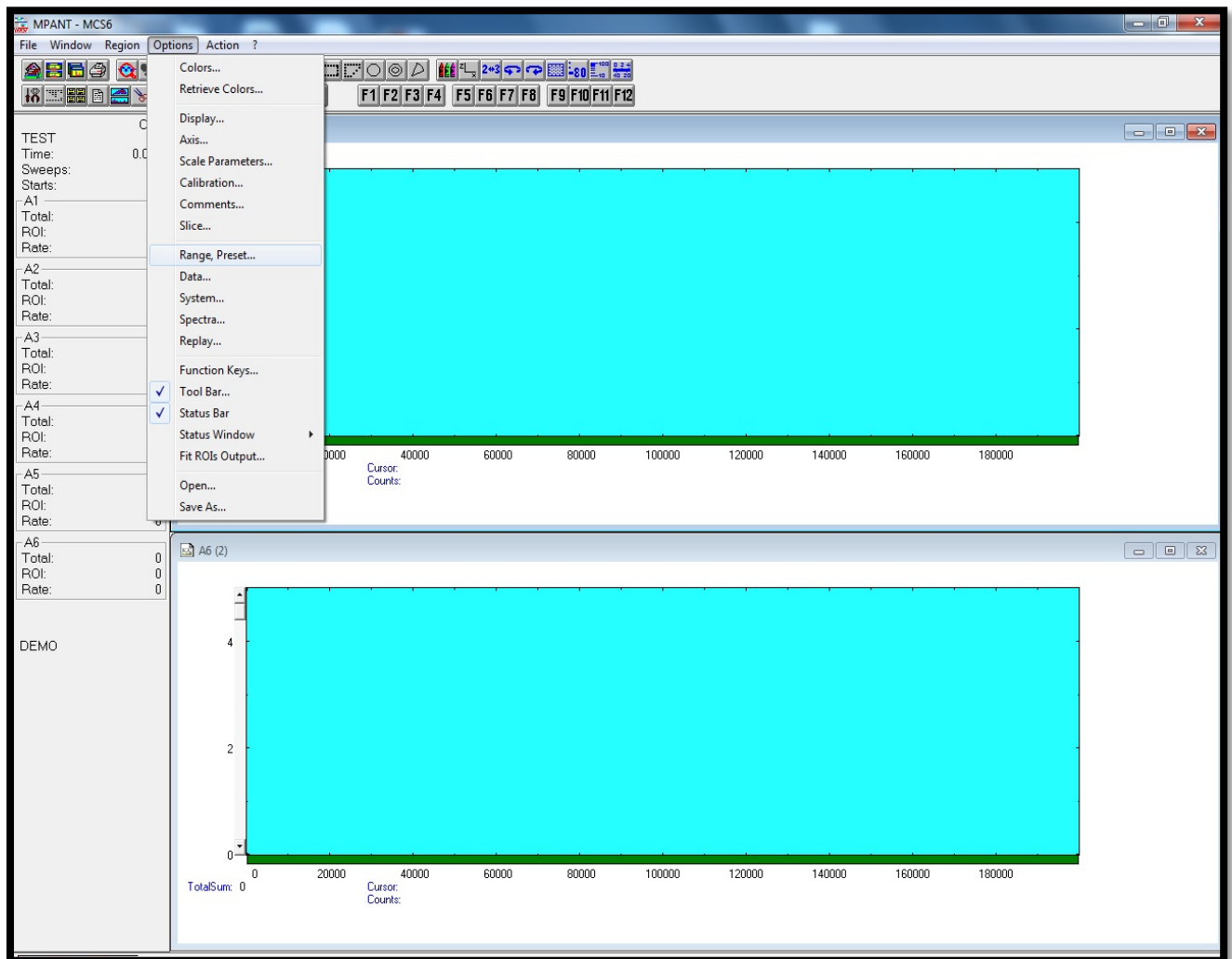


**Figure 4.A.1:** MCS6 TDC graphical user interface

2. Click on ‘Options’ and select “Range, Preset”, it opens another window “MCS6 settings” as shown in the Figure 4.A.2.

- 2.1. Select 'Inputs' on MCS Settings window and open "Input Thresholds and ROI Presets" window
- 2.2. Select CH6 and Ch1 (Since EGT anode signal and external pulser are connected to CH1 and Ch6 respectively)
- 2.3. No Threshold for CH6 and select Threshold value for CH1.
- 2.4. Select 'Edge' as Rising on both and also select "Start with rising edge". For Pulse with mode, select "Under threshold" or Upper threshold.
- 2.5. Click on 'Ok'
- 2.6. Select "Timepreset" value, this is time of measurement.
- 2.7. Select "Bandwidth" as 1 for maximum resolution.
- 2.8. Select Range as 200000 (this corresponds to 20  $\mu$ s), this covers all the mass range we need.
- 2.9. "End of Sweep(s)" time sets automatically to 2.00064e-005 when "Endless" mode is not active; otherwise it sets to 0 s.
- 2.10. Set Acq.Delay (ns) if necessary, this corresponds to acquisition delay.
- 2.11. Set Hold aft.Sweep (ns) if necessary. This is "hold off" time after each sweep.
- 2.12. Click 'Ok'
- 2.13. Click "Action", press "Start" and it start live display on CH1 window.
- 2.14. To save the data file after data acquisition press "Options" and select "Data".

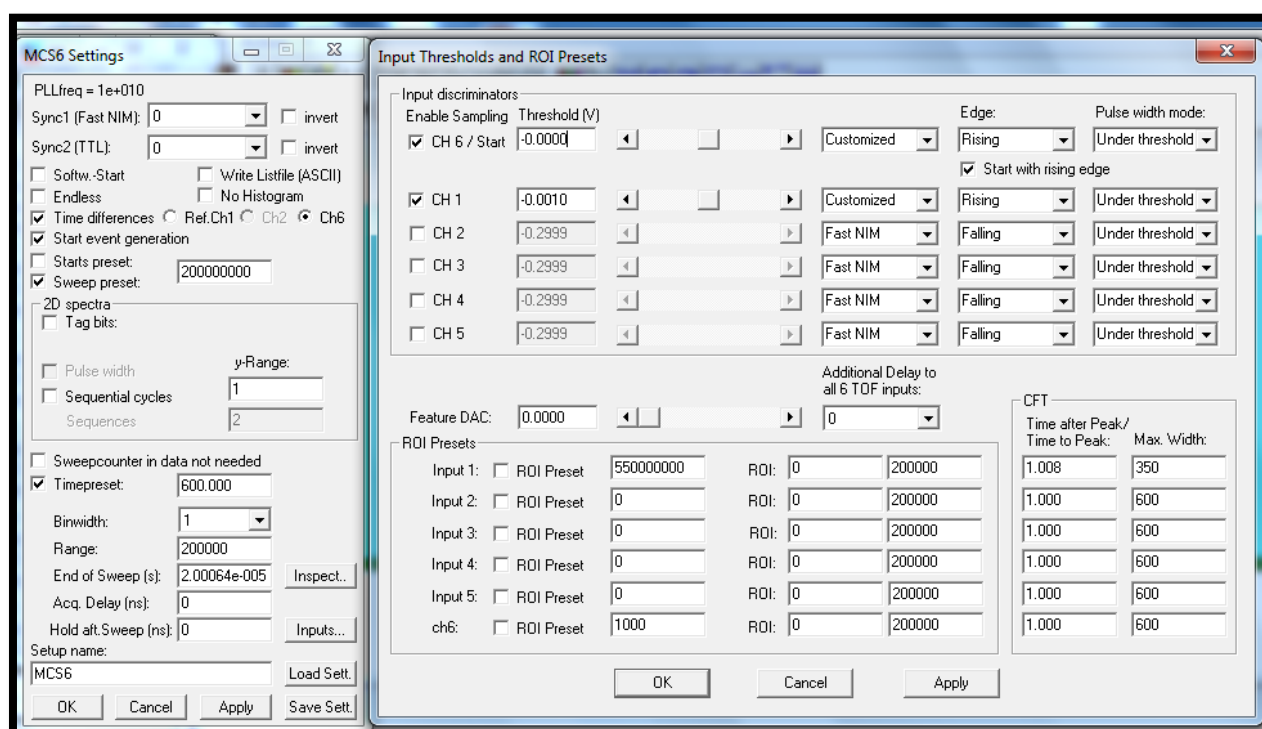


**Figure 4.A.2:** MCS6 Settings window

- 2.15. “Data operations window” consists several options as shown in the Figure4.A.3.

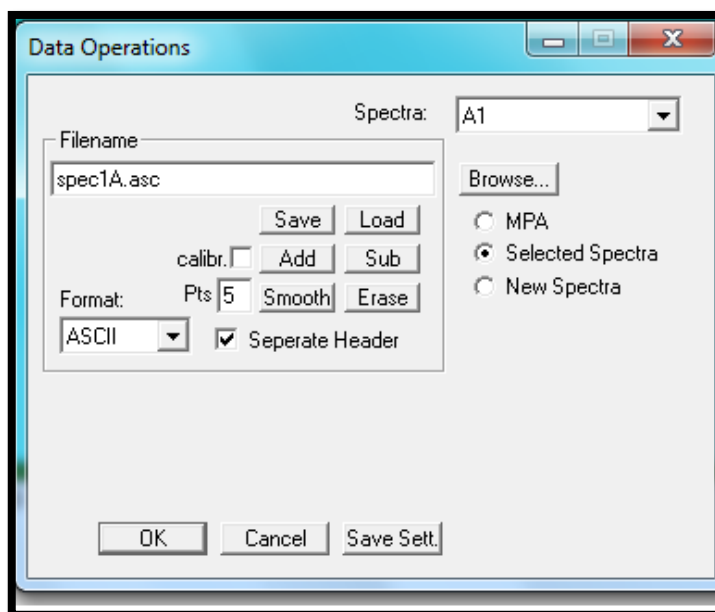


**Figure 4.A.3:** Data operations window of MCS6

- 2.16. Select the spectra need to save and press “Save”, Press “OK”.

## Appendix B.2: ADC hardware

ADC- Agilent U1082A hardware installation settings are available in Acqiris manual (2010) and the drivers and firmware are available from the **acqiris** website.

Internal temperature of the device is displayed on the “Waveform Display” window. Temperature is one of the influencing factors on base noise of the spectra. Increase in internal temperature will increase the noise level. In addition to this maximum operating voltage of ADC is  $\pm 5$  V. We are using a limiter to cut the signals which are more than 5 V to protect ADC from the damage. Other specifications and details about ADC can find in user manual.  
**ADC Software Settings for measurements:**

1. Open “Acqiris Live” software on the desktop, it opens window “Instrument Control”

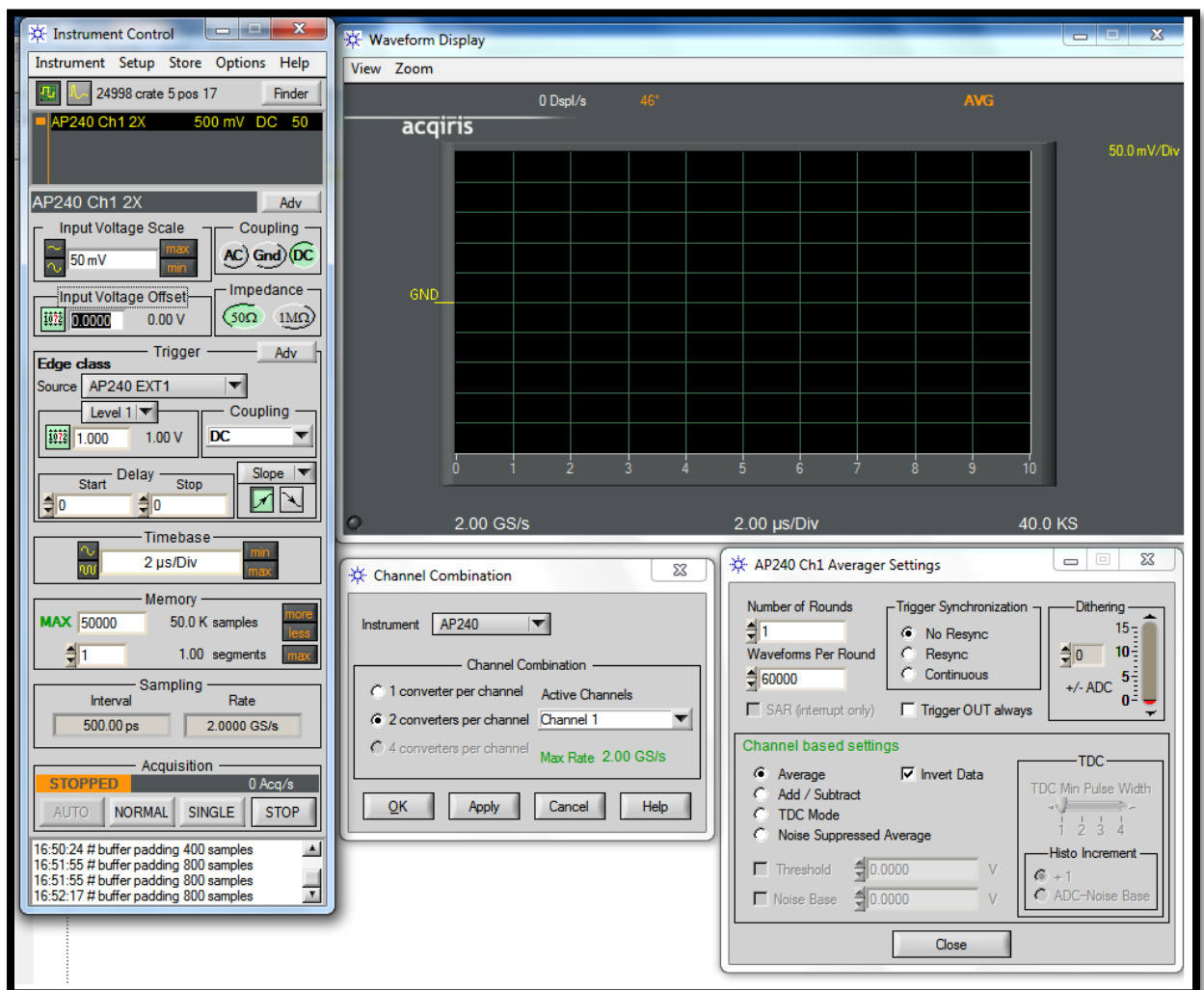


**Figure 4.B.1:** Main GUI window of “Acqiris Live” software and other pop-up windows

2. Click on “instrument”, select “averager”
3. Click on “Options”,

- 3.1. select “combined channels”, it opens pop-up window “Channel Combination”( Since we are using 2 channels)
- 3.2. select “instrument” AP240 ( our instrument model is “AP240”)
- 3.3. select “2 converters per channel” and “channel 1” in in drop down menu of **Active channels**
- 3.4. Press “Apply”
4. Click on “Options”
  - 4.1. Select “averager settings”, it opens pop-up window “AP240 Ch1 Averager Settings”
  - 4.2. Select “Number of rounds” as ‘1’
  - 4.3. Select “Wave forms Per Round” in between 1 to 65,536  
 ADC averager can be used in sequential averaging mode or round-robin sequential averaging mode. In sequential averaging mode is accumulates N number of waveforms in one round and produces a file. In round-robin sequential averaging mode the above process repeats for n- rounds. In our case, we use number of rounds as 1 and wave forms per round as 60000. If we have 1 kHz external pulse frequency it produces 1 spectrum file in one minute. If we use 10000 wave forms per round it produces 6 spectra per minute.
5. Select “ Channel Based Settings”
  - 5.1. Click on “Average” mode (you can also choose other modes of acquisition). We should also give appropriate value for “Threshold” and “Noise Base” if we choose TDC or Noise suppressed average mode
  - 5.2. Select “Invert Data” ( since signal are negative)
  - 5.3. Press “Close”
6. Select “Input voltage full scale” on main window in the range from 50 mV to 5 V and also corresponding “input voltage offset”, it is depending on signal strength.
7. Chose the “Trigger” – “Source” as “AP240 EXT 1” for external triggering and in “Level 1” choose the value in the range  $\pm 2$  V and “Coupling” is DC. Delay is 0 and slope is positive.
8. Select “Time Base” as 2  $\mu$ s which covers 20  $\mu$ s range spectrum (it includes all noble gases)
9. “Memory” settings are the maximum number of points to be acquired, and this could be usually 5M samples and 1 segment. With this the sampling rate interval will be 500 ps and sampling rate (acquisition rate) will be 2 GS/s
10. Click on “Normal” will show the live display on “Waveform Display” window and also zoom features available for this.
11. “Store” menu on main window provides features of data storage. It includes different data format options

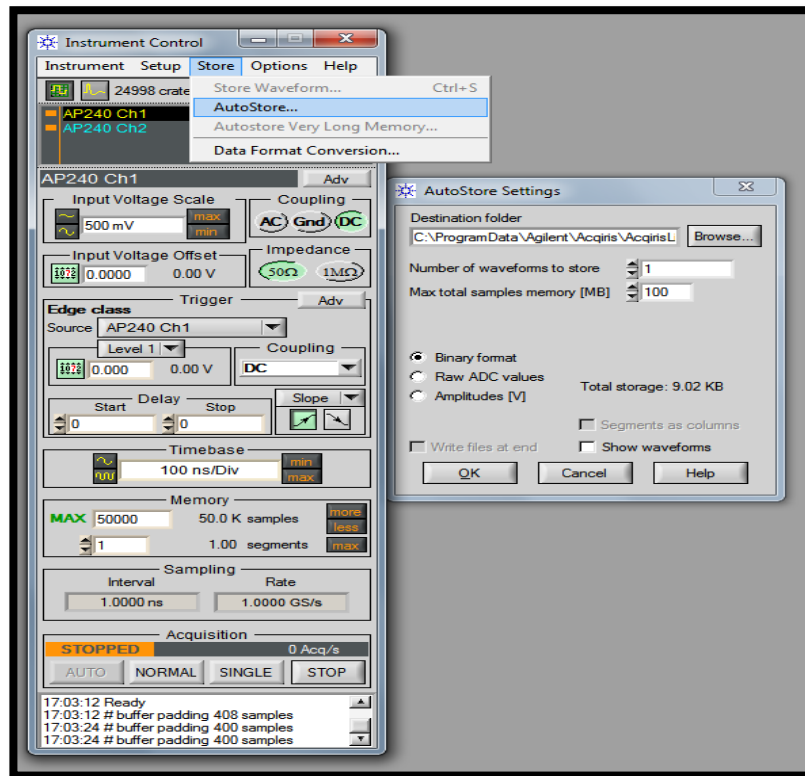


**Figure 4.B.2:** Data store pop-up window

- Select “Number of waveforms to store”, this is the number of files to be created and related to the integration time. For Example, with settings as said in 4.3 above, with 1 kHz external frequency, and 1 round and 60000 waveforms on and 5 for “number of waveforms to store” will take 5 minutes to store and create 5 .awd files in a folder.
- Select “Raw ADC values” which store data file in ASCII format with **.awd** extension. First 19 lines of this files includes different details about the settings like below

```
# c:\Users\ramisetty\Desktop\AcqirisRun_2014-11-09T18-28-11\AP240 Ch1
2X_1.awd
# Date: 2014-11-09T18:28:19
# Number of samples: 40000 S (40.0 KS)
# Time increment: 5.00000000e-10 s (500 ps)
# Gain: 1.95312500e-03 V/LSB (1.95 mV/LSB)
# Offset: 2.38000000e-01 V (238 mV)
# Number of waveforms per average: 60000 Waveforms
# Trigger delay (in samples!): 0.00000000e+00 S (0.00 S)
```

12. These files can be easily accessed by EXCEL or EGTDAS software.

## Appendix C: Glossary

**P-BACE:** Polar Balloon Atmospheric Composition Experiment mission, P-BACE is a joint project between the Esrange Space Center, Sweden, the University of Bern, Switzerland and the Swedish Institute of Space Physics (IRF), Kiruna, Sweden, 2008

**EGT-MS:** Edel Gas Time-of-flight Mass Spectrometer, developed at University of Bern

TOFMS	Time-Of-Flight Mass Spectrometer
keV	kilo electron volts
R-TOF	Reflectron time-of-flight mass spectrometer
EI	Electron Impact Ionization
MCP	Micro channel plates
SEM	Secondary Electron Multipliers
TDC	Time-to-digital converter
ADC	Analog to digital converter
GHz	Giga Hertz
LSB	Least significant bit
SNR	Signal to noise ratio
Chevron	Special configuration of MCP's
Th	Thomson, unit for amu/q
TOF	Time-Of-Flight
SIMION	Ion & electron Optics Simulator Computer Program
EGT-DAS	EGT Data analysis software
STP	Standard Temperature and Pressure
GS/s	Giga Sample per second
FWHM	Full width half maxima
MoRaMi	Modular Rack Measurement Instrument
CF	ConFlat vacuum flanges

## D: References

- 1 **Guilhaus M**, (1995). Principles and Instrumentation in Time-of-flight Mass Spectrometry, JOURNAL OF MASS SPECTROMETRY, VOL. 30, 1519-1532 (1995)
- 2 **Urs Rohner**, James A Whitby and Peter Wurz A miniature laser ablation time-of-flight mass spectrometer for in situ planetary exploration Meas. Sci. Technol. 14 2159
- 3 **Verchovsky A.B.**, (1998). Separated grain size fractions of presolar diamonds from Efremovka Insight into their origin from nitrogen, carbon and noble gas isotope data, Faraday Discuss., 1998, 109, 403-416
- 4 **Abplanalp D**, (2009). "A neutral gas mass spectrometer to measure the chemical composition of the stratosphere", J. Adv. Space Res., 44, 870-878, 2009
- 5 **Abplanalp D**, (2009). Development of a sensitive ToF-Mass Spectrometer for Space Research, PhD thesis University of Bern
- 6 **Abplanalp D**, Peter Wurz, Liliane Huber, Ingo Leya, (2010) An optimised compact electron impact ion storage source for a time-of-flight mass spectrometer International Journal of Mass Spectrometry 294 (2010) 33-39,
- 7 **Acqiris Manual, AP240**, (2010). Agilent Technologies. User Manual: Agilent Acqiris U1084A. June 2, 2010, Release 1.1, U1092-90031
- 8 **Agilent**, (2011). Signal, Noise, and Detection Limits in Mass Spectrometry, Technical note.
- 9 **Agilent Acqiris**, (2012). USER MANUAL AGILENT ACQIRIS AVERAGERS Models covered: AP235/AP240 with Avgr U1082A-AVG AP100/AP200 U1081A <http://literature.cdn.keysight.com/litweb/pdf/U1092-90011.pdf>
- 10 **Balsiger H**, Altwegg K., Bochlser P., Eberhardt P., Fischer J., Graf S., Jäckel A., Kopp E., Langer U., Mildner M., Müller J., Riesen T., Rubin M., Scherer S., Wurz P., Wüthrich S., Arijs E., Delanoye S., De Keyser J., Neefs E., Nevejans D., Réme H., Aoustin C., Mazelle C., M'Edale J.-L., Sauvaud J. A., Berthelier J.-J., Bertaux J.-L., Duvet L., Illiano J.-M., Fuselier S. A., Ghielmetti A. G., Magoncelli T., Shelley E. G., Korth A., Heerlein K., Lauche H., Livi S., Loose A., Mall U., Wilken B., Gliem F., Fiethe b., Gombosi T. I., Block B., Carignan G. R., Fisk L. A., Waite J. H., Young D. T., and Wollik H (2007). Rosina – Rosetta Orbiter Spectrometer for Ion and Neutral Analysis Space Science Reviews Volume 128, No 1-4, pp 745-780
- 11 **Bevington P.R.**, D.K. Robinson., (2003). Data Reduction and Error Analysis. Third Edition, McGraw-Hill Companies.
- 12 **Bieler A** (2012). Design of a novel Time of Flight Mass Spectrometer and practical application of computer optimization to the development and tuning of Mass Spectrometers. PhD thesis University of Bern
- 13 **Boyd S.R.** I P Wright, I A Franchi and C T Pillinger, (1987), .High-precision determination of nitrogen stable isotope ratios at the sub-nanomole level, J. Phys. E: Sci. Instrum. 21 (1987) 865-875.



- 14 **Boyd S.R.**, Boyd S R, Wright I P, Franchi I A and Pillinger C T, (1988). Preparation of sub-nanomole quantities of nitrogen gas for stable isotopic analysis J . Phys. E: Sci Instrum. 21 876-85
- 15 **Boyd S.R.**, Pillinger, C.T., (1990). Determination of the abundance and isotope composition of nitrogen within organic compounds: a sealed tube technique for use in static vacuum mass spectrometers. Meas. Sci. Technol. 1, 1176–1183.
- 16 **Cameron** and Eggers. D.F., (1948). An ion “Velocitron”. Rev. Sci. Instruments., 19(9), 605-607
- 17 **Carr R.H.**, R H Carrt, I P Wright, A W Joines S and C T Pillinger, (1986). Measurement of carbon stable isotopes at the nanomole level: a static mass spectrometer, J. Phys. E: Sci. Instrum. 19 (1986). Printed in Great Britain
- 18 **Daulton T.L.**, D.D. Eisenhour, T.J. Bernatowicz, R.S. Lewis, P.R. Buseck, (1996). Genesis of presolar diamonds: comparative high-resolution transmission electron microscopy study of meteoritic and terrestrial nano-diamonds, Geochimica et Cosmochimica Acta 60 (1996) 4853-4872. Chang et al. (1974) :
- 19 **Dempster A.J.**, (1918). A new Method of Positive Ray Analysis, Phys. Rev. 11, 316 – Published 1 April 1918 Phys Rev 11 , 136
- 20 **Dyson N.** (1998). Chromatographic Integration Methods. Second Edition, The Royal Society of Chemistry, 1998
- 21 **MCS6, (2012).** MCS6 5(6) Input 100ps Multi-stop TDC, Multiscaler, Time-Of-Flight User Manual, 2012
- 22 **Frick U**, Pepin R ,(1981). Microanalysis of nitrogen isotope abundances: associations of nitrogen with noble gas carriers in Allende Earth Planet. Sci. Lett. 56 64-81
- 23 **Glynn EF**, (2007). Mixtures of Gaussians, Stowers Institute for Medical Research ,2007
- 24 **Golay S.** ,(1964). <http://wiki.scipy.org/Cookbook/SavitzkyGolay>
- 25 **Goldschmidt V. M.**, (1938). Geochemische Verteilungsgesetze der Elemente, IX .
- 26 **Gray E.B.** et al (2007). Gray E. Bebout, Bruce D. Idleman , Long Li , Andreas Hilkert, Isotope-ratio-monitoring gas chromatography methods for high-precision isotopic analysis of nanomole quantities of silicate nitrogen, Chemical Geology 240 (2007) 1–10
- 27 **Grix U. R.**, Grüner, G. Li, H. Stroh and H. Wollnik, (1989). An Electron Impact Storage Source for Time-of-Flight Mass Spectrometers. Int. J. Mass Spectr. and Ion Processes, 93, 323-330, 1989.
- 28 **Hamamastu**, (2006). Hamamastu MCP guide ,2006
- 29 **Henzler S.**, (2010). Time-to-Digital Converters Series: Springer Series in Advanced Microelectronics, Vol. 29
- 30 **Huber L**, (2010). Cosmic Ray Exposure Histories of Pallasites and the Characteristics of a New Noble Gas ToF-MS, PhD Thesis, University of Bern, Switzerland,
- 31 **Huber M.C.E.**, (2009): Observing Photons in Space – A Guide to Experimental Space Astronomy M.C.E. Huber, A. Pauluhn, J.L. Culhane, J.G. Timothy, K. Wilhelm, A. Zehnder (Eds.) ISBN 978-1-4614-7803-4, second updated edition published in 2013, printed by Springer
- 32 **JOSEPH**, (1979). MICROCHANNEL PLATE DETECTORS Reprinted from Nuclear Instruments and Methods, Vol. 162, 1979, pages 587 to 601
- 33 **Langtangen H.P.**, (2012). A Primer on Scientific Programming with Python (Texts in Computational Science and Engineering)
- 34 **Levin S .**, (1997). Quantitative work in HPLC, <http://www.forumsci.co.il/HPLC/>
- 35 **Kimball**, (2015). LaB6 cathodes single crystal lanthanum hexaboride manual.

- 36 **Lewis R.S.**, E. Anders, I. P. Wright, S. J. Norris and C. T. Pillinger(1983).a Isotopically anomalous nitrogen in primitive meteorites Nature 305 767-71
- 37 **Lewis R. S.**, Tang M., Wacker J. F., Anders E., and Steel E. (1987) Interstellar diamonds in meteorites. Nature 326, 160–162.
- 38 **Mamyrin**, (1973). The mass-reflectron, a new nonmagnetic time-of-flight mass spectrometer with high resolution Zh. Eksp. Teor. Fiz. 64, 82-89
- 39 **Managadze G.G.**, (1984). R.Z. Sagdeev, and I.Y. Shutyaev (1987), Device for mass-spectrometric analysis of the surfaces of space objects. Soviet Patent No. 1218852. Priority of invention 23.07.1984, registered 15.11.1985. Soviet Inventions Bulletin No. 17, 273.
- 40 **McLaren**, (1955). Time-of-flight mass spectrometer with improved resolution. Rev. Sci. Instruments., 16(12), 1150-1157
- 41 **MCS6 user manual**, FAST ComTec GmbH, (2012). MCS6 Input 100ps Multi-stop TDC, Multiscaler, Time-Of-Flight User Manual, Version 1.75, May 8, 2012
- 42 **Nier A. O.**, (1947). A mass spectrometer for isotope and gas analysis, Rev. Sci. Instrum., 18, 398–411, 1947
- 43 **U. Ott**,(2009).Nanodiamonds in meteorites: properties and astrophysical context, Journal of Achievements in Materials and Manufacturing Engineering 37/2 (2009) 779-784
- 44 **PrimerA.** (2012). on Scientific Programming with Python by Hans Petter Langtangen, Volume 6 , 2012
- 45 **Radzig A.A.**, B.M. Smirnov, (1985). Reference Data on Atoms, Molecules and Ions. Springer Verlag Berlin Heidelberg, 1985
- 46 **Cotter R.J.**, (1993).Time-of-Flight Mass Spectrometry, Instrumentation and Applications in Biological Research. American Chemical Society.
- 47 **Sagdeev R Z**, Zakharov A V (1990) A brief history of the expedition to Phobos Sov. Astron. Lett. 16 125
- 48 **Russell S.S.**, J. W. Arden and C. T. Pillinger, (1996). A carbon and nitrogen isotopic study of diamond from primitive chondrites. Meteoritics & Planetary Science 31:343–355.
- 49 **Scherer S.** (1999). Design of a high performance Reflectron Time-of-Flight mass spectrometer for space applications. PhD Thesis, University of Bern, 1999
- 50 **Stephens** (1946). A pulsed mass spectrometer with time dispersion. Phys. Rev. 69, 691; Bull. American Physical. Socety. 21(2), 22
- 51 **Verchovskiy A.B.**, A.V., Fisenko, L. F. Semjonova and C. T. Pillinger ,(1997) . HETEROGENEOUS DISTRIBUTION OF XE-HL WITHIN PRESOLAR DIAMONDS. 60th Annual Meteoritical Society Meeting,1997
- 52 **Wolf B.**, (1995). Handbook of Ion Sources ,Bernhard Wolf: August 31, 1995 by CRC Press Reference - 560 Pages ISBN 9780849325021 - CAT# 2502
- 53 **Wright I P**, Boyd S R, Franchi I A and Pillinger C T,(1988).High-precision determination of nitrogen stable isotope ratios at the sub-nanomole level J . Phys. E: Sci. Instrum. 21 865-75

# Declaration

## Erklärung

gemäss Art. 28 Abs. 2 RSL 05

Name/Vorname: RAMISETTY RAMAKRISHNA

Matrikelnummer: 11-118-023

Studiengang: PHYSICS

Bachelor ☐

Master ☐

Dissertation ☒

Titel der Arbeit: A NEW TIME-OF-FLIGHT MASS SPECTROMETER FOR NOBLE GAS ANALYSIS

LeiterIn der Arbeit: Prof. Dr. INGO LEYA

Ich erkläre hiermit, dass ich diese Arbeit selbständig verfasst und keine anderen als die angegebenen Quellen benutzt habe. Alle Stellen, die wörtlich oder sinngemäss aus Quellen entnommen wurden, habe ich als solche gekennzeichnet. Mir ist bekannt, dass andernfalls der Senat gemäss Artikel 36 Absatz 1 Buchstabe r des Gesetzes vom 5. September 1996 über die Universität zum Entzug des auf Grund dieser Arbeit verliehenen Titels berechtigt ist. Ich gewähre hiermit Einsicht in diese Arbeit.

Bern, 20/05/2015

Ort/Datum

R. Ramakrishna

Unterschrift

